Final Report
for the period
February 1980 to
March 1983

Modeling of Nonlinear Combustion Instability in Solid Propellant Rocket Motors

February 1984

Authors:
J.D. Baum
J.N. Levine

**Air Force
Rocket Propulsion
Laboratory**

Air Force Space Technology Center
Space Division, Air Force Systems Command
Edwards Air Force Base,
California 93523

AD-A176 271

87 1 15 045

30

REPORT DOCUMENTATION PAGE		READ INSTRUCTIONS BEFORE COMPLETING FORM
1. REPORT NUMBER AFRPL-TR-83-058	2. GOVT ACCESSION NO. AD-A176 271	3. RECIPIENT'S CATALOG NUMBER
4. TITLE (and Subtitle) Modeling of Nonlinear Combustion Instability in Solid Propellant Rocket Motors		5. TYPE OF REPORT & PERIOD COVERED Final February 1980- March 1983
		6. PERFORMING ORG. REPORT NUMBER
7. AUTHOR(s) Joseph D. Baum Jay N. Levine		8. CONTRACT OR GRANT NUMBER(s)
9. PERFORMING ORGANIZATION NAME AND ADDRESS Air Force Rocket Propulsion Laboratory/DYC Stop 24 Edwards AFB, California 93523		10. PROGRAM ELEMENT, PROJECT, TASK AREA & WORK UNIT NUMBERS JON: 2308M1UJ
11. CONTROLLING OFFICE NAME AND ADDRESS		12. REPORT DATE February 1984
		13. NUMBER OF PAGES 299
14. MONITORING AGENCY NAME & ADDRESS(if different from Controlling Office)		15. SECURITY CLASS. (of this report) UNCLASSIFIED
		15a. DECLASSIFICATION/DOWNGRADING SCHEDULE

16. DISTRIBUTION STATEMENT (of this Report)

Approved for Public Release; Distribution Unlimited

17. DISTRIBUTION STATEMENT (of the abstract entered in Block 20, if different from Report)

18. SUPPLEMENTARY NOTES

19. KEY WORDS (Continue on reverse side if necessary and identify by block number)

combustion instability
solid rocket motor stability
shock capturing integration techniques
laboratory pulser units
pulse testing of solid rocket motors

20. ABSTRACT (Continue on reverse side if necessary and identify by block number)

The development of a new, comprehensive model of nonlinear longitudinal combustion instability in solid rocket motors is described in Part 1 of this report. The two primary elements of this stability analysis are a finite difference solution of the two-phase flow in the combustion chamber and a coupled solution of the nonlinear transient propellant burning rate. Although quasi-one dimensional, the model has been generalized to treat realistic variable cross-section and partial length grains. An excellent finite difference shock capturing technique--a combination of the Lax-Wendroff, Hybrid and Artificial Compression

DD FORM 1473 EDITION OF 1 NOV 65 IS OBSOLETE
1 JAN 73

schemes--gives the analysis the ability to treat the multiple shock-wave type of instabilities that are frequently observed in reduced smoke solid rocket motors. Ad hoc velocity coupling models were also incorporated into the analysis. Solutions are presented demonstrating that pressure oscillations in unstable solid rocket motors (with metallized as well as unmetallized propellants) reach the same limit cycle (amplitude and waveform) independent of the characteristics of the initiating disturbance. Results obtained with the velocity coupling models demonstrate the ability to analytically predict triggering, DC pressure shifts, modulated amplitude limit cycle, and strongly nonlinear waveforms; phenomena that have all been observed in actual solid rocket motor firings.

The objective of the research work described in the second part was to develop a model capable of the accurate prediction of pulse induced instabilities in solid propellant rocket motors.

Ballistic models of the pyro, low brisance and piston pulsers were developed utilizing a simple lumped volume treatment. The mass and energy flow rates calculated using these models were utilized as boundary conditions for the chamber combustion instability analysis. The model predicts the temporal and spatial evolution of the resulting waveforms (amplitude and harmonic content) in the combustion chamber. Very good agreement is demonstrated between the predicted and measured pulse amplitudes, wave shapes, limiting amplitudes, mean pressure shifts and growth rates for both laboratory and full-scale pulsed solid rocket motors.

A series of ejecta pulsed motor firings was conducted in which spheres of different sizes and materials were ejected through the nozzle to simulate in-flight partial nozzle blockage due to igniter, propellant or other combustion chamber material fragments. Simple laboratory scale solid rocket motors with full and partial length grains were utilized. All of the motors tested were triggered into sustained nonlinear instability. A simple analysis was developed to calculate the velocity of the ejecta and pulse duration. Good agreement between predicted and measured pulse durations was obtained. Two methods were developed for predicting initial ejecta induced pulse amplitudes: a simple model based on linear wave propagation theory and the assumption of quasi-steady nozzle behavior, and a numerical model which utilizes the quasi-steady nozzle assumption to provide a nozzle entrance boundary condition to a comprenensive combustion chamber nonlinear instability analysis. Comparisons of theoretical predictions with experimental data for both pulse amplitude and the motor response to pulsing are presented. The nonlinear instability analysis was found to be capable of predicting the complete range of nonlinear behavior observed in motor response to ejecta pulsing. Good agreement between measured and predicted initial pulse (amplitude and harmonic content), waveform evolution, growth and decay rates, and DC shift was obtained.

TABLE OF CONTENTS

A-1

TABLE OF CONTENTS (Cont'd)

LIST OF TABLES

LIST OF FIGURES

LIST OF FIGURES (Cont'd)

LIST OF FIGURES (Cont'd)

LIST OF FIGURES (Cont'd)

LIST OF FIGURES (Cont'd)

LIST OF FIGURES (Cont'd)

LIST OF FIGURES (Cont'd)

ABSTRACT

The final report documents the results of a research program designed to further our understanding of the physical mechanisms which control the initiation and severity of nonlinear combustion instability in solid propellant rocket motors. In particular, the investigation was directed towards increased understanding of the physical mechanisms which influence the triggering of instabilities by random finite amplitude events such as the expulsion of motor debris out the nozzle.

The first part of this report describes the formulation and solution of the mathematical models of the physical mechanisms governing nonlinear wave propagation in two phase media and the transient burning response of the propellant to both pressure and velocity oscillations. An exhaustive study was conducted to identify and incorporate the best available "shock capturing" scheme. The recently developed sharp combination of the Lax-Wendroff, Hybrid and Artificial Compression schemes gives the analysis the ability to treat the multiple shock-wave type of instabilities that are frequently observed in reduced-smoke solid rocket motors. Ad hoc velocity coupling models were also incorporated into the analysis. Solutions are presented demonstrating that pressure oscillations in unstable solid rocket motors (with metallized as well as unmetallized propellants) reach the same limit cycle (amplitude and waveform) independent of the characteristics of the initiating disturbance.

The second part of the report describes the development of mathematical models to describe the initial pulse produced in the chamber by several

types of laboratory pulsers. The combination of these models with the chamber instability analysis resulted in a unique capability to predict both the initial pulse characteristics and the motor response to pulsing. The validity of the combined models was evaluated by extensive comparison between the analytical predictions and experimental data from pulse tests obtained (under contract) by Aerojet Tactical Systems Company. The capability of the model to predict the observed motor stability in several test cases was demonstrated. Furthermore, excellent agreement was also demonstrated between the measured and predicted initial pulse amplitudes and waveforms, the temporal evolution of waveforms, and the harmonic content of the waves. This investigation has lead to significantly enhanced understanding of the acoustic energy exchange processes and pulse characteristics which lead to motor triggering.

PART I:

MODEL DEVELOPMENT

CHAPTER I

INTRODUCTION

Tactical solid rocket motors are frequently subject to a combustion instability problem at some point in the design cycle. When instability is encountered it can take one of several forms, e.g., linear or nonlinear, longitudinal, or tangential. Over the last twenty years, considerable resources have been expended to understand, predict, control, and eliminate combustion instability in solid rocket motors. Most of this effort has been devoted to linear instability problems, and as a result, such problems can now be treated in a rational, cost effective manner. Comparatively little work has been accomplished towards the understanding and resolution of nonlinear combustion instability problems. Thus, when nonlinear instabilities are encountered, the solution is too often an expensive cut and try process.

Linear instabilities are characterized by small amplitude, sinusoidal oscillations that originate from the amplification of infinitesimal random disturbances in the motor chamber. On the other hand, nonlinear instabilities are usually characterized by large amplitude oscillations having steep-fronted, shock-like waveforms. Nonlinear axial mode instability in solid propellant rocket motors is initiated by random finite amplitude events such as the expulsion of an igniter or insulation fragment through the nozzle. When instability is initiated in this manner in a motor that is otherwise linearly stable (i.e., stable to infinitesimal disturbances) it is said to be a "triggered" instability. The existence of triggered instabilities is a direct result of the fact that all of the acoustic energy gain or loss mechanisms in a solid rocket motor, e.g., pressure and velocity coupled driving, nozzle and particle damping, acoustic mean flow interactions, etc., are nonlinear, i.e., amplitude dependent to some degree. These same nonlinearities also ensure that a nonlinear instability will not grow without limit, but rather will eventually reach a limit cycle amplitude at which the net gains and losses are balanced.

Nonlinear axial mode instabilities usually result in pressure oscillations that propagate as steep-fronted waves which are actually weak shock waves. The acoustic pressure and velocity oscillations are frequently accompanied by an increase in mean chamber pressure (usually referred to as a DC shift) and increased mean propellant burn rate. This increased burn rate is thought to be primarily a response to acoustic velocity oscillations, thus, it is often referred to as acoustic erosivity.

Certain trends and characteristics of nonlinear instability have been documented. However, attempts to form generally applicable conclusions have been stymied by the number, complexity of, and mutual interactions between the governing physical phenomena. The ability to predict, avoid, or eliminate nonlinear instability is, therefore, clearly contingent upon our ability to understand and model these phenomena.

Efforts to understand and model nonlinear instability date back to the 60's, e.g., References 1-3. The most recent work has been divided between so-called "exact" and "approximate" mathematical approaches. The "exact" methods of Levine and Culick[4] and Kooker and Zinn[5] seek to numerically solve the nonlinear partial differential equations governing both the mean and time dependent flow in the combustion chamber, as well as the combustion response of the solid propellant. The "approximate" methods of Culick[6] and Powell, et. al.,[7] utilize expansion techniques to reduce the problem to the solution of sets of ordinary differential equations. Culick and Levine[8] carried out a brief comparison of results obtained with these two approaches and found that within certain limits the approximate techniques yield quite reasonable results. Each of these methods has certain advantages, disadvantages and limitations with regard to accuracy, computation time, generality, etc.

The previously developed "exact" nonlinear instability programs were not capable of treating the multiple traveling shock wave type of instability that occurs in the reduced and minimum smoke tactical motors that have since been developed. Nor did these analyses contain a model for velocity coupling; something which appears to be required in order to predict the types of triggering events and DC pressure shifts that have been observed. The objective of the present research is to extend and improve the model developed in Reference 4 to the point where it can be used as a tool to enhance our understanding of nonlinear instability; as a means to aid in the design and interpretation of related experimental work; as a means to evaluate the validity of advanced combustion response models; and as a design aid to solve or prevent nonlinear instability problems. An outline of the previously developed nonlinear combustion instability model describing two-phase flow in variable area solid rocket combustion chambers is described in Appendix I.

In order to reach the stated objective, the numerical techniques utilized in Reference 4 had to be replaced by more advanced methods and a model for addressing velocity coupled effects had to be incorporated into the computer program.

A critical investigation of the ability of finite difference integration methods to accurately solve the one-dimensional, nonlinear, two-phase, hyperbolic, equations which govern the propagation of shock waves in combustion chambers was conducted. The extensive numerical study that was conducted and the results obtained for several test cases utilizing several candidate finite difference integration techniques are described in Chapter 2.

As mentioned previously, the older "exact" codes were not capable of treating the multiple traveling shock wave type of instability that occurs in reduced and minimum

smoke motors. The capability of the modified model to accurately predict the propagation of multiple shock waves in variable cross-sectional area rocket chambers was examined. Results of this study are reported in Chapter 3.

The sensitivity of solid propellants to acoustic velocity oscillations parallel to the burning surface has been known for many years. This phenomenon, termed velocity coupling, has been observed in both motors and laboratory burners. These observations also support the hypothesis that velocity coupling can be highly nonlinear, and that it is the most likely cause of triggered instabilities and mean pressure shifts in solid rockets. The development of a new improved model for velocity coupling was not considered to be part of the present investigation. Rather, existing models were reviewed to determine which, if any, should be incorporated into the analysis at this time.

Some of the interesting results obtained with the improved model, including the effect of initial disturbance amplitude and wave form, combustion response, and particle concentration upon limiting amplitude; and the ability of ad hoc velocity coupling models to predict phenomena such as triggering and mean pressure shifts are presented in Chapters 4 and 5, respectively.

CHAPTER 2

A CRITICAL STUDY OF NUMERICAL METHODS FOR THE SOLUTION

OF

NONLINEAR HYPERBOLIC EQUATIONS FOR RESONANCE SYSTEMS

INTRODUCTION

This chapter presents the results of an investigation to select a satisfactory finite difference integration scheme for solving the one-dimensional, Eulerian form of the equations describing the propagation of steep-fronted, shock-like waveforms in variable cross-sectional area ducts and two-phase solid rocket combustion chambers.[4] The suitability of candidate finite difference integration schemes for the intended purpose was tested by applying them to a similar but simpler problem; that of finite amplitude shock-like wave propagation in a closed end tube. The equations describing the flow of gas in the tube are identical to those describing the flow in a uniform cross-sectional area rocket motor - after deleting terms contributed by the presence of particles in the flow and terms describing the addition of mass momentum and energy by the combustion processes.

In order to be acceptable for the intended application, a finite difference integration technique must: preserve the high frequency content of the waveforms; be relatively non-dissipative and non-dispersive after many wave cycles; be capable of describing a shock wave as a sharp discontinuity; and be capable of properly treating the reflection of shock waves from boundaries and the partial reflection and transmission at area discontinuities. Moreover, the test case under consideration involves wave steepening from an initially sinusoidal waveform to a shock wave and, due to entropy generation by the shock wave, the possible return to a sinusoidal waveform after many wave cycles. Thus, it is required that the numerical scheme have minimum diffusive

and dispersive errors for both shock waves and harmonic standing waves propagating for many wave cycles. It should also be pointed out that in solving a combustion instability problem, numerically induced pre- and post-shock "wiggles" do not just impair the accuracy of the solution; they can lead to non-physical solutions by erroneously "triggering" nonlinear combustion instabilities.

A shock wave is described mathematically as a surface of discontinuity with a smooth solution on either side of the shock. The shock solution is governed by jump conditions across the discontinuity. Since the assumption that the solution is smooth is inherent to all standard convergence theorems for numerical schemes, it is possible[9] to construct a solution with the wrong speed of propagation. One option to avoid this problem is to use shock-fitting schemes[10,11,12] that treat the shock as an internal boundary and calculate values across the discontinuity utilizing the Rankine-Hugeniot relations. However, this approach is impractical for the intended application (variable area ducts with discontinuous area changes) due to the large number of shock waves and contact surface discontinuities that are created by internal reflections and intersections. Similarly, finite difference schemes that are modeled after and exploit the mathematical theory of the method of characteristics, methods such as the · scheme[13], the split coefficient scheme[14], or the psuedo-characteristics scheme[15], are impractical for this specific test problem. Shock capturing implicit difference schemes offer no particular advantage since the physical problem of interest typically requires time resolution consistent with the stability restrictions of explicit methods.

An alternative to shock fitting is shock capturing. Methods that capture the shock do so by integrating the governing equations across the shock. The capturing approach to the calculation of discontinuous solutions has two essential defects: 1) A discontinuity in the solution of a partial differential equation is approximated by the

solution of a finite difference scheme which is a continuous transition connecting the states on both sides. It has been shown[16] that when the order of accuracy of the numerical scheme is greater than unity, overshoots or undershoots are produced upon crossing the discontinuity. These oscillations (termed wiggles) can: induce nonlinear instabilities when coupled with combustion; damage the accuracy of and spuriously alter the harmonic content of the numerical solution; trigger convergence to non-physical solutions that violate the entropy condition;[17] or generate non-physical rarefaction shocks[18]. 2) When approximating a contact discontinuity by a continuous transition, the width of the transition grows with time as $n^{1/(1+R)}$, where n is the number of time steps and R is the order of accuracy of the finite difference scheme. Thus, in order to maintain accuracy in the neighborhood of a contact discontinuity, a finer mesh than would otherwise be necessary is required. This can significantly increase the computational time, especially in multi-dimensional calculations.

The standard cure for the first problem (wiggles) has traditionally been the addition of artificial viscosity terms to the differential equations. Several types of artificial viscosity methods capable of suppressing post-shock oscillations have been developed[16,19]. However, such artificially induced diffusion also smears out the discontinuities and dissipates the high frequency harmonics that are part of the physical solution. Moreover, the rate of energy dissipation produced by artificial viscosity can be comparable in magnitude to the net rate of energy gains or losses in many combustion systems. The use of an artificial viscosity also precludes any efforts to determine the actual particulate related energy damping rate in two-phase flow systems.

As a result of the drawbacks of artificial viscosity methods, numerous investigators have sought to develop other alternatives for suppressing pre- and post-shock

oscillations. It has been shown[17] that first order monotone schemes yield the proper shock location and do not generate wiggles upon integrating across a discontinuity. Unfortunately, due to their first order accuracy, such schemes are highly dissipative and excessively smear and damp discontinuities. An alternative to utilizing a monotone scheme everywhere is to use it only near a discontinuity while using a higher order scheme wherever the solution is smooth. The hybrid scheme of Harten and Zwas[20] is an example of such a method. Other techniques use the second order scheme (without artificial viscosity) everywhere and then remove the oscillations by utilizing a Shuman filter[21] or enforce monotonicity on second and third order schemes, as done by Van Leer.[22]

Several methods were developed recently to deal with the smearing of the contact discontinuity. These methods include Chorin's implementation of Glimm's method[23], the Flux Corrected Transport (FCT)-SHASTA Phoenical method of Book and Boris and Hain[24], the Low Phase Error Flux Corrected Transport (FCT)-SHASTA Phoenical schemes of Boris and Book[25], and the Artificial Compression Method (ACM) of Harten[26]. Another recently developed scheme[27] is a combination scheme consisting of the Artificial Compression Method (ACM), combined with the Hybrid scheme[20] and the basic second order scheme of Lax-Wendroff[28] (this combination scheme is termed LW+H+ACM). These schemes were combined to yield oscillation-free, sharp transitions of discontinuities while maintaining a high order of truncation error wherever the solution is smooth.

A starting point in the selection of the best available numerical scheme for this test case was an excellent review paper by Sod.[29] Sod tested several numerical schemes for the shock tube test case. His results demonstrated the superiority of the "advanced" methods such as the FCT or ACM schemes, over the "basic" second order

schemes of Lax-Wendroff or MacCormack. It had been shown that the "basic" schemes generated spurious wiggles upon crossing the discontinuity. Nevertheless, it has been noted by Turkel[30] (in another excellent review report) that "it is not clear whether one needs to remove these oscillations except for aesthetic reasons. This seems to be problem dependent. For problems with combustion, it is imperative to prevent oscillations which falsely trigger the combustion process. . . . for dynamic situations, the situation is not clear." The objective of this study was to clarify this situation, complementing Sod's work, and to evaluate the relative accuracy of the candidate finite difference integration schemes for problems describing shock wave propagation over long periods of time (as compared to 20 to 30 time steps as done by Sod), i.e., to determine whether initial wiggles are just an aesthetic imperfection, or if they yield physically erroneous solutions.

For the following reasons, the random choice method of Glimm, implemented by Chorin[23], was not evaluated. This technique is difficult to implement, as it necessitates the evaluation of the location of the sample point with respect to the slip line, shocks, and rarefraction waves (8 options altogether). This poses an extremely difficult problem, especially when there are several shocks and rarefraction waves traveling and interacting inside a variable area closed end tube (or rocket motor) for many wave cycles. Furthermore, additional developments and applications of this scheme utilizing random sampling[31] or Van der Corput sampling[32] indicate that though the shock itself is captured over two or three grid points, the location of the shock is often wrong. An hybridization of Glimm's method with Godunov's method[33], where Godunov's method is utilized at the vicinity of the discontinuity, resulted in the right shock location. However, the shock resolution can be only as good as obtained by Godunov's method, and hence, the shock discontinuity is captured over 4-5 grid points.

The results (either reported in the original papers, Sod's paper, or results of tests conducted by us) for the shock tube problem, utilizing the upwind second order difference scheme[34], or implicit variations of this scheme combined with central spatial differencing, or alternating explicit upwind[35] combined with MacCormack schemes[36] indicated that these schemes cannot yield results that are as good as those obtained by the FCT or the ACM type schemes for this test case. For the same reasons, the psuedo-characteristic method of Carver[15], the -scheme of Moretti[13], the Split Coefficient scheme[14], and the Upstream-Centered Finite Difference schemes of Van Leer[37], were not tested. Van Leer's second order sequel method to Godunov's[38] is a Lagrangian scheme that was considered unduly complicated for practical applications, especially in view of the results presented for the shock tube problem; results that are good, but no better than the much simpler FCT or ACM schemes.

The numerical schemes tested in combination with the current test problem of finite amplitude propagation in a closed end tube were: the first order scheme of Rusanov[39], Rusanov's method combined with artificial compression, the "standard" second order schemes of Lax-Wendroff[28], Rubin and Burstein[58], and MacCormack[36], the hybrid scheme of Harten and Zwas[20], the Flux Corrected Transport (FCT) SHASTA-Phoenical of Book, Boris, and Hain[24], the FCT-SHASTA-Phoenical Low Phase Error (LPE) of Boris and Book[25], Hyman's predictor-corrector[29], and Harten's Combination of the Artificial Compression Method (ACM), Hybrid and Lax-Wendroff schemes.[27]

In order to facilitate the evaluation of the diffusive and dispersive errors of the different numerical schemes tested, the results of the test problems were spectrally analyzed. Since the pressure-time history calculated at any location along the tube is similar to the pressure-time data that would have been measured by a pressure transducer located at that spatial location in an actual test, an existing spectral

11

analysis capability was utilized. This program was originally developed to perform a spectral analysis of the data measured by a pressure transducer attached to a solid rocket motor case during motor firing. The accuracy of the spectral analysis program is within $\pm 2\%$.

WAVE PROPAGATION IN A CLOSED TUBE

Basic Equations:

The one-dimensional, unsteady, inviscid, Eulerian form of the nonlinear hyperbolic equations of gas dynamics can be written in conservation form as follows:

Continuity $\qquad \dfrac{\partial \rho}{\partial t} + \dfrac{\partial (\rho u)}{\partial x} = 0 \qquad\qquad$ (1)

Momentum $\qquad \dfrac{\partial \rho u}{\partial t} + \dfrac{\partial (p + \rho u^2)}{\partial x} = 0 \qquad\qquad$ (2)

Energy $\qquad \dfrac{\partial}{\partial t}\left[\rho\left(\dfrac{C_p T}{\gamma} + \dfrac{u^2}{2}\right)\right] + \dfrac{\partial}{\partial x}\left[\rho u\left(\dfrac{C_p T}{\gamma} + \dfrac{u^2}{2}\right)\right] = 0 \qquad\qquad$ (3)

Equations (1) through (3) may be written in a vector form as:

$$F_t + G(F)_x = 0 \qquad\qquad (4)$$

where

$$F = \begin{vmatrix} \rho \\[1em] \rho u \\[1em] \rho\left(\dfrac{C_p T}{\gamma} + \dfrac{u^2}{2}\right) \end{vmatrix} \qquad\qquad G = \begin{vmatrix} \rho u \\[1em] p + \rho u^2 \\[1em] \rho u\left(\dfrac{C_p T}{\gamma} + \dfrac{u^2}{2}\right) \end{vmatrix}$$

Boundary Conditions:

The boundary conditions at both ends of the closed tube are those of a rigid wall, i.e., $u = 0$. The method of characteristics was utilized to obtain solutions at the boundary points. Currently, a simple Euler integration along the characteristics is used.

Initial Conditions:

The geometry and unperturbed conditions for the test problems were as follows: tube length 1.22 meter (48 inches), pressure 6.895 MPa (1000 psi), temperature 3488.3°K (6279°R), $\gamma = 1.22$. The transient solution was initiated by perturbing the steady state with a first longitudinal standing wave disturbance (corresponding to a frequency of 526 Hz) having an amplitude of 20 percent of the mean pressure. The initial perturbed density and temperature were calculated using isentropic relations while the velocity remained unchanged. The chamber is divided into 50 equally spaced intervals using 51 grid points. All the schemes were tested at a Courant number (C_n) equal to 0.6. This number was chosen for three reasons: (1) Owing to the large variation of the mean flow inside a rocket motor (as in most flow systems), one has to deal with areas of different velocities, and, hence, different Courant numbers (typically varying from 0.3 to close to one); (2) Since each numerical scheme has a Courant number at which the results are best, operating at that Courant number would favor that specific scheme. Operating at $C_n = 0.6$ seems to be a fair region with respect to all schemes; (3) Sometimes it is necessary to choose a smaller computational mesh in certain parts of the system having large gradients (as happens in nozzles, for example), thus forcing the utilization of a low Courant number in regions of large grid sizes. A testing at $C_n = 0.6$, a value in the middle of the expected operating range, enables a better evaluation of the schemes at C_n other than the one most suitable for the specific

13
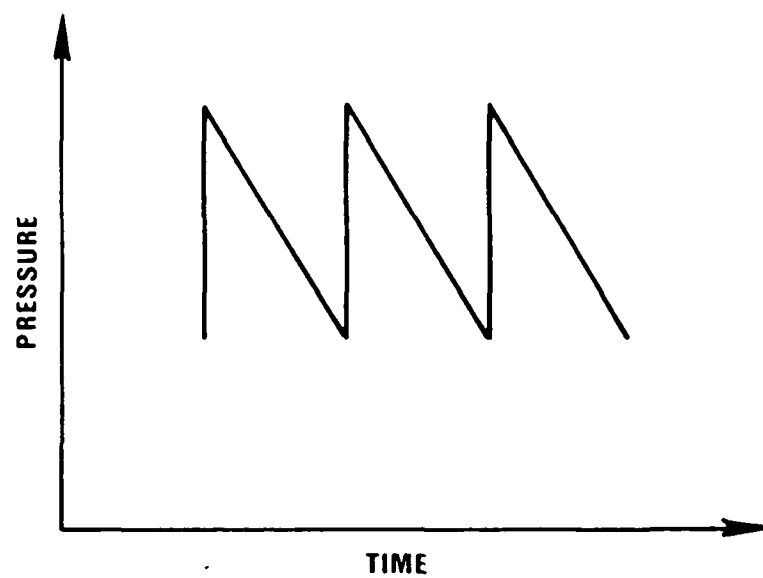
Fig. 1. Repeated shocked sound wave.

14

scheme used. Other solutions were obtained at higher and lower Courant numbers to confirm that the conclusions regarding the relative merits of each scheme are valid in general. Whenever the results obtained at different Courant numbers differed significantly from those obtained at $C_n = 0.6$, they are presented and discussed.

Exact Solution:

An analysis of finite amplitude sound pressure wave propagation in an unbounded medium, neglecting the effects of viscosity and heat transfer, is described in Reference 40. Since the speed of propagation is dependent upon the local temperature, different portions of the wave will travel with different speeds, resulting in wave steepening. It is shown that a finite amplitude waveform will reach a stable sawtooth-like shape, referred to as a shocked sound wave or a repeated shock wave, as shown in Fig. 1. Once the waveform reaches this sawtooth-like shape, effects of entropy production in the fluid due to passage of the shocked wave (when neglecting the effects of viscosity and heat transfer) will attenuate the shocked sound wave, but its shape will not be distorted. Nevertheless, when the amplitude reaches a very low level such that nonlinear wave steepening effects are more than checked by diffusion, the sound wave can no longer maintain its shocked state and will eventually reduce to an harmonic waveform. A spectral analysis of the sawtooth-like waveform (done by Fourier Series representation of the wave) indicates that energy contained in the higher modes falls as $1/n^2$ with respect to the energy contained in the fundamental mode (where n is the mode number). The calculated (based on the exact analysis) amplitude decay rate corresponds very closely to those calculated utilizing the FCT or ACM schemes (which will be shown later).

15

RESULTS

Figure 2a shows the time evolution of pressure oscillations at an end of the tube, obtained by utilizing MacCormack's method. Wave steepening, shock formation, and shock amplitude decay with time are evident in this figure. Expanded views of the pressure oscillations at the end of the tube between nondimensional times of 0 to 10, 20 to 25, and 50 to 55 are shown in Figs. 2b to 2d, respectively. The appearance of wiggles after the wave steepens is shown in Fig. 2b. The time evolution of these wiggles into discrete humps in the waveform is shown in Figs. 2c and 2d. The absence of the higher harmonics is indicated by the discrete humps in the waveform. These figures demonstrate that wiggles are not just a distracting aesthetic phenomenon, but given enough time, develop into an erroneous solution. It should be noticed that the number of discrete humps reduces with time.

Figures 2e through 2g show the time evolution of Power Spectral Density as a function of frequency. It is shown that at the nondimensional time interval of 10 to 20 there is an erroneous amount of energy in the eighth to tenth harmonics. At a later time interval (nondimensional time 20-30), the location of this erroneous energy reaches the sixth to eighth harmonics and finally (nondimensional time 50-60) reaches the fourth to sixth harmonics. The energy in modes higher than the one at which erroneous energy is located vanishes rapidly due to large numerical dissipation. The pressure solution with a number of discrete humps is similar to classical solutions obtained by utilizing a truncated Fourier series representation.

Figure 2h shows the time evolution of accumulative Power Spectral Density as a function of mode number for this test case. It is shown that the erroneous high energy is moving from higher to lower modes with time and that the percentage of energy in

16
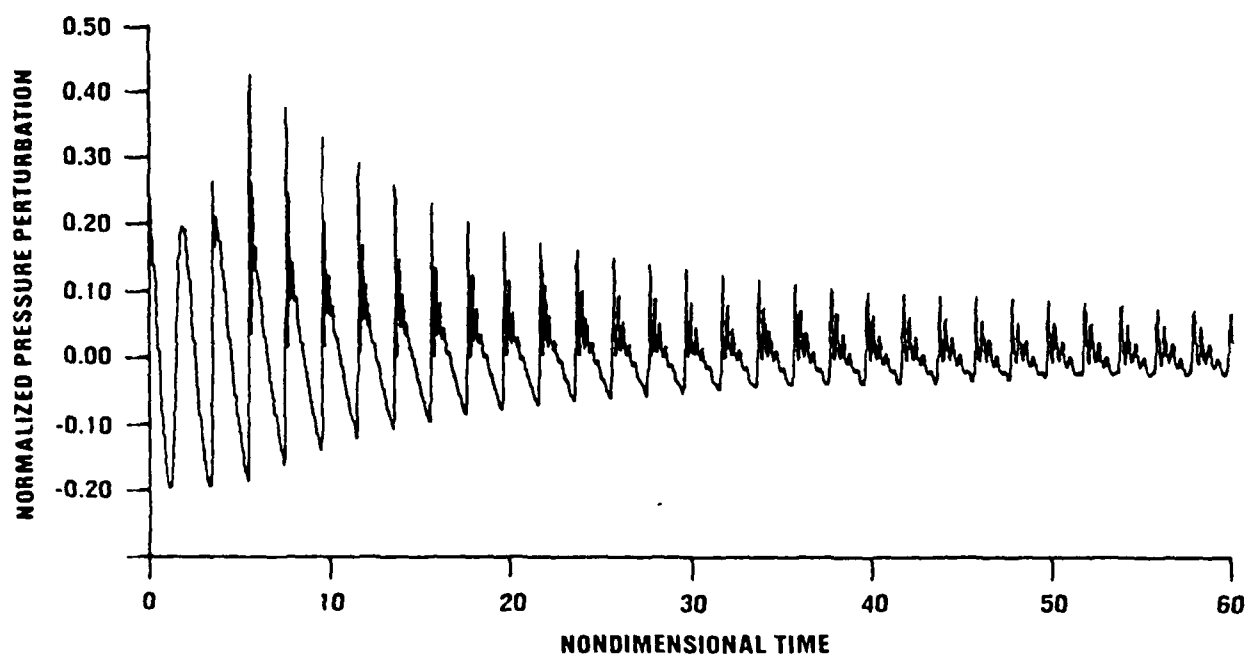
Fig. 2a   Time evolution of normalized pressure oscillations at an end of the chamber (MacCormack).
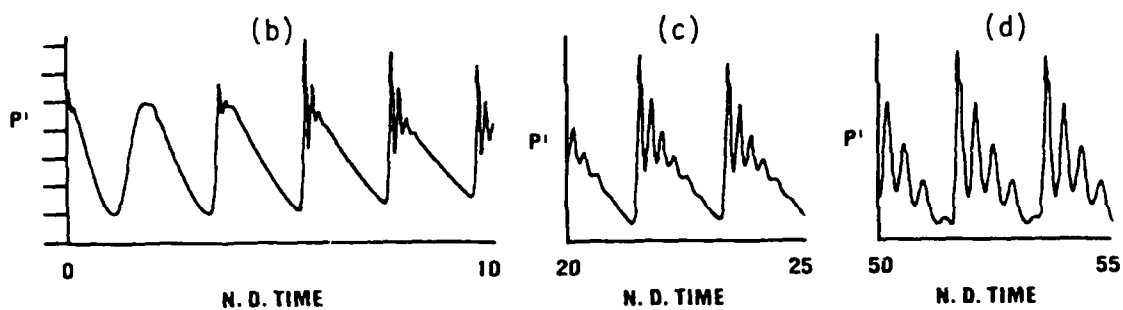
Figs. 2b-d. Expanded views of the normalized pressure oscillations at an end of the chamber (MacCormack).
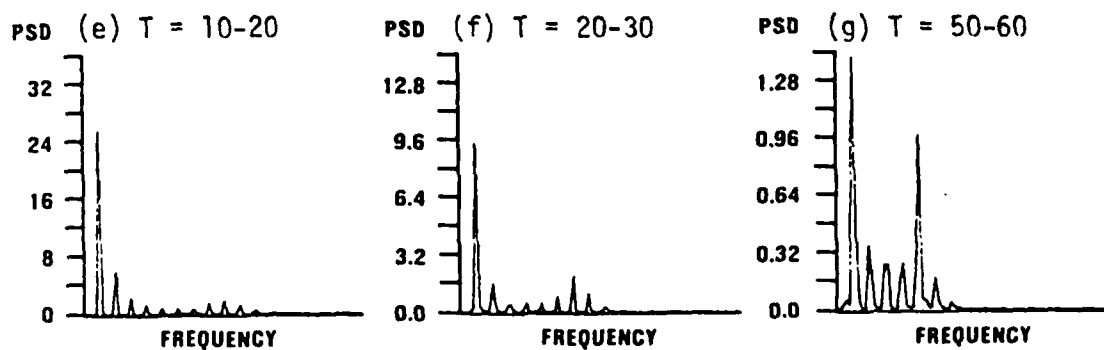
Figs. 2e-g. Time evolution of Power Spectral Density as a function of frequency (MacCormack).

the fundamental mode goes down with time. This constitutes a numerical error since energy transfer among modes happens only as the shock is formed, when energy is transferred from the fundamental mode to higher modes due to wave steepening. Once the shock is formed, no further waveform changes or energy transfer between modes should occur. Moreover, there are no known physical processes present in the system that can cause a transition of energy from a higher mode to a lower mode. Thus, the observed energy transfer from higher to lower modes is a numerically induced phenomena that relates to the truncation error. The time variation of the accumulative power spectrum results from the combination of dissipative and dispersive errors of the numerical scheme, where the dispersive errors cause pressure signals to travel at the wrong speed, while the dissipative error causes over-attenuation of the high frequency modes.

To examine the effect of Courant number on the dissipative and diffusive errors of the MacCormack scheme, the test case was repeated at several Courant numbers ranging from a high of $C_n = 0.98$ to a low of $C_n = 0.2$. Spectral analysis of the results obtained with $C_n = 0.98$ indicates that the initial erroneous energy is contained in the 15 and 16 harmonics. At the nondimensional time of 50 to 60, the erroneous energy is contained in the seventh to ninth harmonics, each containing more energy than the fundamental mode itself (as shown in Fig. 2i). Results obtained with $C_n = 0.3$ indicate that the initial error appears in the seventh to ninth harmonic: at the nondimensional time of 50 to 60, the fourth harmonic contains significantly more energy than the fundamental mode (as shown in Fig. 2j). In this connection it should be mentioned that a decrease in Courant number results in more high harmonic energy dissipation. Examination of the amplitude of the last computed waveform (nondimensional time 58 to 60) indicates that the maximum goes down with Courant number from a value of 13% of the mean pressure with $C_n = 0.98$, to 11% at $C_n = 0.8$, to 9% at $C_n = 0.6$. The

19
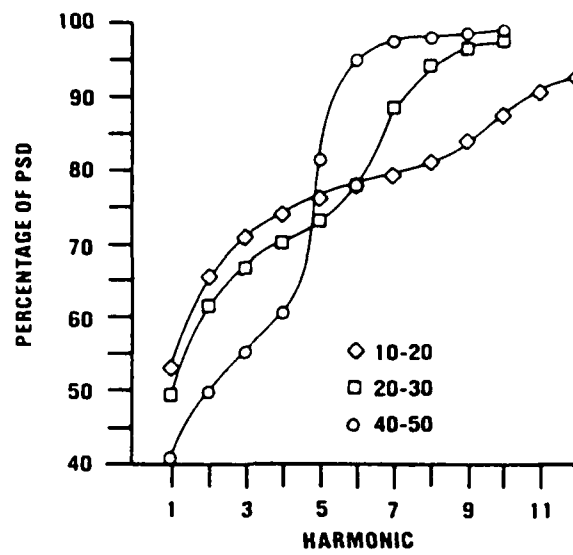
Fig. 2h. Time evolution of accumulated Power Spectral Density as a function of mode number (MacCormack).
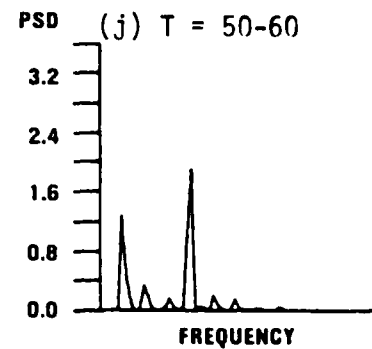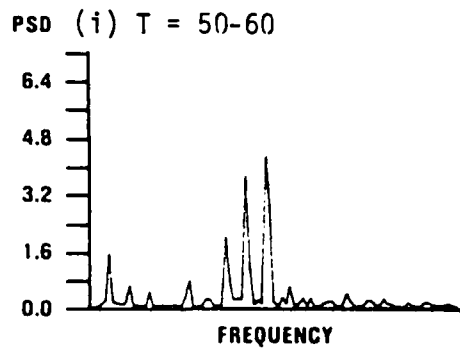
Figs. 2i-j. PSD as a function of frequency (MacCormack): (i) C_n = 0.98, (j) C_n = 0.3.

maximum amplitude value then goes up with further decreases in Courant number, to a value of 11% at $C_n = 0.4$, and 13% at $C_n = 0.2$.

A linear analysis of the dispersive and dissipative errors of the MacCormack scheme as a function of Courant number was conducted in Reference 34. It has been shown that for all Courant numbers, both the dispersive and dissipative errors (per time step) increase with frequency. Dissipative errors increase with increase of Courant number from 0.1 to about 0.6 and then decrease. Dispersive errors decrease with increase of Courant number. These results, although obtained by linear analysis, are in excellent agreement with the results obtained for this nonlinear test case.

The results obtained utilizing the classical second order scheme of Lax and Wendroff are shown in Figs. 3a through 3j. Figure 3a shows the time evolution of pressure oscillations at an end of the chamber. Expanded views between nondimensional time intervals of 0 to 10, 20 to 25, and 50 to 55 are shown in Figs 3b, 3c, and 3d, respectively. It is shown that the initial post-shock oscillations develop in time into a number of discrete humps. The number of humps goes down with time until, at a nondimensional time of 60, there are only 4 humps. The spectral analysis, shown in Figs. 3e, 3f, and 3g for the nondimensional times of 10-20, 30-40, and 50-60, respectively, clearly demonstrates the erroneous transfer of energy. Initially, there is excessive energy at the tenth and eleventh harmonics. This energy propagates towards the lower harmonics until, at the end of the solution, it is shown that there is a significant amount of excessive (erroneous) energy in the fourth to sixth harmonics. It should be noticed that initially 99% of the total energy is contained in the first 15 harmonics. Towards the end of the solution, however, that same percentage of energy is contained in the first seven harmonics, while the energy contained in the harmonics above the eighth has been totally dissipated. Figure 3h which portrays the time

21
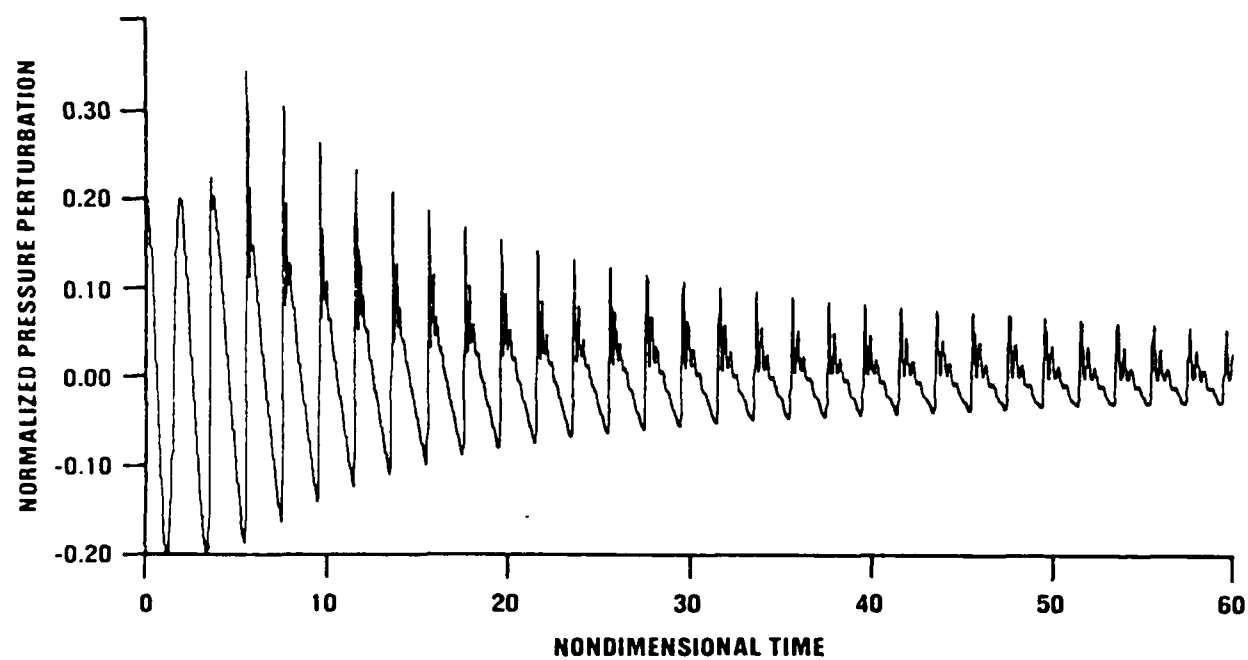
Fig. 3a. Time evolution of normalized pressure oscillations at an end of the chamber (Lax-Wendroff).
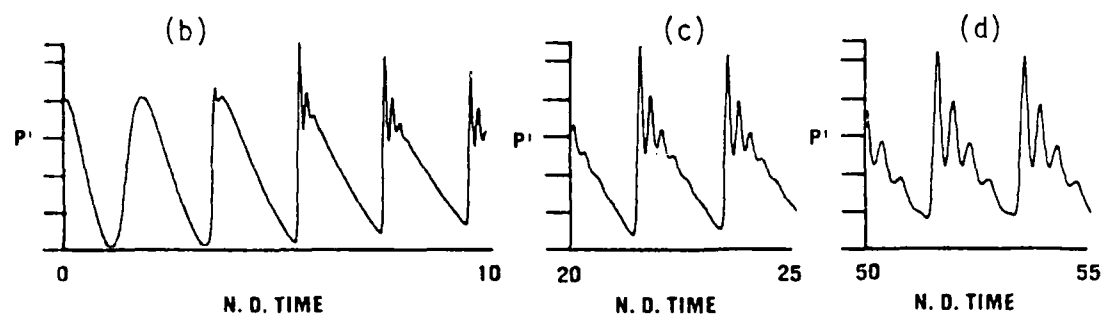
Figs. 3b-d. Expanded views of the normalized pressure oscillations at an end of the chamber (Lax-Wendroff).
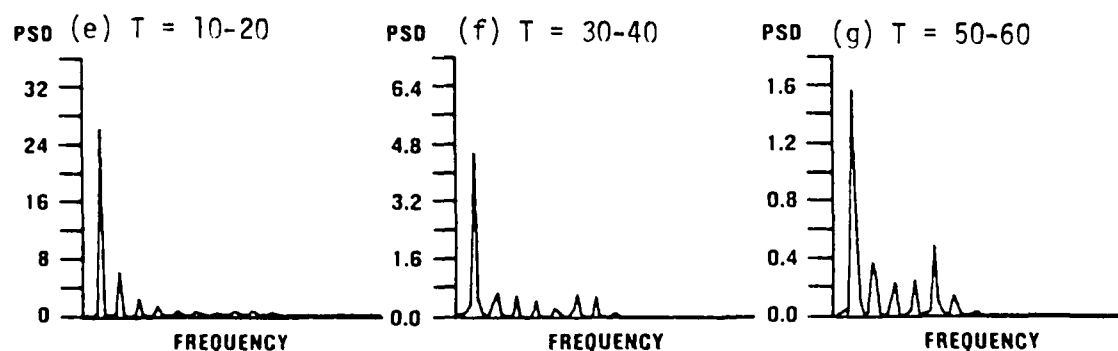
Figs. 3e-g. Time evolution of PSD as a function of frequency (Lax-Wendroff).

variation of the accumulative PSD as a function of the respective harmonics, clearly demonstrates the erroneous energy transfer and the dissipation of energy in the higher harmonics.

An investigation was conducted to examine the effect of variations of Courant number upon the dispersive and dissipative errors of the Lax-Wendroff scheme. Figures 3i and 3j show the time evolution of pressure oscillations between the nondimensional time intervals of 0 to 10 and 50 to 60, respectively, obtained with $C_n = 0.98$. Except for a single overshoot, the solution is almost perfect, as indicated by both the pressure data and the spectral analysis results.

Wiggles appear in the solutions at Courant numbers lower than 0.94. As Courant number is reduced, the location of the erroneous energy shifts to a lower harmonic. Thus, for instance, at the nondimensional time interval 50 to 60, the erroneous energy is located at the sixth and seventh harmonics with $C_n = 0.8$, fourth and fifth harmonics with $C_n = 0.6$, fourth harmonic with $C_n = 0.4$ (about the same energy in the fundamental and the fourth harmonics), third and fourth harmonics with $C_n = 0.2$ (with significantly more energy in the fourth harmonic than in the fundamental mode), and third harmonic with $C_n = 0.1$ (with equal amounts of energy in the first and second harmonics and significantly more energy in the third harmonic). It should be noticed that the amplitude of the last computed waveform (nondimensional time 58 to 60) changes very little with Courant number, in contrast to the results obtained with MacCormack's scheme.

The results obtained utilizing the Lax-Wendroff and Rubin and Burstein schemes are, as expected, very similar. Moreover, the results obtained by these schemes are similar to the results obtained by utilizing MacCormack's scheme. A comparison of the

24
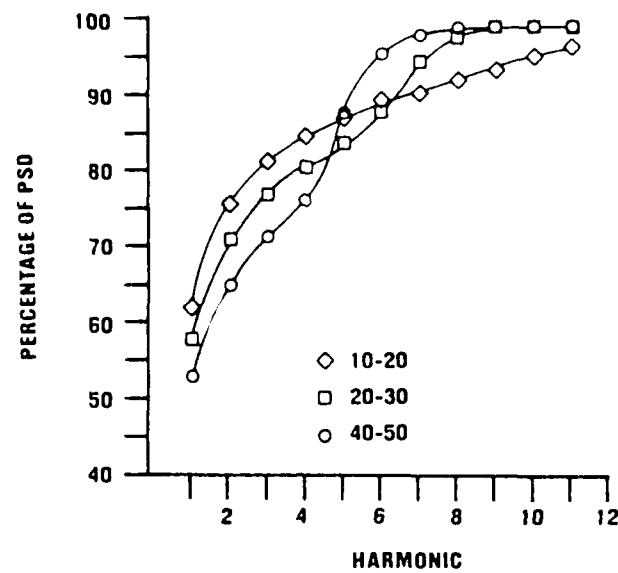
Fig. 3h. Time evolution of accumulated PSD as a function of mode number (Lax-Wendroff).
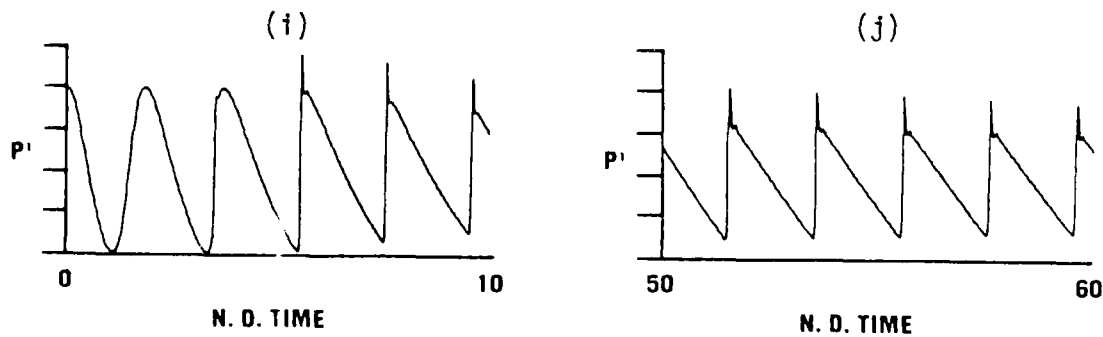
Figs. 3i-j. Time evolution of normalized pressure oscillations at an end of the chamber (Lax-Wendroff).

results indicates that: (1) The first post-shock wiggle appears after the third wave cycle (LW and RB) when the wave is fully shocked, compared to the second wave cycle (with MacCormack) when the wave front is steep, but not yet fully shocked; (2) The percentage of energy (or Power Spectral Density) contained in the fundamental mode is higher, and the excessive high energy in the higher modes is somewhat lower with the Lax-Wendroff and Rubin and Burstein schemes.

All of the earlier methods, i.e., MacCormack, Lax-Wendroff, and Rubin and Burstein were utilized without adding artificial viscosity. The addition of an artificial viscosity term to a numerical scheme was conceived as a way to damp post-shock oscillations. Artificial viscosity does reduce post-shock oscillations, but at the expense of the higher harmonic components of the waveform. The effect of an artificial viscosity on the solution over many wave cycles was explored using Hyman's Predictor-Corrector scheme (as described by Sod[29]). This technique demonstrated poor results for the shock tube tests and was utilized here only to demonstrate the effect of varying the amount of energy dissipated through artificial viscosity. Results obtained utilizing this method with a high value of artificial viscosity (δ equal unity in Hyman's method) indicate that high artificial viscosity prevents a shock from ever forming and the deviations from a perfect sine wave are never large (as shown in Fig. 4). Spectral analysis of this solution shows a complete absence of higher harmonic content. Initially, only the first three harmonics are excited while at a nondimensional time of 60, 99% of the energy is contained in the fundamental mode. Reducing the artificial viscosity coefficient (δ = 0.3, the lowest value at which Hyman's method remains stable) yields a much steeper waveform, but one whose higher harmonic content is still less than it should be (as shown in Fig. 5). Initially, fifteen harmonics are excited, but only the first six harmonics remain excited after 30 wave cycles. As time increases, the action of the artificial viscosity continues to preferentially damp the higher harmonics causing the solution to further degenerate.

26
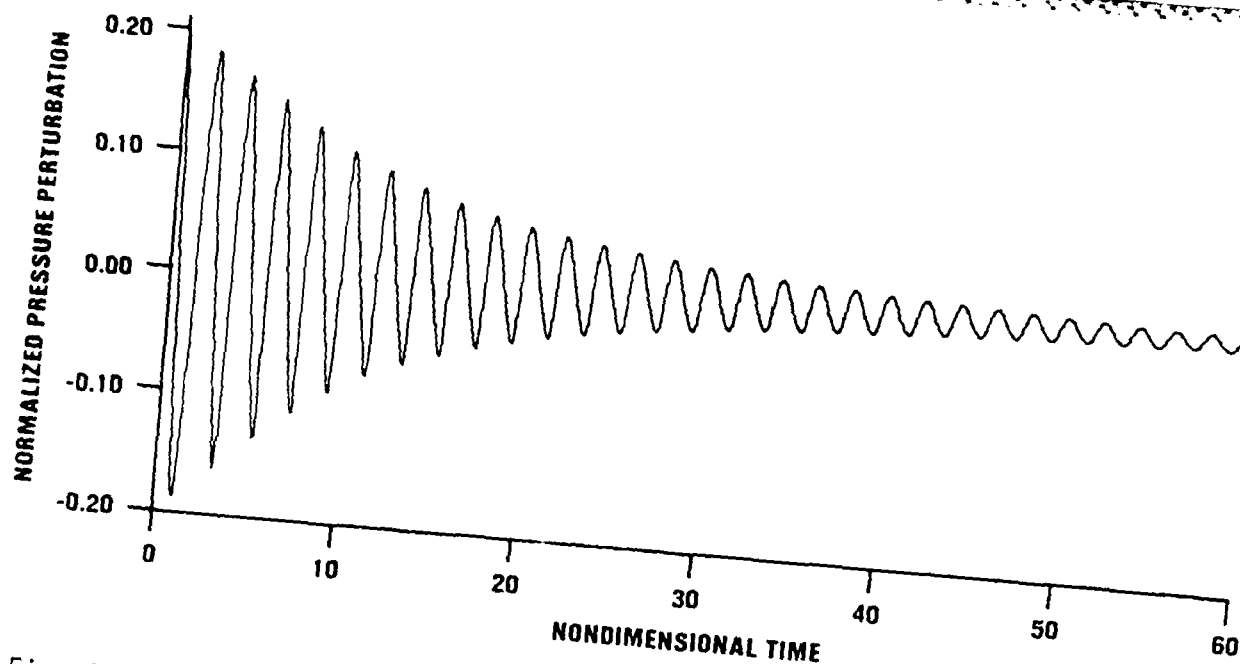
Fig. 4. Time evolution of normalized pressure oscillations at an end of the chamber (Hyman, $\delta = 1.0$).
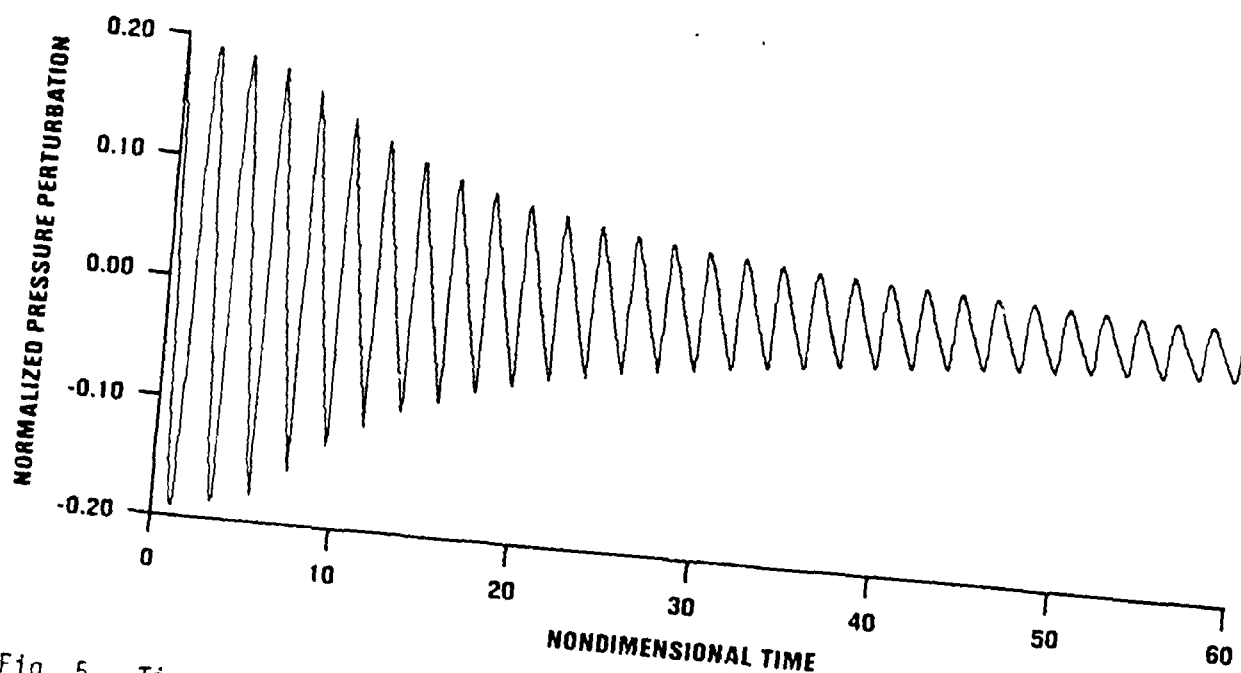
Fig. 5. Time evolution of normalized pressure oscillations at an end of the chamber (Hyman, $\delta = 0.3$).

27

Another scheme that utilizes artificial viscosity to damp pre- and post-shock oscillations is the first order scheme of Rusanov. The results obtained by applying this scheme are strongly dependent on the ratio of ω/C_n where $C_n \leq 1$ and ω is the artificial viscosity coefficient. Figure 6a shows the results of applying this scheme with $\omega/C_n = 1$, where $C_n = \omega = 0.8$. A wiggle appears in the solution after the shock formation. Nevertheless, due to energy dissipation by the artificial viscosity, the wiggle does not develop into a set of discrete humps. The spectral analysis of this case shows that initially as many as 18 harmonics are excited, with erroneous energy contained in the twelfth to fifteenth harmonics. Closer to the end of the run the excessive energy has propagated to the seventh harmonic and energy contained in the twelfth and up harmonics had been totally dissipated.

Figure 6b shows the results of applying Rusanov's scheme with $\omega/C_n = 1.111$, where $C_n = 0.8$. The first post-shock wiggle appears after 4 wave cycles, however, between nondimensional times 40-60 there are no wiggles present and the waveform, although steep, is not in the shocked state. The spectral analysis of this case indicates that initially there is very little excessive energy in the eleventh and twelfth modes, while up to 17 modes are excited. As time progresses, artificial viscosity continuously dissipates the energy in the higher modes until finally, at the nondimensional time interval of 50-60, only 8 modes are excited.

Figure 6c shows the results of applying Rusanov's scheme with an ω/C_n ratio of 1.45, and $C_n = 0.8$. Excessive energy dissipation through artificial viscosity prevents the shock from ever forming and the deviations from a perfect sine wave are just slight. Spectral analysis of this case indicates that initially only the first ten harmonics are excited, while after the nondimensional time of 22, only the first one is excited. The amplitude values reached by the waveforms at the nondimensional time of 60 as a
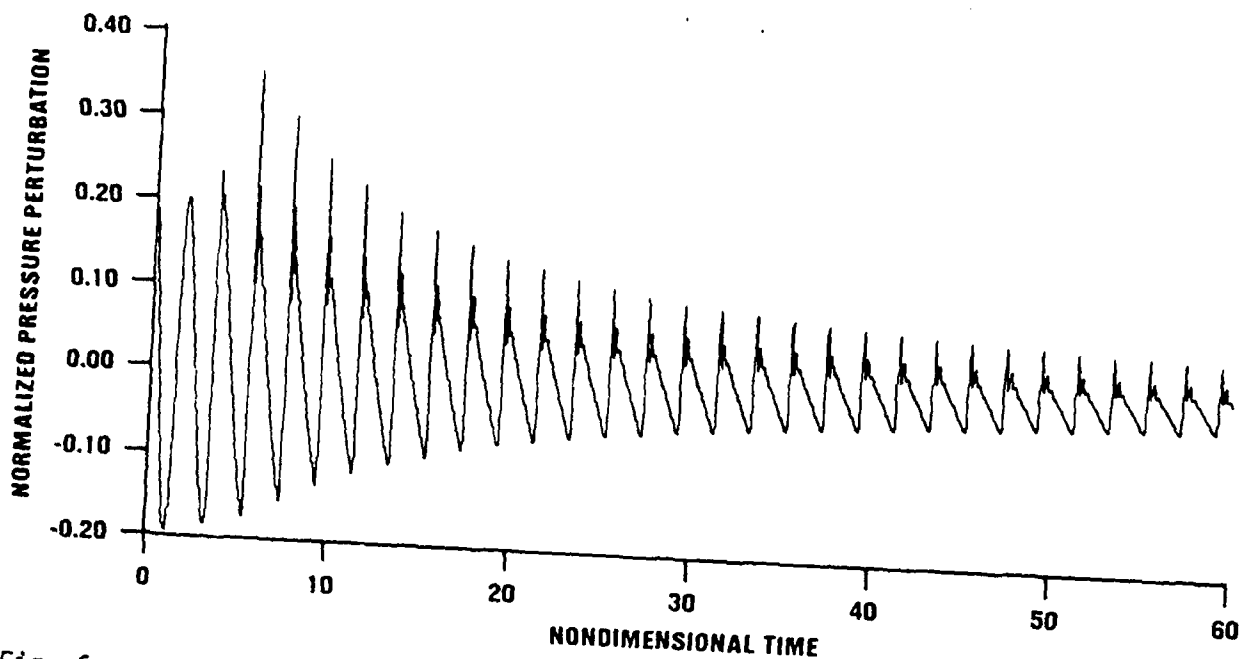
Fig. 6a. Time evolution of normalized pressure oscillations at an end of the chamber (Rusanov, $C_n = \omega = 0.8$).
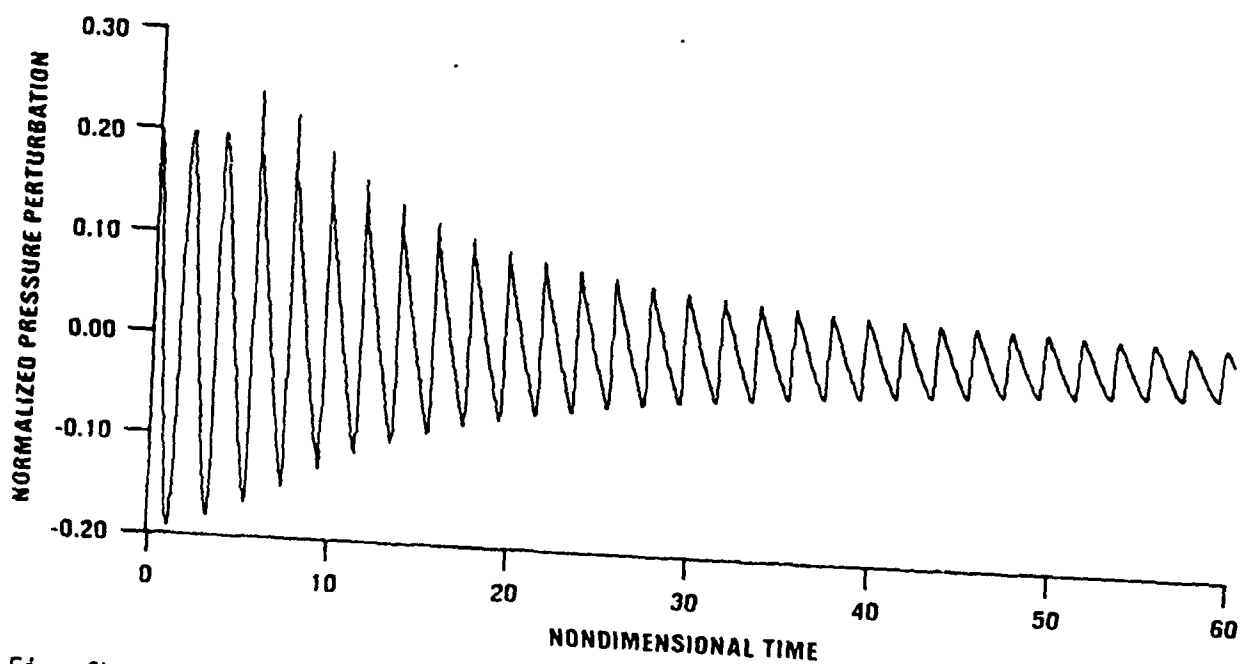
Fig. 6b. Time evolution of normalized pressure oscillations at an end of the chamber (Rusanov, $C_n = 0.8$, $\omega = 0.888$).

function of ω/C_n were tabulated. Analysis of these results indicates that the amplitude is proportional to the ratio ω/C_n to the power of 2.2163. It is concluded that by fine tuning the ratio of ω/C_n (possibly in the region $1.11 \leq \omega/C_n$ 1.25), it is possible to achieve optimum steepening without generating wiggles. Nevertheless, since the spectral analysis of even the best solution (with ω/C_n of 1.111) indicates excessive damping of high modes by the use of artificial viscosity, this optimum solution cannot be as good as the solution obtained by the FCT or ACM type schemes (as will be shown later) that preserve the high frequency content of the waveform. In this connection it should be noted that Sod[29] has shown that results obtained for the shock tube problem with $C_n = 0.9$, $\omega = 1.0$, and $\omega/C_n = 1.111$ are quite poor and that the addition of artificial compression resulted in great improvement. Figure 6d shows the results for a similar test (Rusanov and ACM) with $C_n = 0.85$, $\omega = 1.0$, and $\omega/C_n = 1.17$. This ratio was chosen in accordance with the above study (i.e., optimum region of operation). A wiggle that appeared in the solution after shock formation disappeared at later times, as was the case with the Rusanov scheme itself. The waveforms between nondimensional times 50 and 60 are significantly steeper than with Rusanov's scheme without artificial compression. The spectral analysis data indicates that the addition of ACM resulted in the initial excitation of more higher harmonics (25 modes were excited with ACM compared to 17 without ACM). In addition, despite energy dissipation from the higher modes due to artificial viscosity, the first 20 harmonics are still excited towards the end of the test, resulting in a steeper waveform.

Monotone schemes are known[30] to capture shocks without overshoots and to yield the correct shock location. Unfortunately, linear monotone schemes are only first order accurate. An improvement, suggested by Harten and Zwas[21] was to form a hybrid difference operator which combines the classical second order Lax-Wendroff[26] scheme with a first order monotonic scheme. The first order monotonic scheme is
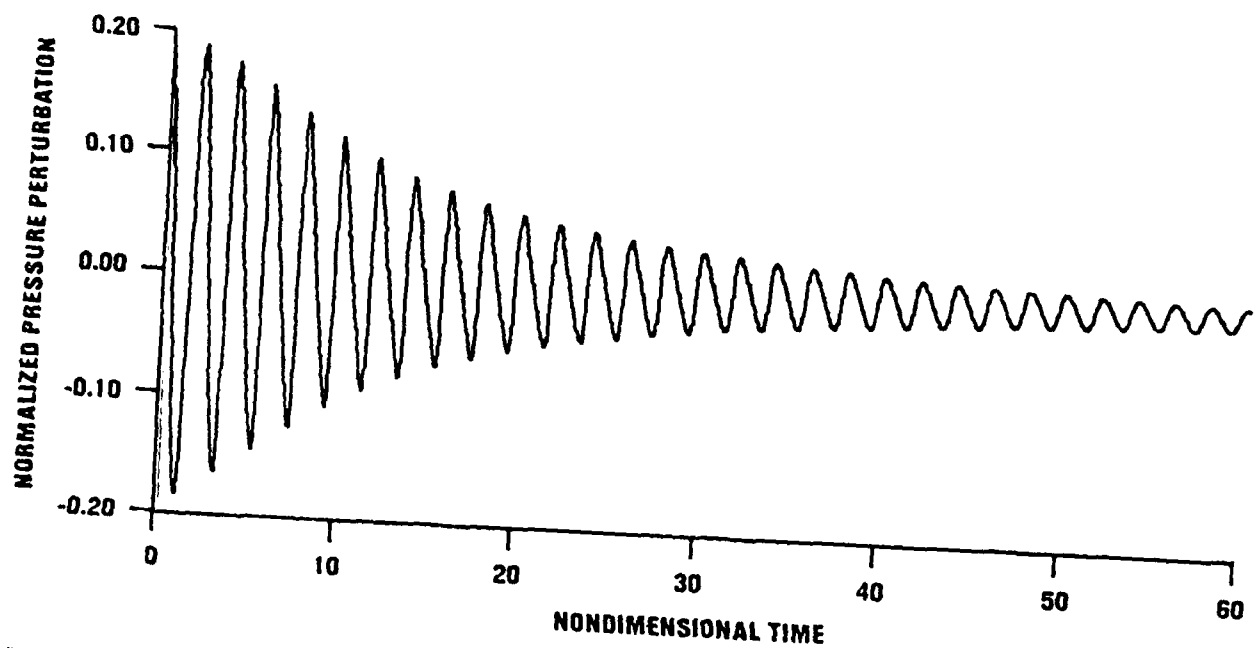
Fig. 6c. Time evolution of normalized pressure oscillations at an end of the chamber (Rusanov, C_n = 0.8, ω = 1.16).
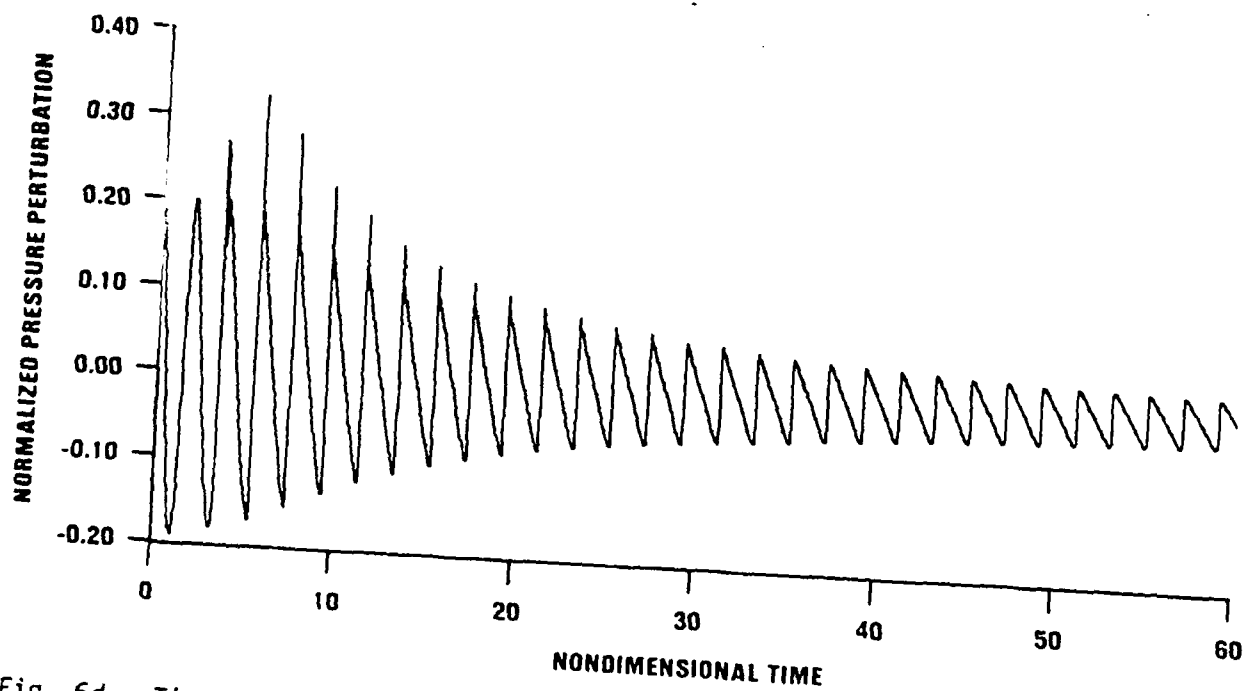
Fig. 6d. Time evolution of normalized pressure oscillations at an end of the chamber (Rusanov + ACM, C_n = 0.85, ω = 1.0).

activated only in the vicinity of admissible discontinuities while the second order scheme is applied to the smooth portion of the flow. Nevertheless, it is recognized that the first order accurate monotone scheme produces excessive smoothing of the shock (i.e., excessive energy in the low frequency modes).

The results obtained utilizing this hybrid scheme are shown in Fig. 7. Figure 7a shows the time evolution of pressure oscillations between nondimensional times 0 and 60. It is shown that a shock is formed after 3 wave cycles, and that the waveform remains steep throughout the duration of the solution. The spectral analysis data indicates that initially the first 25 harmonics are excited, while towards the end of the test, only the first 8 harmonics remain excited. The time variation of the accumulative percentage of Power Spectral Density (PSD) contained in the respective harmonics for this scheme (shown in Fig. 7b) indicates that there are no erroneous shifts of power spectral density among the high order modes. Nonetheless, since the scheme is based upon transfer to a linear (first order accuracy) scheme at shock transitions and contact discontinuities, the lower harmonics contain more energy than should have actually been there (for instance, the fundamental mode contains 70 percent of the total energy), and the energy in the higher modes has been excessively dissipated (99.3 percent of the total energy that was initially contained in the first 15 harmonics is finally contained at the first six harmonics).

Figure 7c shows the dependence of the accumulative PSD upon Courant number and the number of grid points. It is shown that dissipation of energy due to diffusive errors increases significantly as Courant number decreases (as shown by the increase of energy contained in the lower harmonics). Conversely, (as should be expected, due to the first order accuracy of the monotonic scheme), it is shown that the energy dissipation due to diffusive errors decreases with an increase in the number of mesh

32
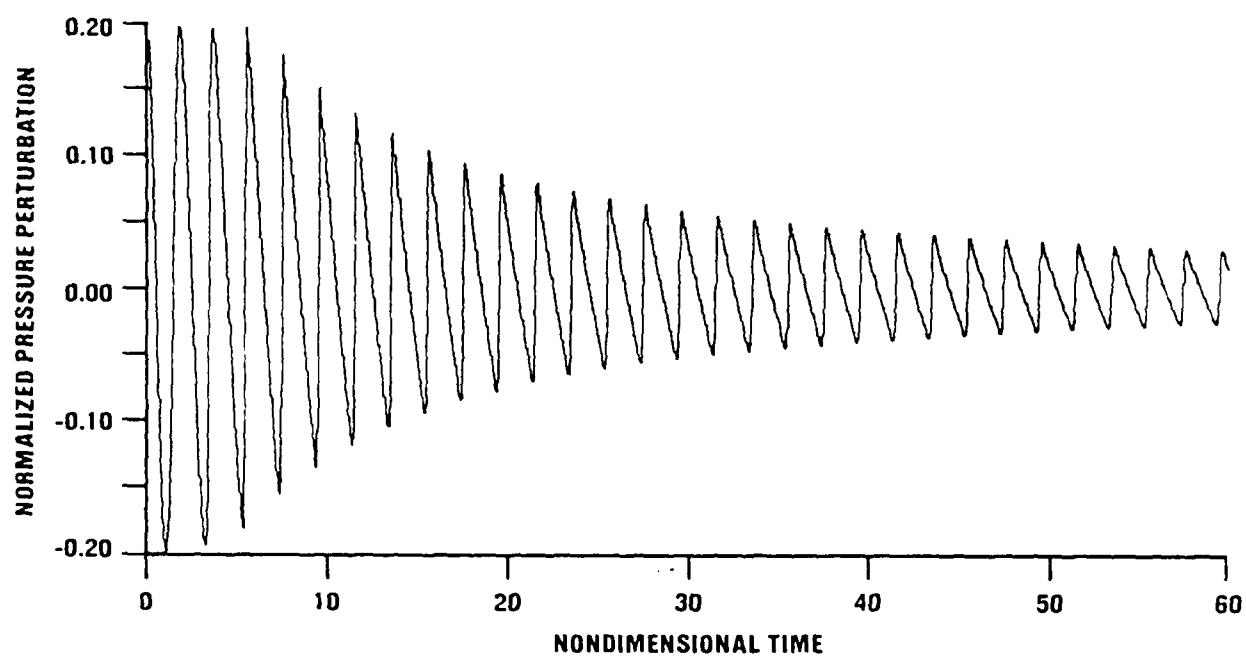
Fig. 7a. Time evolution of normalized pressure oscillations at an end of the chamber (Hybrid).

33
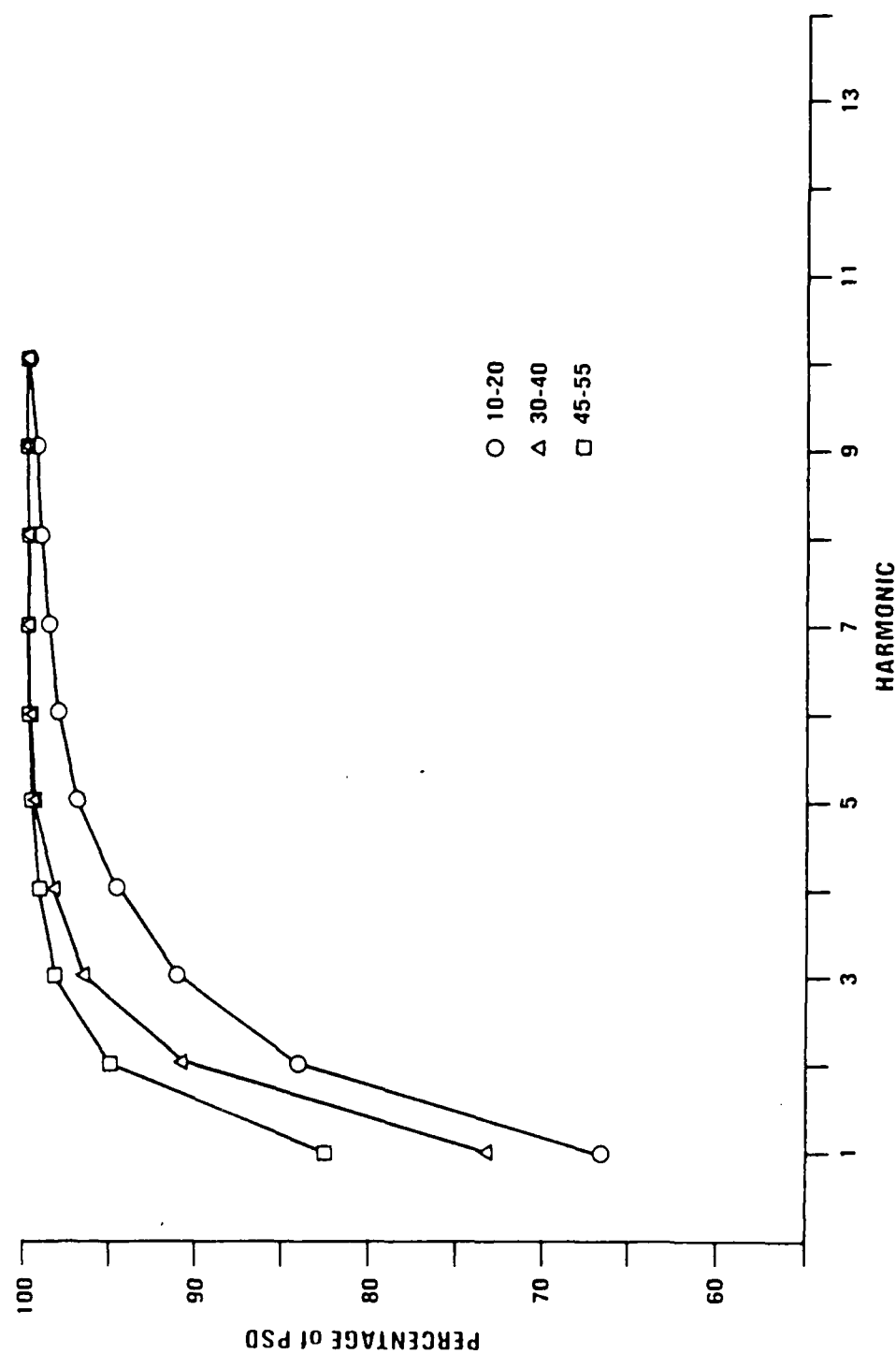
Fig. 7b. Time evolution of the accumulative percentage of PSD.
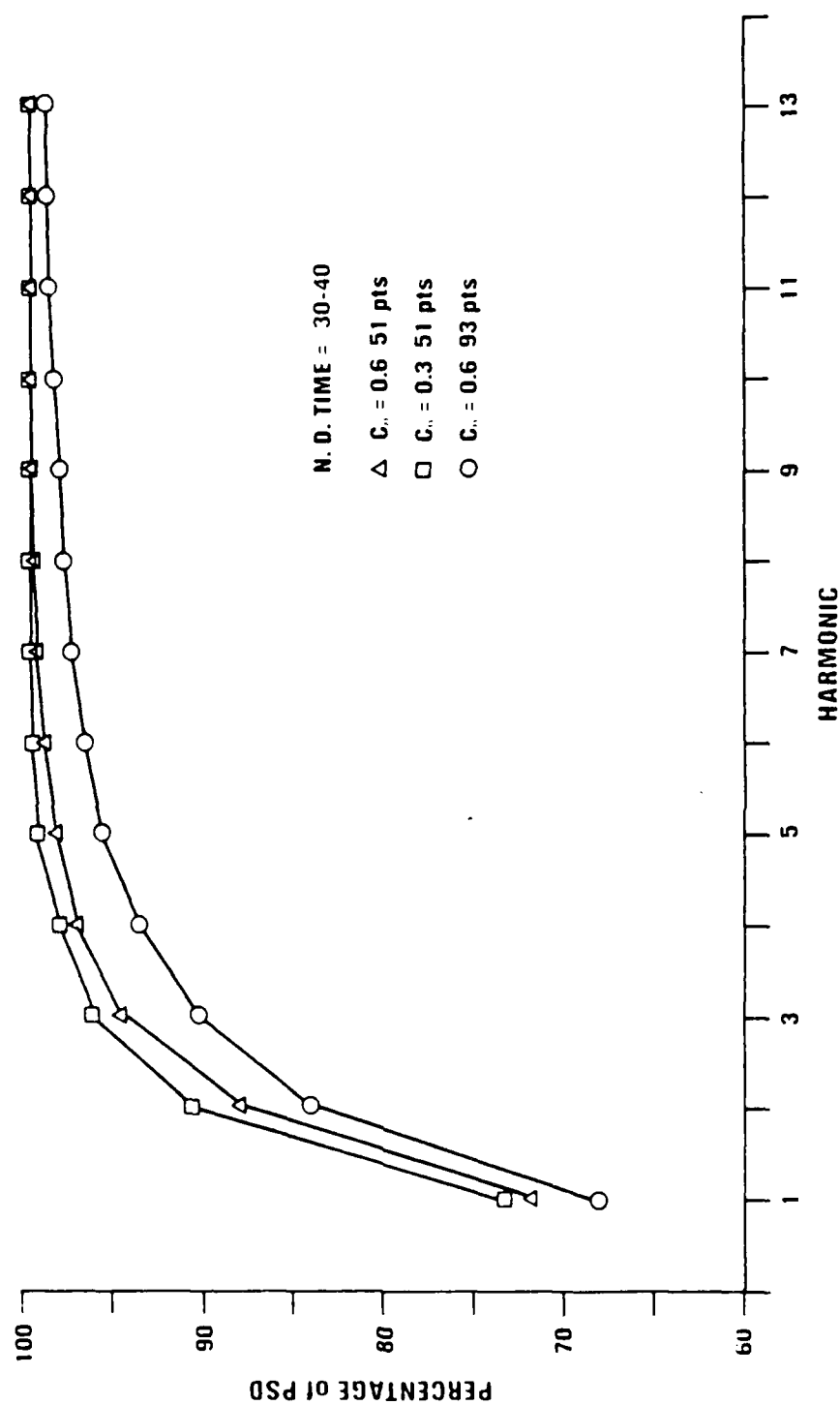
Fig. 7c. Accumulative PSD as a function of Courant number and number of grid points.

35

points. With 93 points, at least 18 harmonics remain excited towards the end of the test. An expanded view of the time evolution of pressure oscillations between nondimensional times 50 to 60 (obtained with 93 mesh points) is shown in Fig. 7d. Excellent shock resolution is demonstrated. In this connection it should be mentioned that the excellent shock resolution obtained with 93 mesh points, combined with a significantly reduced high frequency energy dissipation yields a much better approximation to the exact solution. Indeed, the energy distribution among modes obtained with 93 points is very similar to the energy distribution obtained with the combination scheme of Lax Wendroff, Hybrid and Artificial Compression Method (as will be presented later).

The first of the Flux Corrected Transport (FCT) Schemes tested was the FCT-SHASTA-Phoenical scheme, developed by Boris, Book, and Hain.[24] This method combines the two step Lax-Wendroff scheme with antidiffusive correctors that contain higher order terms which are subject to a limiting routine in order to preserve the monotonicity of the provisional results. Following Sod[29], the variable diffusion/antidiffusion coefficient η was set to 0.125.

Figure 8a shows the time evolution of pressure oscillations at an end of the tube between nondimensional times 0 and 60. The expanded view of the pressure oscillations between nondimensional times 20 to 30, and 50 to 60 are shown in Figs. 8b and 8c, respectively. It is shown that the small initial pre-shock error develops with time into a pre-shock wiggle. Moreover, there is an observed curvature in the center of the expansion wave, instead of the anticipated straight line. The shock itself is captured over 4 grid points, even after 5260 time steps (30 wave cycles).

36
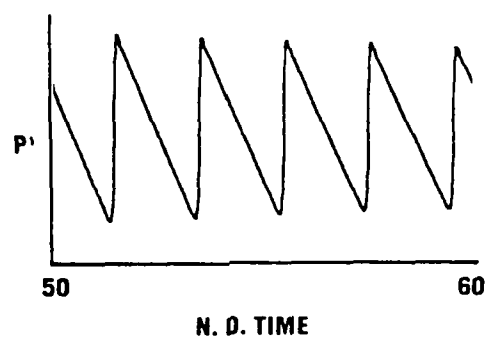
Fig. 7d. Expanded view of the normalized pressure oscillations at the end of the chamber (Hybrid, 93 grid points).
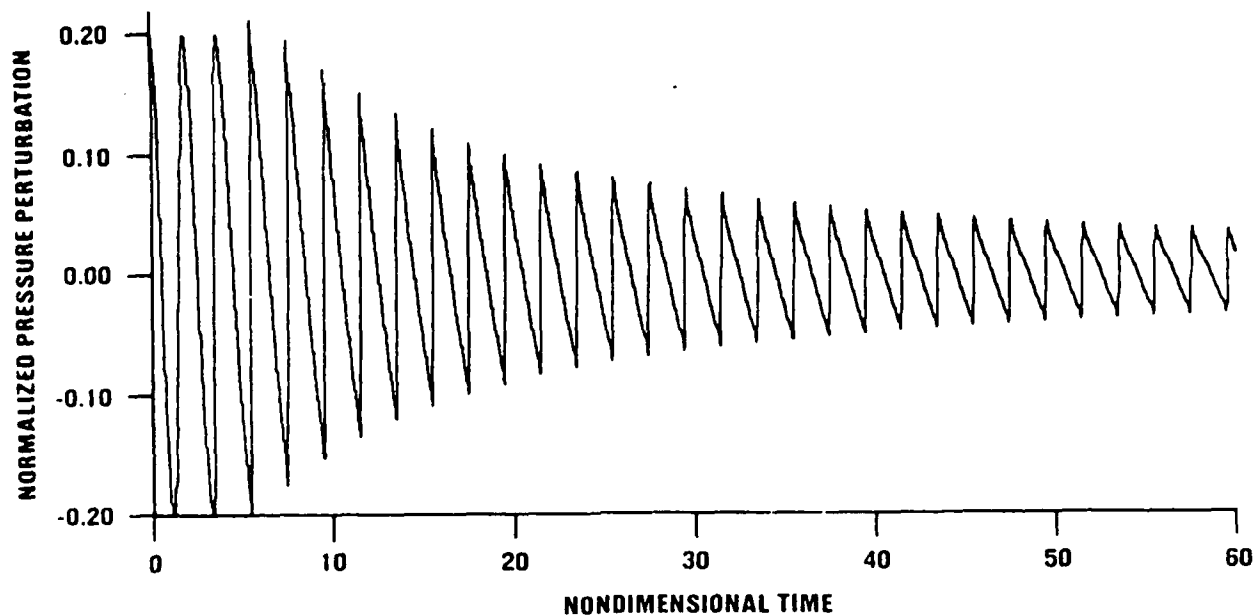
Fig. 8a. Time evolution of normalized pressure oscillations at an end of the chamber (FCT-LW).

The time variation of the accumulative power spectral density as a function of the respective harmonic indicates that after the shock formation, there is a slight decrease in the percentage of energy contained in the fundamental mode and a slight increase in the percentage of energy contained in the second to tenth harmonics, while the percentage of energy contained in the higher harmonic (above ten) has somewhat diminished. In addition, this data shows that there is initially some excessive energy in the 8th and 9th harmonics, that propagates towards the end of the run to the 7th and 8th harmonics. In this connection, it should be mentioned that variations of the energy content above the seventh harmonic are within a quarter of a percent, which is within the error limitations of the spectral analysis program.

Overall, the FCT-SHASTA-Phoenical scheme yielded good results for these test conditions. However, when this scheme was utilized to solve the same problem with initial disturbances of higher amplitudes (0.4 and 0.6 of the mean pressure instead of 0.2) the scheme yielded erroneous results. Figures 8d and 8e show the expanded views of the time evolution of calculated pressure oscillations between nondimensional times, 20 to 30 and 50 and 60, respectively, in response to a fundamental mode disturbance with an amplitude equal to 40% of the steady pressure. Figures 8f and 8g show the time evolution of pressure oscillations between nondimensional times 20 to 30, and 50 to 60, respectively, for an initial disturbance with an amplitude equal to 60% of the steady pressure. These figures show the development of a small imperfection at the center of the expansion wave to either a wiggle, or, for the higher amplitude cases, to a second shock. Analysis of the spectral data indicates only minor changes in the energy distribution among the modes as a function of time, such as a slight energy increase in the fundamental mode and slight energy decrease in the higher harmonics. These minor changes presumably cause the distortion observed in the waveform.
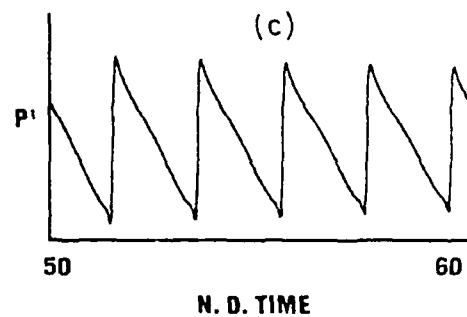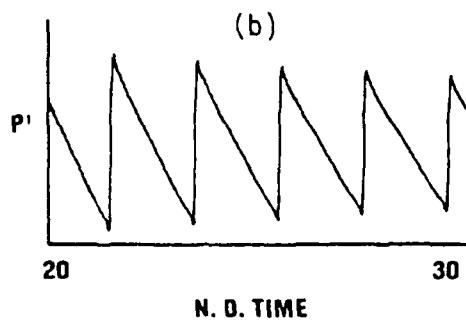
Figs. 8b-c. Expanded views of the normalized pressure oscillations at an end of the chamber (FCT-LW).
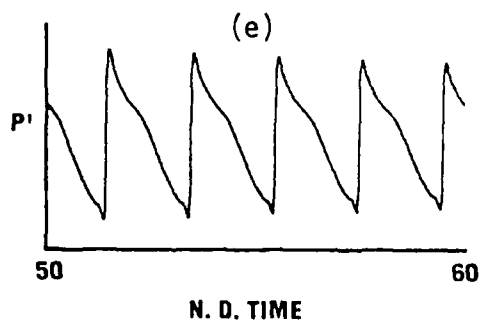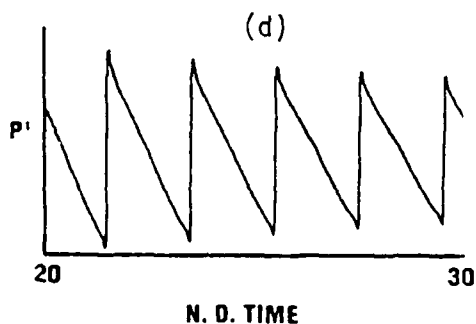
Fig. 8d-e. Expanded views of the normalized pressure oscillations at an end of the chamber (FCT-LW, $\Delta P_o = 0.4\bar{P}$)

39

Figures 8h and 8i show expanded views of pressure oscillations between nondimensional times 20 to 30, and 50 to 60, respectively, obtained with Courant number of 0.6, 93 grid points and an initial disturbance amplitude of 40% of the steady pressure. A comparison with results obtained with the same initial disturbance amplitude for the standard test case (i.e., C_n = 0.6, 51 grid points) indicates that both solutions have a curved expansion instead of the straight line expected from the analytical solution of an N wave). However, the solution obtained with 93 grid points indicates that a numerically induced shock is formed at the center of the expansion wave. The steepening process of an initial error into a second "shock" wave is of great interest. The initial slight "wiggle" is treated by the numerical scheme as an adverse density gradient (or as a compression wave) and thus it acts to steepen it. The density gradient increases until it becomes large enough to be treated by the system as a discontinuity. This process of "artificial steepening" is very similar to the steepening process observed when utilizing a numerical combination scheme that incorporates artificial compression. The addition of artificial compression was conceived as a way to steepen shock transitions that were smeared by the first order monotonic schemes. Unfortunately, most of these combination schemes treat any arbitrary disturbance with a high enough density gradient value as a shock and will steepen it.

The FCT-SHASTA-Phoenical Lax-Wendroff scheme was also tested with several Courant Numbers varying from 0.3 to 0.85. With Courant number of 0.85 the initial single pre-shock wiggle develops into a series of wiggles (as shown in Fig. 8j). In contrast, the results at C_n = 0.3 indicate no pre-shock wiggle; rather, a post-shock wiggle appears in the solution (Fig. 8k).

In conclusion, it has been shown that FCT-SHASTA-Phoenical Lax-Wendroff scheme yields very good results for low amplitude disturbances, but yields erroneous results for high amplitude disturbances, when calculated over many wave cycles.

40
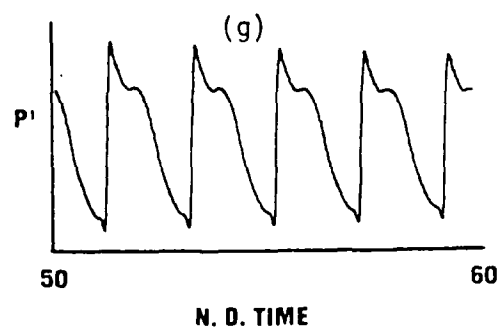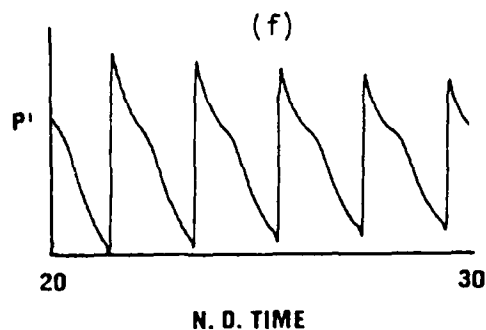
Figs. 8f-g. Expanded views of the normalized pressure oscillations at an end of the chamber (FCT-LW, $\Delta P_o = 0.6\bar{P}$).
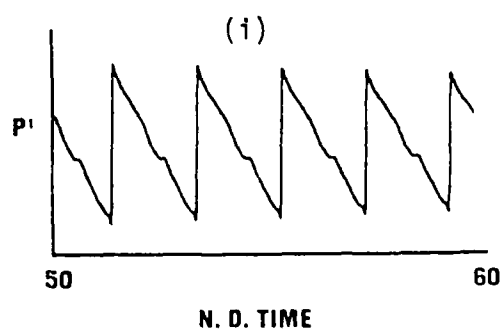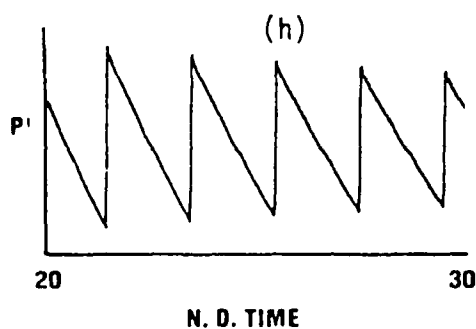
Figs. 8h-i. Expanded views of the normalized pressure oscillations at an end of the chamber (FCT-LW, $\Delta P_o = 0.4\bar{P}$, 93 grid points).

41
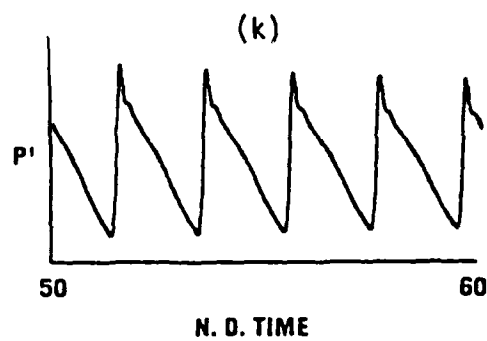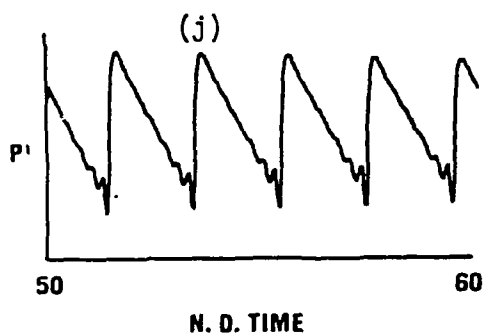
Figs. 8j-k. Expanded views of the normalized pressure oscillations (FCT-LW): (j) $C_n = 0.85$, (k) $C_n = 0.3$.

42

The second of the Flux Corrected Transport schemes tested was the FCT-SHASTA-Phoenical Low Phase Error[25] (FCT-LPE). This scheme minimizes phase errors (i.e., dispersive errors) instead of minimizing diffusive errors. The rationale for this modification is: diffusive errors generally affect the high frequency content (i.e., short wavelength) rather than the low frequency content (i.e., long wavelength). Since the high frequency modes usually also suffer the most dispersive errors, damping of these modes may actually reduce the overall error. The importance of reducing phase errors is enhanced when the velocity is predominantly in one direction (as happens in a rocket motor). For the square wave test case,[25] this scheme demonstrated the best results of all the FCT explicit schemes developed to that date.

Figure 9a shows the time evolution of the oscillatory pressure amplitude at an end of the tube obtained by utilizing this scheme. The expanded view of pressure oscillations between nondimensional times 50 to 60 (shown in Fig. 9b) indicates that the initial pre-shock error develops in time into a pre-shock wiggle. It should be noticed that the initial shock transition is not sharp, but rather is rounded and becomes even more rounded with time, indicating attenuation of energy in the high harmonics. An analysis of the spectral data indicates that: the percentage of energy in the fundamental mode is higher than with the FCT-LW scheme, and that the second through eighth harmonics have slightly less energy; less modes are initially excited than with the FCT-LW scheme; the attenuation of energy in the higher modes is faster; and that the energy in some higher modes (13 and above) had actually been dissipated altogether.

The results obtained by utilizing this scheme to solve the same test problem with higher initial disturbance pressure amplitudes (0.4 and of 0.6 of the steady pressure) are very similar to those obtained with the FCT-SHASTA-Phoenical scheme, except for the addition of a pre-shock wiggle. Similar conclusions are drawn with respect to the

43
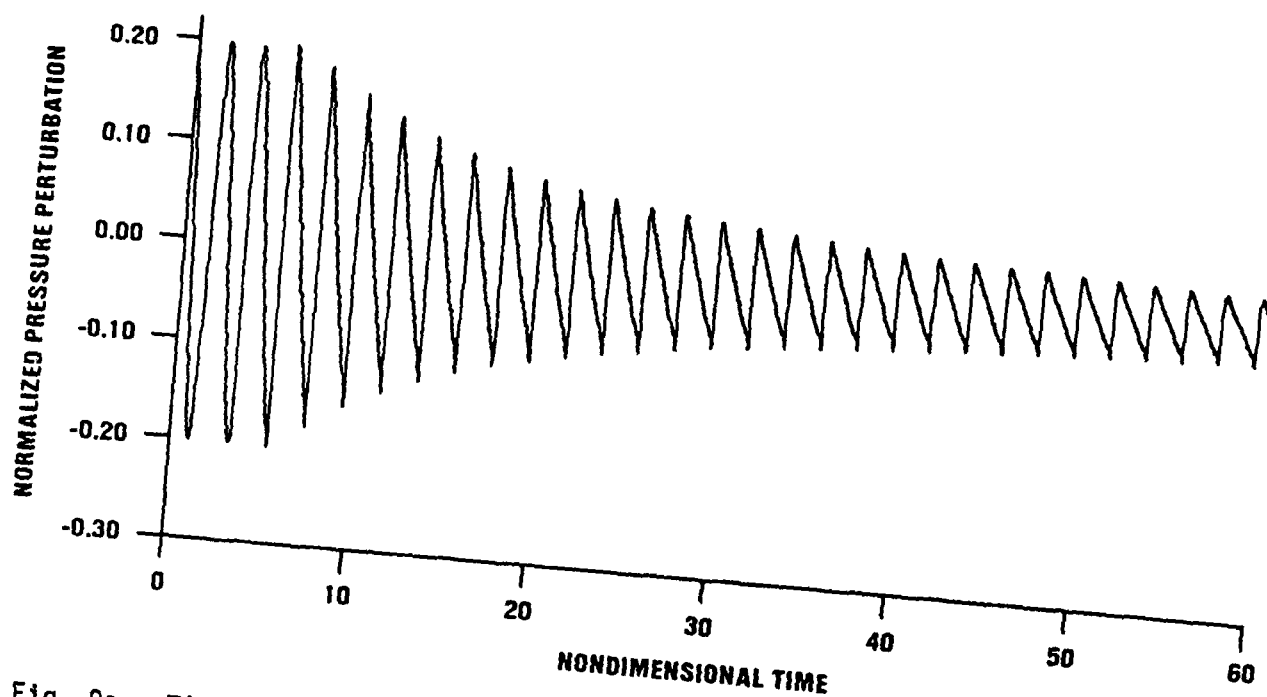
Fig. 9a. Time evolution of normalized pressure oscillations at an end of the chamber (FCT-LPE).
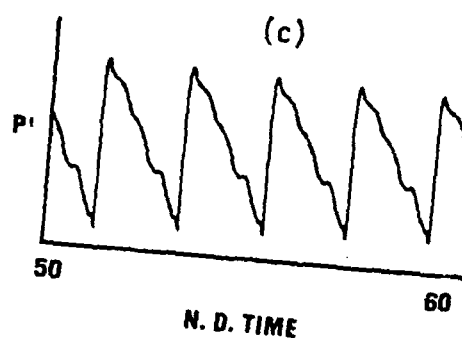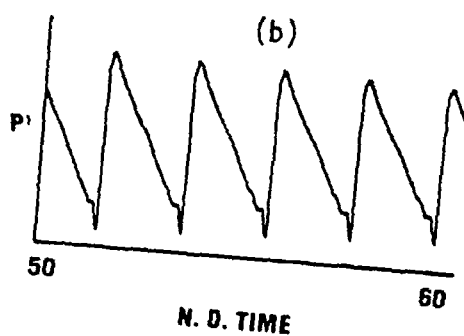
Fig. 9b-c. Expanded views of the normalized pressure oscillations at an end of the chamber (FCT-LPE): (a) 51 grid points, (b) 93 grid points.

results obtained with lower Courant numbers (and 51 grid points) or with 93 grid points (and $C_n = 0.6$). Instead of the expected improvement that should have resulted from reducing the spatial mesh size, the results for this test case (93 grids, $C_n = 0.6$, $\Delta P_o \doteq 0.2\bar{P}$), shown in Fig. 9c, indicate significant errors developing along the rarefaction wave. In conclusion, it seems that for this specific application and this test case conditions, the results obtained by this scheme are actually worse than the results obtained by the FCT-LW.

The last scheme tested was a combination of the Artificial Compression Method[27] with the Hybrid[20] and the Lax-Wendroff schemes[28]. This combination method involves two steps; in the first step the second order Lax-Wendroff scheme is hybridized with the nonoscillatory first order accurate method as described previously, to allow a monotonic (i.e., nonoscillatory) transition across admissible discontinuities. In the second step, an artificial compression correction is applied to sharpen transitions of discontinuities (i.e., restore the energy contained in the high frequency modes), since the hybridized first order accurate method is too dissipative. A switch value based upon flow gradients (density gradients were used herein) is utilized so that the artificial compression and the first order monotonic schemes are activated only in the immediate vicinity of admissible discontinuities. This combined method preserves the second order truncation error of the Lax-Wendroff scheme in smooth regions of the flow and yet has the potential to yield nonoscillatory transitions of both shocks and contact discontinuities (due to the monotone scheme that is activated at the transition regions). In this connection, it should be mentioned that stability considerations restrict this combined scheme to Courant numbers below 0.85. (Further details on this scheme are presented in Appendix 2.)

Figure 10a shows the time evolution of pressure oscillations at an end of the tube between the nondimensional times of 0 and 60, obtained by utilizing the LW + H + ACM

scheme, with a switch value of 0.0002. The expanded views between nondimensional times 20 to 30, and 50 to 60 are shown in Figs. 10b, and 10c, respectively. No erroneous wiggles or oscillations are excited at any time before or after the shock. Ninety-five percent of the shock amplitude is captured over three grid points, even after several thousand time steps. The spectral analysis for this case indicates that (similarly to what has been shown with the FCT-SHASTA-Phoenical scheme) the percentage of energy in the fourth to eighth harmonics grows slightly with time. However, in this case, this growth is not accompanied by dissipation of energy in the higher (above eighth) harmonics, but rather by a slight decrease in the percentage of energy contained in the first to third harmonics. The time evolution of the Power Spectral Density as a function of mode number (shown in Fig. 10d) indicates that once a shock is formed, the acoustic energy distribution among the nodes varies little with time. These results are in excellent agreement with the analytical solution (presented previously) for an N wave.

The switch value responsible for the transition from the Lax-Wendroff to the Hybrid + ACM combination was chosen to be 0.0002. In order to demonstrate that the choice of switch is not limited to a very narrow range, the test was repeated with values of 0.002 and 0.00005. The results obtained in all these tests were identical, indicating the insensitivity of the results to variations in the switch value.

Results obtained with an initial pressure disturbance amplitude of 0.6 of the mean pressure are indistinguishible (qualitatively) from results obtained for the standard test case. Results obtained at low Courant numbers (around 0.3) show increased dissipation of the high harmonic content (a problem inherent to the basic Lax-Wendroff scheme) that result in rounding of the shock top. Nevertheless, 95 percent of the shock is still captured between 3 grid points.
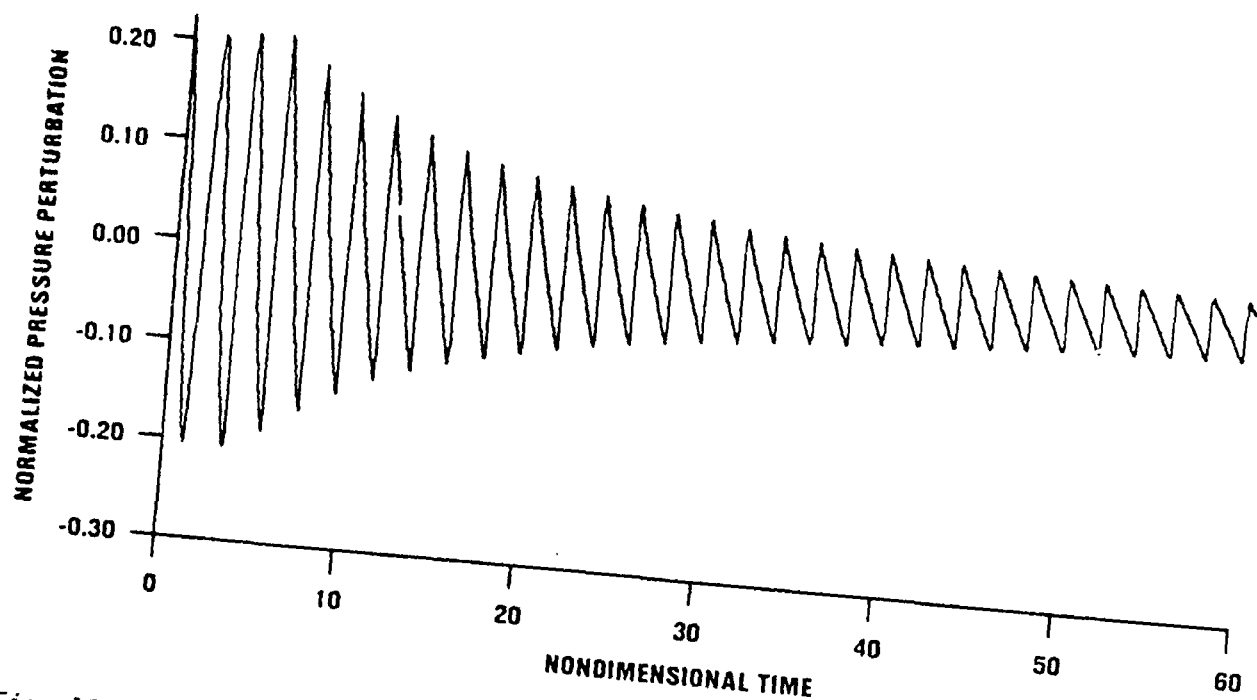
Fig. 10a. Time evolution of normalized pressure oscillations at an end of the chamber (LW+H+ACM).
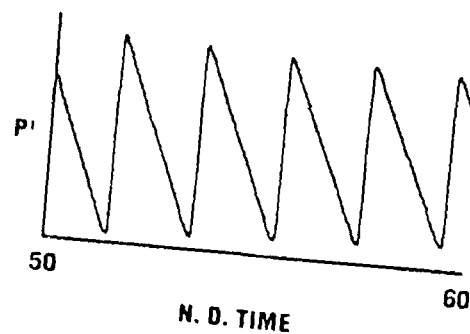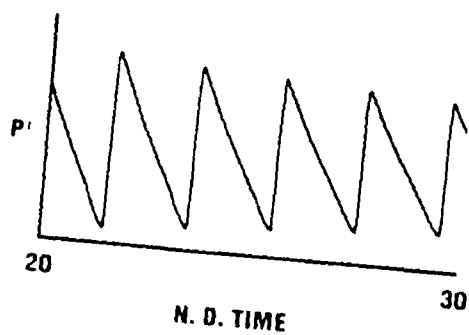
Fig. 10b-c. Expanded views of the normalized pressure oscillations at an end of the chamber (LW+H+ACM).

47

In contrast to the results obtained with the FCT schemes, excellent results are obtained with 93 grid points ($C_n = 0.6$, $\Delta P'_o = 0.6\overline{P}$), as shown in Fig. 10e. The shock remains sharp and oscillation-free even after 11,000 time steps. Spectral analysis data indicates that at least 25 harmonics were excited. In addition, no detectable temporal change was observed in the percentage of energy contained in any of the harmonics.

An additional testimony to the shock capturing capability of the Lax-Wendroff, Hybrid and Artificial Compression combination schemes is shown in Figs. 10f and 10g. Experiments were conducted (more details are given in Part 2) in which closed tubes filled with nitrogen at room temperature were pulsed by a piston pulser attached at one end. The pressure oscillations in the chamber excited by the piston pulser feature a very fast rise and decay. The nonlinear combustion instability program (Appendix I) was modified to model the effect of fore-end pulsing. The predicted spatial evolution of pressure waves in the first half wave period is shown in Fig. 10f. The very fast rise and decay times of the pulse results in a very narrow steep-fronted and steep-backed wave. The spectral analysis results obtained for this pressure wave solution (shown in Fig. 10g) indicates an almost linear decay of energy as a function of frequency; a result significantly different from spectral analysis results obtained for an N-type waveform. The prediction of such waveforms in a sharp-nonoscillatory manner is a formidable test of a numerical scheme. The ability of the LW+H+ACM combination scheme to reproduce these waves with only a slight post-expansion oscillation is another indication of the excellence of this shock capturing technique for all types of wave propagation problems.
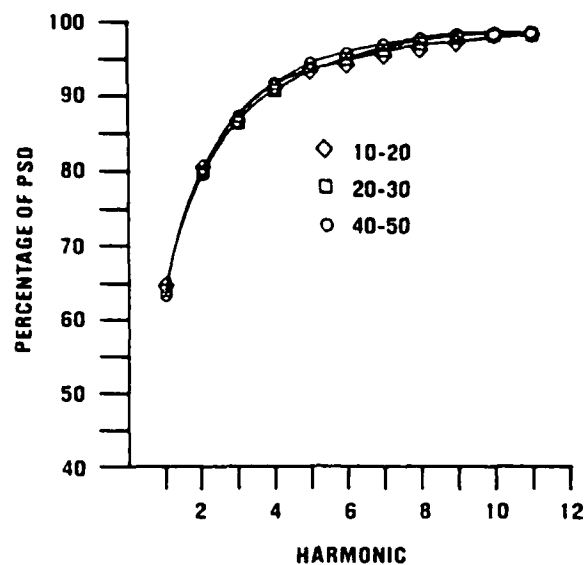
Fig. 10d. Time evolution of accumulated PSD as a function of mode number (LW+H+ACM).
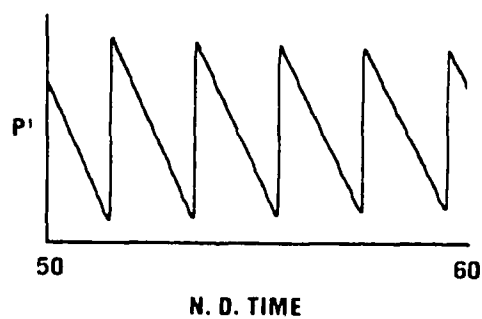
Fig. 10e. Expanded view of the normalized pressure oscillations at an end of the chamber (LW+H+ACM, 93 grid points, $\Delta P_0 = 0.6\overline{P}$).
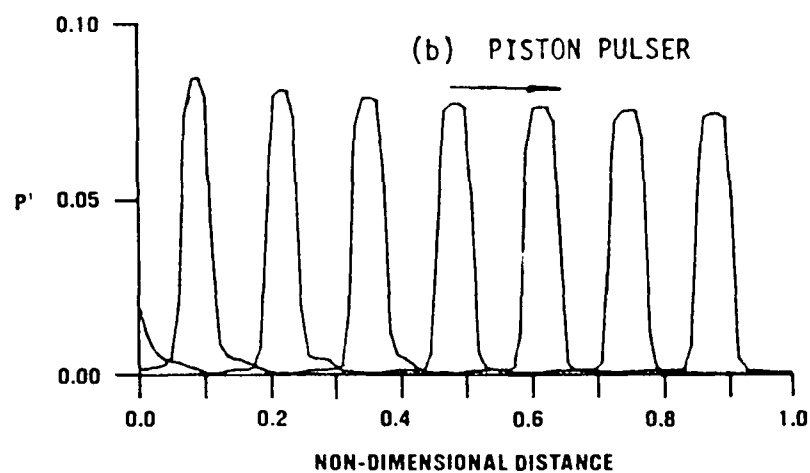
Fig. 10f. Spatial evolution of pressure waves in the chamber initiated by the piston pulser.
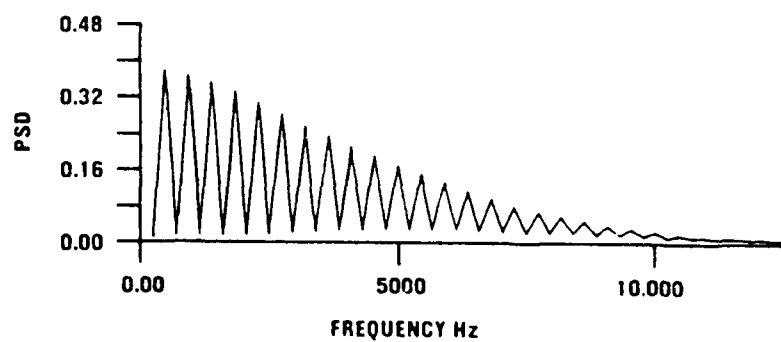
Fig. 10g. Piston pulser; PSD as a function of frequency.

CONCLUSIONS

Several shock capturing techniques were utilized to solve the nonlinear hyperbolic equations describing propagation of finite amplitude waves, wave-steepening, and shock formation and propagation in a closed-end tube for many wave cycles. A spectral analysis capability was incorporated in the program, enhancing the ability to examine the dissipative and dispersive error pattern of the candidate numerical shock capturing schemes.

All the "older" techniques tested (i.e., MacCormack, Lax-Wendroff, and Rubin and Burstein) demonstrated significant diffusive and dispersive errors. The results of an extensive study conducted with MacCormack's scheme demonstrated that: (a) dispersive errors increase with decrease of Courant number; (b) dissipative errors increase with increase in Courant numbers from 0.1 to 0.6 and then decrease; and (c) both dispersive and dissipative errors increase with frequency (for the same Courant number). These results agreed with results obtained by a linear error analysis. Except for some insignificant differences, the results obtained for the Lax-Wendroff and Rubin and Burstein schemes were similar.

Artificial viscosity effects were examined by combining artificial viscosity with Hyman's predictor-corrector and Rusanov's schemes. The use of artificial viscosity was conceived as a way to damp post-shock oscillations (erroneous energy content in the high frequency modes). However, using artificial viscosity for several wave cycles resulted in total dissipation of the energy contained in the high frequency modes. It has been demonstrated (with both schemes) that the total energy loss depends on the value of the artificial viscosity coefficient used; increasing the artificial viscosity coefficient resulted in a faster transition to a pure sinusoidal wave (i.e., elimination of the high frequency modes) and a faster wave amplitude decay.

51

Numerical experiments with the two Flux-Corrected-Transport-SHASTA schemes tested demonstrated very good results (except for some aesthetic pre- or post-shock wiggles) for the standard test case. Nevertheless, these schemes yielded erroneous solutions when tested for initial disturbances of high amplitudes; solutions that exhibited a single or even multiple numerically generated shocks at the center of the expansion wave.

The Hybrid scheme utilizes a first order accurate monotonic scheme in the vicinity of admissible discontinuities and a second order scheme in the smooth portion of the solution. Results obtained with this scheme indicated that for all Courant numbers, grid sizes and initial wave amplitudes tested shocks are captured without oscillations. Nevertheless, since the scheme is based upon a transition to a linear (first order accurate) scheme at shock transitions, the lower harmonics contain more energy than should be there at the expense of the high frequency content of the wave. This energy transition resulted in (after many wave cycles) waveforms that are not fully shocked.

Artificial compression, when combined with the Hybrid scheme, was conceived as a way to restore the high frequency content of the wave. Results obtained by utilizing this combination scheme for several Courant numbers, initial amplitudes and grid size indicated that; (a) shocks are captured in a sharp, nonoscillatory manner over three grid points, even after several thousand time steps; (b) no significant shift of energy among modes has been observed after the process of wave steepening has been completed; (c) energy distribution among modes corresponds very closely to the analytical solution (for an N-wave); and (d) the solution is not very sensitive to the value of the switch utilized. Because of these qualities, the combination of

Lax-Wendroff, Hybrid and Artificial compression was chosen to be incorporated in the nonlinear combustion instability program. Details of the numerical scheme are given in Appendix 2.

CHAPTER 3

SHOCK WAVE PROPAGATION IN VARIABLE AREA DUCTS AND COMBUSTION CHAMBERS

Most practical tactical rocket motor grain configurations have variable cross-sectional port areas. When the rate at which the area varies becomes relatively rapid, or in the limit, discontinuous, the time and spatial evolution of the propagating shock wave type of instability previously discussed becomes even more complex. If a shock wave is traveling from a large area section to a smaller one, part of the shock wave is transmitted and part is reflected. Thus, two shock waves and correspondingly two contact discontinuities are created. In the opposite situation, when a shock travels from a small area to a larger one, the shock wave is transmitted, and an expansion fan is reflected. In an actual motor both of these processes repeatedly occur, creating a very complicated wave structure in the chamber. The presence of such multiple shock wave systems in variable cross sectional motors has been confirmed experimentally (e.g., Ref. 51).

The problem of calculating shock wave propagation phenomena in variable area chambers is clearly a severe test of a finite difference scheme's ability to capture several shocks and describe them in a sharp nonoscillatory manner, even after many wave cycles. In order to evaluate the ability of Lax Wendroff + Hybrid + Artificial Compression technique to treat such complex problems, a simple closed duct problem was solved initially.

The geometry considered is shown in Figure 11. The solution was initiated with a continuous disturbance having an amplitude equal to 20% of the mean chamber pressure 6.894 MPa (1000 psi) and a waveform given by $\cos(\pi X/L)$ (most of the initial

54
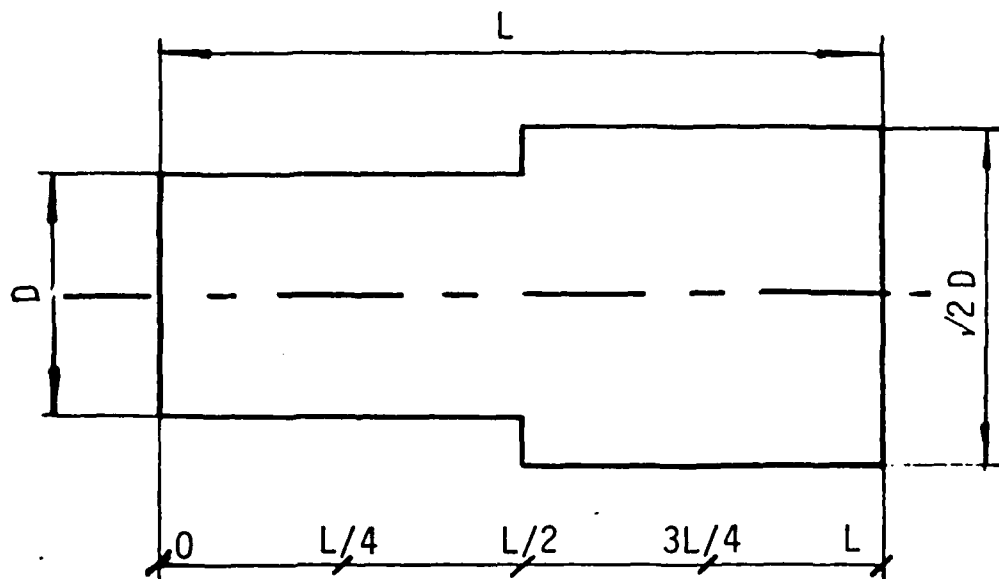
Fig. 11. Variable area duct geometry

disturbances for solutions presented in Part I of this report used this waveform and the percentage given is the zero to peak amplitude of the oscillatory waveform as a percentage of the mean pressure). The solution was continued for approximately 30 complete wave cycles (nondimensional time equals 60). The initially smooth cosine wave quickly steepened into a traveling shock wave, which as previously discussed, is then repeatedly reflected and transmitted as it encounters the area discontinuity and the ends of the tube. Figure 12 shows the calculated waveforms and respective Power Spectral Densities at five different locations along the tube for the ninth and tenth wave cycles. As expected, the wave forms are quite complex and both the waveforms and their spectra vary significantly from one location to another. Based on comparisons with experimental results from cold gas pulse tests, the analytical solution appears to accurately portray the physics of this complex problem[42].

The waveform at the left end of this test problem is dominated by a single shock wave and a single expansion fan. One should notice the sharp, nonoscillatory captured shock, even after many reflections. At the 1/4 point, two strong (relatively) shock waves, two weak shocks, and two expansions are in evidence. The spectral analysis indicates that the second and sixth harmonics are missing, as should be expected. The waveform in the middle consists of traveling shock waves at a frequency double that of the ends, with half the amplitude. The main features at the 3/4 and right end points are four and two shock waves, respectively. One should notice the strong augmented even harmonics at these locations. Since most of the significant acoustic gain and loss mechanisms in solid rocket motors are quite frequency dependent, the strong axial variations in harmonic content in chambers with sharply varying cross-sectional areas can be expected to have a significant effect upon motor stability; an effect that is completely unpredictable on the basis of linear stability analysis.
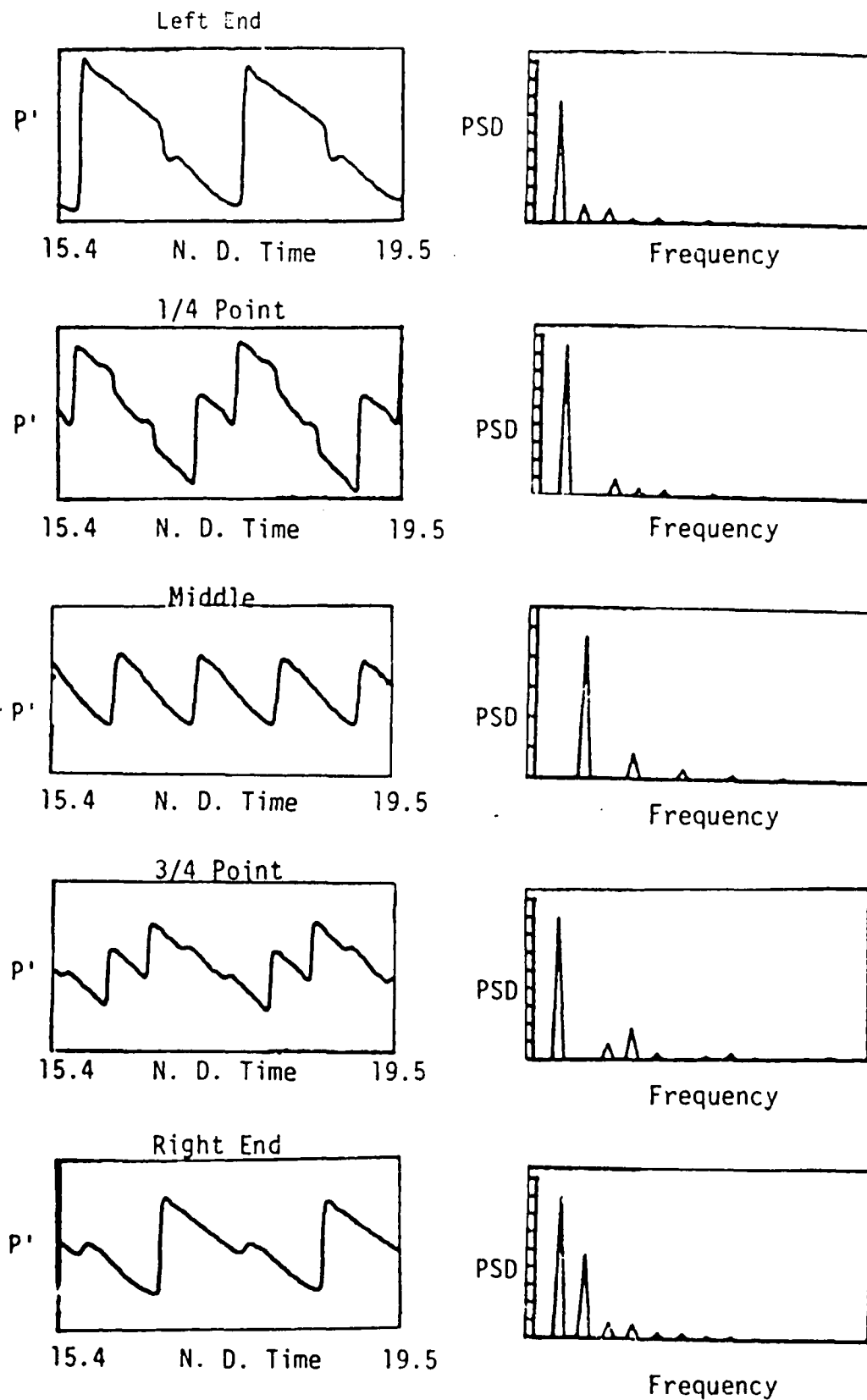
Fig. 12. Expanded views of the calculated pressure histories and PSD at five locations along a chamber with an area discontinuity.

Following the successful solution of the test problem, a solid rocket motor problem having the same geometry as Figure 11 (but with a nozzle at the right end) was solved to demonstrate the capability of the developed model to solve such problems in the presence of mean flow and combustion. Figure 13 shows the calculated pressure waveforms at the left end and 1/4 points of the motor. Except for the rounded tops (attributed to different distribution of energy among the respective harmonics caused by mean flow and complex nozzle end admittance) the waveforms are quite similar to those obtained in the closed duct problem.

Left End $^1/_4$ Point

p'   p'

15.4 N.D. TIME 19.5   15.4 N.D. TIME 19.5
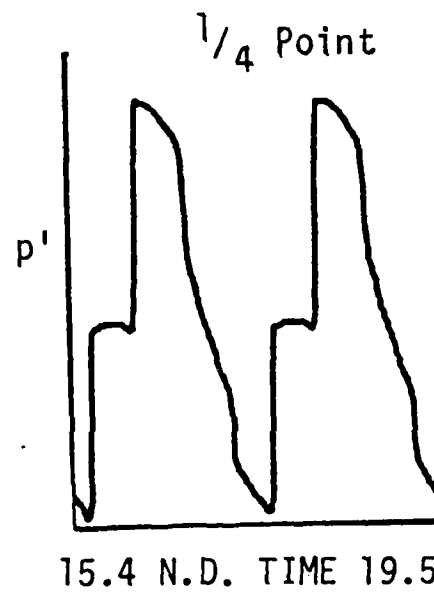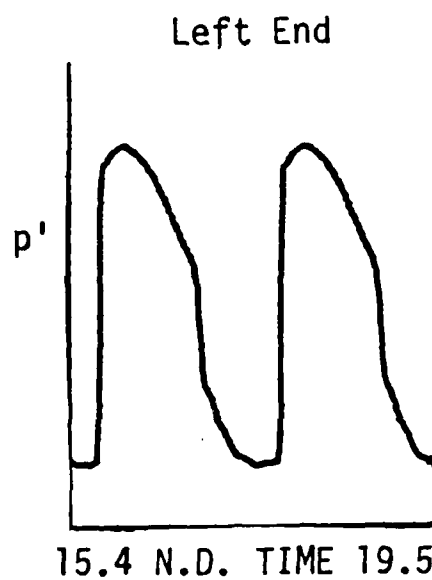
Figs. 13a-b. Expanded views of the calculated pressure histories at two locations along a motor with an area discontinuity.

CHAPTER 4

LIMITING AMPLITUDE STUDIES

From a practical standpoint, the ability to predict the limiting amplitude reached by pressure oscillations in unstable solid rocket motors is important in assessing whether such an instability will be severe enough to warrant design or propellant modifications to eliminate it. For both practical and theoretical reasons it is also important to establish whether limit cycles are unique, i.e., independent of the characteristics of the initiating disturbance.

Even under the most carefully controlled laboratory conditions, it is almost impossible to conduct a series of motor firings in which the only variable is either initial disturbance amplitude or waveform. To the author's knowledge no test series having the primary purpose of establishing the effect of initial disturbance on limiting amplitude has ever been conducted. Results obtained from some tests which approximate the required conditions are not definitive, however, on balance they favor a conclusion that limiting amplitude is independent of the initiating disturbance. It should be emphasized that the above refers to the limit amplitude reached if a motor is pulsed into instability. The fact that the triggering event itself is dependent on pulse characteristics has been clearly demonstrated.

The difficulty in experimentally examining the uniqueness of limit cycles makes the analytical examination of this question all the more important. The question has been previously addressed for both liquid[43,44] and solid[4, 6, 7] rocket motors using both expansion and numerical techniques. Results obtained from expansion solutions indicate that the limit cycle should be independent of the initiating disturbance. However, since

these methods have limits in regard to their applicability to strongly nonlinear situations with very high amplitudes and/or shock-like waveforms, and since not all of the nonlinearities present in tactical solid rocket motors were incorporated in the models, the conclusions must be regarded as relevant, but requiring further substantiation.

Previous results obtained with the present "exact" model seemed to yield apparently conflicting conclusions. Results obtained in Reference 4, for motors with a particle to gas weight flow ratio of 0.36 and 2 micron particles appeared to demonstrate that limiting amplitude is a strong function of initial disturbance amplitude. It was tentatively concluded that the apparently conflicting results were due to nonlinear particle damping effects. Since this previous conclusion was based on a limited number of results it was decided to obtain several more sets of solutions, with and without particles. In this connection it should be mentioned that this investigation addresses the question of limiting amplitude for linearly unstable motor/propellant combinations (i.e., motor/propellant combinations that under the specific motor conditions are unstable to infinitesimal pressure oscillations). In such cases, limit cycles result from the amplitude dependence (nonlinear behavior) of the operative driving and damping mechanisms.

The nonlinear transient burn rate model utilized here[4] is a nonlinear extension of the Denison and Baum model[45] and was discussed in Appendix I. In this connection it should be mentioned that the pressure and velocity coupled response function (R_{pc} and R_{vc}, respectively) values specified in this report are equivalent linear response function values (i.e., obtained by reducing the nonlinear model to the linear limit). These values are given for comparison purposes only. In the program, the instantaneous local burn rate is evaluated utilizing the nonlinear transient burn rate model.

61

The series of results shown in Fig. 14 are for a cylindrically perforated motor 59.7 cm (23.5 in) long with a port area of 21.484 cm^2 (3.33 in^2), a throat area of 2.8322 cm^2 (.439 in^2) and a chamber pressure of 13.19 MPa (1913 psi). These calculations were performed for a propellant without particles, and with a linear pressure coupled response function of 5.35 (no velocity coupling). The solutions were initiated by perturbing the steady state with fundamental mode disturbances of varying amplitudes. In each case the same limit cycle (amplitude and waveform) was reached. Additional solutions for the same motor and operating conditions were obtained with several other pressure coupled response functions. All of the solutions for a given response function reached the same limit cycle condition (i.e., the same amplitude and waveform) but each response function produced a somewhat different limiting amplitude.

Several other series of calculations were then performed with varying sizes and amounts of particles to re-examine the conclusion reached in Reference 4. The first series of calculations (with the same motor geometry used in the results shown in Fig. 14) was conducted with 2 micron aluminum oxide particles and 15% particle to gas weight flow ratio. The results shown in Fig. 15 were enlightening. The computed limit cycle amplitudes were the same (30.4% of mean pressure, peak to peak) even though the initial disturbance was 40% in one case and 2% in the other. Calculations with intermediate initial disturbance also reached the same limit cycle condition .

This last series of results raised serious questions concerning the validity of the conclusion reached in Reference 4. In order to settle the apparent conflict, the earlier results (reported in Ref. 4) were reproduced. This time, however, the solutions were carried out for twice as many wave cycles. Doing so immediately provided the answer to this seeming paradox. The solutions presented in Fig. 16 show that at a nondimensional time of 70 (when the earlier solutions were terminated) the decay rate was quite small, but not zero. It was falsely assumed that continuing the

62
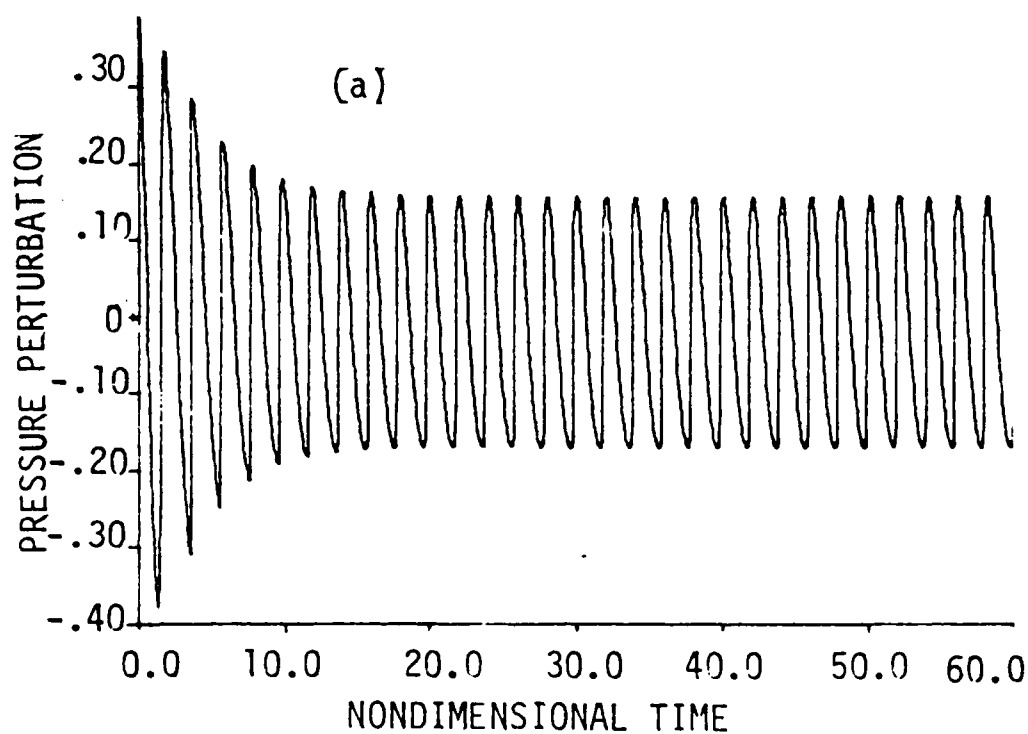
Fig. 14a. Time evolution of normalized pressure oscillations at the head end of the motor, 1st harmonic initial disturbance, no particles, $\Delta P'_0 = 0.4\bar{P}$.
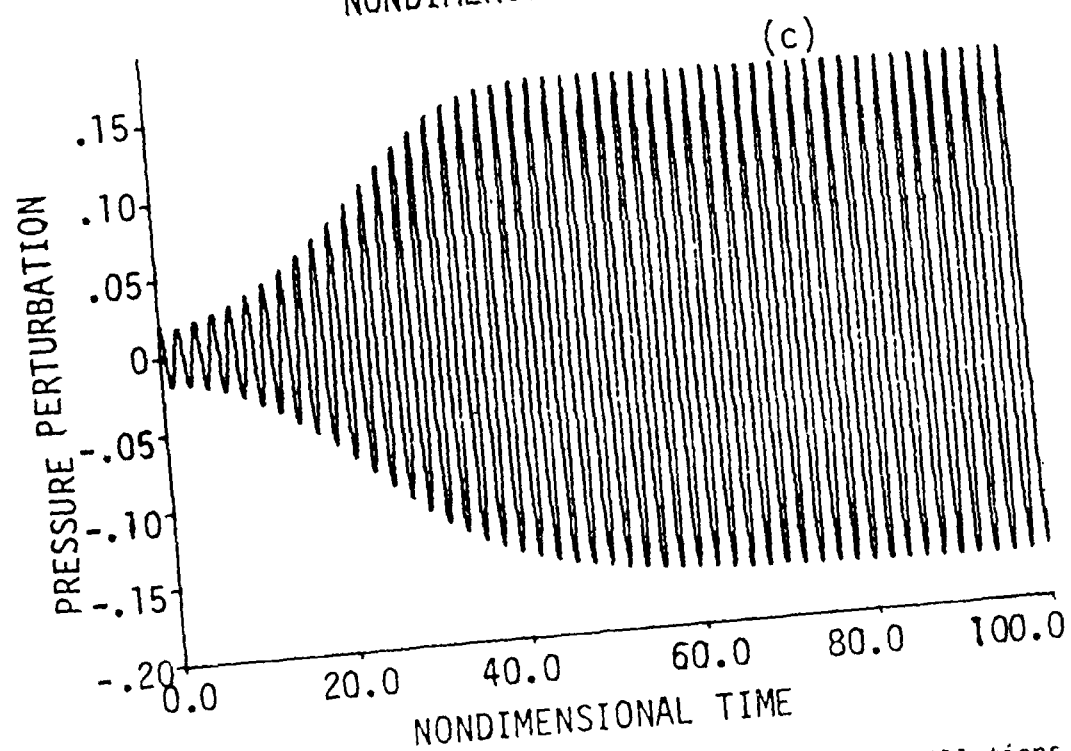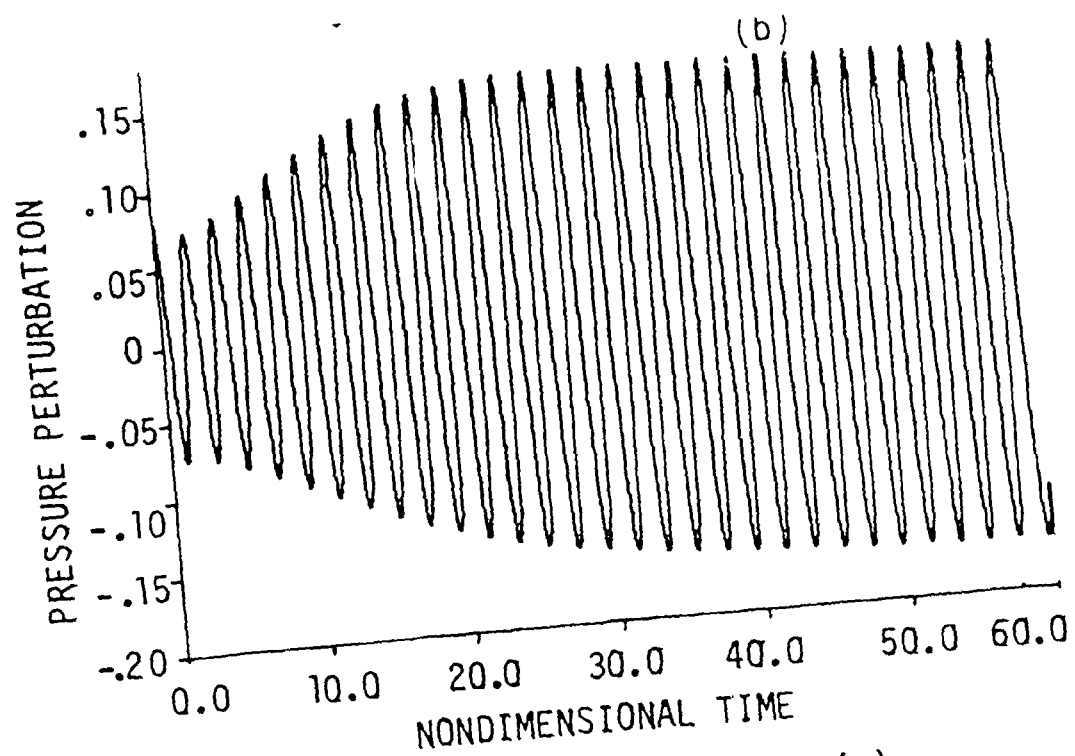
Figs. 14b-c. Time evolution of normalized pressure oscillations at the head end of the motor, no particles: (b) $\Delta P_o' = 0.08\bar{P}$, (c) $\Delta P_o' = 0.02\bar{P}$.

64
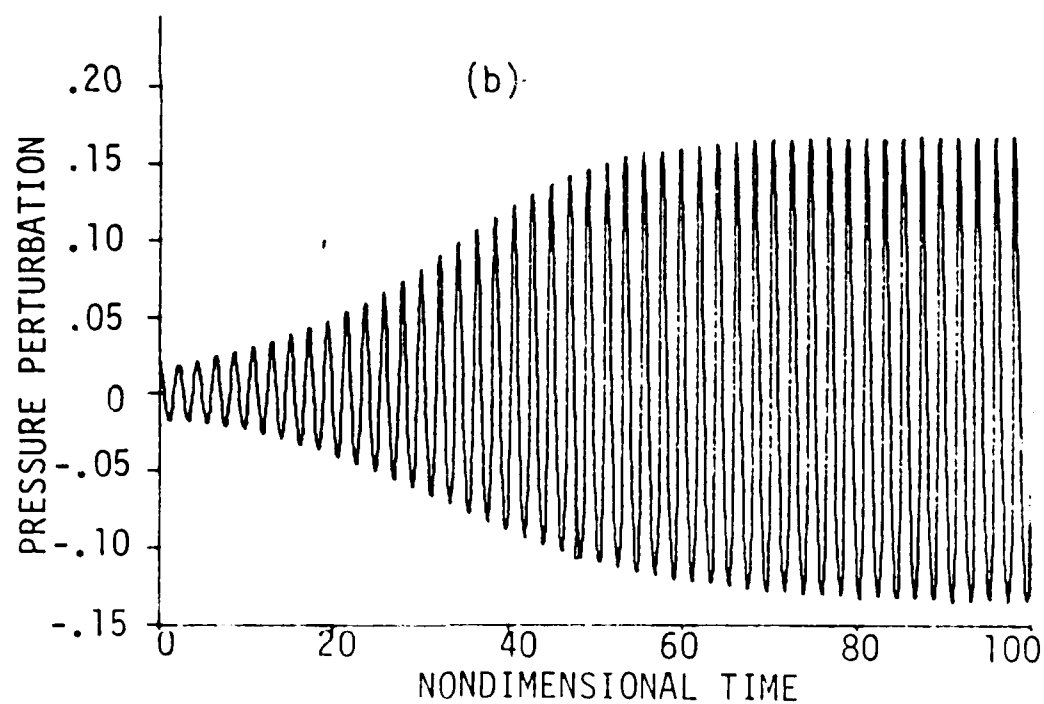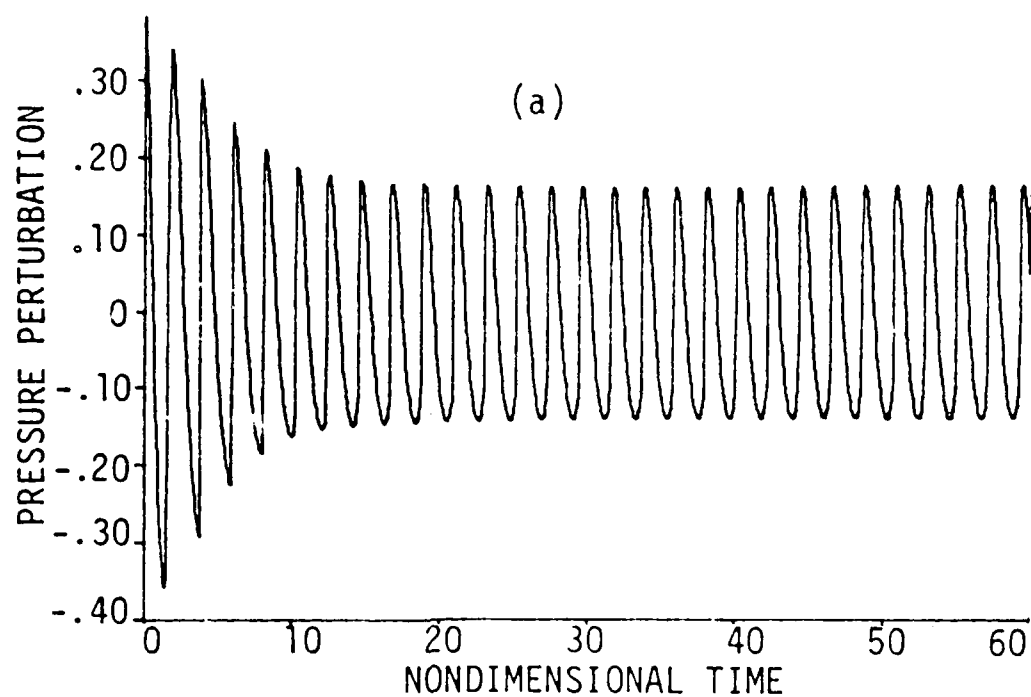
Figs. 15 a-b.   Time evolution of normalized pressure oscillations at the head end of the motor (15%, 2 micron particles):   (a) $\Delta P_0' = 0.4\overline{P}$, b) $\Delta P_0' = 0.02\overline{P}$.

65

solutions would not significantly alter the limit cycle amplitudes. The present calculations show that except for initial perturbations close to 5%, the wave is either still growing or decaying at T=150. All of the solutions were getting closer and closer to the same limiting amplitude, but had yet to reach it. Figures 16 show the present results obtained with 2 micron, 36% particle to gas weight flow ratio and initial disturbance amplitudes of 40% and 2% of the mean pressure. Given the previously presented results for 15% 2 micron particles, it is expected that the solutions will approach the same limiting amplitude. Furthermore, Figs. 16a-b demonstrate that when a particular motor propellant combination is near neutral stability (i.e., very small growth or decay rate), a very long time is needed to reach a limit cycle condition.

To further demonstrate the effect of relative stability on the time needed to reach a limit cycle condition, calculations were made for the same motor and propellant (36%, 2 micron particles), but with an increased pressure coupled response function. The increased combustion driving unbalanced the gains and losses, and as seen in Figs. 17a-b, resulted in the relatively rapid establishment of a limit cycle with an amplitude of 29.6% of the mean pressure. Here again, additional solutions demonstrated that the limit cycle condition (i.e., amplitude and waveform) was independent of initial disturbance amplitude.

An important application of nonlinear instability analyses is the prediction of motor response to pulse type disturbances. The results of two solutions that test the ability of the LW+H+ACM to treat such problems are discussed. In both cases, the initial pressure disturbance waveform was taken to be of the form $\sin^6 (\pi X/L)$ producing a centered symmetric waveform with an amplitude equal to 0.4 of the mean pressure. The difference between the two cases was the initial velocity at t=0. In one case, the nondimensional velocity was taken to be $\Delta P/_{\gamma}$, while in the second case, the
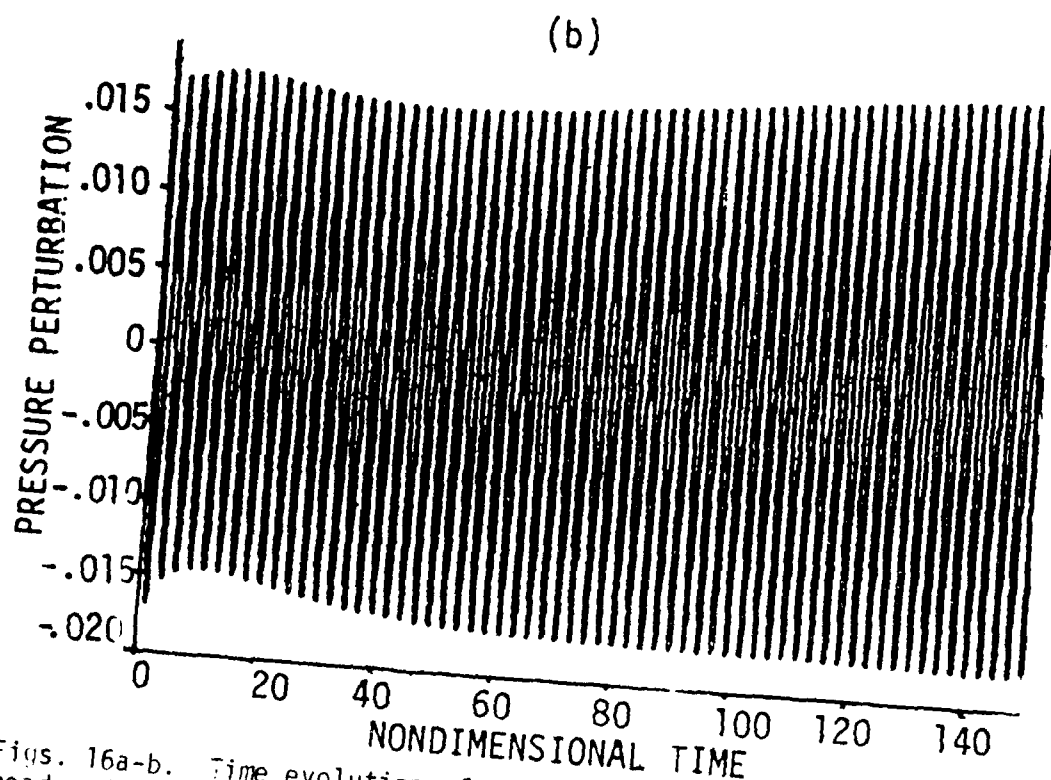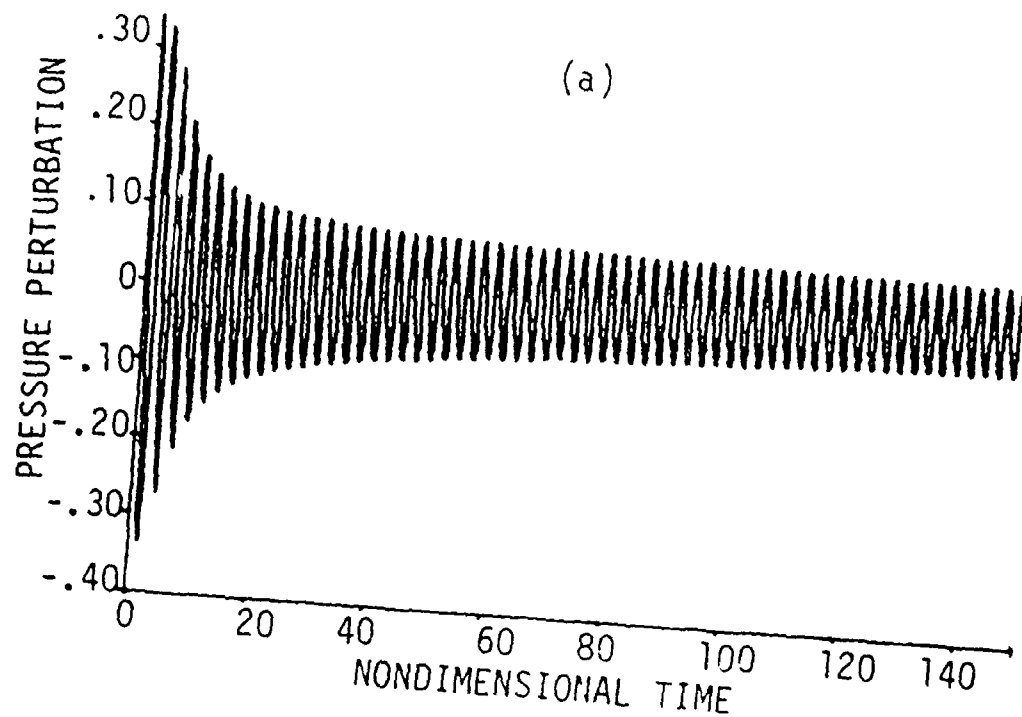
Figs. 16a-b. Time evolution of normalized pressure oscillations at the head end of the motor (36%, 2 micron particles): (a) $\Delta P_0' = 0.4\bar{P}$, (b) $\Delta P_0' = 0.02\bar{P}$.
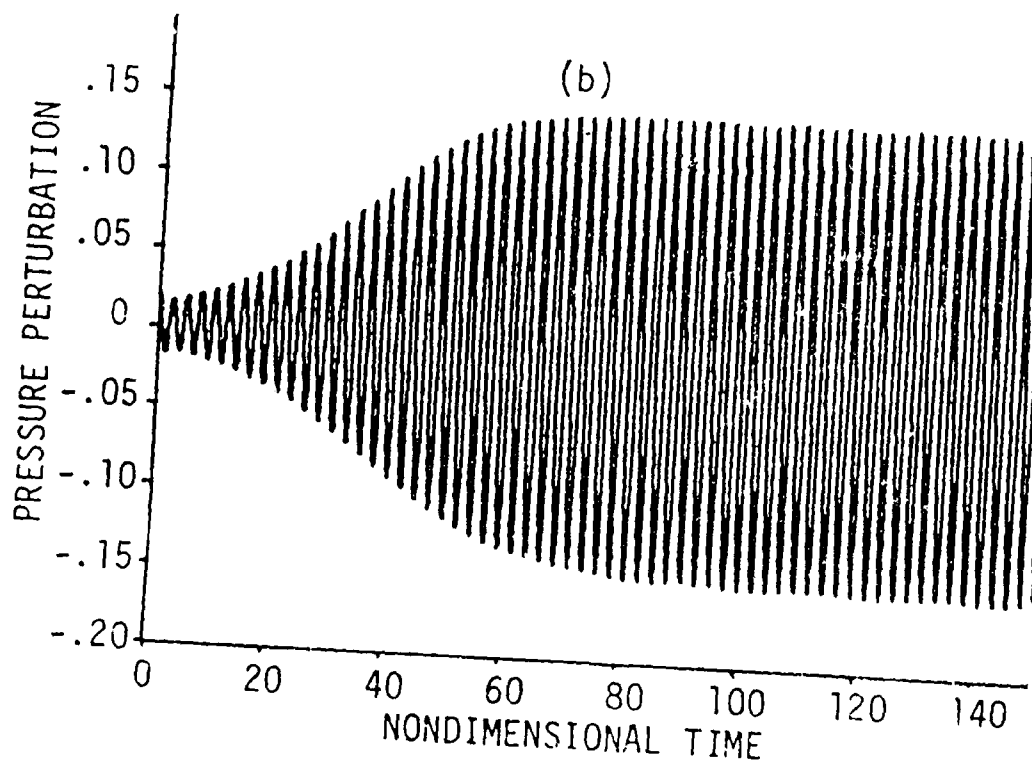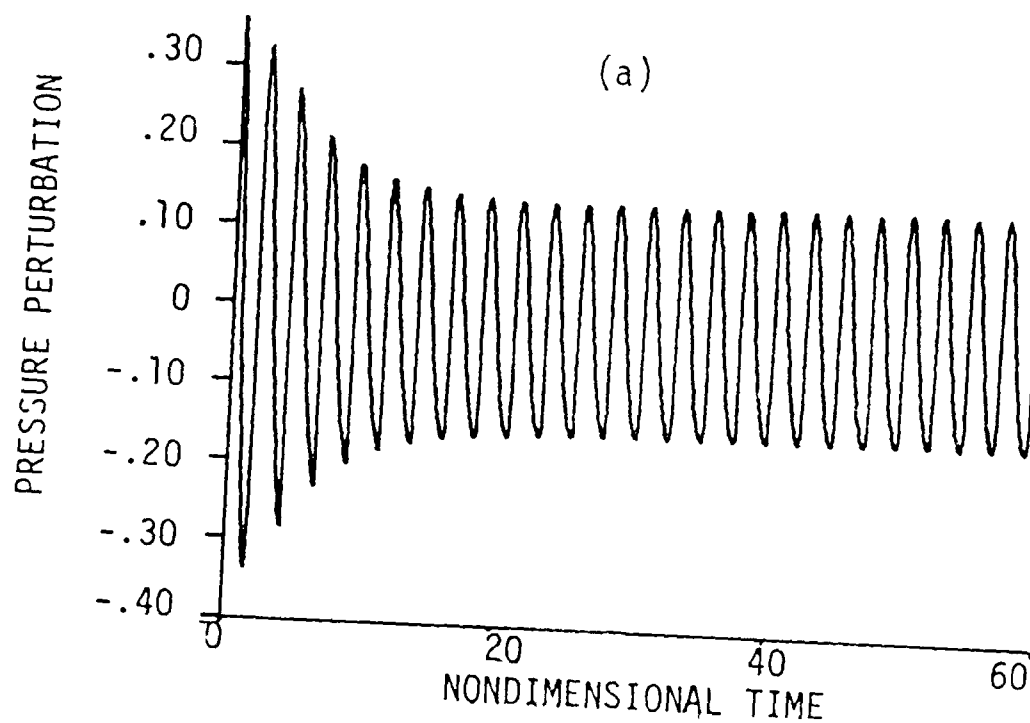
Figs. 17 a-b. Time evolution of normalized pressure oscillations at the head end of the chamber, increased response function (36%, 2 micron particles): (a) $\Delta P_0' = 0.4\bar{P}$, (b) $\Delta P_0' = 0.02\bar{P}$.

68

velocity was taken to be zero. The first case represents a traveling pulse (actually

setting $\Delta v = \Delta p/\gamma$ only produces a pure right traveling wave in the linear limit as

Δv approaches zero). The second case corresponds to a standing pulse. The pulse

propagates as the sum of equal left and right traveling waves, each having half the

initial amplitude.

The calculated pressure histories at the head end of the motor for each of these

disturbances are shown in Fig. 18 (traveling) and Fig. 19 (standing). The dramatic

difference between the results demonstrates the importance of specifying the velocity

disturbance associated with a pressure pulse. The traveling pulse is immediately

transformed into steep-fronted, shock-type waveform and decays until it reaches the

same limit cycle condition as the solutions initiated with first harmonic sinusoidal

disturbances (21.73 percent of the mean pressure). Spectral analysis of this solution

indicated that at early times a large percentage of the energy of the traveling pulse

was contained in the fundamental mode, but a significant higher harmonic content is

also evident.

The pressure history of the standing pulse disturbance is shown in Fig. 19. The

time variation of the waveform is quite complex in this case. The spectral analysis

results shown in Figures 20a to 20c help to clarify what is happening. At early times, a

symmetric standing pulse centered in the motor excited essentially only even harmonics

(Figure 20a), with the 2nd harmonic dominating. The fundamental and odd harmonics

contained an insignificant amount of energy at this time. Since only the fundamental is

unstable for this motor, the even harmonics decay with time, while the fundamental

begins to grow. In the nondimensional time interval of 20 to 40 the waveform becomes

quite complex as it transitions from a steep 2nd harmonic dominated wave to an almost

pure sinusoidal wave at the fundamental frequency. At a later time this solution was
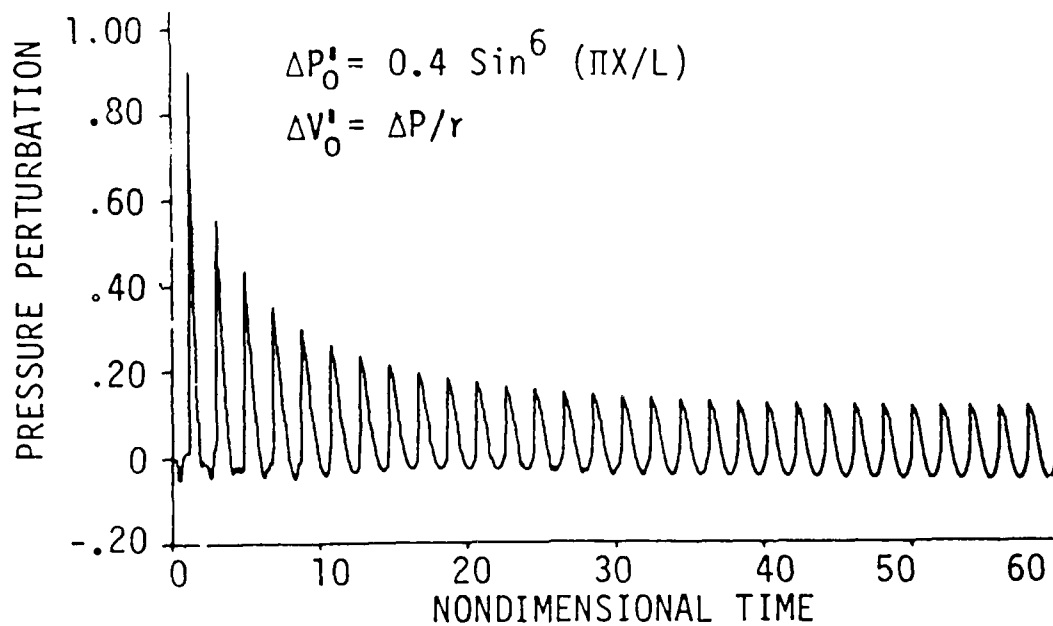
Fig. 18. Time evolution of normalized pressure oscillations at the head end of the motor, traveling pulse.
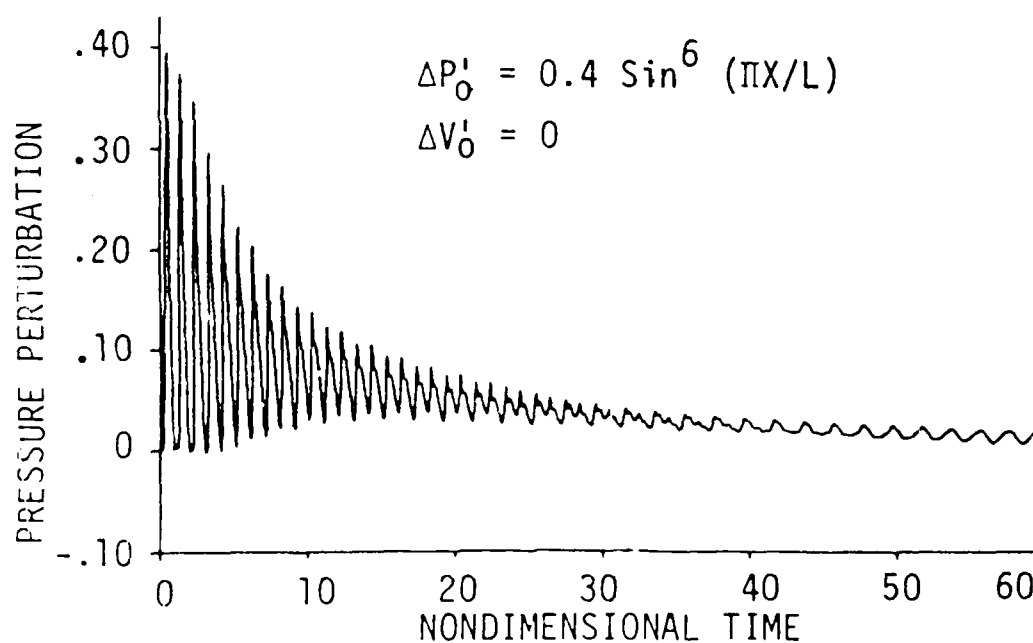
Fig. 19. Time evolution of normalized pressure oscillations at the head end of the motor, standing pulse.

70
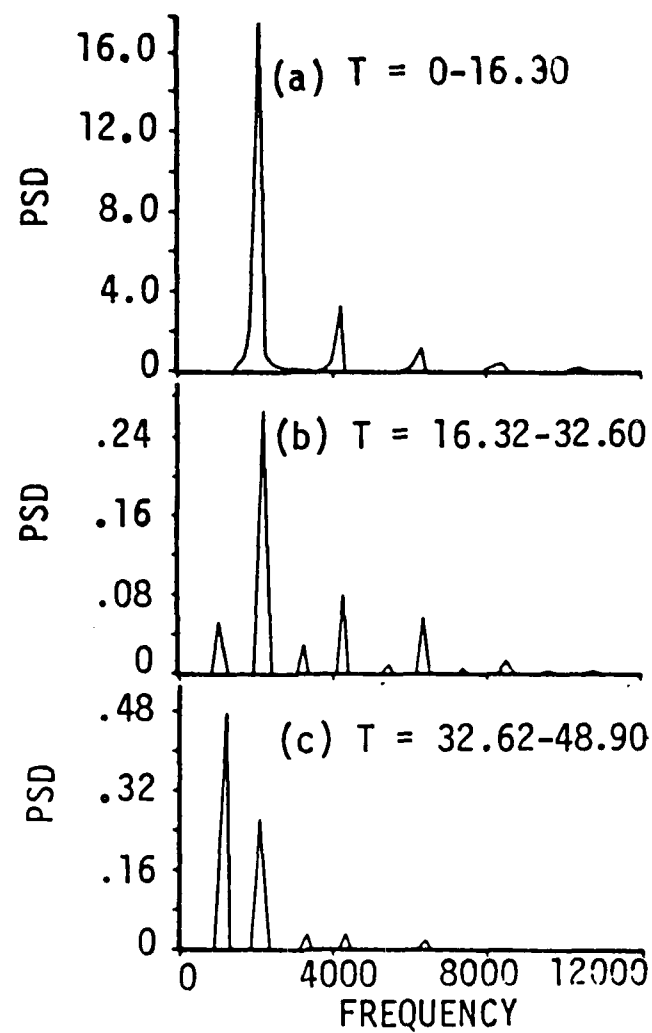
Figs. 20 a-c. Time evolution of PSD as a function of frequency for a standing pulse.

continued out to a nondimensional time of 180. The waveform continued to decay out to about nondimensional time of 100. At this time, the amplitude of the wave was only 1.6% of the mean pressure (compared to 40% initially) and the wave was essentially a pure fundamental sine wave. After t=100, the wave started to grow again. As the wave grew and steepened, higher harmonic content again began to appear as a result of energy transfer from the fundamental to the higher harmonics and the solution reached the same limit cycle achieved with the other initial perturbations. Based on these results, it has been tentatively concluded that the limit cycle condition (amplitude and waveform) is independent of initial disturbance characteristics.

Figures 21a and 21b show the expanded views of the time evolution of the pressure oscillations for the standing pulse test case between the nondimensional times of zero and ten. Figure 10a was computed utilizing the LW+H+ACM method, while Fig. 21b shows the result obtained using the Rubin and Burstein Scheme. The erroneous development of higher modes when utilizing the Rubin and Burstein Scheme is evident after the third wave cycle. Spectral analysis of the Rubin and Burstein solution indicates that the fourth and sixth harmonics contain erroneously high energy at the nondimensional time period of 7.5 to 15 (as shown in Figs. 22a and 22b). Even in this case, in which all modes except the fundamental are stable, the effect of such erroneous higher mode content is not merely cosmetic. When perturbed with a first mode disturbance, the Rubin and Burstein results reached a limiting amplitude which is approximately 50% higher than the limiting amplitude obtained with the LW+H+ACM scheme. Such a difference can be critical when one considers the vibration levels that can be tolerated by guidance and control systems. These results conclusively demonstrate the superiority of the LW+H+ACM scheme over the generalized Lax-Wendroff type schemes for the present class of problems.

Figs. 21 a-b. Expanded views of normalized pressure oscillations at the head end of the motor, standing pulse: (a) LW+H+ACM, (b) Rubin and Burstein.
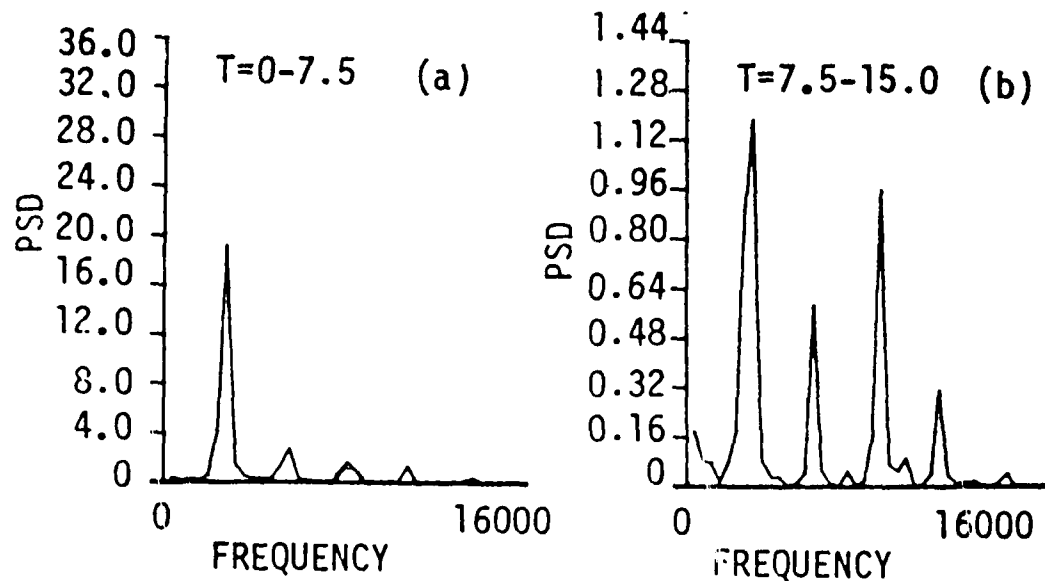
Figs. 22 a-b. Time evolution of PSD as a function of frequency, standing pulse, Rubin and Burstein scheme.

73

CHAPTER 5

VELOCITY COUPLING STUDIES

INTRODUCTION

A survey of past attempts to model or predict the effects of velocity coupling on the stability of solid rocket motors leads one to the conclusion, supported by the results of a recent JANNAF workshop on velocity coupling[46], that very little is known about velocity coupling at this time. All existing models appear to have significant deficiencies. Price's original velocity coupling model[47] is purely empirical. Other investigators sought to modify existing combustion models by introducing an additional source of heat transfer to the propellant surface. For example, in Refs. 48 and 49, a heat transfer term based on an empirical function of velocity was utilized, while in Refs. 50 to 52, additional heat transfer was included on the basis of modifications to steady state turbulent boundary layer theories and/or erosive burning rate models. All of these models ignore some of the fundamental physics of the problem. Turbulent boundary layers in the usual sense are not typically realized in solid rocket motor chambers.[53] While some of the existing velocity coupling models properly reduce to steady state erosive burning models as the limit of zero frequency is approached, none of them properly treat acoustic boundary layer effects that become significant in the normal longitudinal frequency range[54] (say 200 to 1000Hz). In addition, acoustic boundary layer transition and acoustic turbulence interactions may also be important under certain conditions as may the interaction of an unsteady boundary layer with the propellant surface structure.

Due to the deficiencies of currently existing models, no velocity coupling model was selected for incorporation into the overall nonlinear stability program at this time.

Instead, calculations were performed utilizing several different ad hoc functions of velocity to directly augment either the heat transfer to the propellant surface, or the transient burning rate itself.

The primary purpose of this velocity coupling study was to demonstrate the potential usefulness of the present analytical framework in assessing the validity of improved velocity coupling models as they are developed. The initial calculations to be presented herein are for constant cross-sectional area, cylindrically perforated motors. The basic configuration is the same as that used in the previous study.[4] The reasons for selecting a cylindrical configuration to start with were: 1) It is the simplest possible motor configuration; 2) A large body of pressure coupled only solutions was available for these configurations; 3) Linear velocity coupling theory[55] yields no effect of velocity coupling for such configurations, thus, any velocity coupling effects observed would be due to nonlinear effects; and 4) although cylindrical motors often show little evidence of velocity coupling, there are many recorded instances where severe triggered instabilities with large mean pressure shifts have been observed in such motors.[1-3, 42]

All of the velocity coupling models developed to date have retained Denison and Baum's assumption of quasi-steady gas phase behavior in the combustion zone above the propellant surface. Each of the models then makes certain assumptions and hypotheses that lead to a velocity dependent term that enhances the heat transfer from the combustion zone to the propellant surface. In terms of the combustion model which is currently utilized in the present nonlinear analysis, this corresponds to incorporation of an additional term in the surface energy balance.

HEAT TRANSFER AUGMENTATION MODEL

Symbolically, this equation may be written as:

$$
\left. K_g \frac{\partial T}{\partial x}\right|_{-} \qquad =K_g \left. \frac{\partial T}{\partial x}\right|_{+} \qquad + \rho_s r Q_s
$$

(5)

heat transfer   heat transfer   total energy
to solid pro-   from gas phase   released at
pellant   to surface   surface

The term $K_g \left.\frac{\partial T}{\partial x}\right|_{+}$ has to be modified to incorporate the effect of acoustic velocity fluctuations. In the absence of a fundamental physical model, a number of functional forms were considered. Since a functional form of the following type has sometimes been successful in rationalizing observed events it was considered first.

$$
\left[K_g \left.\frac{\partial T}{\partial x}\right|_{+} \right]_{vc} \approx \left[\epsilon_1 (|u| - u_t) - \epsilon_2 (\bar{u} - u_t) \right]
$$

$$
\text{where} \quad \epsilon_1 = \begin{bmatrix} 0 & |u| & <u_t \\ 1 & |u| & >u_t \end{bmatrix}
$$

(6)

$$
\text{and} \quad \epsilon_2 = \begin{bmatrix} 0 & |u| & <u_t \\ 1 & |u| & >u_t \end{bmatrix}
$$

Here u is the total velocity, $u = \bar{u} + u'$; $\bar{u}$ is the mean velocity and u' the local acoustic velocity fluctuation. The term u_t represents a threshold velocity which in reality may, or may not, exist. Justification for this functional form may be found in several references.[47,48]

When $u' \gg u$ and $u_t = 0$, Eq. (6) can be approximated by

$$
\left[K_g \left.\frac{\partial T}{\partial x}\right|_{+} \right]_{vc} \approx |u'|
$$

(7)

According to linear analysis, a term such as shown in Eq. (6) can only be added to the heat transfer. However, in nonlinear analysis a velocity coupled heat transfer term can be incorporated on an additive or multiplicative basis. It was decided to insert a term on a multiplicative basis. The following functional form was adopted:

$$\left[K_g \left. \frac{\partial T}{\partial x} \right|_+ \right]_{pc+vc} = \left[K_g \left. \frac{\partial T}{\partial x} \right|_+ \right]_{pc} \left[1 + \frac{R_{vc}}{R_{pc}} \theta_{vc} F(u) \right] \tag{8}$$

Where $F(u)$ is given by Eqs. (6) or (7), R_{pc} is the pressure coupled response function and R_{vc} is the velocity coupled response function.

For small amplitude oscillations, $u' << u$ and $u_t = 0$, the right hand side of Eq. (6) reduces to u'. Thus, using the combustion model evaluated in the linear limit,[4] it can be shown that for R_{vc} to be equal to R_{pc}, θ_{vc} in Eq. (8) must satisfy

$$\theta_{vc} = \frac{2n(1-H) + \frac{C_p}{C_s} \frac{(n-n_s)}{A}}{(1-H)} \tag{9}$$

In the small amplitude linear limit, Eq. (8) combined with the present combustion model, reduces to the velocity coupled model used by Culick,[48] and Levine and Culick.[49] Equations (8) and (9), together with either (6) or (7), were termed the heat transfer augmentation model.

The calculations shown in Fig. 23 are for the same motor used in the Ref. 9 studies. With a linear pressure coupled response function of 3.3 and no velocity coupling, this motor propellant combination reached a limit amplitude of 21.73% of mean pressure (peak to peak). With the heat transfer augmentation model, Eq. (6),

77

$u_t = 0$ and a velocity coupled response function of 3.3, the calculated waveform (Fig. 23a) is almost the same as with pressure coupling alone. At the limit cycle condition, the lower envelope of the oscillations is almost the same. However, the zero to peak amplitude was increased by 1.2%. Increasing the velocity coupled response function to 19.8% gave the results shown in Fig. 23b. Here again, the lower envelope of the limit cycle remained at the same level, while the zero to peak amplitude was increased by 7.3%. Neither of these two cases demonstrated a measureable mean pressure shift even after 75 wave cycles.

In order to further explore the reasons for this behavior, additional solutions have been obtained with extremely high values of R_{vc}. At a value of $R_{vc}=40$, strong nonlinear effects and a measureable dc shift were produced. At $R_{vc}=66$ (Fig. 23c), a significant dc pressure shift is observed, as well as a modulated limit cycle amplitude.

BURN RATE AUGMENTATION MODEL

In order to explore the ineffectiveness of the heat transfer augmentation model, a second ad hoc velocity coupling formulation was inserted into the nonlinear instability analysis, as follows:

$$W_{pc+vc} = W_{pc} \left[1 + R_{vc} F(u) \right] \tag{10}$$

W is the instantaneous propellant mass burning rate ($W=\overline{W}+W^{l}$), and W_{pc} is the instantaneous mass burning rate computed from the existing pressure coupled model. With $F(u)$ given by Eq. (6), Eq. (10) also reduces, in the low amplitude limit, to the linear velocity coupling model used in the past. The key difference between Eq. (10) and Eq. (8) is that the velocity coupling effect built into Eq. (10) directly modifies the propellant burning rate rather than affecting it indirectly through a model that was developed for pressure coupled response function prediction. Equation (10), termed the burn rate augmentation model, is heuristic and is not meant to imply a particular

78
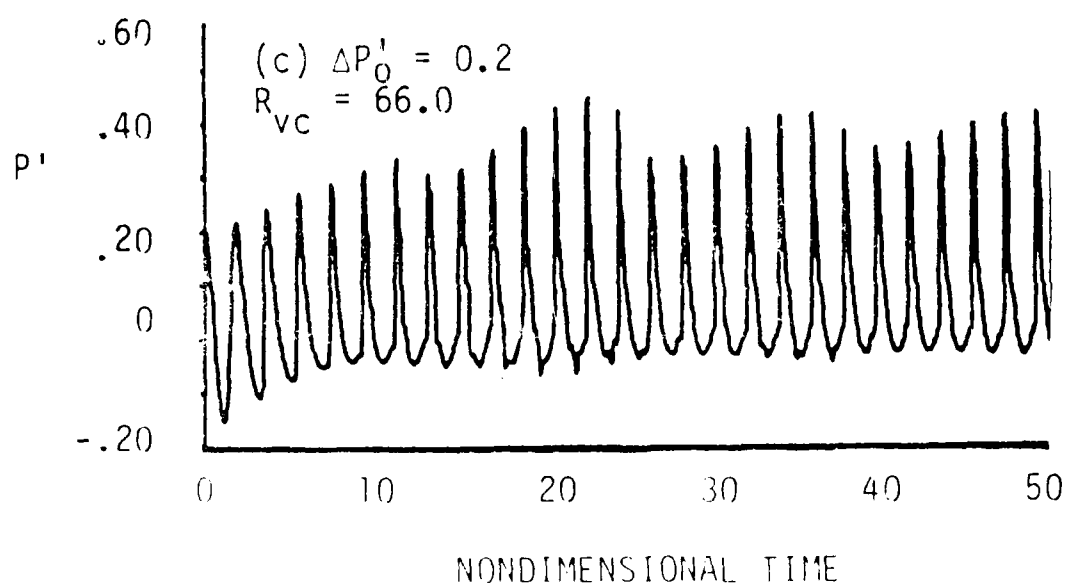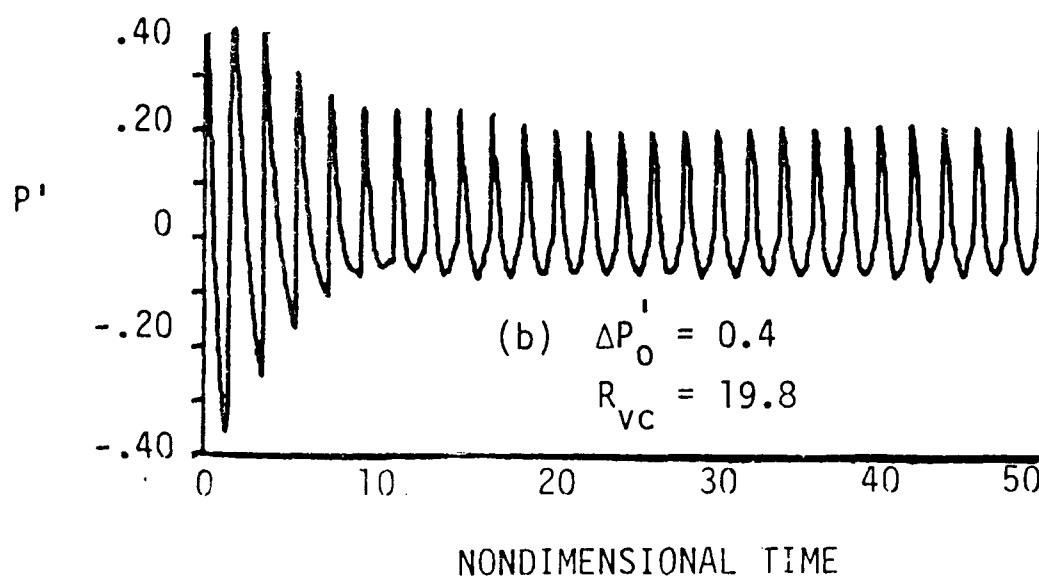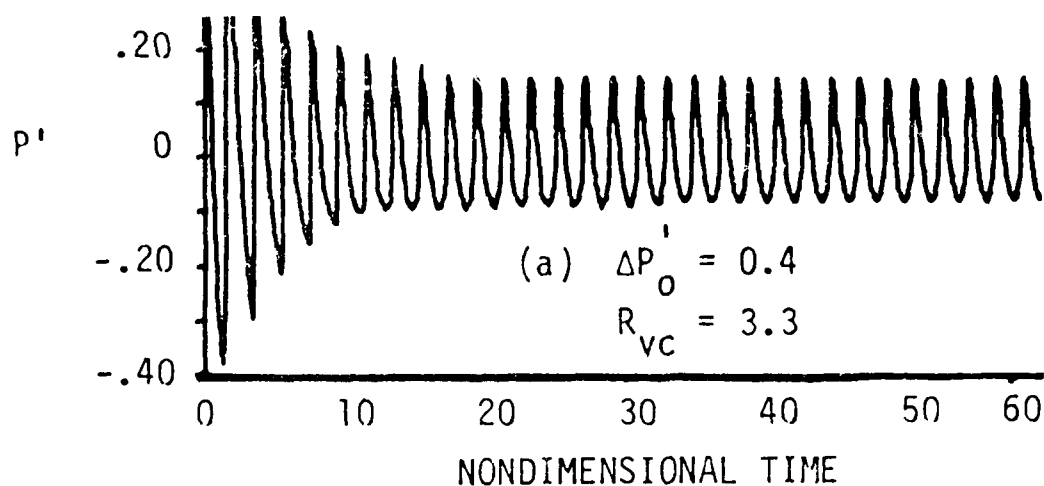
Figs. 23a-c Time evolution of pressure oscillations at the head end of the motor, velocity coupling augmenting the heat transfer to the propellant surface.

physical velocity coupling mechanism. However, it was felt that solutions obtained using it would be instructive.

A series of calculations was then carried out with velocity coupling added on the basis of Eq. (10) with $F(u) = |u'|$, $R_{vc} = 5$ and $R_{vc} = 2.18$. The results obtained with pressure coupling only indicate that this motor/propellant combination is stable, even to high amplitude disturbances, as shown in Fig. 24a. These results are confirmed by linear theory.[55] However, with both pressure and velocity coupling the results are entirely different. With an initial disturbance amplitude of 2% of the mean pressure (Fig. 24b) the disturbance amplitude grows initially, but the overall result indicates a stable motor. With an initial disturbance amplitude of 5% of the mean pressure (Fig. 24c), the oscillations grow to an amplitude of about 25% (peak to peak), appear to start damping, but then grow again. A mean pressure shift of about 12% is observed. With a 40% initial disturbance amplitude (Fig. 24d) the oscillation amplitude decays until it reaches an amplitude of about 20%, maintains that level for a while and then begins to grow again. The mean pressure shift observed is about the same as that resulting from a 5% disturbance.

This last series of calculations demonstrates a number of characteristics of observed nonlinear instabilities; characteristics that the model with pressure coupling alone has not been able to simulate. These characteristics are triggering (Fig. 24b compared to 24c and 24d), waves that grow and then decay (Fig. 24c), mean pressure shifts that appear to be relatively independent of initial amplitude (Fig. 24c, 24d), and a lack of a stable limit cycle behavior, i.e., modulating amplitude (Figs. 24c, 24d). To the author's best knowledge, this is the first time such solutions have been obtained.

Based on these results, it has been concluded that the relative ineffectiveness of the heat transfer augmentation model is a result of the response function versus
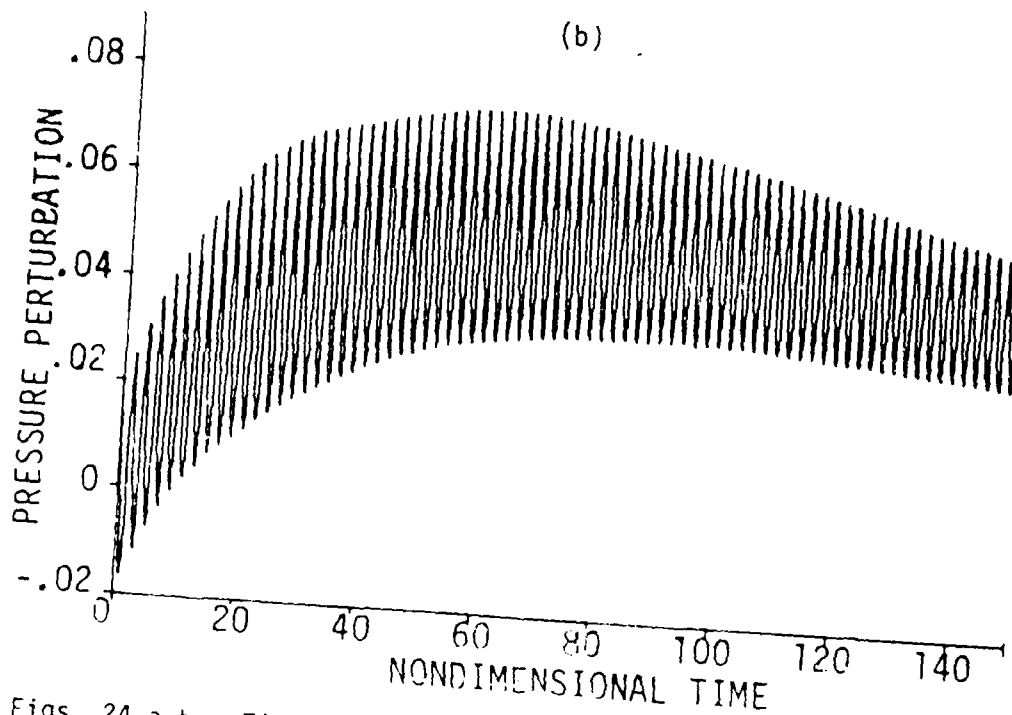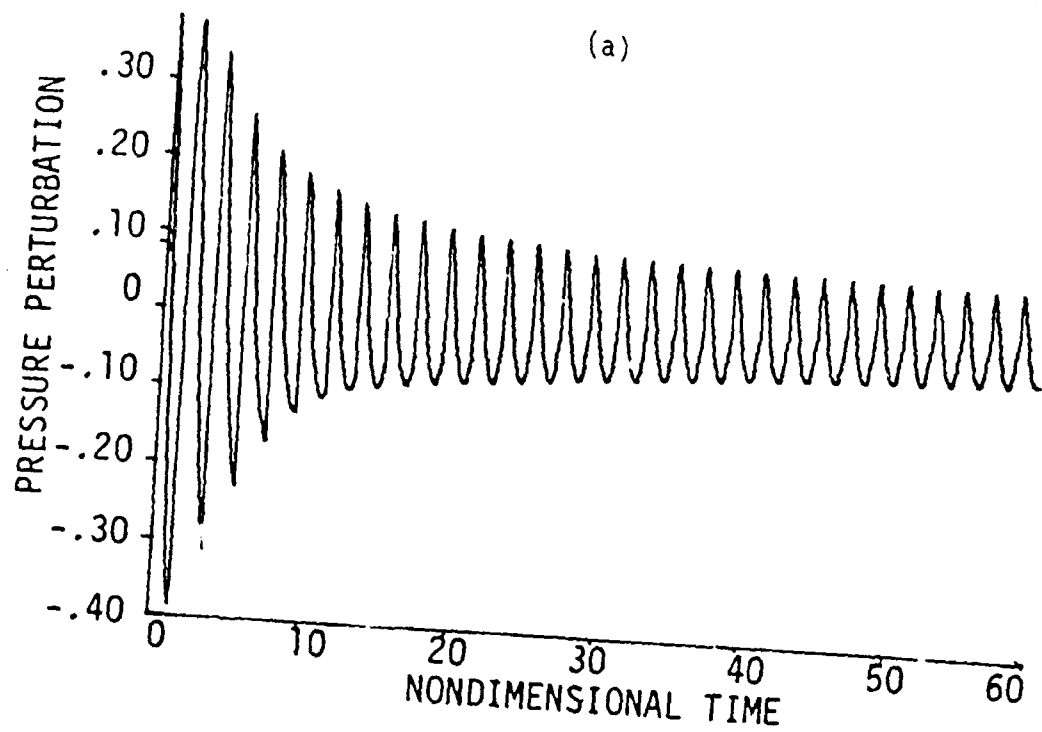
Figs. 24 a-b. Time evolution of normalized pressure oscillations at the head end of the motor, R_{pc} = 2.18: (a) $\Delta P' = 0.4\bar{P}$, pressure coupling only, (b) $\Delta P'_o = 0.02.\bar{P}$, burn rate augmentation model, $R_{vc} = 5.0$.

81

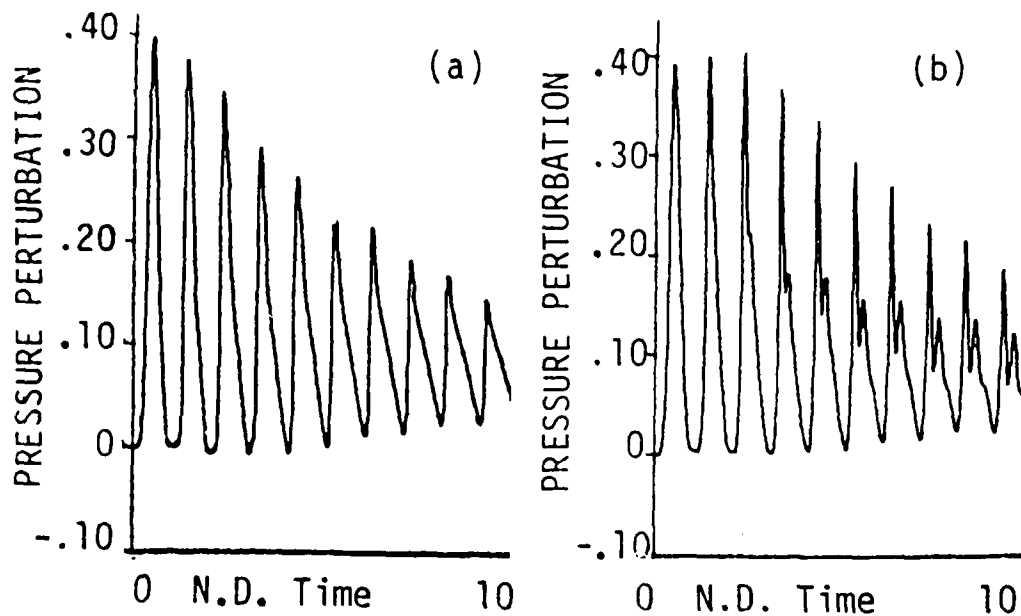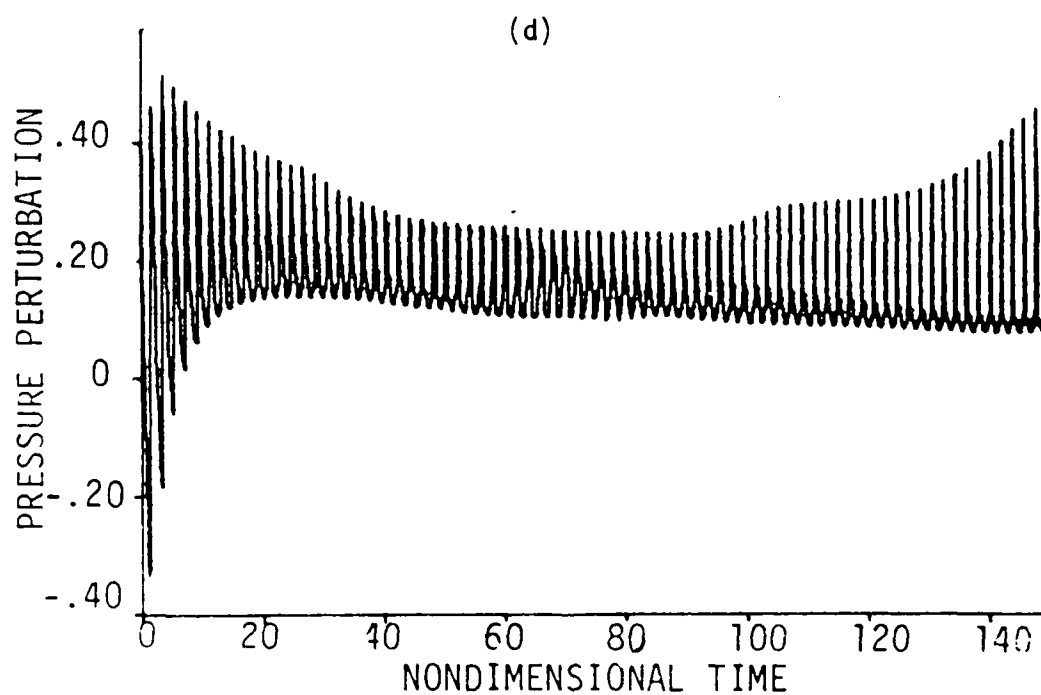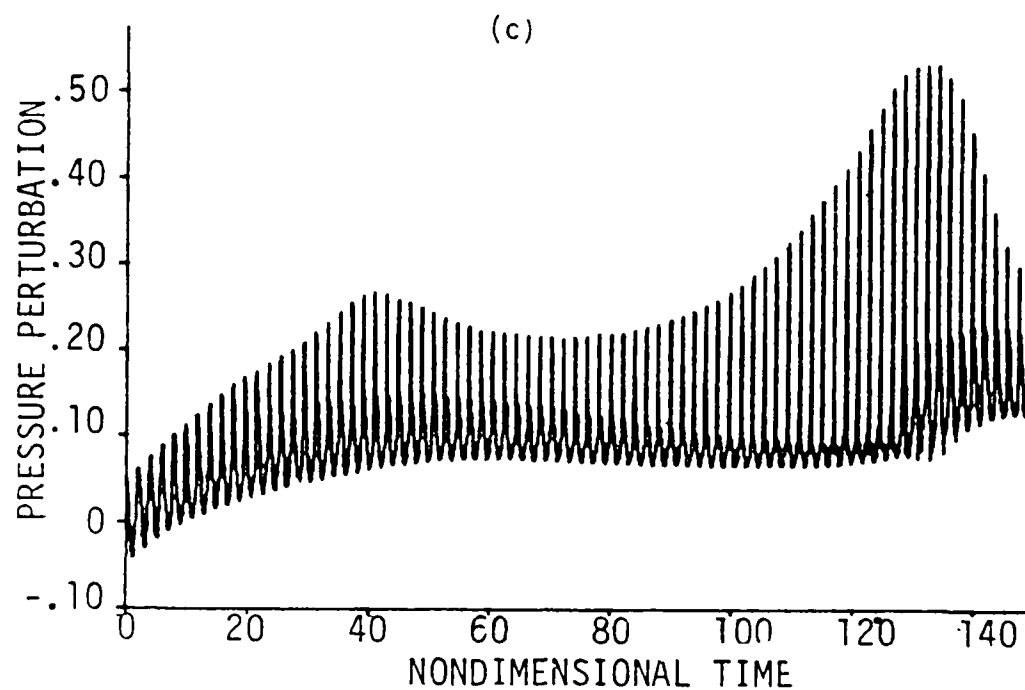Figs. 24 c-d. Time evolution of normalized pressure oscillations at the head end of the motor, R_{pc} = 2.18, burn rate augmentation model, R_{vc} = 5.0: (c) $\Delta P_0'$ = $0.05\overline{P}$, (d) $\Delta P_0'$ = $0.4\overline{P}$.

frequency characteristics implied by Denison and Baum type models. With such quasi-steady combustion models, the gas phase heat transfer (whether from pressure or velocity coupled effects) produces a response function versus frequency curve that has a single narrow peak. Figure 25 depicts the response function versus frequency curve for the parameters used in the calculations shown in Figs. 23, 24, 26, 27, and 28 (A = 5.975, B = .53). At the nondimensional frequency implied by the propellant burn rate parameters and motor operating conditions used in the calculations (Ω = 3.78) the linear pressure coupled response function was equal to 3.3. At the 2nd harmonic frequency Ω = 7.56, the linear pressure coupled response function is only 0.3, while at the higher harmonics, it is even lower. With the heat transfer augmentation model the velocity coupled response function is, to first order, proportional to the pressure coupled response (Note: for the problems being considered, the waves are primarily traveling rather than standing, and the velocity is approximately in phase with the pressure over half the cycle and $180°$ out of phase with the pressure over the other half of the cycle). Thus, for the problem that was solved, the velocity coupled response for the 2nd harmonic was about a factor of 10 lower than the response function at the fundamental mode.

With the mass transfer augmentation model, Eq. (10), the velocity coupling response is independent of the combustion model, and to first order is independent of frequency. Thus, when a velocity coupled response function of 5 was specified, this was the approximate value at all frequencies. Given the nature of Fig. 25, it would require a value of R_{vc}/R_{pc} = 16.6 (which implies R_{vc} = 55 for the first harmonic) in order for the heat transfer augmentation model to produce a similar value of R_{vc} = 5 for the second harmonic.

The above discussion appears to be able to explain the wide disparity between the results obtained with the two ad hoc models. Furthermore, it implies that a realistic

83

velocity coupling model will have to be capable of providing strong driving at the higher harmonic frequencies.

In order to examine the effect of F(u) on the computed results, |u'| was replaced by Eq. (6), and the same series of calculations was repeated. Figure 26 shows the calculated results for an initial disturbance amplitude of 20% of the mean pressure. In this case the motor appears to be marginally stable. To examine the behavior induced by Eq. (6) under unstable conditions, the calculations were repeated with a velocity coupled response function (R_{vc}) equal to 13. Even with such a large velocity coupled response, a stable solution was obtained to an initial disturbance amplitude of 2% (Fig. 27a). Increasing the initial disturbance amplitude to 5% (Fig. 27b), however, produced a large amplitude highly modulated instability, with a significant mean pressure shift.

The sensitivity of the results to changes in the functional form of the velocity perturbation utilized demonstrates that the present nonlinear stability analysis can be useful in assessing the validity of more realistic velocity coupling models, as they are developed.

To further our understanding of the velocity coupling problem in particular, and nonlinear instability in general, the solutions presented in Figs. 24b and 24d were examined in detail;[56] not only at the head and aft ends but also at the one quarter, one half and three quarter points. Analysis of the results demonstrated a very complex behavior that is, undoubtedly, a result of many mutually interacting nonlinear fluid dynamics and combustion phenomena. Some of the complexity of the problem is illustrated in Figs. 28 and 29, which present expanded views of the perturbed pressure, burning rate, and velocity (actually F(u) = |u'|) waveforms at the head end, 1/4, 1/2, and 3/4 points and aft end, for the cases previously presented in Figs 24b
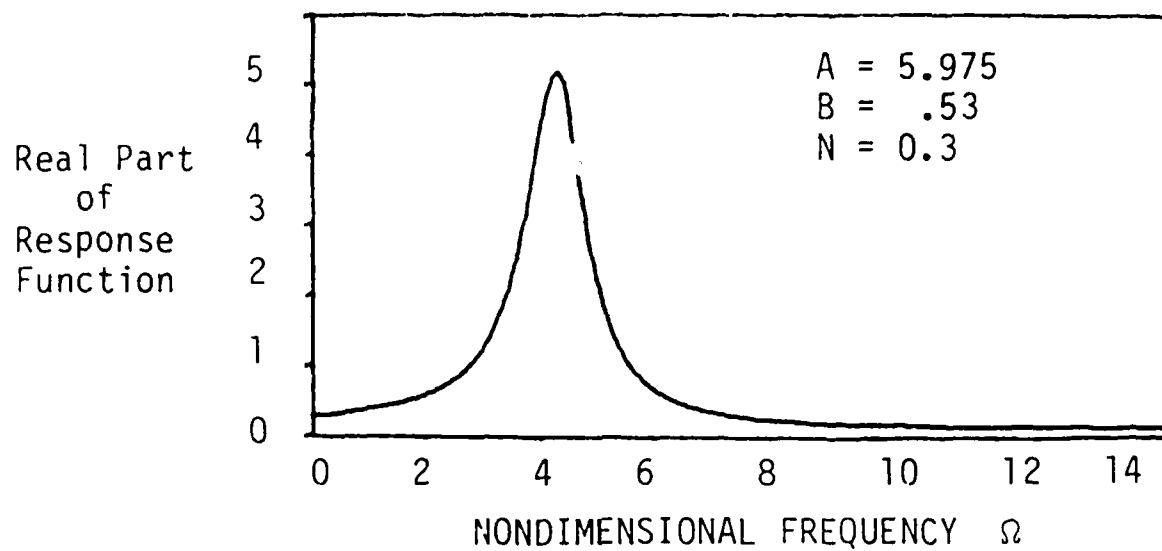
Fig. 25. Real part of response function vs frequency.
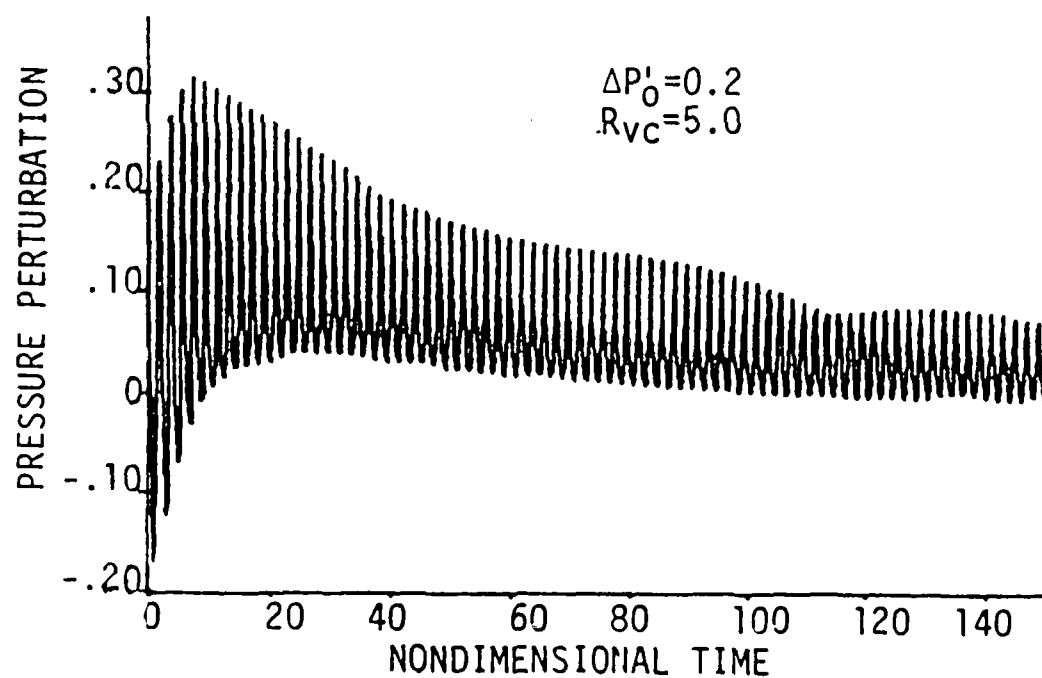
Fig. 26. Time evolution of normalized pressure oscillations at the head end of the motor, burn rate augmentation model, F(u) given by Eqs. (23).
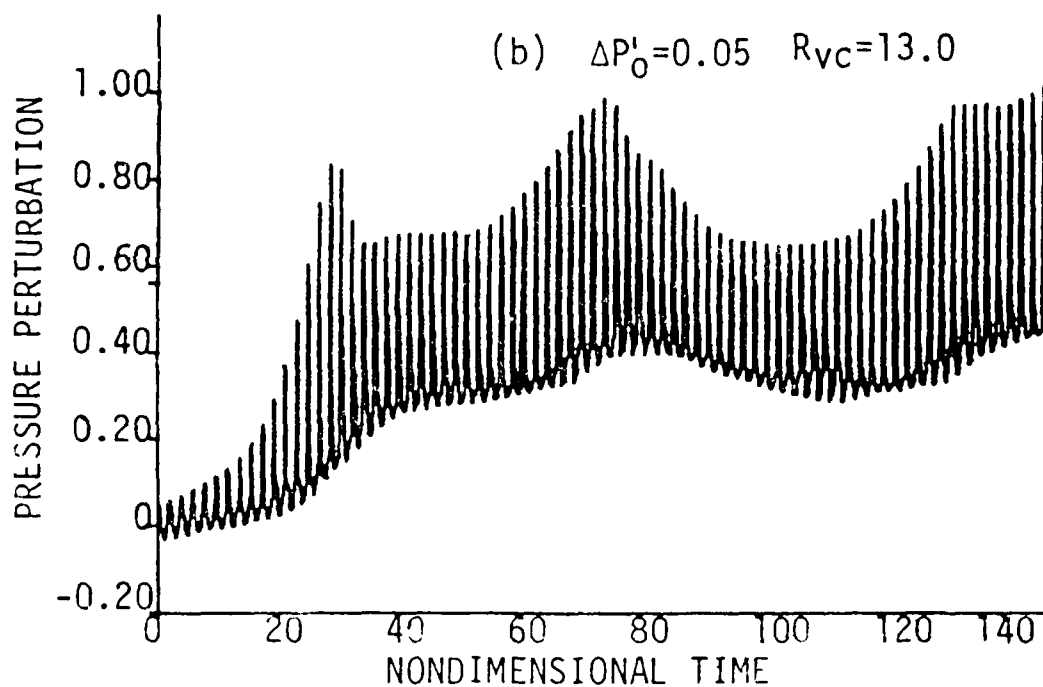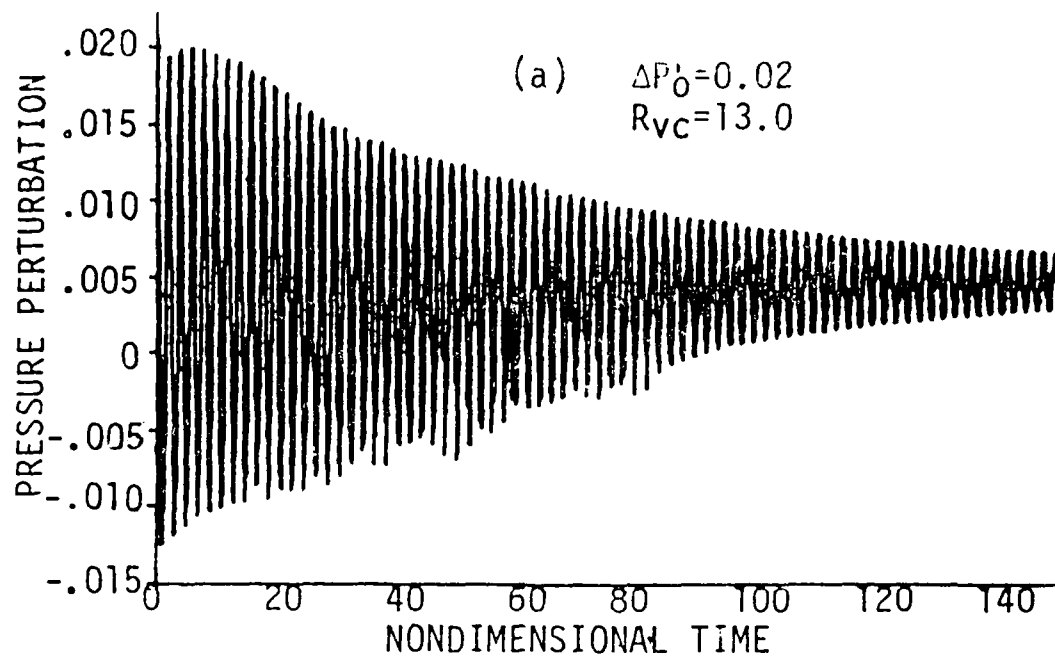
Figs. 27a-b. Time evolution of normalized pressure oscillations at the head end of the motor, burn rate augmentation model, F(u) given by Eqs. (23).

and 24d, respectively. The waveforms are shown in the interval around a nondimensional time of 30 (i.e., after about 15 wave cycles).

If the oscillations were standing waves, the velocity oscillations would be 90° out of phase with the pressure oscillations. On the other hand, if the oscillations were traveling waves, the pressure and velocity would be in phase for half of a wave cycle, and 180° out of phase for the other half of the cycle (Figs. 28 and 29 show | u' | rather than u', thus |u'| should be in phase with p' for the whole cycle). The phase relationship between p' and m' is a very complex function of the frequency, amplitude and phase of the pressure and velocity waves and the characteristics of the propellant. From a stability standpoint, the phase relationship between p' and m' is critical, since the combustion driving is produced by the component of m' that is in phase with p'. The figures were designed only to display the phase relationships between the oscillations; the amplitude scales for each curve are different and are not indicated.

From Fig. 28 (stable) and Fig. 29 (unstable), it can be seen that the waves are primarily, but not completely, travelling waves, since the velocity is close to being in phase with the pressure. This is true even though the calculations were initiated with a standing wave disturbance, and for the stable case, even though the waves are not steep-fronted and are of relatively low amplitude. In addition to the differences in waveforms, there are some other significant differences between the two sets of results. At the head and aft ends, where the velocity oscillations are zero or very small, respectively, the phase relationship between m' and p' is still quite different for the two cases. In the stable case (Figs. 28a and c), the burn rate leads the pressure by about 51°, while in the unstable case (Figs. 29a and c), the burn rate lags the pressure, but only by 8°. At these points (X = 0, X = L) the difference in phase between the two cases can only be attributed to the difference in the pressure waveform. At the 1/4
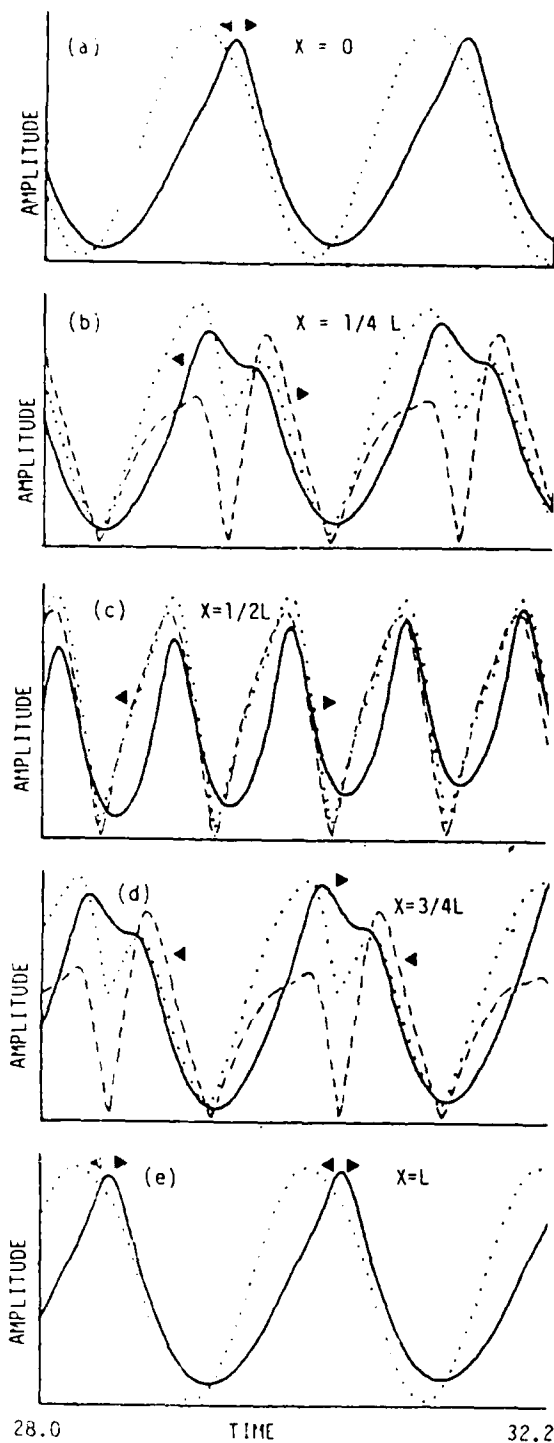
Figs. 28a-e. Expanded views of the pressure, burn rate and velocity (|u'|) waveforms for a stable solution.
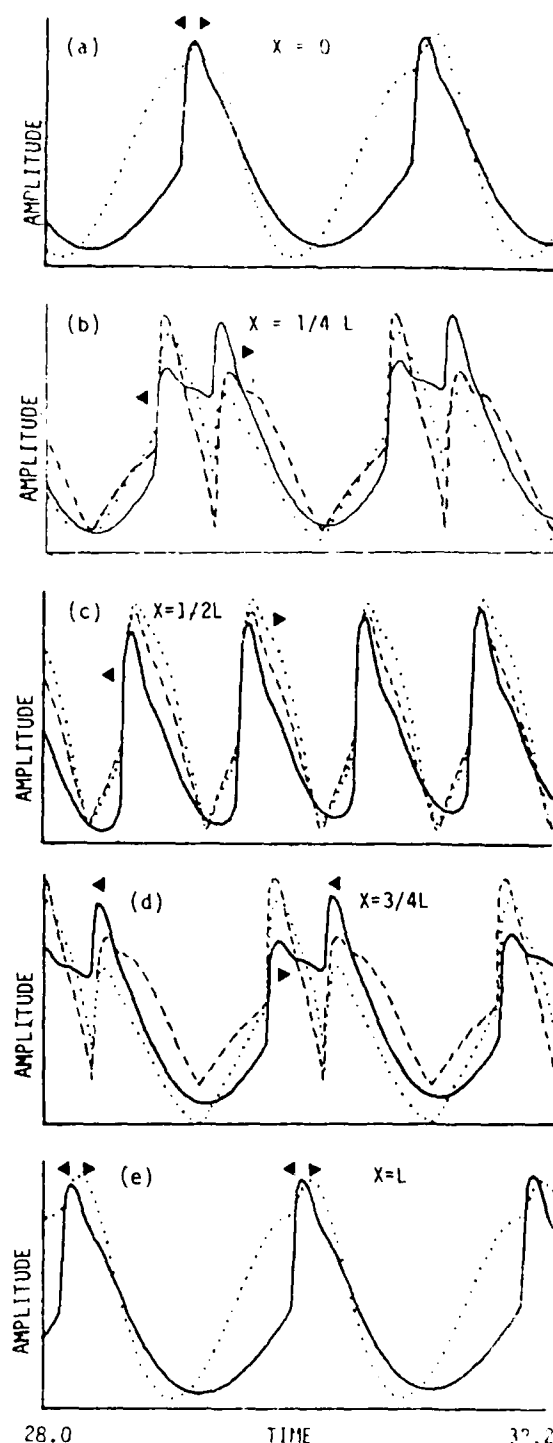
Figs. 29a-e. Expanded views of the pressure, burn rate and velocity (|u'|) waveforms for an unstable solution.

point, the results are somewhat more complicated. For the unstable case (Fig. 29b), the amplitude of the pressure wave is lower when it is traveling towards the head end than after it has been reflected off the head end and is traveling back towards the nozzle. The behavior of the burning rate and velocity waveforms for this case are just the opposite, i.e., they are lower after reflection than before it. For the stable case (Fig. 28b), both the pressure and burning rate are 'ower after reflection, while the velocity is higher after reflection than before it. In addition to the differences in the behavior of the wave amplitudes, the phase relationships in the two cases are also different. In the unstable case (Fig. 29b), the burning rate is almost exactly in phase with pressure over the whole wave cycle, while in the stable case (Fig. 28b), the burning rate leads the pressure by about 20° when the wave is traveling towards the head end, and lags the pressure by about 20° when the wave is traveling towards the nozzle. In the unstable case, the velocity leads the pressure by about 10° when the wave is traveling to the left, and lags the pressure by about 10° when it is traveling to the right. In the stable case, the velocity lead/lag is the same with regard to the direction of travel, but the magnitude of the lead or lag is about double (about 20°).

At the center of the motor (Figs. 28c and 29c), the wave amplitudes are almost the same, regardless of the direction of travel, and the phase differences essentially disappear. In the center, the pressure, velocity, and burning rate are all in phase, in both cases. At the 3/4 point, the amplitude and phase behavior for the two cases is similar to that at the 1/4 point, but in an anti-symmetric fashion in regard to direction of wave travel.

Just from examining these two cases at one point in time, it becomes apparent how complex nonlinear wave propagation can become. The waves are, in general, some combination of traveling and standing waves. The frequency content of the waves and

the phase relationships of the pressure, velocity, and the burning rate vary significantly from one point in the motor to another, and for the same motor and location, vary as a function of the initial disturbance amplitude. In addition, the phase angles between m', u', and p' vary intra-cycle, i.e., from one portion of the wave cycle to another, and also vary in time from one cycle to another. This nonstationary behavior of the phase angle is the most likely cause of the modulated limit cycle amplitudes that are observed in the nonlinear velocity coupling solutions. Results such as those presented above clearly demonstrate why attempts to solve nonlinear instability problems using techniques and understanding based on linear analyses cannot be expected to be uniformly successful.

THRESHOLD EFFECTS

All of the velocity coupling results previously presented herein were for zero threshold velocity. Since threshold effects have been observed,[57] a brief attempt was made to examine their effect within the context of the present ad hoc model. The results presented in Fig. 30 were obtained for the same motor used in the other cases presented herein. The burn rate augmentation model was utilized with $F(u)=|u'|-u_t$. With the pressure and the velocity coupling values used in the Fig. 24 calculation (R_{pc} = 2.18, R_{vc} = 5) an unstable result could not be achieved with a threshold velocity equal to 0.02 (u_t is normalized by the steady state gas sound speed, so u_t = 0.02 corresponds to about 60 ft/sec or 18.29 m/sec). R_{vc} was then increased to 13 and the calculations were repeated. With u_t = .02 and $\Delta p_o'$ = 0.02P, a stable result was obtained again (Fig. 30a). However, when $\Delta p_o'$ was increased to $0.08\overline{P}$, a highly nonlinear instability was produced (Fig. 30b). The threshold velocity was then increased to 0.05. With the increased threshold velocity an unstable result could not be achieved, even with initial disturbance perturbations as large as 40% of the mean pressure (Fig. 31).
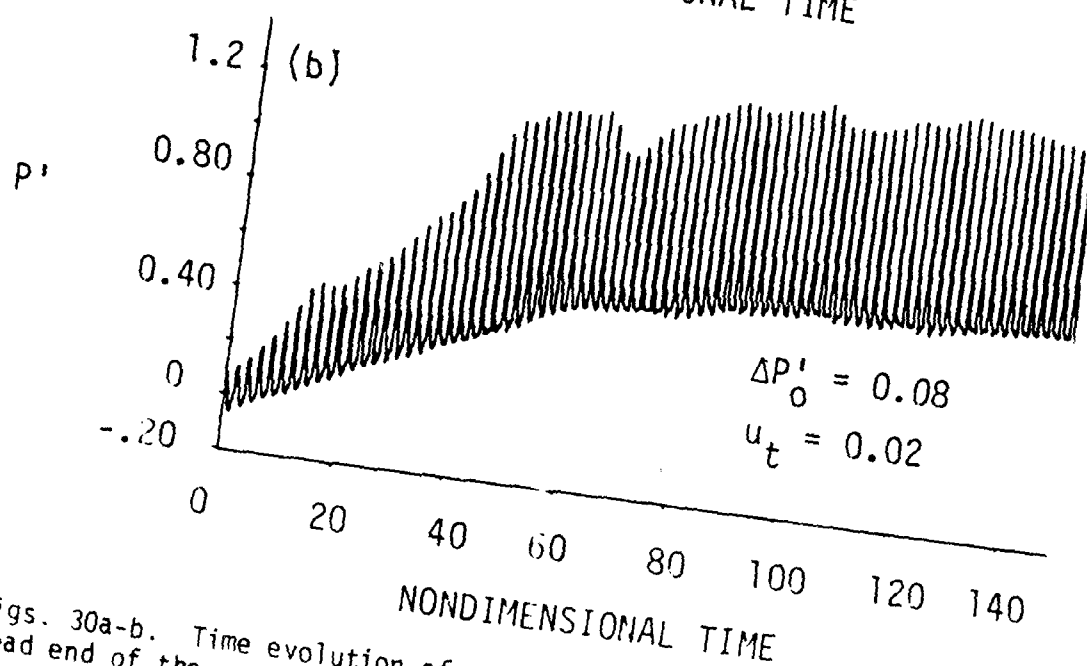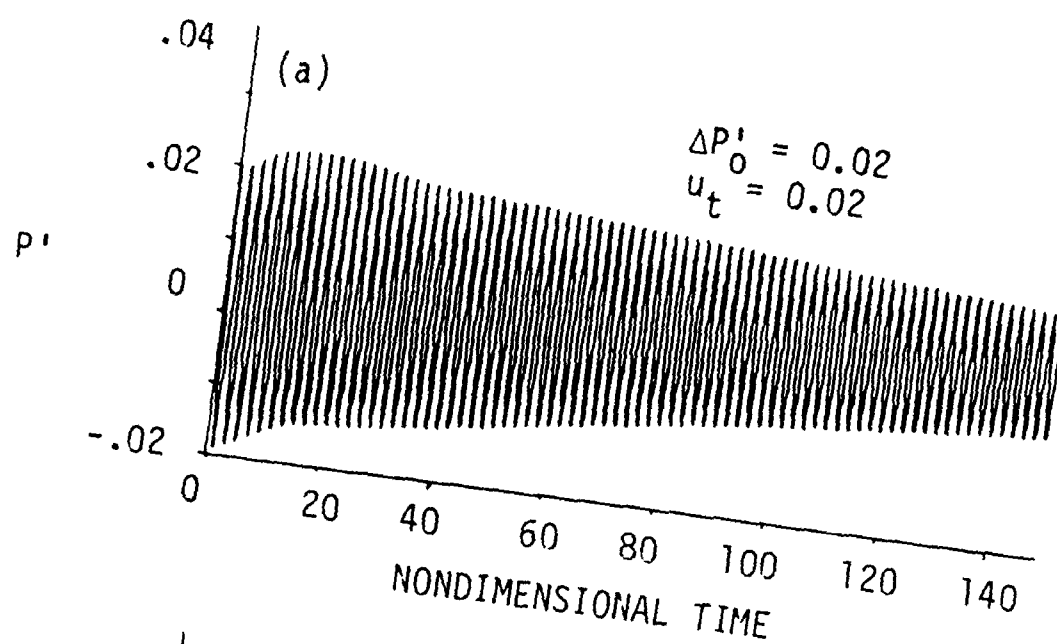
Figs. 30a-b. Time evolution of normalized pressure oscillations at the head end of the motor, burn rate augmentation model with threshold velocity, $R_{vc} = 13.$).

91
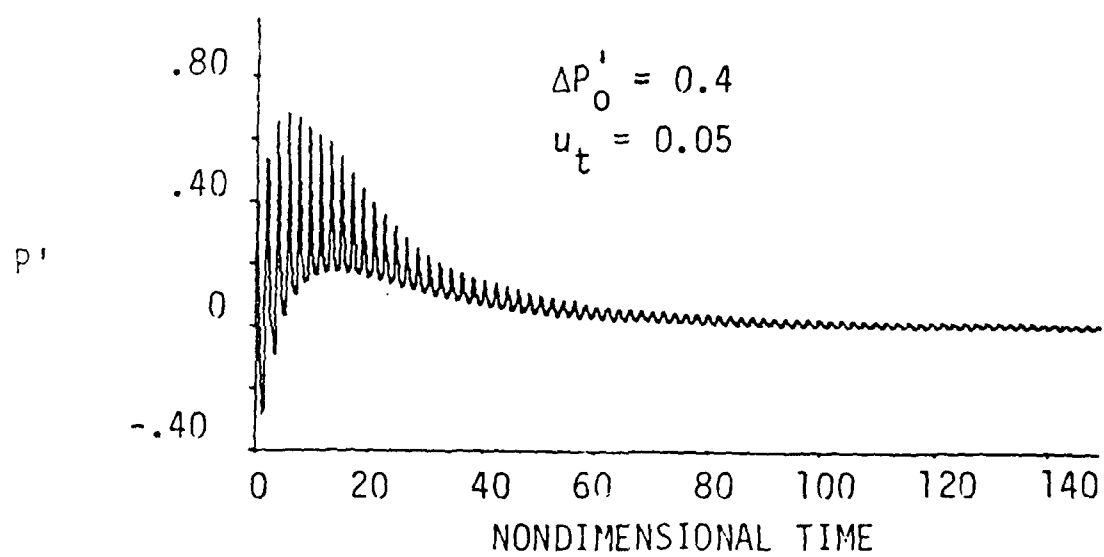
Fig. 31. Time evolution of normalized pressure oscillations at the head end of the motor, burn rate augmentation model with threshold velocity, R_{vc} = 13.0.

Although threshold effects, if they exist, are not expected to be a function of only mean and/or fluctuating velocity, these results indicate that, as expected, threshold effects act to increase the magnitude of the velocity coupled response function required to trigger an instability. The results also imply that propellants with high thresholds will be difficult or impossible to trigger. Threshold effects, variations in R_{vc} as a function of frequency, and nonlinear fluidynamic effects, all interact to determine the nonlinear stability of a given motor propellant combination.

CONCLUSIONS

The complexity of nonlinear instability in solid propellant rocket motors and the large number of mutually interacting physical phenomena which control it, makes it very difficult to form generally valid quantitative conclusions, even from a relatively large number of numerical or experimental results.

The following conclusions can, however, be drawn from the large number of nonlinear instability solutions obtained during the present investigation:

1.   Based on many more solutions than had been available in the past, it is concluded that pressure oscillations will reach a limiting amplitude that is independent of the characteristics (waveform and amplitude) of the initiating disturbance. This conclusion appears to hold for unmetallized as well as metallized solid propellants, but cannot as yet be generalized to include cases when strong nonlinear velocity coupling is present (see number 5 below).

2.   Velocity coupling models based on modifications to standard quasi-steady gas phase, homogeneous solid phase assumptions are not capable of producing strong nonlinear effects at realistic values of velocity coupled response function.

3.   A realistic velocity coupling model must be capable of predicting high combustion response over a wide frequency range for propellants that are known to be able to produce strong nonlinear velocity coupling effects.

4.   Nonlinear oscillations in solid rocket motors are very complex. The oscillations are, in general, a combination of traveling and standing waves, with the traveling component being dominant, even for non steep-fronted waves at relatively low amplitudes.

5.   The phase angles between pressure, velocity and burning rate oscillations vary from one location in the motor to another, and are non-stationary in time. The non-stationary behavior of the phase angles is the most likely cause of the modulated limit cycle amplitudes observed in the solutions and in motors.

6.   The predicted results were quite sensitive to changes in both the magnitude of the velocity coupled response function utilized and its functional dependence. Thus, it is concluded that the present comprehensive nonlinear stability analysis will prove to be valuable in assessing the validity of improved velocity coupling models as they are developed.

7.   Solutions obtained using a threshold velocity imply that propellants with high acoustic velocity thresholds will be difficult or impossible to trigger unless they also have a very high level of velocity coupled response.

CHAPTER 6

SUMMARY AND CONCLUSIONS

A new combustion instability model that describes the combustion and flowfield inside a solid rocket motor has been developed. The capability of this model to predict the multiple shock, triggered type of instability that occurs in modern variable cross-sectional area reduced/minimum smoke solid motors was demonstrated. It has been shown that the model can predict triggering, DC pressure shifts, and modulated amplitude limit cycles; phenomena that are all observed in actual solid rocket motor instability data. The model also predicts waveforms that are in good qualitative agreement with those observed during motor firings.

A finite difference integration method based on a combination of the Lax-Wendroff, Hybrid and Artificial Compression schemes was found to be superior to other schemes tested. This scheme is capable of describing a shock as a sharp discontinuity without generating artificial pre- or post-shock oscillations. The method does not rely on the use of an artificial viscosity, and is capable of preserving the high frequency content of the waveforms. This combination technique can also treat the reflection of shocks from boundaries and has small diffusive and dispersive errors even after many wave cycles.

Pressure oscillations were shown to reach a limiting amplitude that is independent of the characteristics of the initiating disturbance. This conclusion appears to hold for unmetallized as well as metallized solid propellants, but cannot as yet be generalized to include cases when strong nonlinear velocity coupling is present.

Velocity coupling models based on quasisteady gas phase, homogeneous solid phase assumptions are not capable of producing strong nonlinear effects at realistic values of velocity coupled response function. A realistic velocity coupling model must be capable of predicting high combustion response over a wide frequency range for propellants that are known to be able to produce strong nonlinear velocity coupling effects in solid rocket motors.

Nonlinear oscillations in solid rocket motors are very complex. The oscillations are, in general, a combination of traveling and standing waves, with the traveling component being dominant, even for non-steep-fronted waves at relatively low amplitudes. The phase angles between pressure, velocity and burning rate oscillations vary from one location in the motor to another, and are non-stationary in time. The non-stationary behavior of the phase angles is the most likely cause of the modulated limit cycle amplitudes observed in the solutions and in motors.

The predicted results were quite sensitive to changes in both the magnitude of the velocity coupled response function utilized and its functional dependence. Thus, it is concluded that the present comprehensive nonlinear stability analysis will prove to be valuable in assessing the validity of improved velocity coupling models, as they are developed.

REFERENCES

1. Price, E. W., "Axial Mode Intermediate Frequency Combustion Instability in Solid Propellant Rocket Motors," AIAA Paper, Jan 1964.

2. Brownlee, W. G., "Nonlinear Axial Combustion Instability in Solid Propellant Motors," AIAA Journal, Vol. 2, No. 2. Feb 1964, pp. 205-284.

3. Marxman, G. A., and Wooldrige, C. E., "Finite-Amplitude Axial Instability in Solid-Rocket Combustion," Twelfth Symposium (International) on Combustion, The Combustion Institute, Pittsburgh, Pa., 1969, pp. 115-127.

4. Levine, J. N., and Culick, F. E. C., "Nonlinear Analysis of Solid Rocket Combustion Instability," Air Force Rocket Propulsion Laboratory, Edwards AFB, Calif. AFRPL-TR-74-45, Oct 1974.

5. Kooker, D. E. and Zinn, B. T., "Numerical Investigation of Nonlinear Axial Instabilities in Solid Rocket Motors," BRL-CR-141, Mar 1974.

6. Culick. F. E. C., "Nonlinear Behavior of Acoustic Waves in Combustion Chambers," Proceedings of the 10th JANNAF Combustion Meeting, Vol. I, CPIA Publication 243, 1973, pp. 417-436.

7. Powell, E. A., Padmanabahn, M. S., and Zinn, B. T., "Approximate Nonlinear Analysis of Solid Rocket Motors and T-Burners," Air Force Rocket Propulsion Laboratory, Edwards AFB, Calif. AFRPL-TR-77-48, 1977.

8. Culick, F. E. C. and Levine, J. N., "Comparison of Approximate and Numerical Analyses of Nonlinear Combustion Instability," AIAA Paper 74-201, Jan 1974.

9. Zwas, G. and Roseman, J., J. of Computational Physics, Vol. 12, 1973, p. 179.

10. Salas, M. D., "On the Anatomy of Floating Shock Fitting," AIAA Second Computational Fluid Dynamic Conference, 1975, pp. 47-54.

11. Moretti, G., "The Choice of a Time-Dependent Technique in Gas Dynamics," Polytechnic Institute of Brooklyn Report, PIBAL 69-26, 1969.

12. Moretti, G., "A Critical Analysis of Numerical Techniques: The Piston-Driven Inviscid Flow," Polytechnic Institute of Brooklyn Report, PIBAL 69-25, 1969.

13. Moretti, G., Computers and Fluid, Vol. 17, 1979, p. 191.

14. Chakravarthy, S. R., Anderson, D. A., and Salas, M. D., AIAA Paper 80-0268, 1980.

15. Carver, M. B., J. of Computational Physics, Vol. 3, 1980, p. 57.

16. Richtmyer, R. D., and Morton, K. W., "Difference Methods for Initial Value Problems," Interscience, New York, 1967.

17. Harten, A., Hyman, J. M., and Lax, P. D., Communications on Pure and Applied Mathematics, Vol. 29, 1976, p. 292.

18. MacCormack, R. W., and Paullay, A. J., Computer and Fluid, Vol. 2, 1974, p. 339.

19. Majda, A. and Osher, S. A., Numerical Mathematics, Vol. 30, 1973, p. 429.

20. Harten, A. and Zwas, G., J. of Computational Physics, Vol. 9, 1972, p. 568.

21. Harten, A. and Zwas, G., J. of Engineering Mathematics, Vol. 6, 1972, p. 207.

22. Van Leer, B., J. of Computational Physics, Vol. 23, 1977, p. 296.

23. Chorin, A. J., J. of Computational Physics, Vol. 22, 1976, p. 517.

24. Book, D. L., Boris, J. P., and Hain, K., J. of Computational Physics, Vol. 20, 1975, p. 248.

25. Boris, J. P. and Book, D. L., J. of Computational Physics, Vol. 20, 1976, p. 397.

26. Harten, A., Communications on Pure and Applied Mathematics, Vol. 30, 1977, p. 611.

27. Harten, A., "The Artificial Compression Method for Computation of Shocks and Contact Discontinuities: III. Self Adjusting Hybrid Schemes," Courant Institute of Mathematical Sciences Report IMM-415, 1977.

28. Lax, P. D. and Wendroff, B., Communications on Pure and Applied Mathematics, Vol. 13, 1960, p. 217.

29. Sod, G. A., J. of Computational Physics, Vol. 27, 1978, p. 1.

30. Turkel, E., "Numerical Methods for Large-Scale, Time Dependent Partial Differential Equations," Institute for Computer Applications in Science and Engineering, ICASE-79-20, 1979.

31. Colella, P., "An Analysis of the Effect of Operator Splitting and of the Sampling Procedure on the Accuracy of Glimm's Method," Ph. D. Thesis, University of California, Berkeley, 1978.

32. Sod, G. A., "Computation Fluid Dynamics with Stochastic Techniques," Von Karman Institute for Fluid Dynamics, Lecture Series on Computational Fluid Dynamics, Mar, 1980.

33. Godunov, S. K., Math. Sborik., Vol. 47, 1959, p. 271.

34. Warming, R. F. and Beam, R. M., AIAA J. Vol. 14, 1976, p. 1241.

35. Steger, J. L. and Warming, R. F., "Flux Vector Splitting of the Inviscid Equations with Application to Finite Difference Methods." NASA-TM-78605, 1979.

36. MacCormack, R. W., Proceedings of the Second International Conference on Numerical Methods in Fluid Dynamics in "Lecture Notes in Physics" (M. Holt, ed.), 8, Springer - Verlag, New York/Berlin, 1971.

37. Van Leer, B., J. of Computational Physics, Vol. 35, 1980, p. 57.

38.   Van Leer, B., J. of Computational Physics, Vol. 32, 1979, p. 101.

39.   Rusanov, V. V., Comp. Math. Phys., USSR, No. 2, 1962.

40.   Morse, P. M. and Ingard, K. V., "Theoretical Acoustics," McGraw-Hill Book Company, New York, 1968.

41.   Hughes, P. M., and Smith, D. L., "Nonlinear Combustion Instability in Solid Propellant Rocket Motors: Influence of Geometry and Propellant Formulation," 53rd AGARD Meeting, Propulsion and Energetics Panel, Oslo, Norway, Apr 1979.

42.   Baum, J. D., Lovine, R. L., and Levine, J. N., "Pulsing of Solid Propellant Rocket Motors; Modeling and Cold Flow Testing," AIAA Paper 82-0359, 1982.

43.   Zinn, B. T. and Powell, E. A., "Nonlinear Combustion Instability in Liquid Propellant Rocket Engines," Proceedings of the 13th Symposium (International) on Combustion, The Combustion Institute, Pittsburgh, PA., 1971, pp. 491-503.

44.   Powell, E. A. and Zinn, B. T., "The Prediction of Nonlinear Three-Dimensional Combustion Instability in Liquid Rockets with Conventional Nozzles," NASA CR-121279, Oct 1973.

45.   Denison, M. R., and Baum, E., "A Simplified Model of Unstable Burning in Solid Propellants," ARS J., Vol. 31, No. 8, Aug 1961, pp. 1112-1122.

46.   Beckstead, M. W., "Report of the Workshop on Velocity Coupling," Proceedings of the 17th JANNAF Combustion Meeting, Langley, VA. CPIA Publication 324, Nov 1980, pp. 195-210.

47.   Price, E. W., and Dehority, G. L., "Velocity Coupled Axial Mode Combustion Instability in Solid Propellant Rocket Motors," Proceedings of the 2nd ICRPG/AIAA Solid Propulsion Meeting, Anaheim, California, 1967, pp. 213-227.

48.   Culick, F. E. C., "Stability of Longitudinal Oscillations with Pressure and Velocity Coupling in a Solid Propellant Rocket," Combustion Science and Technology, Vol. 2, No. 4, 1970, pp. 179-201.

49.   Levine, J. N., and Culick, F. E. C., "Numerical Analysis of Nonlinear Lognitudinal Combustion Instability in Metallized Propellant Solid Rocket Motors, Vol. I Analysis and Results," Air Force Rocket Propulsion Laboratory, Edwards AFB, Calif., AFRPL-TR-72-88, Jul 1972, p. 22.

50.   Lengelle', G., "A Model Describing the Velocity Response of Composite Propellants," AIAA Journal, Vol. 13, 1975, pp. 315-322.

51.   Condon, J. A., "A Model for the Velocity Coupling Response of Composite Propellant," Proceedings of the 16th JANNAF Combustion Meeting, Monterey, CA Sep 1979, CPIA Publication 308, Vol. III, Dec 1979, pp. 559-574.

52.   Srivastava, R., "Investigation of Chemically Reacting Boundary Layers in Solid Propellant Rockets: Steady and Periodic Solutions," Ph. D. Thesis, Georgia Institute of Technology, Feb 1977.

53.   Beddini, R. A., "Effects of Grain Port Flow on Solid Propellant Erosive Burning," AIAA Paper 78-977, Jul 1978.

54. Flandro, G. A., "Solid Propellant Acoustic Admittance Correlations," _Journal of Sound and Vibration,_ Vol. 36, 1974, pp. 297-312.

55. Lovine, R. L., "Standardized Stability Prediction Method for Solid Rocket Motors", Air Force Rocket Propulsion Laboratory, Edwards AFB, Calif., Vol. I, AFRPL-TR-76-32, May 1976.

56. Levine, J. N., and Baum, J. D., "Nonlinear Velocity Coupled Instability in Solid Rocket Motors," Proceedings of the 18th JANNAF Combustion Meeting, Pasadena, CA, CPIA Publication 347, Oct 1981, pp. 39-48.

57. Medvedev, Yu. I., and Revyagin, L. L., "Unsteady Erosion of a Powder," _Fizika Goreniya i Vzryva,_ Vol. 10, No. 3, May-Jun 1974, pp. 341-345.

58. Rubin, E. L., Burstein, S. Z., "Difference Methods for the Inviscid and Viscous Equations of a Compressible Gas," _J. of Computational Physics_, Vol 2, 1967, pp. 178-196.

NOMENCLATURE

C_n	-	Courant number
c_p	-	specific heat of gas at constant pressure
F	-	vector of the conserved quantities
$F(u)$	-	defined in Eqs. (6) or (7)
G	-	Flux vector
k	-	thermal conductivity
m	-	mass flux from burning surface
P	-	pressure
Q_s	-	net heat of reaction for processes at burning surface
r	-	linear burn rate
T	-	temperature
t	-	time
u	-	velocity
u_t	-	threshold velocity
w	-	mass burning rate, per unit length, per unit cross sectional area
x	-	axial distance
γ	-	gas only isentropic exponent
	-	defined in Eq. 9
	-	thermal diffusivity
	-	density
	-	nondimensional frequency
	-	artifical viscosity coefficient

Subscripts

g   -   gas

pc   -   pressure coupled

s   -   at the burning surface

vc   -   velocity coupled

Superscripts

$(\ )'$ -   denotes a perturbation

$\overline{(\ )}$ -   denotes steady state value

APPENDIX I

Excerpts from AFRPL- TR-74-45

October 1974

Jay M. Levine

F. E. C. Culick

2.   EQUATIONS OF MOTION

2.1   Discussion of the Mathematical Model

The longitudinal instability problem in solid rocket motors contains so
many complex, interacting, phenomena that even with a numerical approach cer-
tain idealizations are required in order to formulate a reasonable mathematical
model. In the present analysis the flow in a metal loaded solid propellant motor
is calculated from the unsteady, inviscid, two-phase equations of motion. This
section is devoted to the enumeration, and discussion, of the assumptions and
simplifications which have been utilized in the process of formulating and solving
these equations.

The gas within the motor has been assumed to be ideal, nonreacting,
and inviscid; with constant specific heats, constant Prandtl number, etc. It has
also been assumed that the flow in the motor is one-dimensional, the time deri-
vative of the cross-sectional area can be neglected, and the particles are spheres
which have uniform internal temperature and do not collide with each other.

The gas and particles coming from the burning surface are assumed to
enter the mean flow normal to the burning surface, at the local transient flame
temperature. The effects associated with propellant surfaces inclined to the
direction of the one-dimensional mean flow, and nonisentropic flame temperature
variations, are properly accounted for.

Most solid rocket combustion chambers do not have rapid variations in
cross-sectional area, hence, a one dimensional analysis should provide a reason-
able approximation to the flow. Rapid, or discontinuous, area variations may be
encountered at grain ends when the propellant is not flush, and in the relatively
short nozzles which characterize most solid rocket motors. Rapid area variations
are allowed in the present model, even when the flow in their immediate vicinity
is basically two dimensional. It is hoped that by doing so the essence, if not
the exact nature, of their effect on motor stability can be demonstrated. The
geometrical description of the motor has been separated into two parts. The area
and perimeter variation in the chamber is assumed to be arbitrary (tabular descrip-
tion), and may include end, partial length, and segmented (with gaps) grains.
The nozzle is assumed to be composed of arcs of circles and straight line segments
as described in Section 3.2.

It is widely known that the majority of the metal oxide particles are generated by combustion of metal droplets in the mean flow, not at the propellant surface. The liquid metal pools, agglomerates, partially oxidizes, and, in some cases, ignites, before leaving the surface. As the relatively large metal agglomerates $(0 \sim 100\mu)$ burn they tend to produce oxide particles in two size ranges[5], so called smoke particles $(< 2\mu)$, and larger particles $(\sim 8-10\mu)$, which represent the residual cores of the initial droplets. If the residence time of the droplets in the chamber is of sufficient duration the droplets will completely oxidize before passing out the nozzle.

The residence time of the droplets, however, varies over a wide range, as a function of position in the chamber. Thus, it may be expected that the particle size distribution and chemical makeup will also vary considerably from one end to the other. The possibility that the aforementioned droplet combustion phenomena may significantly affect the stability of a motor is being increasingly recognized. However, adequate theoretical models of these complex processes have yet to be developed. Quantitative data, which could be used to evaluate such models, is also relatively non-existent.

When satisfactory analytical models of metal combustion in the chamber become available, it will be worthwhile to attempt to incorporate them into the present instability model. In the meantime, it has been assumed the metal is completely oxidized at the burning surface. The resulting inert particles are assumed to be divided into discrete size groups; the weight fraction of each group being invariant with location.

All particles of a given size, at a specific location, are assumed to have the same velocity and temperature. The adequacy and consequences of this assumption are discussed in Reference 1. One of the consequences of this assumption is that the entering particles are forced to instantaneously exchange heat and momentum with the main stream in order to acquire the local velocity and temperature. As discussed in Reference 1, the required momentum and energy exchange can be postulated to occur strictly amongst the particles themselves, through a collisional process; or, the interaction may be assumed to occur directly between the particles and gas. The equations of motion are actually somewhat different, depending on which of the assumptions is invoked. It was suspected that, since

the particle-gas equilibration time tends to be quite small in motors, the choice made little difference. This suspicion was confirmed by solving the equations for both cases. The equations presented in the following section assume the entering particles interact directly with the gas.

The steady state burn rate is assumed to be given by an empirical P^n law modified for the effect of erosivity. The assumptions and details of the nonlinear model used to characterize the transient burning rate of the propellant are presented in Section 5.

The present model should allow for a realistic assessment of the effect of nonlinearities on longitudinal motor stability. Once the basic validity of the model has been verified, and should it prove warranted, the model may be enhanced by the relaxation of one or more of the current assumptions.

2.2 Equations of Motion

The equations of motion, as presented, reflect the model described in the previous section. Actually, two forms of the equations are given; the conservative form and the corresponding non-conservative form (also called the primitive form). Currently, the computer program solves the conservative form of the gas equations, and the non-conservative form of the particle equations. The rational behind this choice is discussed in Section 6.1.

Conservative Equations

Continuity

Gas:

$$\frac{\partial \rho^*}{\partial t^*} + \frac{1}{A^*} \frac{\partial (\rho^* u^* A^*)}{\partial x^*} = \omega^* \tag{2-1}$$

Particles:

$$\frac{\partial (\rho^*_{p_i})}{\partial t^*} + \frac{1}{A^*} \frac{\partial (\rho^*_{p_i} u^*_{p_i} A^*)}{\partial x^*} = \beta_i \omega^* \tag{2-2}$$

where asterisks denote dimensional quantities, ρ^* and $\rho^*_{p_i}$ are the gas and i th particle group densities, respectively; u^* and $u^*_{p_i}$ are respectively, the gas and i th particle group velocities, A^* is the local chamber cross-sectional area, ω^* is the mass flux of propellant gases entering the chamber per unit length, per unit cross-

sectional area, and β_i is the mass fraction of the i th particle group in the mass leaving the surface (mass of i th particle group divided by mass of gas). The quantity t* is time, while x* is the axial coordinate measured along the center-line of the motor.

Momentum

Gas:

$$\frac{\partial(\rho^* u^*)}{\partial t^*} + \frac{1}{A^*} \frac{\partial}{\partial x^*}\left[(P^* + \rho^* u^{*2})A^*\right] = \frac{P^*}{A^*}\frac{dA^*}{dx^*} +$$

$$u^*_{s_{\parallel}} \omega^* + \sum_{i=1}^{N}\left[F^*_{p_i} + \beta_i \omega^*(u^*_{p_{s_{i_{\parallel}}}} - u^*_{p_i})\right] \tag{2-3}$$

Particles:

$$\frac{\partial(\rho^*_{p_i} u^*_{p_i})}{\partial t^*} + \frac{1}{A^*}\frac{\partial(\rho^*_{p_i} u^{*2}_{p_i} A^*)}{\partial x^*} = -\Gamma^*_{p_i} + \beta_i \omega^* u^*_{p_i} \tag{2-4}$$

where the term $F^*_{p_i}$ represents the effect of momentum transfer between the i th particle group and gas, P^* is pressure, and $u^*_{s_{\parallel}}$ and $u^*_{p_{s}}$ represent the tangential velocity components of the gas and i th particle group, $i_{\parallel}$ respectively, as they leave the burning surface (see Figure 3-2). It is assumed that $u^*_{s_{\parallel}}$ and $u^*_{p_{s_{i_{\parallel}}}}$ are equal. N is equal to the number of particle groups.

Energy

Gas:

$$\frac{\partial}{\partial t^*}\left[\rho^*\left(\frac{c^*_p}{\gamma}T^* + \frac{u^{*2}}{2}\right)\right] + \frac{1}{A^*}\frac{\partial}{\partial x^*}\left[\rho^* u^*\left(\frac{c^*_p}{\gamma}T^* + \frac{u^{*2}}{2}\right)A^*\right] =$$

$$-\frac{1}{A^*}\frac{\partial(u^* P^* A^*)}{\partial x^*} + \omega^*\left(c^*_p T^*_f + \frac{1}{2}u^{*2}_s\right) \tag{2-5}$$

$$+ \sum_{i=1}^{N}\left\{Q^*_{p_i} + u^*_{p_i} F^*_{p_i} + \beta_i \omega^*\left[c^*_m(T^*_{p_{f_i}} - T^*_{p_i}) + \frac{1}{2}(u^{*2}_{p_{s_i}} - u^{*2}_{p_i})\right]\right\}$$

Particles:

$$\frac{\partial}{\partial t^*}\left[\rho^*_{p_i}\left(c^*_m T^*_{p_i} + \frac{1}{2}u^{*2}_{p_i}\right)\right] + \frac{1}{A^*}\frac{\partial}{\partial x^*}\left[\rho^*_{p_i} u^*_{p_i}\left(c^*_m T^*_{p_i} + \frac{1}{2}u^{*2}_{p_i}\right)A^*\right] =$$

$$\tag{2-6}$$

$$-Q^*_{p_i} - u^*_{p_i} F^*_{p_i} + \beta_i \omega^*\left(c^*_m T^*_{p_i} + \frac{1}{2}u^*_{p_i}\right)$$

where c_p^* and c_s^* are the heat capacities of the gas and solid propellant respectively, T_f^* and $T_{p_{f_i}}^*$ are the temperatures of the gas and I th particle group as they enter the

mean flow, and $Q_{p_i}^*$ represents the volumetric rate of heat transfer between the I th particle group and the gas. It is assumed that $T_{p_{f_i}}^* = T_f^*$, and that the kinetic energy of the particles and gas at the surface may be neglected.

Non-Conservative Equations

Continuity

Gas:
$$\frac{\partial \rho^*}{\partial t^*} + \frac{\partial(\rho^* u^*)}{\partial x^*} = \omega^* - \frac{\rho^* u^*}{A^*}\frac{dA^*}{dx^*} \tag{2-7}$$

Particles:
$$\frac{\partial \rho_{p_i}^*}{\partial t^*} + \frac{\partial(\rho_{p_i}^* u_{p_i}^*)}{\partial x^*} = \beta_i \omega^* - \frac{\rho_{p_i}^* u_{p_i}^*}{A^*}\frac{dA^*}{dx^*} \tag{2-8}$$

Momentum

Gas:
$$\rho^* \frac{\partial u^*}{\partial t^*} + \rho^* u^* \frac{\partial u^*}{\partial x^*} = -\frac{\partial P^*}{\partial x^*} + \omega^*(u_{s_{\parallel}}^* - u^*)$$
$$+\sum_{i=1}^{N}\left[F_{p_i}^* + \beta_i \omega^*(u_{p_{s_{i_{\parallel}}}}^* - u_{p_i}^*) \right] \tag{2-9}$$

Particles:
$$\frac{\partial u_{p_i}^*}{\partial t^*} + u_{p_i}^* \frac{\partial u_{p_i}^*}{\partial x^*} = -\frac{F_{p_i}}{\rho_{p_i}} \tag{2-10}$$

Energy

Gas:
$$\frac{\rho^* c_p^*}{\gamma}\left(\frac{\partial T^*}{\partial t^*} + u^*\frac{\partial T^*}{\partial x^*}\right) = -P^*\frac{\partial u^*}{\partial x^*} - \frac{u^* P^*}{A^*}\frac{\partial A^*}{\partial x^*}$$
$$+ \omega^*\left[c_p^*(T_f^* - T^*/\gamma) + \frac{1}{2}(u_s^{*2}+u^{*2}) - u^* u_{s_{\parallel}}^* \right]$$
$$+\sum_{i=1}^{N}\left\{ Q_{p_i}^* + (u_{p_i}^* - u^*)F_{p_i}^* + \beta_i \omega^*\left[u^*(u_{p_i}^* - u_{p_{s_i}}^*) + c_m^*(T_{p_{f_i}}^* - T_{p_i}^*) \right.\right.$$
$$\left.\left. + (u_{p_{s_i}}^{*2} - u_{p_i}^{*2}) \right]\right\} \tag{2-11}$$

108

Particles:
$$\frac{\partial T^*_{p_i}}{\partial t^*} + u^*_{p_i} \frac{\partial T^*_{p_i}}{\partial x^*} = - \frac{Q^*_{p_i}}{\rho^*_{p_i} c^*_m} \tag{2-12}$$

Auxiliary Equations

The equations of motion are supplemented by the following equations.

State:
$$P^* = \rho^* R^* T^* \tag{2-13}$$

Steady State
Burn Rate:
$$\overline{r}^* = \widetilde{c}^* \left(\frac{p^*}{P^*_{ref}}\right)^n (1+c^*_k u^*) \tag{2-14}$$

The quantity, ω^*, is related to the burning rate of the solid propellant, r^* as follows:

Mass Burn Rate:
$$\omega^* = \frac{\rho^*_s r^* \ell^*}{A^*(1+\beta)\cos\theta} \tag{2-15}$$

where ρ^*_s is the density of the solid propellant, ℓ^* is the local perimeter of the propellant grain, β is the total weight ratio of particles to gas $(\beta = \sum_{i=1}^{N} \beta_i)$, and θ is the angle between the tangent to the burning surface and the axis of the motor.

Reynolds number:
$$Re_i = \frac{\rho^* |u^*_{p_i} - u^*| D^*_i}{\mu^*} \tag{2-16}$$

where D^*_i is the diameter of the i th particle group, and μ^* is the gas viscosity given by

Viscosity:
$$\frac{\mu^*}{\mu^*_o} = \left(\frac{T^*}{T^*_o}\right)^{\omega_\mu} \tag{2-17}$$

Momentum Inter-
action Term:
$$F^*_{p_i} = \left(\frac{18\rho^*_{p_i}}{\rho^*_m D^{*2}_i}\right) \mu^* (u^*_{p_i} - u^*) \left[1+\left(\frac{Re_i^{2/3}}{6}\right)\right] \tag{2-18}$$

109

where ρ_m^* is the density of the metal oxide particles. The term $F_{p_i}^*$ is equal to the drag force exerted by the particles on the gas, per unit volume. The drag coefficient used in equation (2-18) was obtained from a correlation of the so-called "standard" drag coefficient versus Reynolds number data for single spheres, in steady flow. The drag formula used was originated by Kliachko[6], and is,

$$c_d = \frac{24}{Re} \left(1 + \frac{Re^{2/3}}{6}\right) \qquad (2-19)$$

The second term in this equation represents a correction to the Stokes value, $24/Re$, and allows the formula to be used at Reynolds numbers up to several hundred.

Heat Transfer Term:
$$Q_{p_i}^* = \left(\frac{6c_p^*}{\rho_m^* R^* D_i^{*2}}\right) \mu^* \cdot _{p_i}^* (T_{p_i}^* - T^*) (2 + .459 \, Re_i^{.55} Pr^{.33}) \qquad (2-20)$$

The last set of parenthesis in (2-20) is the expression for Nusselt number suggested by Carlson( ). Here again, the second term represents a correction to the Stokes flow value, i.e., $Nu=2$.

The velocity of the gas leaving the surface, u_s, is calculated by conservation of mass from the known propellant burn rate and density. The parallel component of surface velocity is

$$u_{s_\parallel}^* = u_s^* \sin\theta \qquad (2-21)$$

2.3   Nondimensional Equations

The equations given in the previous section are nondimensionalized before being recast into finite difference form. The resulting normalized variables are more uniform in magnitude. This uniformity is beneficial from a numerical standpoint. The use of nondimensional variables also facilitates the task of interpreting the calculated results. The following nondimensional variables are defined

$$x = x^*/L \qquad T = T^*/T_f^* \qquad A = A^*/L^{*2}$$
$$t = t^*a_f^*/L^* \qquad P = P^*/P_f^* \qquad \omega = \omega^*L^*/\rho_f^*a_f^*$$
$$u = u^*/a_f^* \qquad \rho = \rho^*/\rho_f^* \qquad F_{p_i} = F^*_{p_i}\, L^*/\rho_f^*a_f^{*2} \qquad (2\text{-}22)$$
$$a = a^*/a_f^* \qquad c = c_m^*/c_p^* \qquad Q_{p_i} = Q^*_{p_i}\, L^*/\rho_f^*c_p^*a_f^*T_f^*$$

where T_f^* is the propellant steady state flame temperature, P_f^* is the chamber pressure, ρ_f^* and a_f^* are the density and sound speed evaluated at the chamber conditions, and L^* is a reference length, usually the length of the grain. The dimensional velocities, temperatures and densities (both gas and particle) not listed have been nondimensionalized in the manner of their listed counterparts.

The nondimensional forms of the equations given in Section 2.2 are as follows.

Conservative Equations

Continuity

Gas:
$$\frac{\partial \rho}{\partial t} + \frac{1}{A}\frac{\partial (\rho u A)}{\partial x} = \omega \qquad (2\text{-}23)$$

Particles:
$$\frac{\partial \rho_{p_i}}{\partial t} + \frac{1}{A}\frac{\partial}{\partial x}(\rho_{p_i} u_{p_i} A) = \beta_i \omega \qquad (2\text{-}24)$$

Momentum

Gas:
$$\frac{\partial (\rho u)}{\partial t} + \frac{1}{A}\frac{\partial}{\partial x}\left[\left(\frac{P}{\gamma} + \rho u^2\right)A\right] = \frac{P}{\gamma A}\frac{dA}{dx} + u_{s_{\parallel}}\omega$$
$$+ \sum_{i=1}^{n}\left[\Gamma_{p_i} + \beta_i \omega (u_{p_{s_i \parallel}} - u_{p_i})\right] \qquad (2\text{-}25)$$

Particles:
$$\frac{\partial (\rho_{p_i} u_{p_i})}{\partial t} + \frac{1}{A}\frac{\partial}{\partial x}(\rho_{p_i} u_{p_i}^2 A) = -\Gamma_{p_i} + \omega_{p_i} u_{p_i} \qquad (2\text{-}26)$$

111

Energy

Gas:

$$\frac{\partial}{\partial t}\left[\rho\left(\frac{T}{\gamma(\gamma-1)}+\frac{u^2}{2}\right)\right]+\frac{1}{A}\frac{\partial}{\partial x}\left[\rho u\left(\frac{T}{\gamma(\gamma-1)}+\frac{u^2}{2}\right)A\right]=$$

$$-\frac{1}{\gamma A}\frac{\partial}{\partial x}(uPA)+\omega\left(\frac{T_f}{\gamma-1}+\frac{u_s^2}{2}\right)+\sum_i\left\{\frac{Q_{p_i}}{\gamma-1}+u_{p_i}F_{p_i}\right. \tag{2-27}$$

$$\left.+\beta_i\,\omega\left[\frac{c}{\gamma-1}(T_{p_{f_i}}-T_{p_i})+\frac{1}{2}(u_{p_{s_i}}^2-u_{p_i}^2)\right]\right\}$$

Particles:

$$\frac{\partial}{\partial t}\left[\rho_{p_i}\left(\frac{c}{\gamma-1}T_{p_i}+\frac{u_{p_i}^2}{2}\right)\right]+\frac{1}{A}\frac{\partial}{\partial x}\left[\rho_{p_i}u_{p_i}\left(\frac{c}{\gamma-1}T_{p_i}+\frac{u_{p_i}^2}{2}\right)A\right]=$$

$$-\frac{Q_{p_i}}{\gamma-1}-u_{p_i}F_{p_i}+\beta_i\,\omega\left(\frac{c}{\gamma-1}T_{p_i}+\frac{u_{p_i}}{2}\right) \tag{2-28}$$

Non-Conservative Equations

Continuity

Gas:

$$\frac{\partial\rho}{\partial t}+\frac{\partial(\rho u)}{\partial x}=\omega-\frac{\rho u}{A}\frac{dA}{dx} \tag{2-29}$$

Particles:

$$\frac{\partial\rho_{p_i}}{\partial t}+\frac{\partial(\rho_{p_i}u_{p_i})}{\partial x}=\beta_i\,\omega-\frac{\rho_{p_i}u_{p_i}}{A}\frac{dA}{dx} \tag{2-30}$$

Momentum

Gas:

$$\rho\frac{\partial u}{\partial t}+\rho u\frac{\partial u}{\partial x}=-\frac{1}{\gamma}\frac{\partial P}{\partial x}+\omega(u_s-u)+\sum_i\left[F_{p_i}+\beta_i\,\omega(u_{p_{s_i}}-u_{p_i})\right] \tag{2-31}$$

Particles:

$$\frac{\partial u_{p_i}}{\partial t}+u_{p_i}\frac{\partial u_{p_i}}{\partial x}=-\frac{F_{p_i}}{\rho_{p_i}} \tag{2-32}$$

Energy

Gas:
$$\frac{1}{\gamma(\gamma-1)}\left(\frac{\partial T}{\partial t} + u\,\frac{\partial T}{\partial x}\right) = -\frac{P}{\gamma}\frac{\partial u}{\partial x} - \frac{uP}{A\gamma}\frac{\partial A}{\partial x} + \omega\left[\frac{(T_f - T/\gamma)}{\gamma-1} + \frac{(u_s^2 + u^2)}{2} - u\,u_{s_{\parallel}}\right]$$

$$+ \sum_i \left\{\frac{Q_{p_i}}{\gamma-1} + (u_{p_i} - u)F_{p_i} + \beta_i\,\omega\left[u(u_{p_i} - u_{p_{s_i}}) + \frac{c}{\gamma-1}(T_{p_{f_i}} - T_{p_i}) + (u_{p_{s_i}}^2 - u_{p_i}^2)\right]\right\} \tag{2-33}$$

Particles:
$$\frac{\partial T_{p_i}}{\partial t} + u_{p_i}\frac{\partial T_{p_i}}{\partial x} = -\frac{Q_{p_i}}{c_{p_i}} \tag{2-34}$$

Auxiliary Equations

State:
$$P = cT \tag{2-35}$$

Steady State
Burn Rate:
$$r = \tilde{c}\left(\frac{P}{P_{ref}}\right)^n (1 + c_k u) \tag{2-36}$$

Mass Burn Rate:
$$\omega = \frac{\rho_s r}{A(1+\beta)\cos\theta} \tag{2-37}$$

Reynolds number:
$$Re_i = \left(\frac{\rho_f^* a_f^* D_i^*}{\mu^*}\right)|u_{p_i} - u| \tag{2-38}$$

Momentum Interaction Term:
$$F_{p_i} = \left(\frac{18 L^*\mu^*}{a_f^* \rho_m^* D_i^{*2}}\right)\rho_{p_i}(u_{p_i} - u)\left(1 + \frac{Re_i^{2/3}}{6}\right) \tag{2-39}$$

Heat Transfer Term:
$$Q_{p_i} = \left(\frac{6L^*\mu^*}{a_f^* \rho_m^* D_i^{*2} Pr}\right)\rho_{p_i}(T_{p_i} - T)(2 + .459\,Re_i^{.55}\,Pr^{.33}) \tag{2-40}$$

2.4   Characteristic Equations

In Reference 1 the method of characteristics was used to solve the equations of motion. In the present analysis these equations are solved with a finite difference technique. The reasons for the switch are discussed in Section

113

6.1. The method of characteristics is, however, still utilized in solving the equations at interior and exterior, subsonic, boundary points. Finite difference calculations at these boundaries were found to be unstable.

A method for obtaining the characteristic equations from the equations of motion has been given in Reference 1. Only the final characteristic equations are given here.

Gas

The two families of flow characteristics are given by

$$\frac{dx}{dt} = u \pm a \tag{2-41}$$

Along these lines the compatibility relations are,

$$\frac{1}{\gamma \rho a}\frac{\delta^{\pm} P}{\delta t} + \frac{\delta^{\pm} u}{\delta t} = -\frac{au}{A}\frac{\partial A}{\partial x} + \frac{\omega}{\rho a}\left[T_f + (\gamma-1)(\frac{u^2}{2} - u\,u_{s_{\parallel}})\right] \pm \frac{\omega}{\rho}(u_{s_{\parallel}} - u)$$

$$\pm \frac{1}{\rho}\sum_i \left[F_{p_i} + \beta_i\,\omega(u_{p_{s_{i_{\parallel}}}} - \dot{u}_{p_i})\right] + \frac{(\gamma-1)}{\rho a}\sum_i \left\{ \frac{Q_{p_i}}{\gamma-1} + (u_{p_i} - u)F_{p_i} \right. \tag{2-42}$$

$$\left. + \beta_i\,\omega\left[u(u_{p_i} - u_{p_{s_i}}) + \frac{c}{\gamma-1}(T_{p_{f_i}} - T_{p_i}) + (u_{p_{s_i}} - u_{p_i}^2)\right]\right\}$$

where the total derivatives $\frac{\delta^{\pm}}{\delta t}$ are defined as $\frac{\partial}{\partial t} + (u \pm a)\frac{\partial}{\partial x}$.

The gas streamlines given by

$$\frac{dx}{dt} = u \tag{2-43}$$

are also characteristics, along which the following compatibility relation holds.

$$\rho\,\frac{\delta T}{\delta t} - \frac{\gamma-1}{\gamma}\,\frac{\delta P}{\delta t} = \omega(\gamma-1)\left[\frac{(T_f-T)}{\gamma-1}+\frac{u^2}{2}-u\,u_{s_\parallel}\right] + (\gamma-1)\sum_i\left\{\frac{Q_{p_i}}{\gamma-1}\right.$$

$$\left. + (u_{p_i}-u)F_{p_i} + \beta_i\,\omega\left[u(u_{p_i}-u_{p_{s_{i_\parallel}}})+\frac{c}{\gamma-1}(T_{p_{f_i}}-T_{p_i})+(u^2_{p_{s_i}}-u^2_{p_i})\right]\right\} \qquad (2\text{-}44)$$

where $\dfrac{\delta}{\delta t} = \dfrac{\partial}{\partial t} + u\,\dfrac{\partial}{\partial x}$.

Particles

The particle paths for each particle group

$$\frac{dx}{dt} = u_{p_i} \qquad (2\text{-}45)$$

are dual characteristics. The two compatibility relations along these lines are,

$$\frac{\delta_p u_{p_i}}{\delta t} = -\frac{F_{p_i}}{\rho_{p_i}} \qquad (2\text{-}46)$$

and

$$\frac{\delta_p T_{p_i}}{\delta t} = -\frac{Q_{p_i}}{\rho_{p_i} c} \qquad (2\text{-}47)$$

where $\dfrac{\delta_p}{\delta t} = \dfrac{\partial}{\partial t} + u_{p_i}\dfrac{\partial}{\partial x}$.

The particle continuity equation (2-30) is uncoupled from the remaining equations (since there is no particle equation of state which relates particle density to particle temperature) and cannot be written in characteristic form. It can, however, be written in the following quasi-characteristic form.

$$\frac{\delta_p \rho_{p_i}}{\delta t} = \beta_i\,\omega - \rho_{p_i}\left(\frac{\partial u_{p_i}}{\partial x}+\frac{u_{p_i}}{A}\,\frac{\partial A}{\partial x}\right) \qquad (2\text{-}48)$$

115

2.5   Jump Equations At Gaps In The Grain

The current instability model is capable of treating motor configurations containing arbitrarily located discontinuities (gaps) in the grain. If the web thickness is finite there are area and burning rate discontinuities at both ends of the gap (see Figure 2-1). Furthermore, if the grain ends are uninhibited, the exposed end will burn and create a mass flow discontinuity at the plane of grain end. The assumed one-dimensional inviscid flow model cannot account for the two-dimensional and viscous effects which are, undoubtedly, present in the neighborhood of such gaps. It is hoped, however, that the one dimensional model will allow the essence of the effect of gaps on motor stability to be evaluated.

Uninhibited End $A_2 > A_1$ Inhibited End $A_1 < A_2$

P_1 , u_1 , A_1 , etc. ① | ② P_2 , u_2 , A_2 , etc.
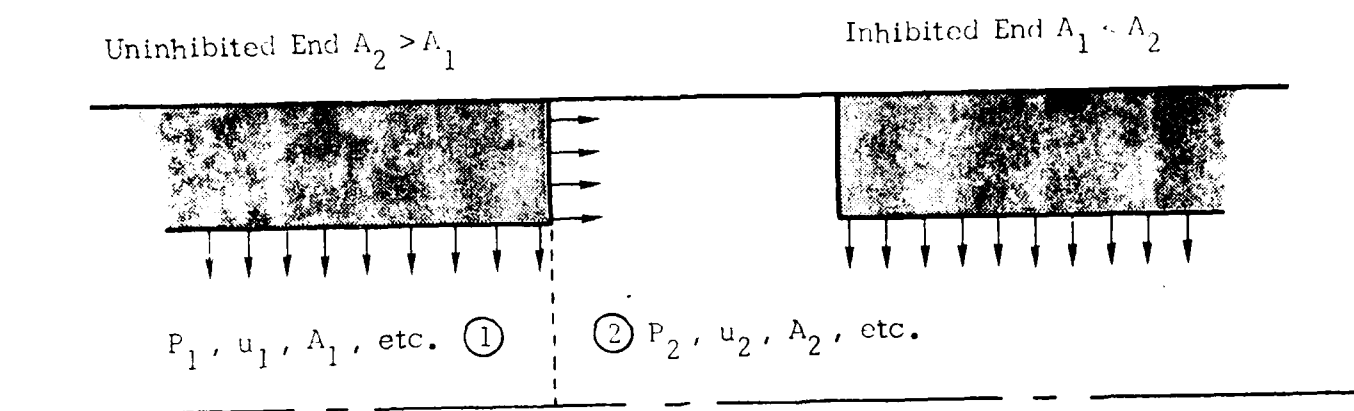
Figure 2-1.   Schematic of Two of the Possible Grain Gap Configurations

In order to obtain a solution at the plane of a discontinuity (hereinafter called an interior boundary) the equations of motions must be supplemented by a set of "jump" equations which express the fact that mass, momentum and energy are conserved, for both the particles and gas, when the flow crosses an interior boundary. The appropriate "jump" equations, in nondimensional form, when $A_2 > A_1$ (see Figure 2-1) are given below. The equations when $A_1 > A_2$ follow from similar considerations and are not shown.

Gas

Mass:
$$\rho_1 u_1 A_1 + \dot{m}_e = \rho_2 u_2 A_2 \qquad (2\text{-}49)$$

Momentum:
$$\frac{P_2}{\gamma}(A_2 - A_1) + A_1\left(\frac{P_1}{\gamma} + \rho_1 u_1^2\right) + \dot{m}_e u_{s_e} = A_2\left(\frac{P_2}{\gamma} + \rho_2 u_2^2\right) \qquad (2\text{-}50)$$

Energy:
$$\rho_1 u_1 A_1\left(\frac{T_1}{\gamma-1} + \frac{u_1^2}{2}\right) + \dot{m}_e \frac{T_{f_e}}{\gamma-1} = \rho_2 u_2 A_2\left(\frac{T_2}{\gamma-1} + \frac{u_2^2}{2}\right) \qquad (2\text{-}51)$$

where $\dot{m}_e$ denotes the rate at which gas is produced at the uninhibited grain end,

$$\dot{m}_e = \frac{\rho_s^* r_e^*}{\rho_f^* a_f^*}\frac{(A_2 - A_1)}{(1+\beta)} \qquad (2\text{-}52)$$

u_{s_e} and T_{s_e} are, respectively, the gas velocity and flame temperature, and r_e is the end burning rate.

Particles

Mass:
$$\rho_{p_{i_1}} u_{p_{i_1}} A_1 + \beta_i \dot{m}_e = \rho_{p_{i_2}} u_{p_{i_2}} A_2 \qquad (2\text{-}53)$$

Momentum:
$$\rho_{p_{i_1}} u_{p_{i_1}}^2 A_1 + \beta_i \dot{m}_e u_{p_{s_{i_e}}} = \rho_{p_{i_2}} u_{p_{i_2}}^2 A_2 \qquad (2\text{-}54)$$

Energy:
$$\rho_{p_{i_1}} u_{p_{i_1}} A_1\left(\frac{c}{\gamma-1} T_{p_{i_1}} + \frac{1}{2} u_{p_{i_1}}^2\right) + \beta_i \dot{m}_e \frac{c}{\gamma-1} T_{f_{i_e}}$$

$$\qquad (2\text{-}55)$$

$$= \rho_{p_{i_2}} u_{p_{i_2}} A_2\left(\frac{c}{\gamma-1} T_{p_{i_2}} + \frac{1}{2} u_{p_{i_2}}^2\right)$$

It is assumed that $u_{p_{s_{i_e}}} = u_{s_e}$ and $T_{f_{i_e}} = T_{f_e}$.

117

3.   MOTOR GEOMETRY AND BOUNDARY CONDITIONS

3.1   Grain Geometry

The nonlinear combustion instability model developed in Reference 1 was
limited to motors having cylindrically bored grains of constant diameter. This sim-
plification was adopted by choice, rather than due to any inherent limitations in
the analytical model. With the feasibility of obtaining nonlinear solutions adequately
demonstrated it was appropriate to extend the range of applicability of the instabi-
lity model to more general, and, hence, more realistic, grain geometries.

The current analysis is not restricted to constant diameter circular cross-
section ports. Solutions can be achieved for grains with variable cross-sectional
area and arbitrary cross-sectional shape, within the confines of a quasi one-dimen-
sional framework. Figure 3-1 contains a pictorial summary of the range of allow-
able configurations. In order to accomodate these geometries within the structure
of the instability model both the equations of motion and boundary conditions had
to be generalized.

In addition to the obvious necessity of keeping terms containing area de-
rivatives, two other effects must be accounted for in order to properly model vari-
able area grains. As shown in Figure 3-2 when the cross-sectional area varies the
burning surface is necessarily oblique to the direction of the mean flow (in one-
dim   ional flow). In such cases an element of length along the burning surface,
ds, i greater than the incremental axial distance, dx. As a result, variable area
grains have more exposed area, per unit of axial distance, than do constant area
grains. This effect is accounted for by modifying the relation between the surface
mass flux per unit cross-sectional area, per unit length, ω, and the burning rate
(see equation 2-15). Also demonstrated in Figure 3-2, is the fact that when $\theta \neq 0$,
the velocity with which the gas and particles emerge perpendicular to the surface
has a component in the direction of the mean flow given by

$$u_{s_{\parallel}} = u_s \sin\theta \qquad (3-1)$$
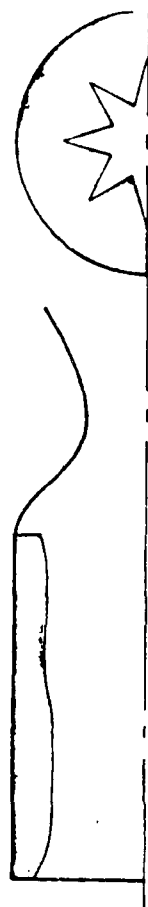
NON-CIRCULAR, VARIABLE
CROSS-SECTION GRAINS
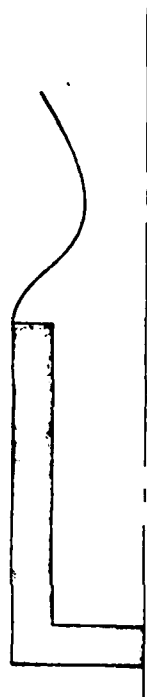
END BURNING AT HEAD END,
OR AT UNINHIBITED GRAIN ENDS
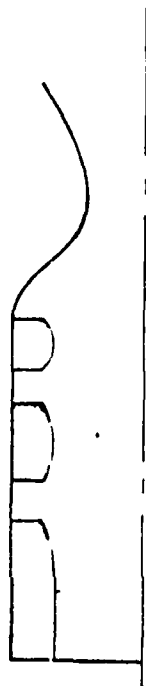
GAPS IN GRAIN
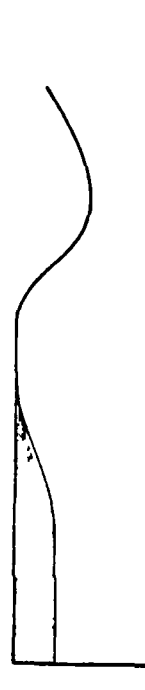
PARTIAL LENGTH GRAINS

Figure 3-1.   Allowed Motor Configurations, Individually, or in Various Combinations

The momentum and energy equations given in Section 2 properly account for the axial momentum content of the combustion products.

Due to burn out, or by design, part of the chamber may not contain grain at a given instant of time. As a result geometrical and/or flow discontiniuties are created. The equations and techniques required to deal with such discontinuities are discussed in Sections 2.5 and 6.4.

The inclusion of end burning effects does not require any modifications to the equations of motion, however, the boundary condition at the head end of the grain is altered, as discussed in Section 3.3.
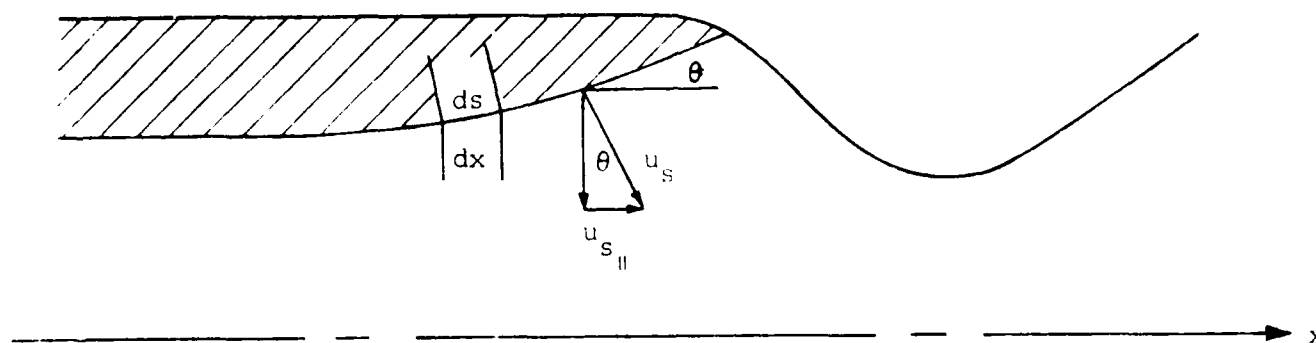
Figure 3-2.   Schematic of a Variable Area Grain

3.2   Nozzle Geometry

In the existing linear stability analyses, and in the nonlinear analysis of Reference 1, the behavior of the nozzle is assumed to be quasi-steady. With this assumption the exact details of the nozzle geometry do not enter into the problem. The current instability program has been modified to integrate through the throat into the supersonic region. This allows the nozzle acoustical impedance to be calculated without resort to the so-called "short nozzle" (quasi-steady) assumption. An option to do quasi-steady nozzle solutions has been retained, however, since this approximation allows solutions to be obtained far more economically. It would be worthwhile to compare instability solutions obtained by integrating the full transient equations through the throat to those obtained with

120

the quasi-steady approximation. In this way one could hope to assess the relative accuracy, and range of applicability of the quasi-steady approximation.

Since the current program provides the option to integrate the equations of motion through the throat, a complete specification of the nozzle geometry is required. Since the area derivative is also required, it is preferable to specify the nozzle shape as an analytic function, rather than via a tabular description. The analytic representation insures that smooth and continuous derivatives will be obtained. The disadvantage of functional descriptions is that they limit the allowed range of geometries, to more, or less, of an extent, depending on their generality. At present, the instability program assumes the nozzle can be described by a circle-cone-circle-cone geometry as shown in Figure 3-3. The nozzle is considered to be composed of four separate regions. The nozzle entrance is located at the beginning of region 1. From this initial location the convergent section of the nozzle is assumed to vary in a circular arc in region 1 and conically in region 2. The throat, region 3, is assumed to be a circular arc, and, finally, the convergent section, region 4, is taken to be conical. A certain degree of flexibility is allowed within the confines of this overall geometric description, however, should this class of nozzles prove to be too restrictive it will be easy to extend the range of allowable nozzle geometries.

In the present nozzle description the following quantities are to be specified by the program user. All areas and radii have been normalized with respect to the throat area and radius, respectively, while all angles are considered to be positive.

Quantity	Description
x_1	Axial location of the nozzle entrance.
A_1	Area ratio at x_1.
θ_1	Wall inclination at x_1.
θ_2	Conical entrance angle.
θ_3	Conical divergence angle.
R_{c_1}	Normalized radius of curvature of the throat.

121
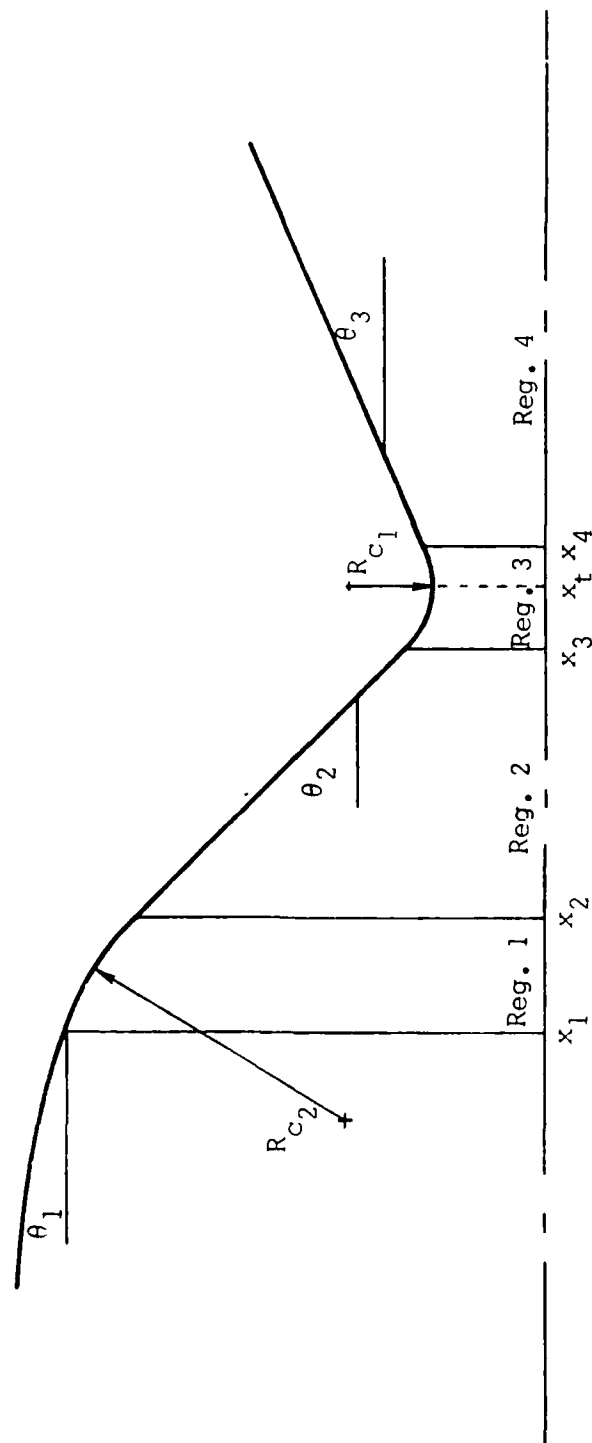
Figure 3-3.   Nozzle Geometry

Quantity	Description
R_{c_2}	Normalized radius of curvature of initial nozzle entrance section.
A_{end}	Area ratio at nozzle exit. (Nozzle exit for computational purposes is not real nozzle exit).

These quantities completely specify the nozzle geometry in all four regions. The equations given below, by region, are used to calculate the area ratio and area derivative at any point in the nozzle. The distance from the nozzle entrance to the throat is given by the important equation

$$x_t - x_1 = R_{c_2} \sin(\theta_2 - \theta_1) + R_{c_1} \sin\theta_2$$

$$+ \frac{A_1^{1/2} - 1 - R_{c_2}\left[1 - \cos(\theta_2 - \theta_1)\right] - R_{c_1}(1 - \cos\theta_2)}{\tan\theta_2}$$

$$(3-2)$$

Region 1: $x_1 \leq x \leq x_2$

$$x_2 = x_1 + R_{c_2} \sin(\theta_2 - \theta_1) \qquad (3-3)$$

$$A = \left\{ A_1^{1/2} - R_{c_2}\left[1 - \cos(\theta_w - \theta_1)\right] \right\}^2 \qquad (3-4)$$

$$\theta_w = \sin^{-1}\left(\frac{x - x_1}{R_{c_2}}\right) \qquad (3-5)$$

$$\frac{dA}{dx} = -2A^{1/2} \tan\theta_w \qquad (3-6)$$

Region 2: $x_2 \leq x \leq x_3$

$$x_3 = x_t - R_{c_1} \sin\theta_2 \qquad (3-7)$$

123

$$A = \left[A_2^{1/2} - (x - x_2) \tan \theta_2 \right]^2 \qquad (3-8)$$

$$\frac{dA}{dx} = - 2A^{1/2} \tan \theta_2 \qquad (3-9)$$

Region 3: $x_3 < x \leq x_4$

$$x_4 = x_t + R_{c_1} \sin\theta_3 \qquad (3-10)$$

$$A = \left\{ 1 + R_{c_1} - \left[R_{c_1}^2 - (x - x_t)^2 \right]^{1/2} \right\}^2 \qquad (3-11)$$

$$\frac{dA}{dx} = 2A^{1/2} (x - x_t) \left[R_{c_1}^2 - (x - x_t)^2 \right]^{-1/2} \qquad (3-12)$$

Region 4: $x_4 < x \leq x_{end}$

$$A = \left[A_4^{1/2} + (x - x_4) \tan \theta_3 \right]^2 \qquad (3-13)$$

$$\frac{dA}{dx} = 2A^{1/2} \tan \theta_3 \qquad (3-14)$$

3.3   Boundary Conditions

If the transient equations are integrated through the throat into the super-
sonic portion of the nozzle only boundary conditions at the head end of the motor
need be specified. No boundary conditions are required at the supersonic exit
plane because all signals from the plane travel downtream only, and, hence, do
affect the previously calculated upstream flow. If the quasi-steady assumption
is utilized a boundary condition must be specified at the nozzle entrance plane.
This boundary condition serves to enforce the choking condition that is, otherwise,
set by the nozzle throat.

By modifying the boundary conditions the instability program can be made
to yield solutions to other problems. Two such modifications have been incorpor-

124

ated into the program. One allows nonlinear particle damping to be studied by specifying a closed end boundary condition at the right boundary. In this way the amplitude behavior of a finite wave initiated in a particle containing closed tube can be calculated. The second modification allows two phase, steady state, nozzle only, solutions to be obtained without having to deal with the throat singularity normally encountered in this problem.

All of the boundary conditions alluded to previously are definitized in the balance of this Section.

Head End - No End Grain

With no end grain present the boundary conditions at the head end are taken to be those corresponding to a rigid wall, i.e.,

$$
\begin{aligned}
u &= 0 \\
u_{p_i} &= 0
\end{aligned}
\tag{3-15}
$$

As discussed in Reference (1), certain assumptions are implicitly invoked when these boundary conditions are utilized. These implied assumptions are, however, no more restrictive that those already listed in Section 2.1.

Head End - With End Grain

When there is a burning grain at the end of the motor the boundary conditions constrain the velocity and temperature of both the particles and gas to be equal to their counterparts in the combustion products, as the products leave the flame and enter the main flow. It is assumed that the velocity and temperature of the particles is equal to that of the gas. The boundary conditions may, thus, be stated as

$$
u_{p_i} = u = u_s
\tag{3-16}
$$

$$
T_{p_i} = T = T_f
$$

Supersonic Nozzle Exit Plane

As previously discussed no boundary condition is required in this case. The properties at the exit plane are currently calculated with a one sided difference technique.

Quasi-Steady Nozzle Boundary Condition

If the quasi-steady nozzle assumption is invoked a boundary condition must be specified at the nozzle entrance. The boundary condition currently utilized requires the mach number at the nozzle entrance to be such that the flow will properly choke at the throat. It is assumed that the two phase flow in the nozzle can be calculated from steady state relations, and that the particles and gas are in equilibrium (no velocity or thermal lags). With these assumptions the two phase mixture behavior is equivalent to that of a perfect gas having the following properties

$$\bar{\gamma} = \frac{\gamma(1 + \beta c)}{1 + \beta c \gamma}$$

$$\bar{c}_p = \frac{c_p(1 + \beta c)}{1 + \beta}$$

(3-17)

The Mach number of the "equivalent" perfect gas, $\overline{M}$, is related to the gas Mach number by

$$\overline{M} = E^{1/2} M$$

(3-18)

where

$$E = 1 + \beta\left[1 + (\gamma - 1)c \frac{(1+\beta)}{(1+\beta c)}\right]$$

(3-19)

The Mach number of the "equivalent" gas, at the nozzle entrance, $\overline{M}_e$, is found by solving the usual isentropic equation for mach number as a function of area ratio

126

$$\left(\frac{A_e}{A_t}\right)^2 = \frac{1}{\overline{M}_e^2} \left\{ \frac{2}{\overline{\gamma}+1} \left[1 + \frac{1}{2}(\overline{\gamma}-1)\overline{M}_e^2 \right] \right\}^{\frac{\overline{\gamma}+1}{\overline{\gamma}-1}} \qquad (3-20)$$

The actual gas Mach number is then found from equation (3-18). The Mach number obtained in this manner assures that the flow will choke at the throat ($\overline{M}_t=1$ at the throat, $M=1$ at some point downstream of the physical throat) within the confines of the quasi-steady, one-dimensional and equilibrium assumptions.

In Reference 1 the quasi-steady boundary condition was obtained in a similar, but more accurate, manner. In that analysis the constant lag assumption (particle velocity and thermal lags are finite, but constant) was used instead of the equilibrium assumption. The quasi-steady analysis of Reference 1 was, however, restricted to particles of a single size, and utilized the linear Stokes flow drag coefficient. It is recommended that the current method of obtaining the quasi-steady boundary condition be upgraded by reinstituting the constant lag analysis, after it has been extended to allow for multiple particle groups and a nonlinear drag coefficient.

Boundary Conditions For Particle Damping Calculations

The instability program can be made to yield nonlinear particle damping solutions by eliminating the grain and applying a closed end boundary condition at both end of the computational mesh. The physical analogy to this situation is a closed end tube filled with particles. If the reference length, L, is chosen to be the length of the tube the boundary conditions become (see head end-no end grain boundary conditions):

$$x = 0, \quad u = u_{p_i} = 0$$
$$x = 1, \quad u = u_{p_i} = 0 \qquad (3-21)$$

Nozzle Only Boundary Condition

The program can be made to solve for the steady state, two phase, flow in the nozzle only by applying steady state boundary conditions on the left hand end of the mesh and treating the right hand end as a supersonic exit plane. The program then obtains the steady state solution as the asymptotic limit of a transient flow. When treated in this manner the behavior of the flow at the throat is not singular, hence, special techniques such as that utilized in Reference 8 are not required in order to continue the integration through the throat.

The proper boundary conditions for this problem require that the total pressure and total temperature at the nozzle entrance be equal to specified values. The state of the particles at the nozzle entrance is determined by their flow history up to that point. Since that portion of the flow is not calculated for this problem some assumption regarding the state of the particles at the nozzle entrance is required. It is assumed that the particles and gas are in equilibrium at the entrance. For most nozzles the mach number and local flow acceleration are small at the nozzle entrance. Thus, the equilibrium state should be closely approximated in the physical situations likely to be encountered.

All of the aforementioned boundary conditions are relatively simple and straightforward. The same cannot always be said for the techniques required to implement them in the numerical solution, (see Section 6.)

4. INITIAL CONDITIONS - STEADY STATE SOLUTION

The stability characteristics of a motor are determined by its transient response to a disturbance away from steady state operating conditions. The effort to numerically simulate those stability characteristics must, therefore, begin with a determination of the steady state. The initial conditions for the instability problem are then generated by adding a perturbation to the steady state solution.

There are two different routes which may be followed in seeking a steady state solution. One way is to directly solve the steady state equations of motions, obtained by setting the time derivatives in the equations of Section 2.2 equal to zero. Alternately, one can obtain the steady state solution as the long time ($\text{limit} \to \infty$) asymptotic limit of a transient problem in which the propellant burning rate is assumed to obey the steady state P^n burn rate law, for all time. The latter approach is the one currently utilized.

The chief advantage of the transient approach is that the numerical techniques and computer program subroutines required to obtain a steady state solution are the same as those utilized in the transient instability solution. The direct approach to the steady state problem, on the other hand, requires the development of additional numerical techniques and another set of computer subroutines. By eliminating the need for additional subroutines, the transient approach to obtaining steady state solutions results in a program which is simpler, and easier to use, modify, and understand.

A disadvantage of the transient approach to a steady state solution is encountered with explicit difference methods (the type presently utilized) when the solution is to be continued through the throat, i.e. when the quasi-steady nozzle approximation is not employed. This disadvantage is a practical one, resulting from the relatively long computer times required to obtain steady state solutions for such cases. (See Section 6.2).

When the current effort was initiated there was no intention of treating the nozzle in other than a quasi-steady manner. Thus, the existing difference techniques were evaluated purely from that perspective. As the program progressed it was recognized that the option to integrate the equations all the way through the throat could be incorporated into the program with little additional effort. It was

...ch a modification would be advantageous, since the adequacy of the
...dy approximation could then be directly examined. Should it prove to
...e to integrate through the throat as a matter of course, rather than in
...d cases, it could be quite worthwhile to switch to a more suitable num-
...nique.

...he transient method of seeking steady state solutions proceeds as fol-
...=0 initial values are selected for the flow variables throughout the
... interest. Since the exact solution is not known, these initial values
...atisfy the steady state equations of motion. The integration procedure
...d; then, provided that steady state boundary conditions are applied,
...teady state burning rate law is utilized, the calculated flowfield will
...cally approach the one respresentative of a true steady state solution.
...er words, the time derivatives of the transient flow eventually approach
...which time the flow variables will exactly satisfy the steady state
...e of motion. In reality, this limit can only be approached to within a
...: tolerance; to reach the limit would, literally, take forever. As would
...ted, the number of calculations of required to reduce the time derivatives
...a specified tolerance is significantly dependent upon the quality of the
...ate, i.e. the degree to which it differs from the correct solution. The
...e is tolerant of poor initial guesses, however, much computational time
...aved by providing a means of selecting a reasonably accurate initial
...The procedure presently used to generate the initial state is briefly de-
...below.

...he calculations for the initial gas properties assume the two phase mix-
...in dynamic equilibrium. The isentropic exponent which characterizes the
... state expansion process for such a mixture is given by equation (3-17)
...n (3-20) can then be solved to obtain the "equivalent" gas mach number as
...tion of area ratio in the nozzle. The Mach number is then assumed to linearly
...e to zero from the nozzle entrance (usually the end of the grain) to the head
... the motor. The gas properties are then established from the isentropic re-
...s as a function of Mach number. In the chamber the equilibrium assumption
...d to generate the particle properties, i.e.

130

felt that such a modification would be advantageous, since the adequacy of the quasi-steady approximation could then be directly examined. Should it prove to be desirable to integrate through the throat as a matter of course, rather than in very limited cases, it could be quite worthwhile to switch to a more suitable numerical technique.

The transient method of seeking steady state solutions proceeds as follows. At t=0 initial values are selected for the flow variables throughout the domain of interest. Since the exact solution is not known, these initial values will not satisfy the steady state equations of motion. The integration procedure is initiated; then, provided that steady state boundary conditions are applied, and the steady state burning rate law is utilized, the calculated flowfield will asymptotically approach the one respresentative of a true steady state solution. Or in other words, the time derivatives of the transient flow eventually approach zero, at which time the flow variables will exactly satisfy the steady state equations of motion. In reality, this limit can only be approached to within a specified tolerance; to reach the limit would, literally, take forever. As would be expected, the number of calculations of required to reduce the time derivatives to within a specified tolerance is significantly dependent upon the quality of the initial state, i.e. the degree to which it differs from the correct solution. The technique is tolerant of poor initial guesses, however, much computational time can be saved by providing a means of selecting a reasonably accurate initial state. The procedure presently used to generate the initial state is briefly described below.

The calculations for the initial gas properties assume the two phase mixture is in dynamic equilibrium. The isentropic exponent which characterizes the steady state expansion process for such a mixture is given by equation (3-17) Equation (3-20) can then be solved to obtain the "equivalent" gas mach number as a function of area ratio in the nozzle. The Mach number is then assumed to linearly decrease to zero from the nozzle entrance (usually the end of the grain) to the head end of the motor. The gas properties are then established from the isentropic relations as a function of Mach number. In the chamber the equilibrium assumption is used to generate the particle properties, i.e.

$$u_{p_i} = u$$

$$T_{p_i} = T \qquad (4-1)$$

$$\sigma_{p_i} = \beta_i \rho$$

In the nozzle the particles are assumed to lag the gas. The amount of lag is assumed to vary with area ratio from zero at the nozzle entrance to a specified value at the throat.

Once the steady state solution has been obtained, initial conditions for the instability calculation are generated by perturbing the flow from the steady state. The following types of perturbations are currently built into the program.

Harmonic Perturbations

$$P' = \sum_{n=1}^{10} a_n \cos\left[n\pi\left(\frac{x - x_o}{x_p - x_o}\right)\right] \qquad (4-2)$$

and/or

$$u' = \sum_{n=1}^{10} b_{n'} \sin\left[n\pi\left(\frac{x - x_o}{x_p - x_o}\right)\right] \qquad (4-3)$$

where the a_n and b_n are arbitrary constants, x_o is the head end of the motor, and x_p is the location at which the disturbance terminates.

Pulse Perturbations

$$x_o < x \leq (x_p - x_o)/2$$

$$P' = a_1 \sin\left[\pi\left(\frac{x - x_o}{x_p - x_o}\right)\right]^{c_1} \qquad (4-4)$$

and/or

$$u' = b_1 \sin\left[\pi\left(\frac{x - x_o}{x_p - x_o}\right)\right]^{d_1} \qquad (4-5)$$

131

$(x_p - x_o)/2 < x$

$$P' = a_1 \sin\left[\pi\left(\frac{x - x_o}{x_p - x_o}\right)\right]^{c_2} \tag{4-6}$$

and/or

$$u' = b_1 \sin\left[\pi\left(\frac{x - x_o}{x_p - x_o}\right)\right]^{d_2} \tag{4-7}$$

where a_1, b_1, c_1, d_1, c_2, d_2 are arbitrary constants. The c's and d's control the effective width of the pulse; the a's and b's control the amplitude. If $c_1 \neq c_2$ or $d_1 \neq d_2$ the pulse will be asymmetric.

5. NONLINEAR TRANSIENT BURNING RATE

The mathematical model for the instability problem is not complete until a method for computing the transient burning rate response of the propellant has been specified. Most of the previous transient burning rate analyses have been linear[9], including the burn rate analysis in the author's previous instability model [1]. It became evident from our previous work that a linear transient burning rate model has serious limitations. Typical pressure fluctuation levels in motors, coupled with response functions on the order of three, can yield fluctuations in burning rate on the order of 50%, or more, of its steady state value. One could hardly expect linear theory to be valid at these large amplitudes, since it is based on the assumption that all quantities depart only slightly from their steady state values. Thus, to extend the range of applicability of the instability analysis a nonlinear transient burning rate model has been developed, and incorporated into the computer program.

Past investigations of nonlinear burning rate response have been carried out by Friedly and Peterson[10], Brown and Muzzy[11], and Novizhilov[12], using expansion procedures, and by Krier, et. al.,[13] using a numerical procedure. The expansion procedures are quite cumbersome, and difficult to modify and extend, especially when carried to higher orders. Thus, a numerical approach to the solution of the heat conduction equation in the solid was favored. Recently, two nonlinear transient burning rate models have been developed[14,15], and solved using numerical techniques. The analysis reported in Reference[14] was performed during the current contract. These models are quite similar, both to each other, and to that of Ref. (13), however, there are subtle differences between them. The numerical methods utilized in each of these investigations also differ. While, in basic agreement, the results of References (14) and (13) and (15) differ in regards to the nonlinear behavior of the burn rate predicted when so-called "intrinsic instability" occurs. In References (13) and (14), burning rate "runaway", i.e. an unbounded increase in burning rate, is observed under intrinsically unstable conditions. In Reference (15) a so-called "spiking" behavior is observed. The burning rate periodically increases rapidly, reaches a limit, and then decays, in response to an applied, fixed amplitude, harmonic disturbance. It has yet to be established whether this difference can be attributed to the use of different numerical techniques, or to the slightly different assumptions made regarding gas

phase energy release. Too much effort should not be devoted to understanding the behavior of propellants under intrinsically unstable conditions. Some of the assumptions upon which these analyses are based are seriously violated during such extreme behavior, so the results obtained are invalid. The chief goal in regard to intrinsic instability should be to determine if real propellants can ever exhibit such behavior. Hopefully, the present theories can be utilized to determine the limiting conditions at which this behavior is incipient.

The burning rate of a metalized solid propellant is undoubtedly sensitive to both pressure fluctuations and fluctuations in the velocity parallel to the burning surface. All of the aforementioned nonlinear burning rate theories treat only the pressure coupled response. The linear burning rate theory developed in Reference (1), and other linear theories References (16 through 20), have attempted to account for the effect of velocity fluctuations. These velocity coupling models are crude, and have little, or no, theoretical basis. The effect of a velocity field parallel to the burning surface can easily be incorporated into the nonlinear models by including a velocity dependent heat flux term in the interfacial energy balance at the burning surface. Unfortunately, there has yet to be a proven mechanistic explanation of how a velocity field actually modifies the surface burning rate and, or, energy release. Until physically based theoretical models of velocity coupling are developed, and verified, the results of velocity coupling calculations will remain speculative, at best.

The nonlinear transient burning rate model currently used in the instability analysis is presented in the balance of this Section. The assumptions upon which the burning rate model is based are similar to those employed in the previous mentioned analyses. The gas and solid phases are treated as homogenous, and only one dimensional variations in the direction normal to the burning surface are accounted for. It is assumed that all of the solid is converted to gas at an infinitesimally thin interface at the burning surface; subsurface reactions are not considered. The gas phase is assumed to respond in a quasi-steady manner. The flame is taken to be anchored at the surface, with uniform distributed heat release out to the edge of the flame. The gas reaction rate is assumed to be a function of pressure only, and the presence of metal in the propellant is not directly accounted for. The specific heats and thermal conductivities are taken to be constant, for convenience, but unlike previous nonlinear analyses the gas and propellant specific

134

heats may differ. The surface pyrolysis rate is assumed to be given by an Arrhenius law modified to account for pressure coupled surface reactions. With these assumptions the calculation of the transient burning rate at a given chamber location reduces to the solution of the nonlinear heat conduction equation with a nonlinear boundary condition. For reasons of computational efficiency burning rate solutions are not obtained at every finite difference mesh point at which there is burning. Instead, transient burn rate solutions are obtained as a series of axial locations; with burn rates at intermediate locations being found by high order interpolation. Since the propellant cannot respond instantaneously to disturbances the axial variation in burn rate tends to be smoother than that of the flow variables, and the interpolation procedure works quite well.

With the approximations listed previously, in a coordinate system fixed to the gas/solid interface, the heat conduction equation may be written as

$$\frac{\partial T}{\partial t} + r \frac{\partial T}{\partial x} = \chi \frac{\partial^2 T}{\partial x^2} \tag{5-1}$$

In this coordinate system the solid appears to be flowing in from the left at a rate given by $r(t)$. The source of the nonlinearity in this equation is the convection term $r \partial T/\partial x$. Two boundary conditions must be given to complete the specification of the problem. At the propellant back wall it is assumed that the temperature remains at a specified constant value, thus, the boundary condition there may be stated as

$$T_{(-\infty, t)} = T_\infty \tag{5-2}$$

The boundary condition at the surface, $x=0$, is obtained by performing a mass and energy balance for an infinitesimally thin control volume encompassing the gas/solid interface (see Figure 5-1). The mass balance at the interface yields

$$\rho_s r = \rho_g u_g = m \tag{5-3}$$

(since the presence of metal in the propellant is not directly accounted for)

Combustion products enter main flow

Flame Zone

Surface

Solid Propellant

$$-\dot{q}_s = k_s \left.\frac{\partial T}{\partial x}\right|_- \qquad \longleftarrow \qquad \longleftarrow \qquad -\dot{q}_g = k_g \left.\frac{\partial T}{\partial x}\right|_+$$
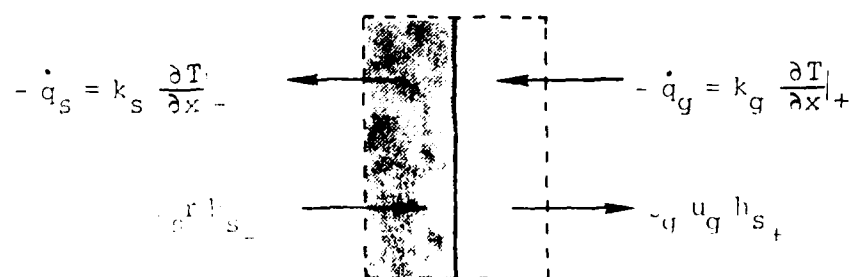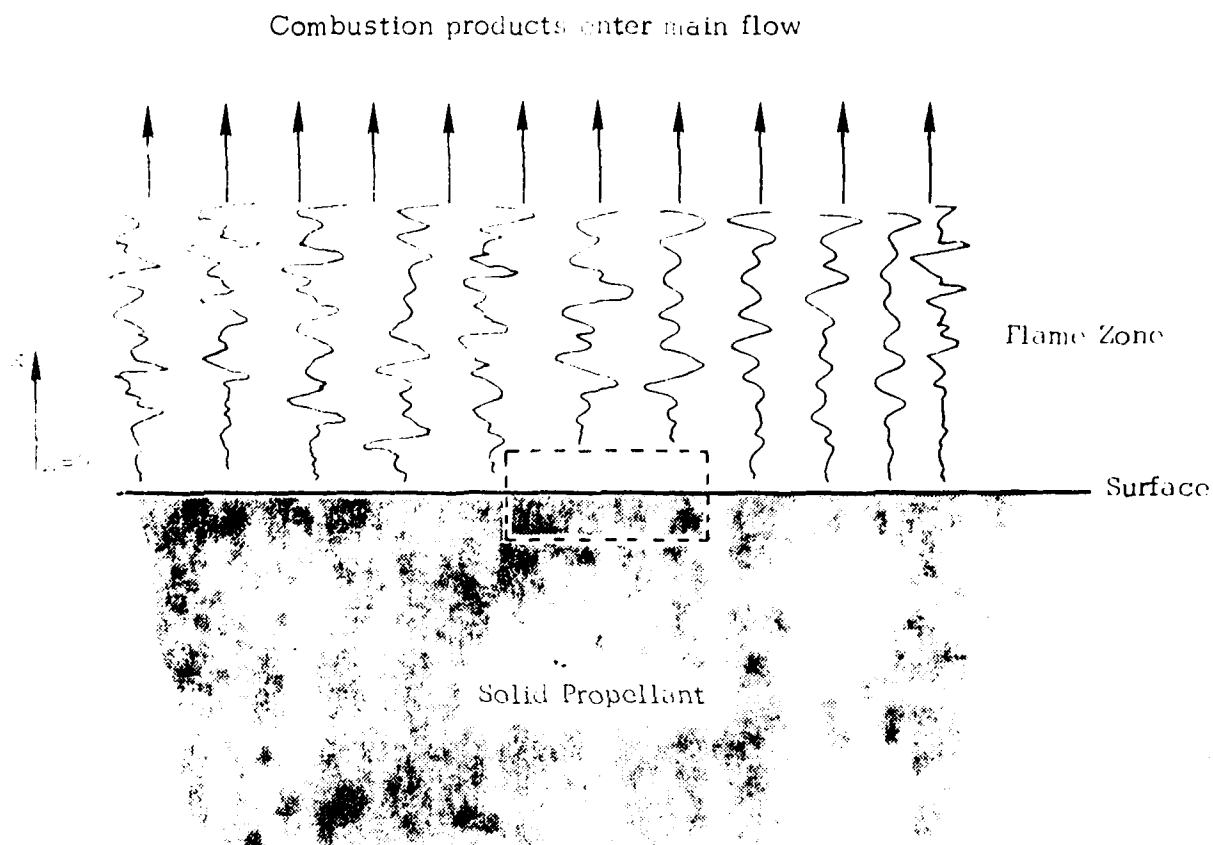
$$\longrightarrow \qquad \longrightarrow \qquad \dot{q}_g u_g h_{s_+}$$

Figure 5-1. Schematic Representation of Combustion Model And Gas-Solid Interfacial Energy Balance

136

where ρ_g and u_g are the density and velocity of the gas at the propellant surface. The energy balance leads to

$$\rho_s r h_{s_-} - k_s \frac{\partial T}{\partial x}\Big|_- = \rho_g u_g h_{s_+} - k_g \frac{\partial T}{\partial x}\Big|_+ \qquad (5\text{-}4)$$

in which the enthalpies on the solid and gas sides of the interface are h_{s_-} and h_{s_+}, respectively. The net heat released at the surface, per unit mass, is equal to the difference between the enthalpies of the solid and gas on their respective sides of the interface. If the quantity Q_s is taken to be positive when the net heat release is exothermic one may write

$$Q_s(T_s) = h_{s_-} - h_{s_+}$$
$$\qquad (5\text{-}5)$$
$$= c_s T_s + \Delta h^\circ_{f_-} - c_p T_s - \Delta h^\circ_{f_+}$$

where $\Delta h^\circ_{f_-}$ and $\Delta h^\circ_{f_+}$ are the heats of formation, at zero degrees Kelvin, of the solid and gas respectively. It is convenient to define a quantity, $\overline{Q}_s$, equal to the net surface heat release at the steady state surface temperature $\overline{T}_s$.

$$Q_s(\overline{T}_s) \quad \overline{Q}_s = c_s \overline{T}_s + \Delta h^\circ_{f_-} - c_p \overline{T}_s - \Delta h^\circ_{f_+} \qquad (5\text{-}6)$$

With (5-6), (5-5) may be written as

$$(h_{s_-} - h_{s_+}) = Q_s(T_s) = \overline{Q}_s + (c_s - c_p)(T_s - \overline{T}_s) \qquad (5\text{-}7)$$

Substituting (5-3) and (5-7) into the energy balance (5-4) yields

$$k_s \frac{\partial T}{\partial x}\Big|_- = k_g \frac{\partial T}{\partial x}\Big|_+ + m\left[\overline{Q}_s + (c_s - c_p)(T_s - \overline{T}_s)\right] \qquad (5\text{-}8)$$

The term $k_g \frac{\partial T}{\partial x}\Big|_+$ is evaluated from a solution of the gas phase. Subject to the aforementioned assumptions the quasi-steady energy equation for the gas phase is

$$m c_p \frac{dT}{dx} = k_g \frac{d^2 T}{dx^2} + Q_f w \qquad (5-9)$$

where Q_f is the heat release per unit mass, and w is the reaction rate times the gas density. Integrating equation (5-9) once, applying the boundary condition $\partial T/\partial x = 0$ at $x = \infty$, and evaluating the solution at $x=0$ yields[13]

$$k \frac{dT}{dx}\Big|_+ = \frac{Q_f k_g}{c_p} \left[1 - \exp(-m c_p x_f / k_g) \right] \frac{w}{m} \qquad (5-10)$$

which, as shown in Reference (1), is well approximated by

$$k \frac{dT}{dx}\Big|_+ = \frac{Q_f k_g}{c_p} \frac{w}{m} \qquad (5-11)$$

In order to utilize (5-11) an expression for w must be specified. It is at this juncture that the current model and that of Reference (2) depart. In both cases it is assumed that w is a function of pressure only. In Reference (2) it is assumed that $w \sim P^\epsilon \exp -E_f / R_o T_f{}^+$. However, in the present model it is assumed that the dependency of w on pressure is the same as that in the steady state, without ever specifying what that dependency is. The current assumption is more general since a simplistic approximation to the steady state burn rate mechanism is not invoked.

It is easily shown that the steady state solution to the heat conduction equation (5-1) is

$$\frac{\overline{T} - T_\infty}{\overline{T}_s - T_\infty} = \exp(\overline{r} x / \varkappa) \qquad (5-12)$$

So, the steady state temperature derivative in the solid, at the interface, is

$$k \frac{\overline{dT}}{dx}\Big|_- = \rho_s \overline{r} c_s (\overline{T}_s - T_\infty) \qquad (5-13)$$

+This is a result of assuming a simple one step, second order, reaction rate model.

Using the interfacial energy balance, (5-6), (5-13) may be written as

$$\overline{k_g \frac{dT}{dx}}\Big|_+ = \overline{m}\left[c_s(\overline{T}_s - T_\infty) - \overline{Q}_s\right] \qquad (5\text{-}14)$$

Combining (5-14) with (5-11) yields a relation for w, in the steady state

$$\overline{w} = \frac{c_p}{Q_f k_s}\overline{m}^2\left[c_s(\overline{T}_s - T_\infty) - \overline{Q}_s\right] \qquad (5\text{-}15)$$

In order to find w as a function of pressure the surface temperature is written in terms of the burning rate through the assumed Arrhenius pyrolysis rate.

$$m = \rho_s r = B_s P^{n_s} \exp(-E_s/R_o T_s) \qquad (5\text{-}16)$$

or, solving for temperature,

$$T_s = \frac{E_s/R_o}{\ln\left[B_s P^{n_s}/\rho_s r\right]} \qquad (5\text{-}17)$$

The burning rate, r, is, in turn, written in terms of pressure using the steady state burning law $r = aP^{n+}$.

Quasi-steady
$$T_s = \frac{E_s/R_o}{\ln\left[B_s P^{(n_s-n)}/(\rho_s a)\right]} \qquad (5\text{-}18)$$

Substitution of (5-18) into (5-15) yields the steady state dependence of w on pressure

$$\overline{w} = \overline{w}(P) = \frac{c_p \rho_s^2 a^2 \overline{P}^{2n}}{Q_f k_g}\left\{\frac{c_s E_s/R_o}{\ln\left[B_s \overline{P}^{(n_s-n)}/(\rho_s a)\right]} - c_s T_\infty - \overline{Q}_s\right\} \qquad (5\text{-}19)$$

+Any analytical, or empirical, burning rate law desired can be inserted into the current model at this juncture.

139

The quasi-steady analogy to (5-19) is found by replacing $\overline{P}$ and $\overline{Q}_s$ in (5-19) with P and Q_s (since Q_s varies with T_s and T_s varies with P). Using (5-18) to eliminate T_s yields the final equation for w

$$w = \frac{c_p \rho_s^2 a^2 P^{2n}}{Q_f k_g} \left\{ c_p \left[\frac{E_s/R_o}{\ln\left(\dfrac{B_s P^{(n_s-n)}}{\rho_s a}\right)} - \overline{T}_s \right] + c_s(\overline{T}_s - T_\infty) - \overline{Q}_s \right\} \quad (5\text{-}20)$$

The desired surface boundary condition for the heat conduction equation is then obtained by inserting (5-20) into the gas phase solution (5-11), and then using the interfacial energy balance (5-8) to arrive at

$$\frac{\partial T}{\partial x}\bigg|_- = \frac{c_s^2 a^2 P^{2n} c_s}{k_s} \left\{ \frac{c_p}{c_s} \left[\frac{E_s/R_o}{\ln\left(\dfrac{B_s P^{(n_s-n)}}{\rho_s a}\right)} - \overline{T}_s \right] + \overline{T}_s - T_\infty - \frac{\overline{Q}_s}{c_s} \right\} \frac{1}{m}$$

$$+ \frac{m}{k_s} \left[\overline{Q}_s + (c_s - c_p)(T_s - \overline{T}_s) \right] \quad (5\text{-}21)$$

With this boundary condition the specification of the heat conduction problem is complete. It is convenient to introduce the following nondimensional variables:

$$\tilde{t} = \frac{\overline{r}^2 t}{\varkappa_c} \qquad \xi = \frac{\overline{r} x}{\varkappa} \qquad R = \frac{r}{\overline{r}} \qquad \theta = \frac{T - T_\infty}{\overline{T}_s - T_\infty} \qquad P_{\cdot} = \frac{P}{\overline{P}}$$

$$(5\text{-}22)$$

hence,

$$dt = \frac{\varkappa_c}{\overline{r}^2} d\tilde{t} \qquad dx = \frac{\varkappa_c}{\overline{r}} d\xi \qquad r = \overline{r} R \qquad dT = (T_s - T_\infty) d\theta$$

The heat conduction equation (5-1) can then be written as

$$\frac{\partial \theta}{\partial \tilde{t}} + R \frac{\partial \theta}{\partial \xi} = \frac{\partial^2 \theta}{\partial \xi^2} \quad (5\text{-}23)$$

140

The back wall boundary condition (5-2) becomes

$$\theta = 0 \quad \text{at} \quad \xi = -\infty \tag{5-24}$$

After considerable algebraic manipulation the surface boundary condition (5-21) can be written as

$$\frac{\partial \theta}{\partial \xi}\bigg|_{-} = \frac{\underline{P}^{2n}}{R} \left\{ \frac{c_p}{c_s} \frac{E}{A} \left[\frac{1}{1 + \frac{(n_s - n)}{E} \ln \underline{P}} - 1 \right] + 1 - H \right\}$$

$$+ R \left[H + (1 - \frac{c_p}{c_s})(\theta_s - 1) \right] \tag{5-25}$$

where the following nondimensional burning rate parameters have been defined:

$$E = E_s / R_0 T_s \tag{5-26}$$

$$A = E(1 - \frac{T_\infty}{T_s}) \tag{5-27}$$

$$H = \frac{\overline{Q}_s}{c_s (\overline{T}_s - T_\infty)} \tag{5-28}$$

The burning rate ratio, $R = r/\overline{r}$, can also be written in terms of nondimensional variables as follows. From (5-16)

$$R = \underline{P}^{n_s} \exp \left[E \left(1 - \frac{\overline{T}_s}{T_s} \right) \right] \tag{5-29}$$

which, after some manipulation, can be shown to equal

$$R = \underline{P}^{n_s} \left[\frac{A(\theta_s - 1)}{1 + \frac{A}{E}(\theta_s - 1)} \right] \tag{5-30}$$

141

In terms of the nondimensional variables the solution to the steady state heat conduction equation, (5-12) becomes

$$\overline{\theta} = e^{\xi} \tag{5-31}$$

The nonlinear transient burning rate model previously outlined is solved numerically using the implicit Crank-Nicolson technique. The details of this procedure are described in Section 6.5.

5.1 Nonlinear Equation For Flame Temperature
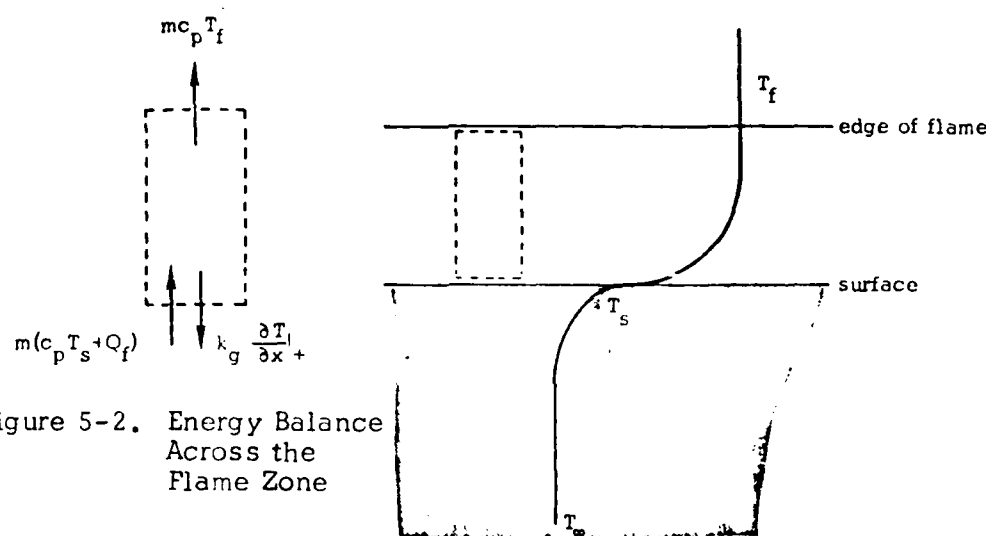
Figure 5-2. Energy Balance Across the Flame Zone

In this section a nonlinear, nonisentropic, equation for the transient flame temperature response is developed, based on the preceding burning rate model. A heat balance across the reaction zone yields (see Figure 5-2).

$$m \left[Q_f - c_p (T_f - T_s) \right] = k_g \frac{\partial T}{\partial x} \Big|_+ \tag{5-32}$$

In steady state (5-32) becomes

$$\overline{m} \left[Q_f - c_p (\overline{T}_f - \overline{T}_s) \right] = k_g \frac{\partial T}{\partial x} \Big|_+ \tag{5-33}$$

142

Subtracting (5-33) from (5-32) yields

$$\frac{k_g \frac{\partial T}{\partial x}\big|_+}{m} + - \frac{k_g \frac{\partial \overline{T}}{\partial x}\big|_+}{\overline{m}} = c_p \left[(\overline{T}_f - \overline{T}_s) - (T_f - T_s) \right] \qquad (5\text{-}34)$$

If (5-11) and (5-20) are used to evaluate $k_g \frac{\partial T}{\partial x}\big|_+$, and $k_g \frac{\partial \overline{T}}{\partial x}\big|_+$ is evaluated from (5-14), equation (5-34) may be written as

$$T_f - \overline{T}_f = T_s - \overline{T}_s - \frac{a^a P^{an}}{r^a} \frac{c_s}{c_p} \left\{ \frac{c_p}{c_s} \left[\frac{E_s/R_o}{\ln\left(\frac{B_s P^{(n_s-n)}}{\rho_s a}\right)} - \overline{T}_s \right] + \overline{T}_s - T_\infty \right.$$

$$\left. - \frac{\overline{Q}_s}{c_s} \right\} + \frac{c_s}{c_p} \left[\overline{T}_s - T_\infty - \frac{\overline{Q}_s}{c_s} \right] \qquad (5\text{-}35)$$

In terms of the previously defined nondimensional variables and parameters (5-35) becomes

$$\theta_f - \overline{\theta}_f = \theta_s - 1 - \frac{P^{an}}{R^a} \frac{c_s}{c_p} \left\{ \frac{c_p}{c_s} \frac{E}{A} \left[\frac{1}{1 + \frac{(n_s-n)}{E} \ln \underline{P}} - 1 \right] + 1 - H \right\} \qquad (5\text{-}36)$$

$$+ \frac{c_s}{c_p} (1 - H)$$

The form of the flame temperature equation used in the numerical solution of the equations of motion is obtained by writing (5-36) in terms of T, rather than θ. In doing so equation (5-30) is used to eliminate the quantity $(\theta_s - 1)$. The resulting equation is

$$\frac{T_f}{'f} \quad , \quad \frac{\overline{T}_s}{\Gamma_f} \left[\frac{\ln(R/\underline{P}^{n_s})}{E - \ln(R/\underline{P}^{n_s})} \right] - \frac{\overline{T}_s}{\overline{T}_f} \frac{P^{an}}{R^a} \frac{c_s}{c_p} \left\{ \frac{c_p}{c_s} \left[\frac{1}{1 + \frac{(n_s-n)}{E} \ln \underline{P}} - 1 \right] \right.$$

$$\left. + \frac{A}{E} (1-H) \right\} + \frac{\overline{T}_s}{\overline{T}_p} \frac{c_s}{c_p} \frac{A}{E} (1-H) \qquad (5\text{-}37)$$

5.2   Linear Transient Burning Rate and B Parameter

In order to properly assess the nature and magnitude of the nonlinear burn-
ing rate effects one should compare the results of two sets of calculations in which,
except for the burn rate nonlinearities, all things are equal. The ability to carry
out this assessment has been provided for in the current investigation by incorpora-
....g both the nonlinear transient burning rate model, previously described, and the
linear model derived from it, into the instability program.

The linear equations result from evaluating the nonlinear burning rate
theory in the limit of infinitesimal perturbations. Thus,

$$\frac{P'}{\overline{P}} = (\underline{P} - 1) << 1$$

$$\frac{r'}{\overline{r}} = (R - 1) << 1 \tag{5-38}$$

$$\theta'_s = (\theta_s - 1) << 1$$

etc.

In order to obtain a linear form of the conduction equation, which could be
easily solved by the same computer code as the nonlinear equation (with minor mod-
ifications) the nonlinear term in equation (5-23) was removed, as follows. The
term, $R \, \partial\theta/\partial\xi$, may be written as

$$(1 + \frac{r'}{\overline{r}}) \, (\frac{\partial\overline{\theta}}{\partial\xi} + \frac{\partial\theta'}{\partial\xi}) \tag{5-39}$$

The nonlinear term is

$$\frac{r'}{\overline{r}} \, \frac{\partial\theta'}{\partial\xi} \tag{5-40}$$

which may be written as

$$(R - 1) \, (\frac{\partial\theta}{\partial\xi} - \frac{\partial\overline{\theta}}{\partial\xi}) \tag{5-41}$$

144

Using (5-31) to evaluate $\partial \bar{\theta}/\partial \xi$ results in

$$(R-1) \left(\frac{\partial \theta}{\partial \xi} - e^{\xi} \right) \tag{5-42}$$

Subtracting the nonlinear term, (5-42) from (5-23), then yields the linear form of the heat conduction equation

$$\frac{\partial \theta}{\partial \widetilde{t}} + \frac{\partial \theta}{\partial \xi} = \frac{\partial^2 \theta}{\partial \xi^2} - (R - 1)e^{\xi} \tag{5-43}$$

The other nonlinearities, which occur in the surface boundary condition, the Arrhenius Pyrolysis law, and the equation for the flame temperature, must also be eliminated. To obtain the linear forms of these equations the variables are all written as the sum of a steady state value and a small perturbation (see 5-38). Expanding the relevant equations, (5-25), (5-30) and (5-37), in Taylor series about the steady state, keeping terms only up to first order in the perturbation quantities, yields the desired linear equations. Without going into the details of the procedure, the results are

Surface Boundary Condition:

$$\frac{\partial \theta}{\partial \xi}\bigg|_{-} = 1 + n(\underline{P} - 1) \left[2(1 - H) + \frac{c_p}{c_s} \frac{1}{A} - \frac{n_s}{nA} \right] + (R - 1) \left[2H - 1 \right.$$
$$\left. + (1 - c_p/c_s)/A \right] \tag{5-44}$$

Arrhenius Relation:

$$R = 1 + A(\theta_s - 1) + n_s(\underline{P} - 1) \tag{5-45}$$

145

Flame Temperature:

$$\frac{\overline{T}_f}{\overline{T}_s} \left(\frac{T_f}{\overline{T}_f} - 1\right) = -n(\underline{P} - 1) \frac{c_s}{c_p} \left[\frac{c_p}{c_s} \frac{1}{E} + 2 \frac{A}{E} (1 - H)\right]$$

$$+ (R - 1) \frac{c_s}{c_p} \left[\frac{c_p}{c_s} \frac{1}{E} + 2 \frac{A}{E} (1 - H)\right] \tag{5-46}$$

The steady state solution (5-31) and back wall boundary condition (5-24) are indentical in the linear and nonlinear cases. This set of linear equations and boundary conditions can be solved as is, however, in order to facilitate the task of relating the present results to those obtained from other, similar, or equivalent, linear models (such as the linear model developed in Reference 1) the often used parameter, B, is introduced.

The parameter, B, is defined in Reference 1 as

$$B = \frac{1}{A} \left[A(1 - H) + \frac{c_p}{c_s} E \Lambda^2 + \frac{c_p}{c_s}\right] \tag{5-47}$$

where

$$\Lambda^2 = \frac{Q_f k_g \overline{w}}{\overline{m}^2 c_p^a \overline{T}_s} \tag{5-48}$$

Substituting (5-15) into (5-48), and the result into (5-47) yields the desired relation for B

$$B = \frac{1}{A} \left[2A(1 - H) + \frac{c_p}{c_s}\right] = 2(1 - H) + \frac{c_p}{c_s} \frac{1}{A} \tag{5-49}$$

In terms of B the linear surface boundary condition and flame temperature equations take the following somewhat simpler forms.

146

Surface Boundary Condition:

$$\frac{\partial \theta}{\partial \xi}\bigg|_{-} = 1 + n(\underline{P} - 1)(B - \frac{n_s}{nA}) + (R - 1)(1 - B + 1/A) \qquad (5\text{-}50)$$

Flame Temperature:

$$\frac{T_f}{\overline{T}_f} = 1 + \frac{\overline{T}_s}{\overline{T}_f} \frac{c_s}{c_p} \frac{AB}{E}\left[(R - 1) - n(\underline{P} - 1)\right] \qquad (5\text{-}51)$$

The equivalency of the present linear equations to those used previously[1] is now relatively easy to establish. For instance, equation (5-51) is easily shown to be identical to the equivalent equation in Reference 1.

6.   NUMERICAL CONSIDERATIONS

The numerical methods used to solve the equations of motion and their associated boundary conditions are described herein, as is the numerical technique utilized in solving for the nonlinear transient burning response of the propellant.

6.1   Finite Difference Method For Solving The Equations Of Motion

When the method of characteristics was selected as the numerical technique in Reference 1, the nature of the transient burning rate analysis was unknown. As is turned out, the need for pressure histories at fixed axial locations was satisfied by interpolation and rectification of the characteristics mesh at each time step. These extra calculations which increase the solution time and adversely affect the accuracy of the results, are not required if the computations are initially performed in a rectilinear mesh. Finite difference methods for hyperbolic equations are normally designed to operate with such a mesh, and, hence, are attractive for solving the equations of motion. Finite difference methods are also, in general, more efficient than the method of characteristics.

Shock waves are not usually observed in actual solid rocket motors which are naturally (spontaneously) unstable, and are only infrequently observed even when motors are subjected to artificial pulsing. Thus, shock waves were only a secondary concern in the present investigation. In the absence of shock waves the adequacy of the computed results is not critically dependent upon the choice of finite difference technique. Hence, an intensive evaluation of the relatively large number of existing finite difference methods was not carried out.

The available difference techniques can be differentiated on the basis of accuracy, i.e., first order, second order, third order truncation error; and by type, i.e., explicit or implicit. Third order methods were not seriously considered because, for the present problem, their full inherent accuracy cannot be realized (the transient burning rate calculations cannot be efficiently performed to equivalent accuracy) to offset their added complexity. First order methods were also eliminated. These methods are the simplest, and are attractive for that reason, however, second order methods are considerably more accurate, without being unduly complicated.

The bulk of our attention was, thus, devoted to second order techniques. Implicit methods such as those due to Gary[21], Gourlay and Morris[22] and Masson[23], are more involved, both from a program development, and computational standpoint, but have the advantage of being unconditionally stable. Explicit method are simpler, but are subject to the Courant-Friedrichs-Lewy (CFL) stability criterion given by[24]

$$(|u| + a) \frac{\Delta t}{\Delta x} < 1 \qquad (6-1)$$

which limits the size of the time step which may be taken. It was decided to go with explicit methods since their relative simplicity allows one to easily change from one method to another. This flexibility was deemed to be advantageous since with nonlinear problems it is impossible to predict, ahead of time, all ot the pitfalls which may be encountered with a given method.

After considering a number of second order explicit methods including those due to Mc Cormack[25], Lax-Wendroff[26], Rubin and Burstein[27], and Gourlay and Morris[22], Rubin and Bursteins'[27] method was selected as the first method to be tried. The Rubin and Burstein technique has performed admirably in the present application. No numerical problems attributable to the use of this method were encountered during the course of this study. As a result the other methods were never fully evaluated.

In principle, finite difference methods of the type considered, and selected, are applicable to flow problems containing shock waves, provided the conservative form of the equations of motion is utilized.* With these methods a shock wave is not treated as a discontinuity. Instead, the discontinuous jumps associated with the shock front are smeared out over several mesh points. If the shock

---

*In two phase flow problems only the gas equations need be integrated in conservation form. The particle flow properties are not discontinuous across a shock wave, hence, the simpler non-conservative particle equations can be utilized.

wave is too strong, or too few mesh points are employed, spurious oscillations are observed in the finite difference solutions, especially on the downstream (high pressure) side of the shock. The magnitude of these spurious oscillations, for a given shock wave, is quite dependent upon the exact nature of the finite difference method. One of the reasons for selecting the Rubin and Burstein method was the authors' contention that their method was superior in that respect. In many applications[28] a so-called "artificial viscosity" is employed in conjunction with these finite difference methods. The function of this "artificial viscosity" being to damp, or entirely eliminate the spurious oscillations in the vicinity of the shock wave. The use of an artificial viscosity would not be appropriate in the present application, however, since there are real physical dissipative mechanisms resulting from the interactions between the particles and the gas. Thus, it would be quite difficult, in this case, to separate the real and artificial dissipative effects.

As stated earlier, flows containing shock waves were not the immediate concern of the present investigation. No direct attempts to calculate such flows were made during this investigation. Shock waves, accompainied by spurious oscillations, did appear, by chance, towards the end of some nonlinear particle damping calculations, however the mesh sizes employed in those calculations was far too large to expect that a shock wave could be adequately treated. Thus, the ability of the present technique to handle flows containing shock waves has yet to be adequately tested. If solid rocket motor flows containing shock waves should become of practical interest, and should the present method fail, or become inordinately inefficient, in such cases, other techniques could be incorporated into the program.

The instability analysis reported in Reference 2 is quite similar to the present analysis, in most respects, however, the authors were more concerned about the presence of shock waves and opted to use Moretti's shock tracking method.[29] This method results in a much more comples, and inflexible, code, however, its success is evidenced by the results achieved[15]. A simpler approach that holds promise of being able to adequately treat shock waves is the flux controlled transport difference method recently developed at NRL[30].

Before presenting the difference equations obtained using the Rubin and Burstein method, it is convenient to first write the equations of motion in short hand notation.

Gas Equations (conservation form)

$$\frac{\partial F}{\partial t} + \frac{\partial G}{\partial x} = Z \qquad (6-2)$$

where F, G, and Z are the following vectors,

$$F = \begin{bmatrix} \rho A \\ \rho u A \\ \rho \left[\dfrac{T}{\gamma(\gamma-1)} + \dfrac{u^2}{2} \right] A \end{bmatrix} \qquad (6-3)$$

$$G = \begin{bmatrix} \rho u A \\ \left[\dfrac{\rho}{\gamma} + \rho u^2 \right] A \\ \rho u A \left[\dfrac{T}{\gamma-1} + \dfrac{u^2}{2} \right] \end{bmatrix} \qquad (6-4)$$

$$Z = \begin{array}{c} \omega A \\ \dfrac{P}{\gamma}\dfrac{dI}{dy} + A\left\{ u_{s_{\shortparallel}}\omega + \sum_i \left[F_{p_i} + \beta_i\,\omega(u_{p_{s_i}} - u_{p_i}) \right] \right\}_{\shortparallel} \\[2ex] \omega A\left(\dfrac{T_s}{-1} + \dfrac{u_s^2}{2} \right) + A\sum_i \left\{ \dfrac{Q_{p_i}}{\gamma-1} + u_{p_i}F_{p_i} + \right. \\[2ex] \left. \beta_i\,\omega\left[\dfrac{c}{\gamma-1}(T_{p_{s_i}} - T_{p_i}) + \dfrac{1}{2}(u^2_{p_{s_i}} - u^2_{p_i}) \right] \right\} \end{array} \qquad (6-5)$$

Particle Equations (non-conservation form)

$$\frac{\partial F_i}{\partial t} + A_i \frac{\partial F_i}{\partial x} = Z_i \qquad\qquad i=1 \ldots N \qquad (6\text{-}6)$$

where F_i and Z_i are vectors and A_i is a (3x3) matrix,

$$F_i = \begin{bmatrix} \rho_{p_i} \\[2mm] u_{p_i} \\[2mm] T_{p_i} \end{bmatrix} \qquad\qquad (6\text{-}7)$$

$$A_i = \begin{bmatrix} u_{p_i} & \rho_{p_i} & 0 \\[2mm] 0 & u_{p_i} & 0 \\[2mm] 0 & 0 & u_{p_i} \end{bmatrix} \qquad\qquad (6\text{-}8)$$

$$Z_i = \begin{bmatrix} \beta_i \omega - \dfrac{\rho_{p_i} u_{p_i}}{A} \dfrac{dA}{dx} \\[3mm] - F_{p_i}/\rho_{p_i} \\[3mm] - Q_{p_i}/c\,\rho_{p_i} \end{bmatrix} \qquad\qquad (6\text{-}9)$$

The Rubin and Burstein method is a second order predictor-corrector technique. An unusual characteristic of the method is that the predicted and corrected quantities are both evaluated at the full time step, as shown in Figure 6-1.

The finite difference solution to equation (6-2) is given by

Conservative Difference Equations

$$\widetilde{F}_{j+1/2, k+1} = \frac{F_{j+1, k} + F_{j,k}}{2} + \Delta t \left[\frac{Z_{j+1, k} + Z_{j,k}}{2} - \frac{(G_{j+1, k} - G_{j,k})}{\Delta x} \right] \quad (6\text{-}10)$$

152

$$\tilde{F}_{j,k+1} = F_{j,k} + \frac{\Delta t}{2}\left[Z_{j,k} + \frac{\tilde{Z}_{j,1/2,k-1} + \tilde{Z}_{j-1/2,k+1}}{2} - \frac{(G_{j+1,k} - G_{j-1,k})}{2\Delta x} - \frac{(\tilde{G}_{j+1/2,k+1} - \tilde{G}_{j-1/2,k+1})}{\Delta x}\right] \tag{6-11}$$

where a denotes predicted quantities, k refers to the old time, t, and k+1 is the advanced time t+Δt.

k + 1

Δ t

k

Δ x

j-2   j-1   j   j+1   j+2

○ Known point

□ Predicted point

◇ Corrected point
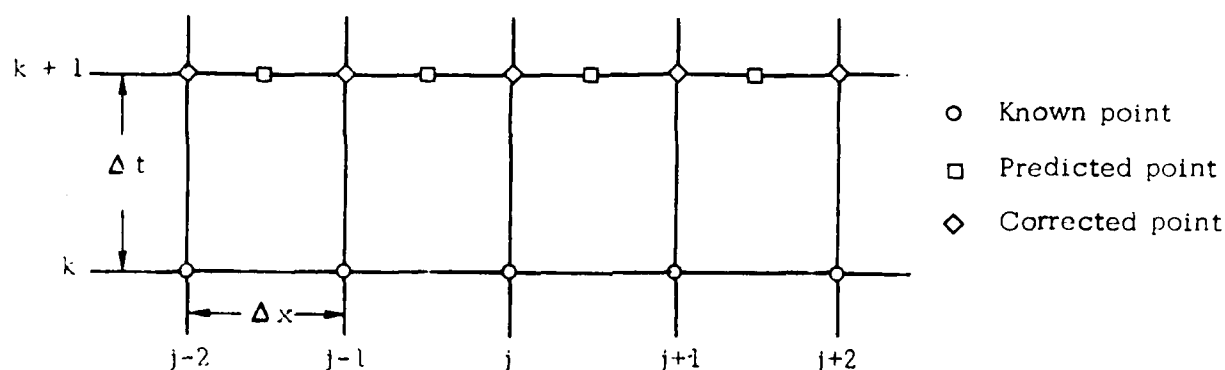
Figure 6-1.   Finite Difference Mesh for Rubin and Burstein Method

The finite difference solution to equation (6-6) is as follows,

Non-Conservative Difference Equations

$$\tilde{F}_{j+1/2,k+1} = \frac{F_{j+1,k} + F_{j,k}}{2} + \Delta t\left[\frac{Z_{j+1,k} + Z_{j,k}}{2} - \frac{(A_{j+1,k} + A_{j,k})}{2}\frac{(F_{j+1,k} - F_{j,k})}{\Delta x}\right] \tag{6-12}$$

$$F_{j,k+1} = F_{j,k} + \frac{\Delta t}{2}\left[Z_{j,k} + \frac{\widetilde{Z}_{j+1/2,k+1} + \widetilde{Z}_{j-1,k+1}}{2} - A_{j,k}\frac{(F_{j+1,k} - F_{j-1,k})}{2\Delta x} - \right.$$
$$\left. \frac{(\widetilde{A}_{j+1/2,k+1} + \widetilde{A}_{j-1/2,k+1})}{2}\frac{(F_{j+1/2,k+1} - F_{j-1,k+1})}{\Delta x}\right] \qquad (6-13)$$

The difference solution to the conservative gas equations (6-10) and (6-11), yields values for the conserved quantities given by (6-3). The usual flow variables are then calculated from these quantities as follows,

$$u = \frac{F_2}{F_1} \qquad (6-14)$$

$$\rho = \frac{F_1}{A} \qquad (6-15)$$

$$T = \gamma(\gamma-1)\left[\frac{F_3}{F_1} - \frac{1}{2}\left(\frac{F_2}{F_1}\right)^{2}\right] \qquad (6-16)$$

pressure being obtained from the perfect gas law (2-35).

The successive application of equations (6-10) to (6-16) yields the required solution at all mesh points lying between the boundaries of the problem, as illustrated in Figure 6-2.

There are four types of boundaries that may be encountered. Left hand boundary points located at the head end of the motor. Interior boundary points, in pairs, since these "boundaries" denote the locations of discontinuities. A quasi-steady nozzle boundary point, located at the nozzle entrance, if the quasi-steady boundary condition is invoked; or a nozzle exit boundary point, if the solution is continued out to a supersonic exit plane. The numerical procedures utilized to obtain solutions at these boundary points are presented in the Sections 6.3 and 6.4.

6.2   Numerical Stability and Its Influence On Computation Time

A linear stability analysis of the present finite difference technique[27] yields the expected Courant stability condition, given by (6-1), for a single phase system. In nonlinear problems, (6-1) is a necessary, but not sufficient, condition for stability. In the solutions obtained to date nonlinear numerical instability effects have not been encountered.

| Known | Unknown | Only if solution continued to supersonic exit plane |

| Left Bdy. (Head End) | Interior Bdy. (Discontinuities) | Int. Bdy. or Quasi-steady Nozzle Bdy. | Nozzle Exit Plane (if Applicable) |
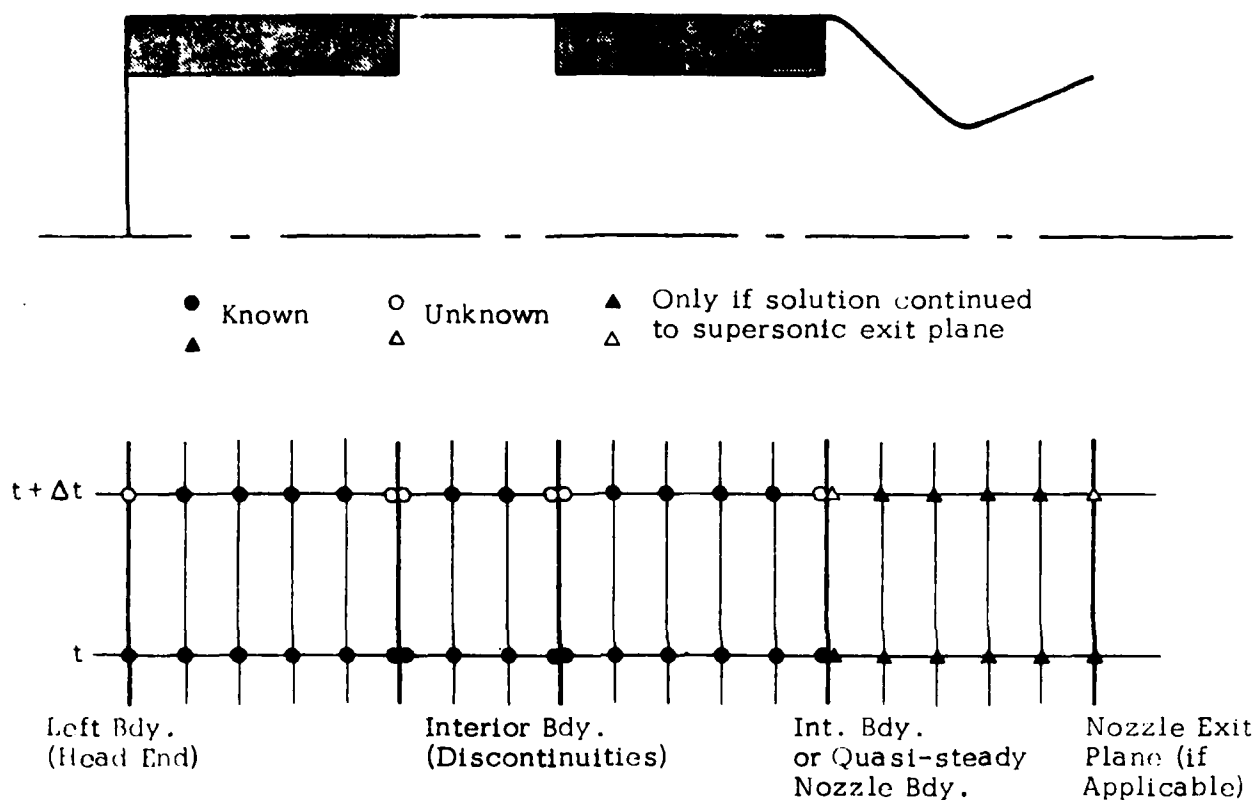
Figure 6-2. Status of Solution After Finite Difference Sweep

For the combined, particle-gas, two phase flow equations the CFL condition (6-1) is also necessary, but not sufficient, for stability. A formal stability analysis of the two phase flow equations has been carried out in Reference 31. The particle momentum and energy equations (2-32) and (2-34) can be written in the form analyzed in Reference 31 as follows,

$$\frac{Du_{p_i}}{Dt} = -\frac{\Gamma_{p_i}}{c_{p_i}} \qquad (6-17)$$

155

$$\frac{DT_{p_i}}{Dt} = -\frac{Q_{p_i}}{\rho_{p_i} c} \qquad (6\text{-}18)$$

or, using (2-39) and (2-40)

$$\frac{Du_{p_i}}{Dt} = -\frac{(u_{p_i} - u)}{\tau_v} \qquad (6\text{-}19)$$

$$\frac{DT_{p_i}}{Dt} = -\frac{(T_{p_i} - T)}{\tau_t} \qquad (6\text{-}20)$$

where τ_v, the velocity relaxation time (time interval required for particles to approach the local gas velocity), is given by,

$$\tau_v = \frac{a_f^* \rho_m^* D_i^{*2}}{18 L^* \mu^* \left(1 + \frac{Re_i^{2/3}}{6}\right)} \qquad (6\text{-}21)$$

and, τ_T, the thermal relaxation time is given by

$$\tau_T = \frac{a_f^* \rho_m^* D_i^{*2} cPr}{6 L^* \mu^* (2 + .459\ Re_i^{.55} P_r^{.33})} \qquad (6\text{-}22)$$

For explicit integration methods, it is shown in Reference 31 that equations of this type are subject to the conditional stability criterion

$$\Delta t < c_1 \tau \qquad (6\text{-}23)$$

where c_1 is a constant depending on the type of explicit method utilized, and τ is the time constant for the system. For second order methods, like the present one, the constant c_1 is normally about unity. Thus, in addition to the CFL condition the present integration method is subject to the following approximate stability conditions

$$\Delta t \lesssim \tau_v$$
$$\qquad\qquad (6\text{-}24)$$
$$\Delta t \lesssim \tau_T$$

156

One, or the other, of this conditions will be more restrictive. The ratio τ_T/τ_v is

$$\frac{\tau_T}{\tau_v} = \frac{3cPr(1+\dfrac{Re_i^{2/3}}{6})}{2+.459\ Re_i^{.55}Pr^{.33}} \qquad (6-25)$$

$$\frac{3cPr}{2} \text{ in Stokes flow limit.}$$

If $\tau_T/\tau_v > 1$ the momentum equation controls the stability of the system, or, conversely, if $\tau_T/\tau_v < 1$ the energy equation is controlling. From (6-21) and (6-22) it can be seen that, regardless of the controlling equation, the allowable step size decreases when L^* (essentially the length of the motor) and Re_i increase. Our experience, to date, indicates that (6-24) is a reliable stability condition for this problem to within about 10%.

The relative efficiency with which an instability solution may be obtained is critically dependent upon the stability conditions given by (6-1) and (6-24).

Let: Δx_{min} = the minimum value of Δx for the mesh

$N_{\Delta x}$ = the number of mesh points in the axial direction

N_{cyc} = the number of wave cycles for which the solution is to be computed

M_{max} = maximum value of mach number within the flowfield

Δt_{max} = the maximum time step allowed by combined stability conditions

The sound speed does not vary significantly in the motor so (6-1) can be approximated by

$$\Delta t_{max}^{CFL} = \frac{\Delta x_{min}}{(1+M_{max})} \qquad (6-26)$$

since the smallest step is likely to be used in the throat region where $M \approx M_{max}$. Assuming Δt_{max} does not vary much with time the total number of mesh point cal-

157

culations that will be made in N_{cyc} wave cycles is approximately

$$N_{Tot} \approx \frac{2 \, N_{cyc}(1+M_{max}) \, N_{\Delta x}}{\Delta x_{min}}$$ (6-27)

or, if Δx is constant throughout the mesh,

$$N_{Tot} \approx \frac{2 \, N_{cyc}(1+M_{max})}{\Delta x^2}$$ (6-28)

Thus, as a result of the CFL condition, the size of the smallest axial step has a profound influence on the total computation time required to obtain a solution. If, uniform axial steps are used (6-28) shows that the computation time will quadruple if Δx is reduced by a factor of two. The reason quasi-steady nozzle solutions are so much more efficient than solutions continued all the way through the throat is quite evident from the relations. In most solid rocket motors the nozzle usually represents, at most, 10% of the total length of the motor. Since the flow gradients are quite large in the nozzle, especially in the neighborhood of the throat, the axial step size required to obtain relatively accurate solutions tends to be rather small. Typically, the smallest step size (or step size, if Δx is constant) will be on the order of 1/50 the length of the nozzle, or about 1/500 the length of the motor. Thus, $\Delta x_{min} \approx .002$ in this case. Even with variable step size $N_{\Delta x}$ will run on the order of 100, and at the throat $M_{max} \approx 1$; so, for solutions out to the nozzle exit plane, equation (6-27) yields

$$N_{Tot} \approx 200,000 \, N_{cyc}$$ (6-29)

For a quasi-steady nozzle calculation, typically $\Delta x_{min} = \Delta x \approx .02$, and $M_{max} << 1$. In this case (6-28) yields

$$N_{Tot} \approx 5000 \, N_{cyc}$$ (6-30)

Or, in other words, the solution time for the equations of motion is roughly about 40 times faster when the quasi-steady nozzle assumption is utilized. In calcula-

158

ting the steady state solution for a motor only the equations of motion are solved, so this factor of 40 is representative of the relative times required to obtain the two types of solutions. In the instability solution, itself, much of the computation time is devoted to solving the transient burning rate equations at a series of mesh points. The total computation time for the burning rate solutions tends to run about 2 times that required for solving the quasi-steady nozzle fluidynamic problem. As a result, instability solutions carried through the throat take about 15 times longer than the equivalent quasi-steady nozzle solution.

Equations (6-26) to (6-28) represent the results imposed by the CFL stability condition. The two-phase numerical stability criteria (6-24) must also be satisfied. If

$$\tau_v < \frac{\Delta x_{min}}{(1+M_{max})}$$

or
$$\tau_T < \frac{\Delta x_{min}}{(1+M_{max})}$$
(6-31)

the maximum allowable time step is less than that given by (6-26) and the total number of mesh points to be calculated per cycle will increase. For instance, if either of the relations (6-31) is true, and the particle size is halved, the solution time for the equations of motion will quadruple.

Assuming for the moment that $\tau_v < \tau_T$ (see (6-25)), and taking typical numbers for a_f^* (4000 ft/sec), ρ_m^* (7.76 slugs/ft^3), and μ^* (1.85x10^{-6} lb. sec/ft^2), equation (6-21) is, approximately (for Re$_i$ << 1)

$$\tau_v \approx \frac{.01 D_i^2 \text{ (microns)}}{L^* \text{ (ft)}}$$
(6-32)

The ratio of (6-32) to (6-26) determines which stability condition is controlling the maximum allowable time step.

$$\frac{\tau_v}{\Delta t_{max}^{CFL}} \approx \frac{.01(1+M_{max}) D_i^2 \text{ (microns)}}{\Delta x_{min} L^* \text{ (feet)}}$$
(6-33)

159
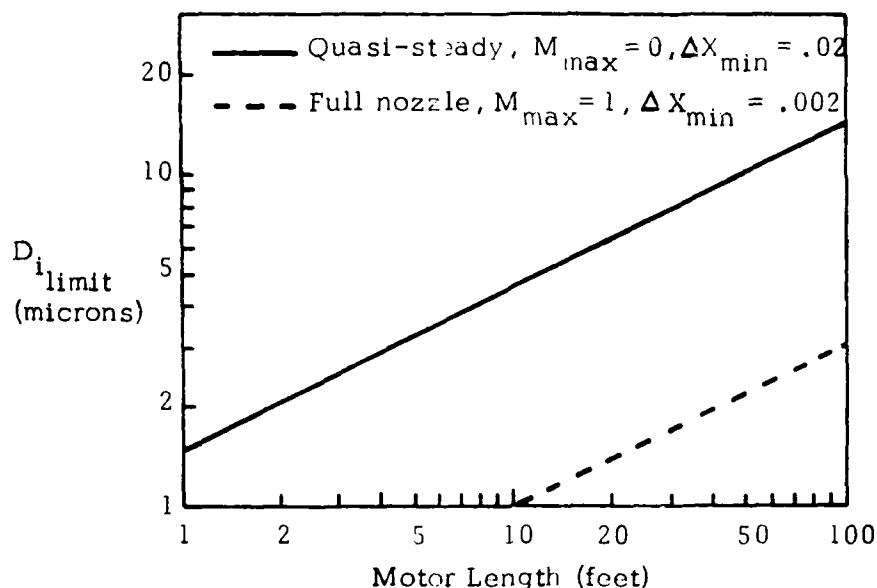
Figure 6-3. Stability Limiting Particle Size
Versus Motor Length

Figure (6-3) shows the particle size, $D_{i_{limit}}$, at which the allowable
step size begins to be controlled by the two phase stability conditions, as a func-
tion of motor length. The previously mentioned values of Δx_{min} and M_{max} for
typical full and quasi-steady nozzle calculations were utilized. For particle
sizes below $D_{i_{limit}}$ the allowable step size will decrease as the particle size
squared,

Max. time step when $D_i < D_{i_{limit}}$

$$\Delta t_{max} = \Delta t_{max}^{CFL} \left(\frac{D_i}{D_{i_{limit}}} \right)^2 \qquad (6-34)$$

For example, from Figure (6-3) and equation (6-34) one finds that for
a quasi-steady nozzle solution in an 8 foot motor with 2 μ particles, the allowable
Δt is one-quarter the CFL limiting time step; or in a 100 foot motor with 2 μ particles
$\Delta t_{max} = \Delta t_{max}^{CFL}/50$. When full nozzle solutions are calculated the CFL limiting time
step is so small the two phase stability limit is of much less importance. For
instance, Δt_{max} for full nozzle solutions is not influenced by the particles until

160

the motor exceeds about 100 feet in length for 3 μ particles and 40 feet in length for 2 μ particles.

When an explicit finite difference method was selected for use in the instability solution the ramifications of the aforementioned stability conditions were not fully appreciated. As a result of the previous discussion it is evident that solutions continued through the throat, or solutions for large motors with small particles, could be obtained much more efficiently with an implicit finite difference method. Implicit methods are unconditionally stable, hence, the size of the integration time step is governed solely by truncation error considerations.

6.3   Head-End and Nozzle Boundaries

It is possible to postulate a large number of numerical techniques by which solutions may be obtained at the boundaries. These include various types of extrapolation and one sided differences, as well as the method of characteristics. As discussed in Reference 32, the method of characteristics is the prefered method for handling the boundary conditions. It is more accurate and general than the other techniques, mainly due to its uniqueness and consistency. By uniqueness it is meant that when treated by the method of characteristics the number of available equations at a boundary point is exactly equal to the number of unknowns. When extrapolation or one-sided differences are employed the number of available equations becomes redundant, i.e. there are more equations to choose from than there are unknowns. The solution at the boundary is, therefore, not unique, but is dependent upon which of the available equations is arbitrarily dropped.

The other factor, consistency, refers to whether or not the numerical method implies a violation of the signaling, or information transfer rules, for a compressible flow. By definition the method of characteristics is consistent, as information is carried through the flow along the characteristics. The other methods are inconsistent, to varying degrees. The chief virtue of one sided differences, and, especially extrapolation, is simplicity. Conversely, the only drawback to the method of characteristics is the additional analysis and programming required to implement it. In many cases, despite their redundancy and inconsistences, one sided differences and/or extrapolation can yield acceptable results. In such cases their simplicity warrants their use. In other cases, the method of character-

161

istics must be utilized to obtain acceptable boundary point solutions.

In the present problem the only boundary at which a non-characteristic method is completely acceptable is the supersonic exit plane. At this boundary there is essentially no back information transfer to the domain of interest, hence, errors made at this point do not measurably influence the computation. One sided differences are currently employed to compute points at the nozzle exit. At the head-end, closed boundary, one sided differences are better than extrapolation, but not completely acceptable, so the method of characteristics is utilized. At the interior boundary points, discussed in Section 6.4, both extrapolation and one sided differences are numerically unstable. The method of characteristics, however, yields stable and accurate solutions at these points.

Head-End, No End Burning

As previously mentioned the method of characteristics is utilized at this boundary. Curently, a first-order solution is obtained using simple Euler integration along the characteristics. Second order solutions could (and possibly should) be easily obtained by using modified Euler integration. The boundary conditions at this boundary are, from equation (3-15), $u = u_{p_1} = 0$.

The finite difference form of the characteristics equations (2-41) to (2-48) are used in the manner illustrated in Figure 6-4, in order to obtain a solution at the left boundary. The solution is known at points 1 and 2 at time equal t, and is sought at point 3, at time equat $t + \Delta t$. Point 1' represents the location where the left running characteristic through point 3 crosses the line time = t. As a result of the CFL stability condition (6-1), point 1' must be between points 1 and 2. On the first iteration the velocity, $u_{1'}$, and sound speed, $a_{1'}$, are set equal to the respective quantities at point 1. The first step in the solution is to locate point 1' using (2-41) for a left running characteristic (minus sign).

$$x_{1'} = x_1 - (u_{1'} - a_{1'}) \Delta t \tag{6-35}$$

All of the flow and geometrical properties at point 1' are then established by linear interpolation. The pressure at point 3 is then found from the compatibility relation (2-42) as

162

$$P_3 = P_{1'} + \gamma \rho_{1'} a_{1'} (RHS^- \Delta t + u_3 - u_{1'}) \qquad (6-36)$$

where $u_3 = 0$, as a result of the boundary condition, and RHS^- is equal to the right hand side of (2-42) evaluated at point 1'.

When there is no end burning the line $x=0$ is a streamline, and if particles are present, a particle path line. The temperature at point 3 is then found from (2-44) as

$$T_3 = T_2 + \frac{1}{\rho_2}\left[RHS \, \Delta t + (\frac{\gamma-1}{\gamma})(P_3 - P_2)\right] \qquad (6-37)$$

where RHS is equal to the right hand side of (2-44) evaluated at point 2. If there are particles present u_{p_i}, T_{p_i} and ρ_{p_i} are calculated from (2-46), (2-47) and (2-48), respectively.

$$u_{p_{i_3}} = u_{p_{i_2}} - \frac{F_{p_{i_2}}}{\rho_{p_{i_2}}}\Delta t \qquad (6-38)$$

$$T_{p_{i_3}} = T_{p_{i_2}} - \frac{Q_{p_{i_2}}}{c\rho_{p_{i_2}}}\Delta t \qquad (6-39)$$

$$\rho_{p_{i_3}} = \rho_{p_{i_2}} + \left\{\beta_i\omega_2 - \rho_{p_{i_2}}\left[\left(\frac{u_{p_{i_1}} - u_{p_{i_2}}}{x_1 - x_2}\right) + u_{p_{i_2}}\frac{dA}{dx}\Big|_2\right]\right\}\Delta t \qquad (6-40)$$

At this point the density at point 3, ρ_3, is found from the perfect gas law (2-35) and the whole solution is reiterated starting with the newly calculated values of $a_{1'}$ and $u_{1'}$. (Note: this iteration does not improve the theoretical accuracy of the calculation, it remains first order; however, it is found that, in practice, better results are achieved). At the conclusion of the boundary point solution the conserved F quantities, defined by (6-3) are calculated, for use in the next finite difference integration step.

Head-End, End Burning

The method of characteristics solution at the head end, when there is end burning, is at once, simpler, yet more complex, than its inert counterpart. (See Figure 6-5). The solution is the same up to the equation for P_3, (6-36). When there is end burning u_3 equals the velocity of the gases leaving the surface, u_s. At this point, the boundary conditions (3-16) that need be applied yield the values for the remaining variables,

$$T_3 = T_f \qquad (6\text{-}41)$$

$$u_{p_{i_3}} = u_s \qquad (6\text{-}42)$$

$$T_{p_{i_3}} = T_f \qquad (6\text{-}43)$$

$$\rho_{p_{i_3}} = \beta_i \rho_3 \qquad (6\text{-}44)$$
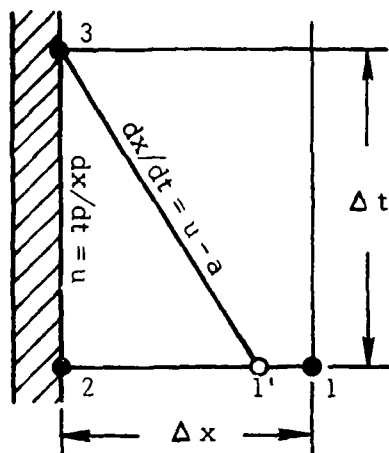
Figure 6-4. Characteristics Mesh at Left Boundary--No End Burning
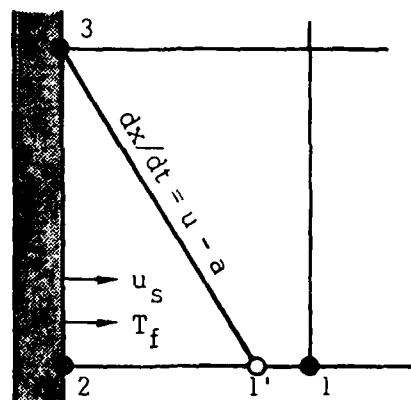
Figure 6-5. Characteristic Mesh at Left Boundary--End Burning

The potential complexity derives from the fact that the properties of the combustion gases leaving the surface, u_s, T_f etc. depend upon the pressure, P_3, and vice-versa. When such coupling exists, solutions may be obtained by iteration, or, as in the present case, by making a simplifiying assumption. Currently, the calculation is uncoupled by replacing that the properties of the combustion products leaving the surface at $t + \Delta t$ by their counterparts at time = t.

Quasi-Steady Nozzle Boundary

When the nozzle is treated in a quasi-steady manner the right hand boundary is treated in much the same manner as the head end. In this case, however, the left running characteristic is the missing one, and the boundary condition fixes the mach number at the nozzle entrance such that the flow will choke at the throat. Another difference at the right boundary is that the streamlines and particle paths through point 3 are not known, a priori, as they are at the head end.

The points and characteristics used in the right hand boundary point solution are shown in Figure 6-6.
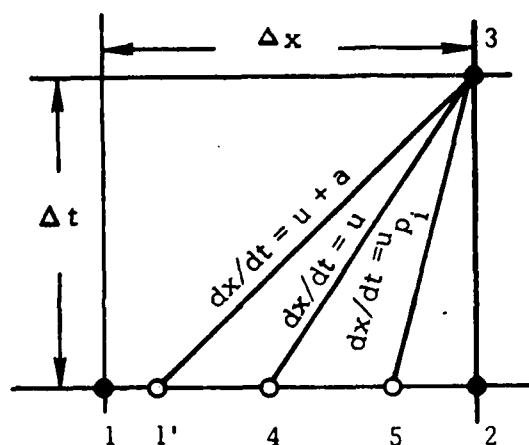
Figure 6-6. Characteristics Mesh at Quasi-Steady
Noz. 'e Boundary

Point 1' is located by tracing the right running characteristic through point 3 back to time = t.

$$x_{1'} = x_2 - (u_{1'} + a_{1'}) \Delta t \qquad (6-45)$$

On the first iteration only $u_{1'}$ and $a_{1'}$ are set equal to u_1 and a_1, respectively. The flow and geometrical properties at point 1' are established by linear interpolation. The pressure at point 3 can then be found from the compatibility relation for a right running characteristic equation (2-42) (plus sign).

$$P_3 = P_{1'} + \gamma \rho_{1'} a_{1'} (RHS^+ \Delta t - u_3 + u_{1'}) \qquad (6-46)$$

where RHS^+ is equal to the right hand side of (2-42) evaluated at point 1'. The velocity at point 3, u_3, is taken to be equal to u_2 on the first iteration, thereafter, u_3 is found from the mach number boundary condition, once T_3 has been established.

The temperature at point 3 is found using the streamline characteristic (2-43). Point 4 is located as

$$x_4 = x_2 - u_4 \Delta t \qquad (6-47)$$

The other properties at point 4 are found by linear interpolation, T_3 can be calculated from (2-44) as

$$T_3 = T_4 + \left[RHS \, \Delta t + (\tfrac{\gamma - 1}{\gamma})(P_3 - P_4) \right] \frac{1}{\rho_4} \qquad (6-48)$$

where RHS is equal to the right hand side of (2-44) evaluated at point 4. The sound speed at point 3 is then

$$a_3 = \left(T_3 \right)^{1/2} \qquad (6-49)$$

The boundary condition, and perfect gas law then yield, respectively,

$$u_3 = a_3 M_e \qquad (6-50)$$

$$\rho_3 = P_3/T_3 \qquad (6-51)$$

If particles are present, point 5 is then located using the equation for a particle pathline (2-45)

$$x_5 = x_2 - u_5 \Delta t \qquad (6-52)$$

166

The quantities $u_{p_{i_3}}$, $T_{p_{i_3}}$ and $\rho_{p_{i_3}}$ may then be found from the compatibility relations (2-46) to (2-48) in the manner indicated in (6-38) to (6-40), by replacing point 2 with point 5. The discussion given after equation (6-40) is, again, pertinent at this point.

Supersonic Nozzle Exit Boundary

As indicated previously, no boundary conditions need be satisfied at this point. The equations of motion are integrated at this boundary using a one sided, second order, difference approximation for the x derivatives. Let y stand for any quantity, then the derivative at the boundary is given by

$$\frac{\partial y}{\partial x}\Big|_i = \frac{3y_i - 4y_{i-1} + y_{i-2}}{2\Delta x} \tag{6-53}$$

The relation assumes that the axial step size Δx is constant. The gas properties are found by integrating the equation in conservation form (6-2) as follows

$$F_i(t+\Delta t) = F_i(t) + (Z_i(t) - \frac{\partial G}{\partial x}\Big|_i) \Delta t \tag{6-54}$$

The solution for the j th particle group is found by integrating (6-6)

$$F_{j,i}(t+\Delta t) = F_{j,i}(t) + (Z_{j,i}(t) - A_{j,i} \frac{\partial F_j}{\partial x}\Big|_i) \Delta t \qquad j = 1\ldots N \tag{6-55}$$

The time integrations in (6-54) and (6-55) are accurate only to first order. The x derivatives in these equations are evaluated using (6-53).

6.4   Interior Boundary Points

As discussed in Section 2.5, interior boundary points are located at axial stations corresponding to gaps in the grain. At these locations the burning rate and area may be discontinuous, therefore, the jump equations (2-49) to (2-55) are required in to obtain a solution at such points. An alternative use of interior boundaries is to separate regions of different step size. The axial step size must

167

be constant within each region, but may vary from region to region. If the axial gradients are much larger in a given section of the motor (usually the throat section) than elsewhere, the section may be treated as a special region with correspondingly smaller axial steps. This is somewhat more efficient than using the smaller steps throughout the motor, however, as discussed in Section 6.2, the overall efficiency of the calculation is mainly controlled by the size of the smallest step. If an interior boundary is created as a means of changing step size alone, the solution procedure outlined below reduces to the normal method of characteristics field point solution; the jump equations are trivial (no jump) in such cases.

An interior boundary point is really two points, one on each side of the discontinuity. The method of characteristics, in conjuction with the jump equations, is used to obtain solutions at these points.

At a general interior boundary point the unknowns are ρ, u, T, P, ω, ρ_{p_i}, u_{p_i} and T_{p_i} on both sides of the boundary. If there are N particle groups the total number of unknowns is equal to 10+6N. The same number of equations must be available if there is to be a unique solution. There are 3+N characteristic lines which intersect the boundary, along which there are 3+3N compatibility relations (the particle pathline is a triple characteristic, given the quasi-characteristic form of the particle continuity equation). An additional 3+3N equations come from conservation of mass, momentum and energy for the gas and particles (jump equations). The remaining four equations are the perfect gas law and the heat conduction equation (for ω), on both sides of the boundary (ω may be zero on one or both sides of the boundary).

Unlike the simpler head-end and quasi-steady boundaries, many different flow situations may exist at an interior boundary. The number of situations being a function of the number of particle groups. Figure 6-7 illustrates the four characteristic diagrams that are possible when there is one particle group. There is always one left running and one right running characteristic intersecting the boundary as shown. The differences are created by the signs of the gas and particle velocities. If the velocities are positive the streamline or pathlines carry information from the left side to the boundary, and if the velocities are negative, the directions of these characteristics is reversed. Since, in general, the par-

168
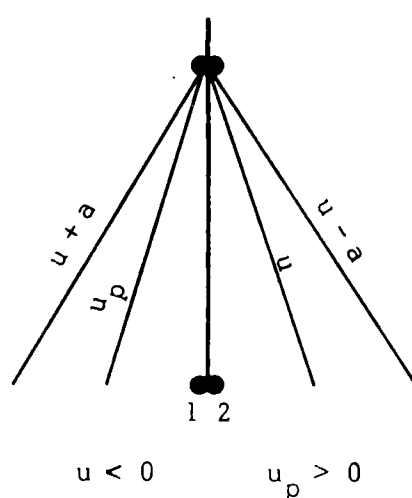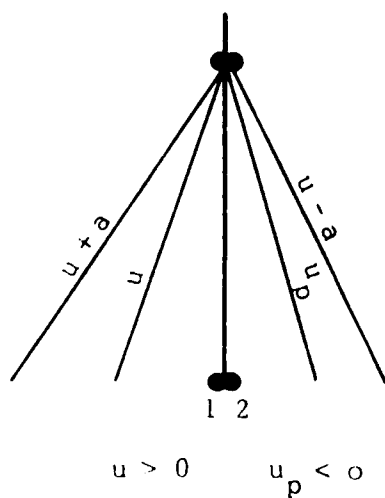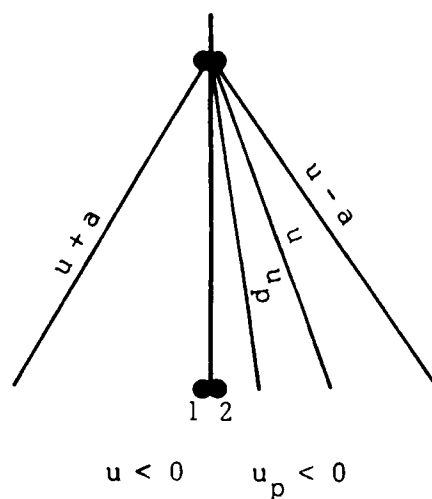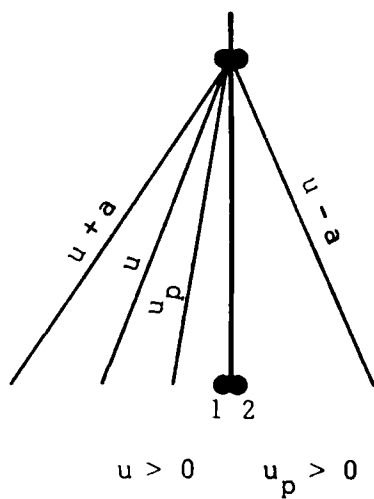
Figure 6-7. Four Possible Characteristic Diagrams at an
Interior Boundary, With One Particle Group

169

ticle velocity may lead or lag that of the gas, the gas may be moving in one direction and the particles in the other direction.

A general solution to the interior boundary problem has been formulated, however, which allows all of the possible flow configurations to be treated in a unified manner. The unified jump equations, and their solution, are presented first, following by a discussion of the overall solution procedure.

Unified Gas Jump Equations

Equations (2-49) to (2-51) may be rewritten in the following general manner, so that they apply to all possible geometric and flow situations. The following definitions are made:

1   subscript denotes the point on the left side of the boundary.

2   subscript denotes the point on the right side of the boundary.

$$\underline{\text{for } u_1 \geq 0} \quad \text{Let:} \quad s=1, \quad A_R = \frac{A_2}{A_1}, \quad j=1, \quad j+1=2 \tag{6-56}$$

$$\underline{\text{for } u_1 \leq 0} \quad \text{Let:} \quad s=-1, \quad A_R = \frac{A_1}{A_2}, \quad j=2, \quad j+1=1 \tag{6-57}$$

$$\underline{\text{for } A_R \geq 1} \quad \text{Let:} \quad a=0, \quad b=1 \tag{6-58}$$

$$\underline{\text{for } A_R \leq 1} \quad \text{Let:} \quad a=1, \quad b=0 \tag{6-59}$$

The general forms of (2-49) to (2-51) may then be written as follows, (using $\dot{m} = \rho u A$, and $P = \rho T$).

$$\underline{\text{Mass:}} \qquad\qquad \dot{m}_j + s\,\dot{m}_e = \dot{m}_{j+1} \tag{6-60}$$

$$\underline{\text{Momentum:}} \quad \left(\frac{\dot{m}_j \, T_j}{u_j \, \gamma}\right) A_R^a + \dot{m}_j \, u_j + s\,\dot{m}_e \, u_{s_e} = \left(\frac{\dot{m}_{j+1} \, T_{j+1}}{u_{j+1}\gamma}\right)\frac{1}{A_R^b} + \dot{m}_{j+1} u_{j+1} \tag{6-61}$$

170

$$\dot{m}_j \left(\frac{T_j}{\gamma-1} + \frac{u_j^2}{2} \right) + s\,\dot{m}_e \frac{T_{f_c}}{\gamma-1} = \dot{m}_{j+1} \left(\frac{T_{j+1}}{\gamma-1} + \frac{u_{j+1}^2}{2} \right) \tag{6-62}$$

Equations (6-60) to (6-62) can be directly solved for the quantities at $j+1$. The solution is

$$\dot{m}_{j+1} = \dot{m}_j + s\,\dot{m}_e \tag{6-63}$$

$$u_{j+1} = \frac{\alpha - \left[\alpha^2 - 4(1-K/2)K\,\beta\dot{m}_{j+1} \right]^{1/2}}{(2-K)\,\dot{m}_{j+1}} \tag{6-64}$$

$$T_{j+1} = (\gamma-1) \left(\frac{\beta}{\dot{m}_{j+1}} - \frac{u_{j+1}^2}{2} \right) \tag{6-65}$$

$$\rho_{j+1} = \frac{\dot{m}_{j+1}}{u_{j+1} A_{j+1}} \tag{6-66}$$

where the following quantities are defined[+]

$$\alpha = \frac{\dot{m}_j\, T_j}{u_j \gamma} A_R^a + \dot{m}_j\, u_j + s\,\dot{m}_e\, u_{s_e} \tag{6-67}$$

$$\beta = \dot{m}_j \left(\frac{T_j}{\gamma-1} + \frac{u_j^2}{2} \right) + s\,\dot{m}_e \frac{T_{f_e}}{\gamma-1} \tag{6-68}$$

$$K = \left(\frac{\gamma-1}{\gamma} \right) \frac{1}{A_R^b} \tag{6-69}$$

Unified Particle Jump Equations

The general particles jump equations are more easily solved. With the following definitions

$$\frac{u_{p_i}}{p_{i_1}} \cdot 0 \qquad\qquad s = 1 \qquad\qquad j = 1,\ j+1 = 2 \tag{6-70}$$

[+] The definitions given for α, β, and K apply only to this analysis, they have other meanings elsewhere.

$$\frac{u_{p_{i_1}}}{} \leq 0 \qquad s = -1 \qquad j = 2, \; j + 1 = 1 \qquad\qquad (6\text{-}70)$$

the general forms of (2-53) to (2-55) can be directly solved for the variables at j+1. The solution is

$$\dot{m}_{p_{i_{j+1}}} = \dot{m}_{p_{i_j}} + s\,\beta_i\,\dot{m}_e \qquad\qquad (6\text{-}71)$$

$$u_{p_{i_{j+1}}} = \frac{\dot{m}_{p_{i_j}} u_{p_{i_j}} + s\beta_i \dot{m}_e u_{p_{s_{i_e}}}}{\dot{m}_{p_{i_{j+1}}}} \qquad\qquad (6\text{-}72)$$

$$T_{p_{i_{j+1}}} = \frac{\gamma-1}{c}\left[\frac{\dot{m}_{p_{i_j}}(\frac{c}{\gamma-1}T_{p_{i_j}} + \frac{1}{2}u^2_{p_{i_j}}) + s\beta_i \dot{m}_e \frac{c}{\gamma-1}T_{s_e}}{\dot{m}_{p_{i_{j+1}}}} - \frac{1}{2}u^2_{p_{i_{j+1}}}\right](6\text{-}73)$$

$$\rho_{p_{i_{j+1}}} = \frac{\dot{m}_{p_{i_{j+1}}}}{u_{p_{i_{j+1}}} A_{j+1}} \qquad\qquad (6\text{-}74)$$

General Boundary Point Solution

The general solution at an interior boundary is obtained by combining the method of characteristics with the jump solutions previously given. The characteristics solution is carried out using back values at time = t only, hence, it is a first order solution. With a first order method the solutions for the gas and particles may be uncoupled. In the present case the solution for the gas phase is obtained first. There is a problem with regard to the evaluation of $\dot{m}_e$, u_{s_e} and T_{f_e} when uninhibited end burning takes place at an interior boundary. The flow in the neighborhood of a gap in the grain is subject to both two dimensional and viscous effects. It is, thus, difficult to characterize the pressure on the end

172

burning face in a one-dimensional, inviscid, model. Here again, an assumption has to be made. Presently, for the purpose of calculating burning rate only, it is assumed that the pressure on the burning face is equal to the pressure at the end point of the adjacent lateral burning surface. For the example shown in Figure 6-8 the pressure on the end face is assumed to be P_1, the pressure at Point A. It is further assumed that since $P_{face}=P_1$, the burning rate and flame temperature solutions at point A can be used to characterize $\dot{m}_e$, u_{s_e} and T_{f_e}. This assumption neglects any difference in erosive effects between the two locations. These aforementioned assumptions were not necessary, but they are reasonable, and allow a solution to be obtained more conveniently. Should it prove to be warranted, other treatments of the uninhibited end burning can be considered.

Burn Rates of Uninhibited End Faces Assumed Equal
to Burn Rates at Respective "A" Points

Figure 6-8. Uninhibited End Burning Model

A solution for the gas phase may be directly obtained by solving the complete set of nonlinear algebraic equations generated by the combination of the jump equations, (6-60) to (6-62), and the characteristic compatibility relations.

This approach yields the solution on both sides of the boundary by simultaneously solving all of the equations numerically. A means of utilizing the closed form solution of the jump equations, given by (6-63) to (6-66), has been developed, however, obviating the need for a numerical solution of these nonlinear algebraic equations. The closed form gas jump solutions yield all of the gas variables on one side of the boundary when all of these variables are known on the other side. Unfortunately, the characteristics equations do not allow all of the gas properties on one side of the boundary to be calculated directly. As shown in Figure 6-7 there are always two gas characteristics on one side of the boundary, and one characteristic on the other side. Therefore, an indirect, iterative, approach has been developed. First, the side on which there are two characteristics is deter- mined from the sign of the gas velocity at time t. An initial estimate of the velo- city on this side of the boundary, at time t+Δt, is then obtained by three point extrapolation. Between the velocity estimate and the two characteristic equations there is enough information to calculate all of the gas properties on one side. The jump equation solutions are then utilized to calculate the properties on the other side of the boundary. These gas properties must satisfy the remaining character- istic relation, to within a specified tolerance in order to claim a complete solution. In general, this characteristic relation will not be satisfied by the solution ob- tained using the first estimated velocity. The initial velocity estimate is then varied, and the solution repeated, until the remaining characteristic relation is satisfied. A modified secant technique is used in order to speed the convergence of this iterative procedure. The details of this procedure are given below.

Figure 6-9 shows the two possible situations which may be encountered at an interior boundary located at the j th mesh point. If the gas velocity is posi- tive there are two characteristics on the left side. If the velocity is negative the streamline intersects the boundary from the right side. By defining the following quatities a single characteristic solution can be made to apply to both cases.

$\underline{u_j \geq 0}$ Let: 1 subscripts denote point j-1
2 subscripts denote point j
2p subscripts denote point j+1   at time = t
1p subscripts denote point j+2

3 subscripts denot point j
3p subscripts denote point j+1   at time = t+Δt

s = 1

174

$u_j \leq 0$ Let: 1 subscripts denote point j+2
                          2 subscripts denote point j+1
                          1p subscripts denote point j-1   at time = t
                          2p subscripts denote point j   (6-75)

                          3 subscripts denote point j+1
                          3p subscripts denote point j   at time = t+Δt

                          s = -1

The value of u_3 is obtained by extrapolation from the adjacent interior points previously obtained using the finite differece technique. The pressure and temperature at point 3 are then obtained in the manner shown for the quasi-steady nozzle boundary, but with a slightly generalized form of the characteristics equations. An explanation of the characteristic solution procedure may be found in Section 6.3. Only the final equations which differ from those used at the nozzle boundary are given here.

$$x_{1'} = x_3 - (u_{1'} + a_{1'}s)\, \Delta t \qquad (6-76)$$

$$P_3 = P_{1'} + \gamma \rho_{1'} a_{1'} \left[RHS^{(s)}\, \Delta t - s\,(u_3 - u_{1'}) \right] \qquad (6-77)$$

where $RHS^{(s)}$ is equal to the right hand side of (2-42) evaluated at point 1' with the $\pm$ signs evaluated according to the sign of s. The temperature at point 3 is found using (6-47) and (6-48). Density and sound speed are calculated from (6-49) and (6-51), respectively.

A relation to be used after the jump equations are solved to check the validity of the interior boundary calculation is then obtained from the compatibility relation along the remaining characteristic. Without going into all of the details, the relation is,

$$P_{3p} = c_1 + c_2\, u_{3p} \qquad (6-79)$$

where c_1 and c_2 are constants which depend on the values of the gas parameters at point 1p'.

With u_3 ,P_3 ,T_3 and ρ_3 ,as obtained above, equations (6-63) to (6-66) are used to calculate u_{3p}, P_{3p}, T_{3p} and ρ_{3p} (one should equate 3 here, with j in

175
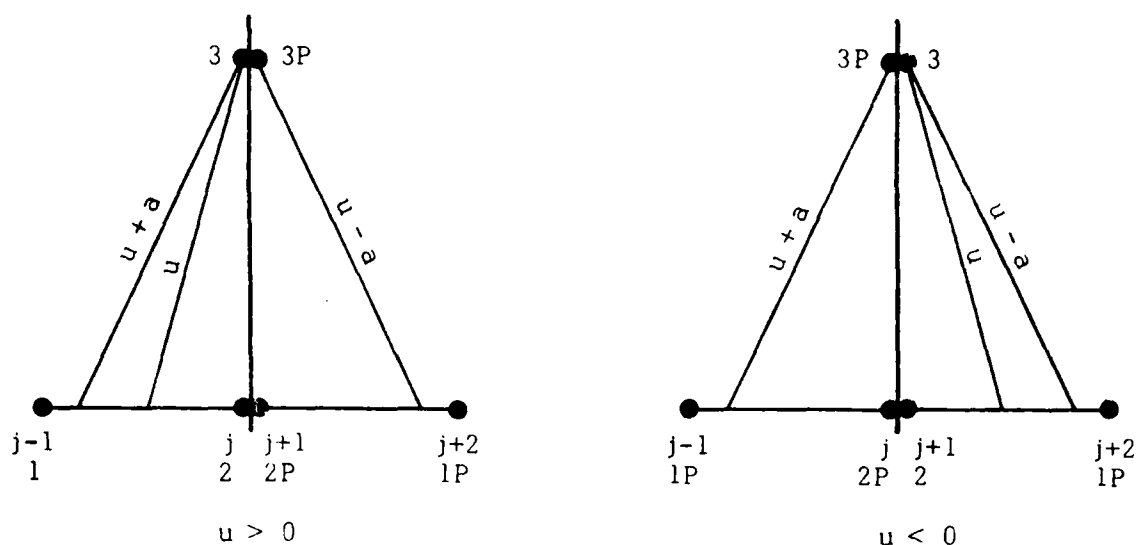
Figure 6-9. Gas Phase Characteristics Solution
at Interior Boundary

the jump equations, and 3p should be equated to j+1). The values of u_{3p} and P_{3p}, so obtained, are checked to see if they satisfy (6-78). If

$$P_{3p} - c_1 - c_2 \, u_{3p} < \text{specified tolerance}$$

a solution has been achieved. If not, a new value for u_3 is selected and the procedure is repeated.

The particle solution at the interior boundary points is obtained after the gas solution is completed. Since the particle pathline is treated as a triple characteristic u_{p_1}, T_{p_1} and ρ_{p_1} can be directly obtained on the side of the boundary which the pathline intersects. If the definitions given by (6-75) are made for $u_{p_1} \geq 0$ and $u_{p_1} < 0$, the equations used to calculate the particle solution at a quasi-steady nozzle boundary point can be utilized directly to solve for the particle variables on the side of the boundary where the pathline is located. The generalized solution for the particle jump equations, equations (6-71) to (6-74), then yields the particle solution on the other side of the boundary.

6.5   Transient Burning Rate Solution

The nonlinear transient burning rate response is obtained by solving

176

the nondimensional heat conduction equation (5-23), subject to the boundary conditions (5-24) at $\xi = \infty$, and (5-25) at the burning surface. The steady state solution, used as an initial condition, is given by (5-31). Once the burning rate has been found, the flame temperature is calculated from (5-37). Alternately, linear transient burning rate solutions may be obtained by using (5-43), (5-50) and (5-51) in place of (5-23), (5-25) and (5-37).

Transformed Equations

The temperature gradients in the solid are greatest at the surface and decay exponentially with distance into the solid. For this reason it desirable to transform to a coordinate system in which constant increments in the transformed plane correspond to small increments near the surface and larger ones as depth increases in the physical coordinate. Also, the boundary condition

$$\theta_s = 0 \text{ at } \xi = -\infty \tag{6-79}$$

could be applied at a large but, finite value of ξ. However, it is possible to find a transformation that has the previous characteristic and also maps $\xi = -\infty$ to a finite value. There are many possible transformations, the one selected is actually a restricted form of what is known as the "Euler" transformation

$$Z = \frac{-\xi}{\alpha - \xi} \qquad \alpha = \text{const.} \tag{6-80}$$

The interval $\xi = 0 \rightarrow -\infty$ is transformed to $Z = 0 \rightarrow 1$. The inverse of the transformation is

$$\xi = \frac{\alpha Z}{(Z-1)} \tag{6-81}$$

Also,

$$\frac{dZ}{d\xi} = Z' = \frac{-(Z-1)^2}{\alpha}$$

$$\frac{d^2 Z}{d\xi^2} = Z'' = \frac{2(Z-1)^3}{\alpha^2} \tag{6-82}$$

177

In order to transform the differential equations the following relations are needed:

$$\frac{\partial}{\partial \xi} = Z' \frac{\partial}{\partial Z}$$

$$\frac{\partial^2}{\partial \xi^2} = Z'' \frac{\partial}{\partial Z} + Z'^2 \frac{\partial^2}{\partial Z^2}$$

(6-83)

Using (6-83), the nonlinear equation (5-23), and linear equation (5-43), become

Nonlinear:

$$\frac{\partial \theta}{\partial \tilde{t}} + (RZ' - Z'') \frac{\partial \theta}{\partial Z} - Z'^2 \frac{\partial^2 \theta}{\partial Z^2} = 0$$

(6-84)

Linear:

$$\frac{\partial \theta}{\partial \tilde{t}} + (Z' - Z'') \frac{\partial \theta}{\partial Z} - Z'^2 \frac{\partial^2 \theta}{\partial Z^2} = -(R-1)e^{\xi}$$

(6-85)

The transformed boundary conditions are

$$\theta = 0 \text{ at } Z = 1$$

(6-86)

and,

$$\frac{\partial \theta}{\partial Z}\bigg|_- = \frac{1}{Z'(0)} \frac{\partial \theta}{\partial \xi}\bigg|_-$$

(6-87)

where $\frac{\partial \theta}{\partial \xi}\bigg|_-$ is given by (5-25) and (5-50) for the nonlinear and linear models, respectively. The steady state solution, (5-31), may be written as

$$\theta_{\tilde{t}=0} = e^{\xi} = \exp\left[\frac{\alpha Z}{Z-1}\right]$$

(6-88)

Finite Difference Solution

Equations (6-84) and (6-85), subject to the boundary conditions (6-86) and (6-87), and the initial cordition (6-88) are solved using the Crank-Nicolson finite difference scheme. A network of mesh points is created as shown in Figure 6-10.

With the Crank-Nicolson method the derivatives and coefficients in the differential equation are evaluated at the midpoint $m+1/2$, $n+1/2$. The resulting

178
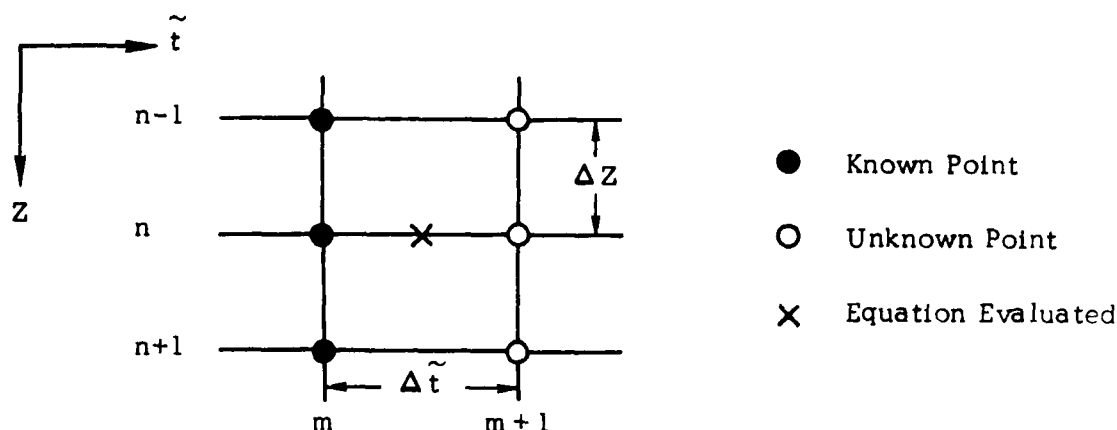
Figure 6-10. Finite Difference Mesh

solutions are accurate to second order. For nonlinear problems the difference equations are normally linearized, enabling a solution to be achieved by solving a coupled set of linear, rather than nonlinear, algebraic equations. In such cases, one iteration must be performed to regain second order accuracy. The following representations of the derivatives are used:

$$\frac{\partial \theta}{\partial Z} = 1/2 \left[\frac{(\theta_{m,n+1} - \theta_{m,n-1})}{2\Delta Z} + \frac{(\theta_{m+1,n+1} - \theta_{m+1,n-1})}{2\Delta Z} \right] \quad (6\text{-}84)$$

$$\frac{\partial^2 \theta}{\partial Z^2} = 1/2 \left[\frac{(\theta_{m,n+1} - 2\theta_{m,n} + \theta_{m,n-1})}{\Delta Z^2} + \frac{(\theta_{m+1,n+1} - 2\theta_{m+1,n} + \theta_{m+1,n-1})}{\Delta Z^2} \right] \quad (6\text{-}90)$$

$$\frac{\partial \theta}{\partial \tilde{t}} = \frac{\theta_{m+1,n} - \theta_{m,n}}{\Delta \tilde{t}} \quad (6\text{-}91)$$

From this point on only the equations for the nonlinear solution are presented, the linear equation follow from similar considerations. After replacing all of the derivatives in (6-84) by their central difference analogs, (6-89) to (6-91), the following set of difference equations is obtained

179

$$\frac{\theta_{m+1,n} - \theta_{m,n}}{\Delta \tilde{t}} + (R_{m+1/2} Z'_n - Z''_n) \frac{1}{4\Delta Z} (\theta_{Z_{m,n}} + \theta_{m+1,n+1} - \theta_{m+1,n-1}) -$$

$$\frac{Z'^2_n}{2\Delta Z^2} (\theta_{ZZ_{m,n}} + \theta_{m+1,n+1} - 2\theta_{m+1,n} + \theta_{m+1,n-1}) = 0 \qquad (6\text{-}92)$$

$$n = 2,3,\ldots N\text{-}1 \qquad \begin{array}{l} 1 = \text{surface} \\ N = \text{backwall} \end{array}$$

where:

$$\theta_{Z_{m,n}} = \theta_{m,n+1} - \theta_{m,n-1}$$

$$\qquad (6\text{-}93)$$

$$\theta_{ZZ_{m,n}} = \theta_{m,n+1} - 2\theta_{m,n} + \theta_{m,n-1}$$

after collecting terms (6-92) can be written in the condensed form

$$A_n \, \theta_{m+1,n-1} + B_n \, \theta_{m+1,n} + C_n \, \theta_{m+1,n+1} = D_n \qquad n = 2\ldots N\text{-}1 \quad (6\text{-}94)$$

where

$$A_n = -(b_n + e_n) \qquad B_n = 1 + 2e_n \qquad C_n = b_n - e_n$$

$$D_n = \theta_{m,n} - b_n \, \theta_{Z_{m,n}} + e_n \, \theta_{ZZ_{m,n}} \qquad\qquad (6\text{-}95)$$

$$b_n = (R_{m+1/2} \, Z'_n - Z''_n) \frac{\Delta \tilde{t}}{4\Delta Z} \qquad e_n = \frac{Z'^2_n \Delta \tilde{t}}{2\Delta Z^2}$$

Once the boundary conditions have been applied, (6-94) yields a set of N-2, tri-diagonal, linear algebraic equations, which may be efficiently solved using a simple Gaussian elimination algorithm. To reduce equations (6-94) to tridiagonal form the boundary conditions at Z=0 and Z=1 must be used to evaluate the terms

$$A_2 \, \theta_{m+1,1} \text{ and } C_{N-1} \, \theta_{m+1,N} \qquad\qquad (6\text{-}96)$$

The backwall boundary condition (6-86) gives $\theta_{m+1, N}=0$. The surface boundary condition is nonlinear and may be treated in numerous ways. The method currently being used iteratively selects values for $\theta_{m+1, 1}$ until the derivative at the surface given by (6-87) is equal to the calculated derivative, to within a specified tolerance. The calculated surface derivative is evaluated using a four point formula

$$\frac{\partial \theta}{\partial Z}\bigg|_{Z=0} = \frac{(-11\theta_{m+1, 1} + 18\theta_{m+1, 2} - 9\theta_{m+1, 3} + 2\theta_{m+1, 4})}{6 \Delta Z} \qquad (6-97)$$

The solution to the set of equations, (6-94), provides values for the nondimensional temperature, θ, at each mesh point. The temperature at the surface, $\theta_s = \theta_1$, together with the local pressure, determine the burning rate through (5-30). The transient flame temperature is then obtained from (5-37).

The solution procedure, as given, assumes that the local pressure at the burning surface is known. In reality, however, the local pressure depends on the burning rate. In order to avoid a simultaneous, iterative, solution of the combined flow and burning rate equations, the equations of motion are solved using burning rate values obtained by linear extrapolation from previously calculated values. The pressure can then be assumed to be known, as required by the above analysis. This procedure for uncoupling the burning rate calculation from the fluid mechanics appears to work satisfactorily.

Burning Rate Interpolation

As discussed in Section 5, transient burning rate solutions are not obtained at each mesh point. Instead, within each burning region, burn rate solutions are calculated only at every n th mesh point. The burning rates at intermediate mesh points are found by interpolation. This procedure was instituted in order to economize on the amount of computer time devoted to solving the heat conduction equation. If burning rate solutions were obtained at each x location, every time step, the total computation time for these solutions would be more than ten times that required to solve the equations of motion. By using high order methods the error made in the interpolation procedure can be kept within quite reasonable bounds.

The waveform of the burning rate in the chamber tends to be smooth and harmonic, since the burning surface does not respond instantaneously to disturbances. The burning rate response to the fundamental pressure mode generates axial burning rate waveforms which typically vary as $\cos(\pi x)$. In order to obtain quantitative estimates of the error introduced by the interpolation procedure a short study was carried out. Three different interpolation methods were investigated:

1. Linear interpolation
2. Five point overlapping parabolic interpolation
3. Overlapping spline fit coupled with cubic interpolation

For equally spaced points method (1) is first order, method (2) third order and method (3) fourth order. The results of a comparison of the three methods applied to the curve $y = .1\cos(\pi x)$ are briefly summarized in the following table.

Method	Number of points at which function was specified		
	26	13	7
	Approximate Average Relative Error in %		
Linear	.2	.75	3.0
Aver. Parab.	6×10^{-4}	.015	.3
Spline-Cubic	6×10^{-5}	.002	.2

The exact value of the function was specified at either 26, 13, or 7 points. Each method was then used to find the value of the function at 51 equally spaced points. The relative percentage error at each point was then computed. The average errors shown in the table are approximate, but are adequate for qualitative purposes. It is evident from the table that the higher order methods as expected, are considerably more accurate than linear interpolation. It is also evident that when high order methods are used the spacing between burning rate solutions can be relatively large. The results indicate that if burning rate solutions are obtained at every seventh mesh point, the resulting interpolation need not generate errors of more than a few tenths of a percent. The accuracy of the finite difference solutions to the equations of motion and heat conduction equation, with the normal range of step sizes, is typically of the same order. Thus, the interpolation procedure can

reduce the computation time for the burning rate solutions by a factor of five, or more, without significantly affecting the overall accuracy of the total instability solution. The second method, 5 point averaged parabolic interpolation, is the one currently utilized.

9. REFERENCES

1. Levine, Jay N. and Culick F. E. C., "Numerical Analysis of Nonlinear Longitudinal Combustion Instability In Metalized Propellant Solid Rocket Motors, Vol. 1 Analysis and Results" AFRPL Technical Report TR-72-88, July 1972.

   or

   Levine, Jay N. and Culick, F. E. C., "Numerical Analysis of Nonlinear Longitudinal Combustion Instability In Metalized Propellant Solid Rocket Motors" 9th JANNAF Combustion Meeting, Vol. 1, Naval Postgraduate school, Monterey, California, September 1972, CPIA Pub. 231.

2. Kooker, D. E., "Numerical Solution of Axial-Mode Instability Problems In Solid Propellant Rocket Motors", BRL Contract Report No. 141, March 1974.

   or

   Kooker, D. E., and Zinn, B. T., "Numerical Solution of Axial Instabilities In Solid Propellant Rocket Motors" 10th JANNAF Combustion Meeting Vol. 1, Naval War College, Newport R.I., Aug. 1973, CPIA pub. 243.

3. Culick, F. E. C., "Nonlinear Behavior of Acoustic Waves In Combustion Chambers" 10th JANNAF Combustion Meeting, Vol. 1, Naval War College, Newport, R.I., August 1973, CPIA pub. 243.

4. Culick, F. E. C. and Levine, J. N., "Comparison of Approximate and Numerical Analyses of Nonlinear Combustion Instability" AIAA 12th Aerospace Sciences Meeting, Washington, D. C., Jan. 197 , AIAA paper No. 74-201.

5. Price, E. W. "Comments on Role of Aluminum in Suppressing Instability in Solid Propellant Rocket Motors", AIAA j., Vol. 9, No. 5, (May 1971), pp. 987-990.

6. Rudinger, G., "Effective Drag Coefficients for Gas-Particle Flow in Shock Tubes" Project Squid Technical Report CAL-97-PU, March 1969.

7. Carlson, D. J. and Hoglund, R. F., "Particle Drag and Heat Transfer in Rocket Nozzles", AIAA J., Vol. 2, Nov. 1964, pp. 1980-84.

8. Glauz, R. D. "Combined Subsonic-Supersonic Gas-Particle Flow", ARS Propellants Combustion and Liquid Rockets Conference, April 1961, Paper No. 1717-61.

9. Culick, F. E. C., "A Review of Calculations for the Unsteady Burning of a solid Propellant", AIAA J., Vol. 6, No. 12 (Dec. 1968) pp. 2241-2255.

10. Friedly, J. C., and Peterson, E. E., "Influence of Combustion Parameters on Instability in Solid Propellant Motors. Part II, Nonlinear Analysis", AIAA J. Vol. 4, No. 11 (Nov. 1966) pp. 1932-1937.

11. Brown, R. H., and Muzzy, R. J., "Linear and Nonlinear Pressure Coupled Combustion Instability of Solid Propellants", AIAA J. Vol. 8, No. 8 (August 1970) pp. 1492-1500.

12. Novozhilov, B. V., "Nonlinear Oscillations of Combustion Velocity of Powder", Soviet Journal of Applied Mechanics and Technical Physics, Vol. 7, No. 5, (May 1966) pp. 31-41.

13. Krier, H., et al, "Nonsteady Burning Phenomenon of Solid Propellants: Theroy and Experiment", AIAA J. Vol. 6, No. 2 (Feb. 1968) pp. 278-285.

14. Levine, J. N. and Culick, F. E. C. "Nonlinear Longitudinal Combustion Instability in Solid Rocket Motors", 10th JANNAF Combustion Meeting, Vol. 1, Naval War College, Newport, R.I., August 1973, CPIA pub. 243.

15. Kooker, D. E., and Zinn, B. T., "Triggering Axial Instabilities in Solid Rockets: Numerical Predictions", AIAA/SAE 9th Propulsion Joint Specialists Meeting, Las Vegas, Nevada, (Nov. 1973), AIAA Paper No. 73-1298. (also see Ref. 2)

16. Hart., R. W., Bird, J. F., and McClure, F. T., "The Influence of Erosive Burning on Acoustic Instability in Solid Propellant Rocket Motors", Progress in Astronautics and Rocketry, Vol. 1, Solid Propellant Rocket Research (Academic Press, N.Y., 1960) pp. 423-499.

17. McClure, F. Tl, Bird, J. R., and Hart, R. W., "Erosive Mechanism for Nonlinear Instability in the Axial Mode of Solid Propellant Rocket Motors", ARS J., Vol. 32, No. 3 (Mar. 1962) pp. 274-378.

18. Bird, J. F., Hart, R. W., and McClure, F. T., "Finite Acoustic Oscillations and Erosive Burning in Solid Fuel Rockets", AIAA J., Vol. 3, No. 12 (Dec. 1965) pp. 2248-2256.

19. Price, E. W., and Dehority, G. L., "Velocity Coupled Axial Mode Combustion Instability in Solid Propellant Rocket Motors", Proceedings of the 2nd ICRPG/AIAA Solid Propulsion Meetin, Anaheim, California (1967) pp. 213-227.

20. Culick, F. E. C., "Stability of Longitudinal Oscillations With Pressure and Velocity Coupling in a Solid Propellant Rocket", Combustion Science and Technology, Vol. 2, No. 4 (1970), pp. 179-201.

21. Gary, J. "On Certain Finite Difference Schemes For Hyperbolic Systems", Math. Comp., Vol. 18, pp. 1-18.

22. Gourlay, A. R. and Morris, J. L., "Finite Difference Methods For Nonlinear Hyperbolic Systems", Math. Comp. Vol. 22, (1968), pp. 28-39.

23. Masson, B. S., "A Study of Implicit Finite Difference Techniques For Compressible Viscous Flow", Ultrasystems, Inc., Report No. SN262, Jan. 1973.

24. Courant, RJ, Friedrichs, K. O. and Lewy, H. L., "Ueber die Partiellen Differenzgleichungen der Mathematischen Physick", Math. Ann., Vol. 100, pp. 32-74 (1928).

25. Mac Cormack, R. W., "The Effect of Viscosity in Hypervelocity Impact Cratering", AIAA paper No. 69-354.

26. Lax, P., and Wendroff, B., Comm. Pure Appl. Math 13, 217-237, (1960)

27. Rubin, E. L. and Burstein, S. Z., "Difference Methods for the Inviscid and Viscous Equations of a Compressible Gas", PIBAL Report No. 989, June 1967.

                                        or

     Rubin, E. L., and Burstein, S. Z. Journal of Computational Physics, Vol. 2, (1967), pp. 178-96.

28. Richtmyer, R. D. and Morton K. W., Difference Methods for Initial Value Problems, Second ed., Interscience Publishers, Inc., (1967).

29. Moretti, G., "A Critical Analysis of Numerical Techniques: The Piston-Driven Inviscid Flow", PIBAL Report No. 69-25, Polytechnic Institute of Brooklyn (July 1969).

30. Boris, J. P., "A Fluid Transport Algorithm That Works", NRL Memorandum Report #2357, Nov. (1971).

31. Tyson, T. J. and Kliegel, J. R., "An Implicit Integration Procedure For Chemical Kinetics", AIAA Paper No. 68-180, Jan. 1968.

32. Abbett, M. J., "Boundary Condition Calculations Procedures for Inviscid Supersonic Flow Fields", AIAA Computational Fluid Dynamics Conference, Palm Springs, California, (July 1973).

33. Michell, P. L., Aerojet General Solid Propulsion Company
                                (Private Communication)

34. Kliegel, J.R., "Gas Particle Nozzle Flows" Ninth Symposium On Combustion, The Combustion Institute, Pittsburg, Pa. pp. 811-826 (1963).

NOMENCLATURE

A	–	cross section area, or transient burning rate parameter
A_e	–	area at nozzle entrance
A_t	–	throat area
a	–	gas only, sound speed
a_t	–	sound speed based on P_f and T_f
B	–	transient burning rate parameter, Eq. (5-49)
B_s	–	constant in Arrhenius pyrolysis law, Eq. (5-16)
c	–	ratio of particle to gas specific heats, c_m/c_p
$\tilde{c}$	–	constant in steady state burn rate, Eq. (2-14)
c_d	–	particle drag coefficient
c_k	–	erosive burning constant, Eq. (2-14)
c_m	–	specific heat of metal oxide
c_p	–	specific heat of gas at constant pressure
c_s	–	specific heat of solid propellant
D_i	–	diameter of the i th particle group
D_p	–	port diameter
E	–	normalized surface activation energy, $E_s/R_o T_s$, also used differently in Eq. (3-19)
E_s	–	activation energy of surface reactions
F	–	conserved quantities, Eq. (6-3)
F_{p_i}	–	particle-gas interaction force per unit volume, for the i th particle group, Eq. (2-18)
G	–	conserved quantities, Eq. (6-4)
H	–	nondimensional surface heat release parameter, Eq. (5-28)
Δh_{f_o}	–	heat of formation at $0^o K$
h	–	enthalpy
K	–	fractional lag constant
k	–	thermal conductivity
L	–	reference length
ℓ	–	perimeter of the grain
M	–	mach number
$\overline{M}$	–	mach number of "equivalent" perfect gas

M_e	–	mach number at nozzle entrance
m	–	mass flux from burning surface
$\dot{m}_e$	–	mass flux from uninhibited end burning faces
N	–	number of particle groups
Nu	–	Nusselt number
n	–	pressure exponent in steady state burn rate law
n_s	–	exponent of pressure dependence of surface reaction rate, Eq. (5-16)
P	–	pressure
$\underline{P}$	–	nondimensional pressure, Eq. (5-22)
P_f	–	chamber pressure
P_{ref}	–	reference pressure in steady state burn rate law
Pr	–	Prandtl number
Q_f	–	heat release, per unit mass, in flame
Q_{p_i}	–	particle gas heat transfer rate per unit volume, for the i th particle group
Q_s	–	net heat of reaction for processes at burning surface, Eq. (5-5)
$\overline{Q}_s$	–	surface heat of reaction at $\overline{T}_s$, Eq. (5-6)
R	–	gas constant
R_o	–	universal gas constant
Re_i	–	Reynolds number for the i th particle group, based on particle diameter, and particle gas relative velocity
RHS	–	right hand side of characteristic compatibility relations
r	–	linear burn rate
S_b	–	total area of burning surface
s	–	equal to ± 1
T	–	temperature
T_f	–	flame temperature of the propellant
T_o	–	reference temperature in viscosity law
T_s	–	temperature at the propellant surface
T_∞	–	backwall temperature of the propellant
t	–	time

$\tilde{t}$	–	nondimensional time, Eq. (5-22)
u	–	velocity
u_s	–	velocity of the combustion products as they enter the main flow
$u_{s_{11}}$	–	axial component of u_s
w	–	gas reaction rate times gas density
x	–	axial distance
x_0	–	location of head end
x_p	–	axial location at which initial perturbation terminates
z	–	transformed depth coordinate in heat transfer solution, Eq. (6-80), also terms in conservative equations, Eq. (6-5)
α	–	growth constant, also used as a constant in coordinate transformation, Eq. (6-80)
α_p	–	particle damping constant
β	–	total particle to gas weight flow ratio, $\epsilon \beta_i$
β_i	–	particle to gas weight flow ratio of i th particle group
γ	–	gas only isentropic exponent
$\bar{\gamma}$	–	isentropic exponent for "equivalent" perfect gas, Eq. (3-17)
θ	–	angle with respect to axial direction, or nondimensional temperature, Eq. (5-22)
κ	–	thermal diffusivity
λ	–	defined by Eq. (5-48)
μ	–	viscosity
ξ	–	nondimensional depth coordinate, $\bar{r}x/\kappa$
ρ	–	density
τ_v	–	characteristic relaxation time for particle velocity, Eq. (6-21)
τ_T	–	characteristic relaxation time for particle temperature, (Eq. 6-22)
Ω	–	nondimensional frequency, $\omega\kappa/\bar{r}^2$
ω	–	mass burning rate, per unit length, per unit cross sectional area
ω_μ	–	power in viscosity vs temperature law

Subscripts

f   –   flame

g   –   gas

p_i –   i th particle group

s   –   at the burning surface

t   –   at the nozzle throat

Superscripts

$(\ )^*$ –   denotes a dimensional variable

$(\ )'$ –   denotes a small perturbation

$\overline{(\ )}$ –   denotes steady state value, except in Sections 3 and 4 where used to denote equivalent gas value

$(\ )^+$ –   right running characteristic

$(\ )^-$ –   left running characteristic

$(\ )^{(r)}$ –   real part of

APPENDIX II

APPENDIX 2

The one-dimensional, Eulerian form of the equations of gas dynamics for an inviscid, non-heat conducting fluid in cartesian coordinates may be written in the following conservative vectorized form:

$$U_t + F(U)_x = 0,$$

$$U = \begin{pmatrix} \rho \\ m \\ e \end{pmatrix} \quad \text{and} \quad F(U) = \begin{bmatrix} m \\ (m^2/\rho) + p \\ (m/\rho)(e + p) \end{bmatrix} \tag{1}$$

where e, the energy per unit volume is $\qquad e = \rho\varepsilon + \tfrac{1}{2}\rho u^2,$

and ε, the internal energy per unit mass, is $\qquad \varepsilon = \dfrac{p}{(\gamma-1)\rho}$

Equation (1) is solved using the Lax-Wendroff + Hybrid + Artificial Compression Combination Scheme. The first step in the solution is the application of the standard Lax-Wendroff predictor.

$$\underline{u}_{i+\frac{1}{2}}^{n+\frac{1}{2}} = \tfrac{1}{2}(\underline{U}_{i+1}^{n} + \underline{U}_{i}^{n} - \frac{\Delta t}{2\Delta x}(\underline{F}_{i+1}^{n} - \underline{F}_{i}^{n})) \tag{2}$$

The corrector step is the standard Lax-Wendroff operator hybridized with a first order scheme, as follows;

$$\underline{u}_i^{n+1} = \underline{U}_i^{n} - \frac{\Delta t}{\Delta x}(\underline{F}_{i+\frac{1}{2}}^{n+\frac{1}{2}} - \underline{F}_{i-\frac{1}{2}}^{n+\frac{1}{2}}) + \frac{1}{8}\left[\theta_{i+\frac{1}{2}}^{n}(\underline{u}_{i+1}^{n} - \underline{u}_{i}^{n}) - \theta_{i-\frac{1}{2}}^{n}(\underline{u}_{i}^{n} - \underline{u}_{i-1}^{n})\right] \tag{3}$$

The last term in equation (3) is the correction term that reduces the second order Lax-Wendroff scheme to first order in the neighborhood of admissible discontinuities. The switch, θ, was chosen here to be based on density gradients and is defined by;

$$\theta_{i+\frac{1}{2}}^{n} = \max(\hat{\theta}_i, \hat{\theta}_{i+1}) \tag{4}$$

where $\hat{\theta}_i = \left\{ \begin{array}{ll} \left| \dfrac{|\Lambda_{i+\frac{1}{2}}| - |\Lambda_{i-\frac{1}{2}}|}{|\Lambda_{i+\frac{1}{2}}| + |\Lambda_{i-\frac{1}{2}}|} \right|, & \text{for } |\Lambda_{i+\frac{1}{2}}| + |\Lambda_{i-\frac{1}{2}}| > 0 \\ \\ 0 & , \text{ otherwise} \end{array} \right\}$

and $\quad \Lambda_{i+\frac{1}{2}} = \rho_{i+1} - \rho_i$

The concept of artificial compression is then utilized to restore the high frequency content that has been diminished by the first order accurate Hybrid scheme. The difference representation g_i of the artificial compression flux g, is $\underline{g}_i = \alpha_i \underline{\Delta}_i$,

where $\quad \underline{\Delta}_i = \underline{\tilde{u}}_{i+1} - \underline{\tilde{u}}_{i-1}$

and
$$\alpha_i = \max \left\{ 0, \min_k \left[\frac{\min \left(|\delta_{i+\frac{1}{2}}^k|, \delta_{i-\frac{1}{2}}^k \cdot \text{sgn} \left(\delta_{i+\frac{1}{2}}^k \right) \right)}{|\delta_{i+\frac{1}{2}}^k| + |\delta_{i-\frac{1}{2}}^k|} \right] \right\} \tag{5}$$

where k refers to the kth component of the $\underline{\tilde{u}}$ (i.e., ρ, m or e) $\delta_{i+\frac{1}{2}}^k = \tilde{u}_{i+1}^{(k)} - \tilde{u}_i^{(k)}$. Let $\underline{S}_{i+\frac{1}{2}}$ represent the vector whose kth component is $\text{sgn}(\delta_{i+\frac{1}{2}}^k)$. Then the difference scheme which applies the ACM to the given solution $\underline{\tilde{u}}_i^{n+1}$ is:

$$\underline{u}_i^{n+1} = \underline{\tilde{u}}^{n+1} - \frac{\Delta t}{2\Delta x} (\underline{g}_{i+1} - \underline{g}_{i-1})$$

$$+ \frac{\Delta t}{2\Delta x} (|\underline{g}_{i+1} - \underline{g}_i| \underline{S}_{i+\frac{1}{2}} - |\underline{g}_i - \underline{g}_{i-1}| \underline{S}_{i-\frac{1}{2}}) \tag{6}$$

$$= \underline{\tilde{u}}_i^{n+1} - \frac{\Delta t}{2\Delta x} (\underline{G}_{i+\frac{1}{2}}^n - \underline{G}_{i-\frac{1}{2}}^n),$$

where $\underline{G}_{i+\frac{1}{2}}^n = \underline{g}_i^n - \underline{g}_{i+1}^n - |\underline{g}_{i+1}^n - \underline{g}_i^n| \underline{S}_{i+\frac{1}{2}}$,

Since the Artificial Compression method must not be used in smooth regions, the switch value is used again to limit the operation of the ACM corrector to the areas of admissible discontinuities only. Thus, the final stage in the computation is:

$$\underline{u}_i^{n+1} = \underline{\tilde{u}}_i^{n+1} - \frac{\Delta t}{2\Delta x} (\theta_{i+\frac{1}{2}}^n \underline{G}_{i+\frac{1}{2}}^n - \theta_{i-\frac{1}{2}}^n \underline{G}_{i-\frac{1}{2}}^n) \tag{7}$$

PART 2:

APPLICATION OF THE DEVELOPED NONLINEAR INSTABILITY ANALYSIS TO THE
STUDY OF PULSE TRIGGERED INSTABILITY IN SOLID ROCKET MOTORS

CHAPTER I

INTRODUCTION

 ...linear axial mode instabilities in solid propellant rocket motors can be
 ...ted by random finite amplitude events such as the expulsion of an igniter or
 ...lation fragment through the nozzle. Such instabilities are usually characterized by
 ...e amplitude oscillations having steep-fronted, shock-like waveforms and are often
 ...ompanied by significant increases in mean chamber pressure. When instability is
 ...tiated in this manner in a motor that is otherwise linearly stable (i.e., stable to
 ...nitesimal disturbances), it is said to be a "triggered" instability. The existence of
 ...gered instabilities is a direct result of the amplitude dependence of the acoustic
 ...rgy gain or loss mechanisms in a solid rocket motor, e.g., pressure and velocity
 ...pled driving, nozzle and particle damping, acoustic mean flow interactions, etc.
 ...is amplitude dependence also accounts for the formation of limit cycles in which the
 ...l gains and losses are balanced. Triggering of instabilities in solid rocket motors by
 ...tural finite amplitude pulses suggests that artificial laboratory pulsers can be used to
 ...vestigate this phenomenon.

 To help assure the stability of production tactical motors, the Air Force has,
 ...efore, recently been requiring that contractors pulse prototype motors during
 ...velopment. If done properly, the pulse testing of solid rocket motors should virtually
 ...liminate the unexpected occurrence of instability in solid rocket motors. However,
 ...he use of pulses that are too strong, or pulses that do not simulate natural pulsing
 ...enomena, could easily result in the unjustified expenditure of resources to solve a
 ...oblem that, in reality, did not exist. Alternatively, tests utilizing pulses that are
 ...dvertently too weak might be no better than not testing at all. Thus, there is a need

for rational pulsing guidelines directly related to the natural self-pulsing characteristics of solid rocket motors.

The concept of evaluating motor stability by pulsing has been utilized in the past to test both liquid[1] and solid propellant rocket motors.[2-6] It has been demonstrated many times that a given linearly stable motor design can be pulsed into instability. However, the physical mechanisms responsible for the pulse initiation of nonlinear instability are not yet fully understood. The influence of all of the pulse characteristics (amplitude and frequency content of the pressure and velocity waveforms) on triggering is also not completely understood at this time. The importance of properly describing the pressure and the velocity waveforms of the pulse were demonstrated theoretically in Chapter 3 of Part I, wherein dramatically different motor responses were obtained for standing and traveling pulse type disturbances. Therefore, a complete study of pulsing phenomena must include not only the characterization of the waveforms induced by both natural pulses and pulse generating devices, but also an investigation of the response of the motor to various types of pulses. With this information, it should be possible to design pulse units that will simulate the triggering potential of natural pulsing mechanisms such as ejection of inert materials through the nozzle.

A previous investigation of pulsing criteria for solid rocket motors[6] yielded a semi-empirical model that was limited to predicting the maximum initial pressure amplitude of the pulse. No attempt was made to predict the pulse waveform and pulse velocity or to couple this model with a stability analysis of the motor itself. This investigation is the first attempt to predict, a priori, all of the pulse characteristics generated by several types of laboratory pulser units. Moreover, this investigation is the first attempt to combine the pulser performance models with a nonlinear combustion instability analysis of the motor.

The development of ballistic models for three different pulsers (pyrotechnic, piston, and reduced brisance) was the first step in the overall model development[7]. Ballistic analysis of the pulser designs provides the mass and energy fluxes that are injected into the motor. A nonlinear combustion instability program[8] (described in Appendix I of Part I of this report) that solves the partial differential equations that govern the associated flow and combustion in solid propellant rocket motors was then modified to model the effect of fore-end pulsing based on the mass and energy flux data provided by the pulser ballistic analysis. Combining these models allows a priori predictions of both the injected pulse and the combustion response to this pulse to be performed.

In order to examine the validity of the pulse prediction models, experiments were conducted in which closed tubes filled with cold nitrogen and helium and motors filled with hot combustion products were pulsed by the three different pulsers. Predicted and measured pulse amplitudes and waveforms were then compared. The pulser performance models, the modifications made to couple these models to the chamber analysis, and a comparison of predicted and experimentally measured pulse waveforms are reported in Chapter 2.

The ability of the overall pulser and nonlinear stability model to quantitatively predict actual pulse-triggered solid rocket motor instability data for both laboratory and full-scale rocket motors is evaluated in Chapter 3. The ability of the present analysis to a priori predict the nonlinear stability of motors is inhibited by deficiencies in existing pressure and velocity coupling combustion response models (as described in Chapter 5 of Part I). Modeling deficiencies are further exacerbated by the lack of accurate measured values for key propellant parameters such as surface temperature, activation energy and net heat release rate of the surface decomposition reaction, thermal diffusivity etc. Moreover, as pointed out previously[9], existing velocity

coupling models, including the present ad hoc model, are not based on an understanding of the fundamental physical mechanisms. Given the present state of combustion response modeling, the key issues to be addressed in this investigation were: the ability of the overall model to predict the relative nonlinear stability of motor/propellant combinations as a function of grain geometry, operating conditions, and pulse amplitudes (for a fixed propellant formulation); and the ability of the model to predict all of the nonlinear characteristics observed in motor firing data. The first issue was addressed by comparing predictions and measured data for a series of laboratory scale motor firings. The second issue was addressed by comparing predictions and data for both Laboratory and full scale motor firings. Comparisons of theoretical predictions with experimental data for a series of laboratory scale tests and for two full scale motor tests are presented in Chapter 3.

The pyrotechnic, piston and reduced brisance pulsers that were mentioned previously have been designed to facilitate laboratory investigations of nonlinear instability and they all share the common feature of inducing disturbances by discharging gaseous combustion products (at a controlled rate) into the motor combustion chamber. However, the point of discharge is usually the fore-end of the motor, as opposed to the aft-end point of origination for naturally induced nozzle ejecta pulses. Thus, a second study designed to simulate naturally induced nozzle ejecta pulses was conducted.

The present ejecta pulsing study, described in Chapter 4, involves both experiments and the development of models designed to simulate ejection of combustion chamber material through the nozzle. Pulse tests were conducted in which spheres of different densities and sizes were ejected at the head end. The test data was used to identify the characteristics of oscillations resulting from nozzle ejecta and their

capability to initiate sustained pressure oscillation in a solid rocket combustion chamber. The test data was also used to examine the validity of the concurrently developed models.

The modeling work consisted of several parts. First, a simplified model was developed to calculate the motion of an ejecta through the nozzle[10]. Two methods for predicting the resulting pulse amplitude were then developed. A semi-empirical method (based on a linearized analysis) that predicts the amplitude of ejecta induced pulses at the nozzle entrance, was developed. The second approach utilized the existing nonlinear combustion instability model described in Part 1 of this report, modified to accept a time dependent Mach number boundary condition at the nozzle entrance, as determined from the calculated throat constriction time history. Comparisons of predictions obtained utilizing the first model and the measured initial pulse amplitudes are presented in Chapter 3. Finally, it is shown that the modified nonlinear instability analysis is capable of accurately predicting the initial pulse amplitude and the motor response to pulsing, as observed in waveform evolution, growth rate and mean chamber pressure.

CHAPTER 2

MODELING AND COLD FLOW TESTING

PULSER PERFORMANCE MODELS

Three different types of laboratory pulsers were employed in the present study: the pyro, piston, and low brisance pulsers. Only a brief overview of their design and operation is given here. Further details are given in Ref. 7.

Pyrotechnic Pulser

A schematic of the pyro pulser is shown in Fig. 1. A squib initiator ignites a pyrotechnic charge (Red Dot double base powder) in the combustion chamber. The gaseous combustion products increase the pressure in the chamber to the rupture pressure of the burst diaphragm. As the diaphragm bursts, the combustion products plus a fraction of the remaining unburned pyrotechnic charge expand into the pulser barrel and are then vented into the chamber. A typical pressure history obtained with the pyro pulser is shown in Fig. 2. With this pulser the mass and energy flux rates reach a maximum value in a fraction of a millisecond after the diaphragm bursts and then decay in an approximately exponential manner as the combustion products are vented into the chamber. The pulser is typically designed to provide a vent time of approximately 20% of the period of the fundamental acoustic mode of the chamber. By varying the design of the pulser, it is possible to control the venting time. The main features of the pulse produced by this pyro pulser are a very fast rise in the pressure and mass flow rate up to a predetermined maximum value followed by an exponential decay with a controllable decay rate.
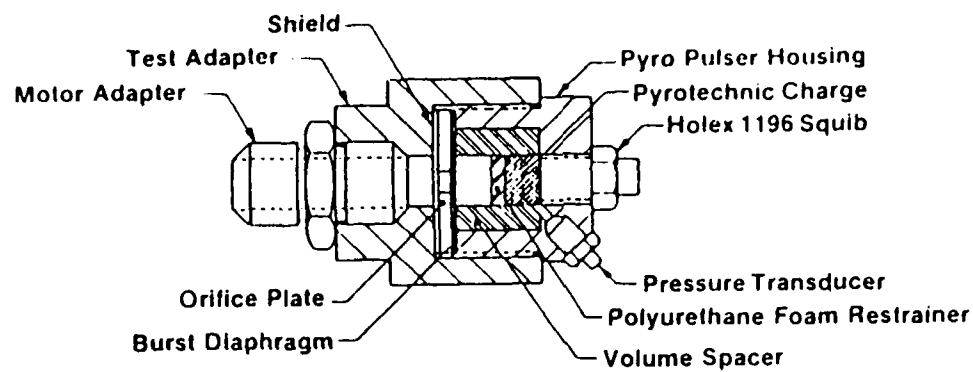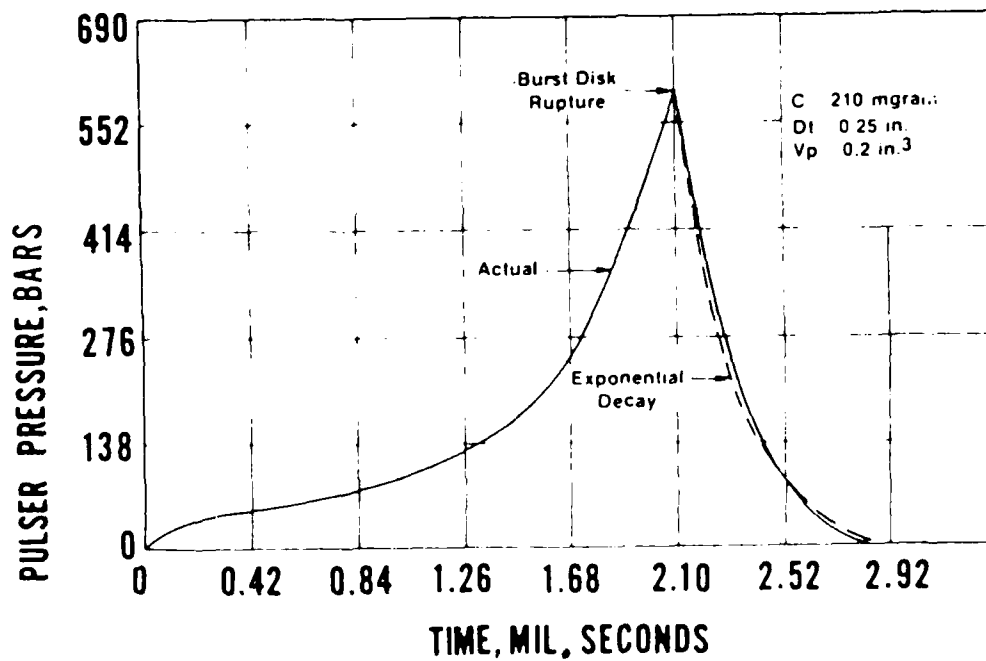
Fig. 1. Schematic of the pyro pulser unit.

Fig. 2. Pyro pulser pressure-time function.

Performance analysis of the pyro pulser is posed as a simple lumped volume venting problem, neglecting dynamic effects. The analysis is based on the solution of the bulk mass and energy balances as applied to the pulser combustion chamber. Since the pressure ratio across the vent is very high, the vent can be assumed to be choked during most of the injection period. The pulser model also assumes that the back pressure (chamber pressure) does not increase significantly. Thus, it is possible to uncouple the pulser ballistics from the chamber flowfield solution, even for the short time at the end of the injection during which the vent is not choked.

The conservation equations to be solved are[7]:

$$\text{Mass} \qquad \frac{dm}{dt} = \dot{m}_b - \dot{m}_o \qquad (1)$$

$$\text{Energy} \qquad \frac{dc_v Tm}{dt} = c_v T_o \dot{m}_b - c_p T \dot{m}_o \qquad (2)$$

The mass flow rate through the vent is:

$$\dot{m}_o = C_s C_d C_w A p / (T/T_o)^{1/2} \qquad (3)$$

Where

$$C_s = \begin{cases} K(p_c/p)^{1/\gamma} \left[1 - (p_c/p)^{\frac{\gamma-1}{\gamma}} \right]^{1/2}, & p_c/p > (\frac{2}{\gamma+1})^{\frac{\gamma}{\gamma-1}} \\ 1, & p_c/p < (\frac{2}{\gamma+1})^{\frac{\gamma}{\gamma-1}} \end{cases} \qquad (4)$$

$$K = \left(\frac{2}{\gamma-1}\right)^{1/2} \left(\frac{\gamma+1}{2}\right)^{\frac{\gamma+1}{2(\gamma-1)}} \qquad (5)$$

and

$$C_w = \left(\frac{g\gamma}{F}\right)^{1/2} \left(\frac{2}{\gamma+1}\right)^{\frac{\gamma+1}{2(\gamma-1)}} \qquad (6)$$

The coefficient C_s provides the mass flow reduction due to subsonic flow, while C_w is the sonic flow coefficient. Using the equation of state for a perfect gas, the mass and energy balances can be manipulated to form the following set of ordinary differential equations:

204

$$\frac{dT}{dt} = [FC\dot{s}(1-T/T_o) - (\gamma-1)(T/T_o)^{1/2} C_w' Ap]T/(pv/F) \qquad (7)$$

$$\frac{dp}{dt} = [FC\dot{s}-\gamma(T/T_o)^{1/2} C_w' Ap](F/v) \qquad (8)$$

Where

$$C_w' = C_s C_d C_w \qquad (9)$$

Solution of this set of equations with initial conditions (pressure, temperature, and fraction of charge consumed evaluated at the time the burst disc fails) yields the output mass flux m_o and energy flow rate $\dot{m}_o C_p T$. These values are utilized as fore-end boundary conditions for the chamber flow model.

Low Brisance Pulser

When pulsing solid propellant rocket motors for qualification purposes, simulation of natural motor pulsing phenomena is desirable. For this purpose, a pulser with longer rise and decay times that simulates ejection of inert material through the nozzle is desirable. Pulses with similar characteristics can be produced with ejecta pulsers[6] that eject inert plugs into the motor. Nevertheless, since it is not always possible to use ejecta pulsers with real motors, an alternative device called the low brisance pulser was developed. This device utilizes a variable vent area to increase the rise time of the pulse. A schematic of the low brisance pulser is shown in Fig. 3. Upon firing of the pyrotechnic charge and burst of the rupture disc, the pressure generated by the expanding combustion products acts on the piston base. The piston is driven back and the vent begins to open. As the piston traverses the vent opening, the mass flux into the motor increases exponentially from zero to a maximum value and then decays back to zero. A typical performance curve for the low brisance pulser is shown in Fig. 4. Both the mass injection rate and its rise time can be controlled by varying the
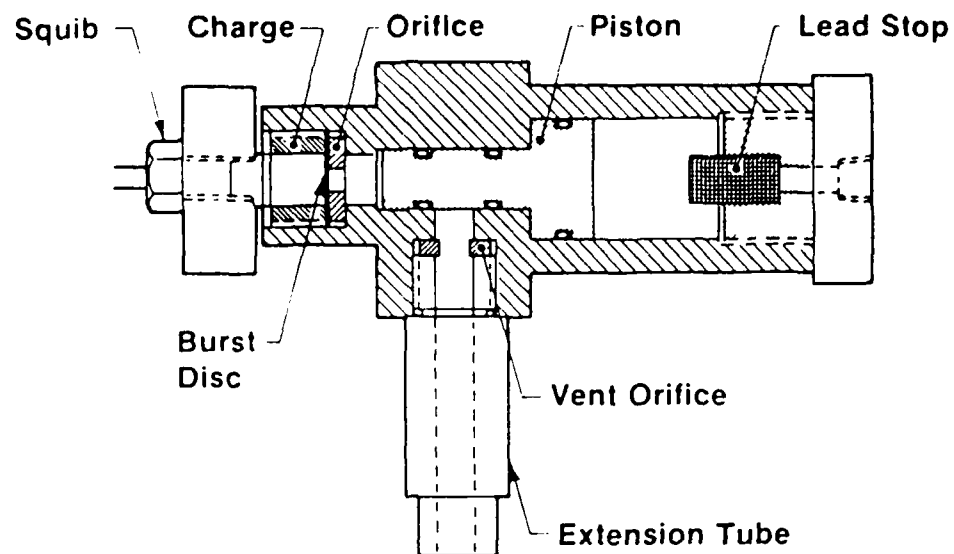
Fig. 3. Schematic of the low brisance unit.
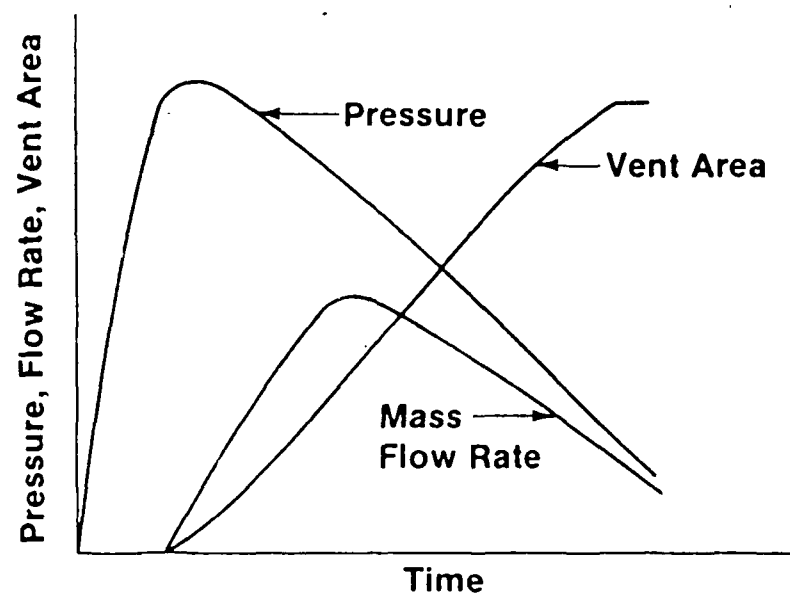
Fig. 4. Low brisance pressure-time function.

parameters which affect the piston velocity. Calculation of the mass and energy flow rates for this pulser design is based upon the bulk balance of mass and energy in the chamber and a force balance on the piston. Mass and energy conservation equations are given, respectively, as:

$$\frac{dm}{dt} = \dot{m}_i - \dot{m}_o \tag{10}$$

$$\frac{dc_v Tm}{dt} = c_p T_i \dot{m}_i - c_p T \dot{m}_o - pA_p u \tag{11}$$

The mass and energy flow rates into the breech, $\dot{m}_i$ and $\dot{m}_i c_p T_i$, are equal to the corresponding flow rates out of the charge holder. The ballistic performance of the charge holder is identical to that of the pyro pulser. The mass and energy flow rates out of the pulser (into the motor port), $\dot{m}_o$ and $\dot{m}_o c_p T$, depend on the amount of vent area exposed by the moving piston. The equation describing the mass flow rate through the vent is similar to the one obtained with the pyro pulser, but with an added multiplying factor, f_v which represents the fraction of the vent area uncovered by the moving piston.

$$\dot{m}_o = f_v C_s C_d C_w Ap/(T/T_o)^{1/2} \tag{12}$$

Let x_v be the distance the piston must travel before the edge of the vent is reached, x the distance traveled, and d_v the vent diameter. Then,

$$f_v = \begin{cases} 0, & x < x_v \\ 1/2 + (1/\pi)(y\sqrt{1-y^2} + \tan^{-1}(y/\sqrt{1-y^2})), & o < x - x_v < d_v \\ 1, & x - x_v > d_v \end{cases} \tag{13}$$

Where $y = ((x - x_v)/r_v) - 1.$ (14)

207

Manipulation of the mass and energy balances results in the following set of ordinary differential equations having pressure and temperature as dependent variables:

$$(v_o + A_p x)\frac{dp}{dt} = \gamma RT_i \dot{m}_i - \gamma \overline{RT}m_o - \gamma p A_p u \tag{15}$$

$$\frac{1}{T}\frac{dT}{dt} = (((\gamma T_i/T)-1)RT\dot{m}_i - (\gamma-1)RT\dot{m}_o -$$
$$(\gamma-1)pA_p u)/(p(v_o + A_p x)) \tag{16}$$

Piston Pulser

In order to allow for even more variation in the range of pulse characteristics available for motor test and research purposes, another type of pulser called the piston pulser was designed. A schematic of the piston pulser is shown in Fig. 5. After rupture of the burst diaphragm, the combustion gases and the unburned fraction of the charge enter the breech volume. As the pressure increases, the piston accelerates into the bore volume. The gases in the bore are compressed by the piston and are vented into the motor. An idealized performance curve for the piston pulser is shown in Fig. 6. In reality, the pressure decay from the maximum amplitude to chamber pressure is not a discontinuous jump, but rather a rapid decay. The reason being that when the piston stops, the venting of the gases left in the vent volume takes a finite amount of time. With the piston pulser the mass and energy flow rates increase exponentially with time and decay rapidly. This is in contrast to the exponential decay only that is observed with the pyro pulser, and the significantly (typically) slower rise and decay periods observed with the reduced brisance pulser. The piston pulser rise time and mass flow rate can be controlled by varying the breech charge or volume, the piston weight or stroke and the vent area. Since the volume of the piston pulser is in practice limited,
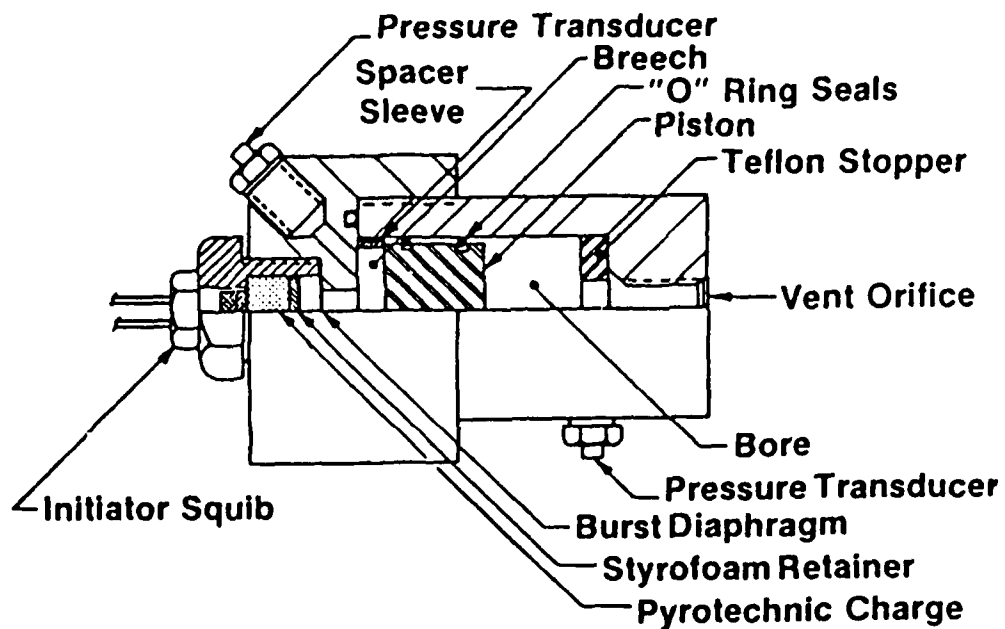
Fig. 5. Schematic of the piston pulser unit.
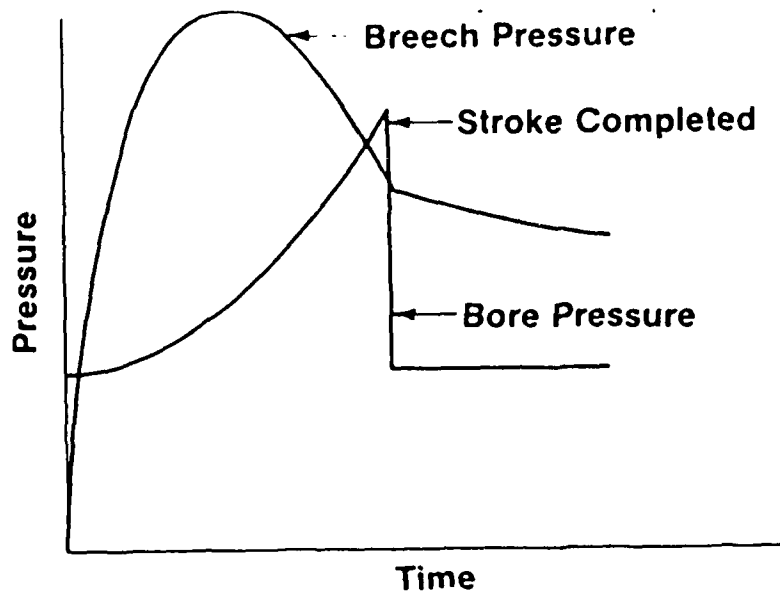
Fig. 6. Piston pulser pressure-time function.

the amount of mass that can be injected into a motor is relatively small. Thus, in order to produce relatively high amplitude pulses, the piston pulser must be designed with very short rise and decay times. This produces a very brisant blip-like pulse.

Mass and energy injection rates are evaluated from conservation of mass and energy and a force balance on the piston. Since mass is not expelled, the breech mass balance is trivial. Conservation of the energy in the breech is written as follows:

$$\frac{dc_v Tm}{dt} = c_v T_o \dot{m}_b - pA_p u \tag{17}$$

Conservation of mass and energy in the bore are written, correspondingly, as:

$$\frac{dm}{dt} = -\dot{m}_o \tag{18}$$

$$\frac{dc_v Tm}{dt} = p_b A_p u - c_p T_f \dot{m}_o \tag{19}$$

Finally, a force balance on the piston yields

$$m\frac{du}{dt} = A(p-p_b) \tag{20}$$

The initial pressure in the breech is the rupture pressure of the burst disc. Initial conditions in the bore are identical to the initial conditions in the chamber.

CHAMBER MODEL

As mentioned previously in the Introduction, a priori prediction of pulse characteristics and the combustion response to this pulse requires coupling of the pulser performance model to a chamber flowfield and combustion model. In order to achieve this coupling, an existing nonlinear combustion instability model that solves the partial differential equations that govern two-phase flow in variable cross-sectional area solid

propellant rocket motors (described in Part I of this report) was modified to accept the pulser mass and energy flow rates as boundary conditions.

The flow field created by injection of pulser gases into a motor resembles an under-expanded plume until such time when the gases (or the pressure waves created by injection) reach the walls of the chamber. The flow field is two-dimensional, and strong mixing will take place within a few orifice diameters downstream of the pulser exit. Rather than attempt to model this complex problem, the present work sought to determine if, by the use of judicious engineering approximations, a simple one-dimensional model of the problem could yield reasonably accurate and useful results.

When developing a one-dimensional model for the solution of this problem, one has to resolve the problem of specifying the boundary conditions at the fore-end and the problem of mixing between the pulser and chamber gases. Since the flow out of the pulser is supersonic (during most of the pulsing period with the pyro and low brisance pulsers and during the interval when most of the mass is expelled from the piston pulser), the flow variables at the pulser exit are completely dependent upon conditions inside the pulser. Nevertheless, most of the fore-end is a hard wall at which the gas axial velocity is zero. This head end velocity discontinuity cannot be treated properly with a one-dimensional model, so additional approximations had to be made. Since the pulser orifice is usually very small relative to the chamber diameter, and since the velocity difference between the injected pulser gases and the chamber gases is large, mixing should rapidly reduce the velocity of the gases to a subsonic level. Based on these considerations, the following simplified model was developed. During the pulsing period the pulser mass and energy flow rates, as predicted by the pulser performance models, are specified as boundary conditions. When the pulser flow stops, the boundary treatment reverts back to the normal treatment for a hard wall. Mixing per se was not

modeled, but its presence was implicitly accounted for by assuming that the pulser gases become subsonic in the process of instantaneously expanding to fill the head end of the chamber.

The equations representing this model are as follows:

Continuity $$\dot{m}_1 = \rho_1 \, u_1 \, A_1 \qquad (21)$$

Energy $$\dot{E}_1 = \dot{m}_1 \, (C_p T_1 + 1/2 \, u_1^2) \qquad (22)$$

State $$P_1 = \rho_1 \, RT_1 \qquad (23)$$

Characteristic Relation $$P_1 = P_1' + \rho_1' \, a_1' \, (u_1 - u_1') \qquad (24)$$

COMPARISON OF EXPERIMENTAL AND ANALYTICAL RESULTS

The experimental results presented in Figs. 7, 8, 10a, 11, and 13a were obtained by pulsing a closed cylindrical chamber having a length of 1.22 meters (48 inches) and an internal diameter of 0.077 meter (3.056 inches). The chamber was filled with nitrogen at room temperature pressurized to 0.689 MPa (100 psi) chamber pressure. By utilizing chambers filled with inert gases the characteristics of the different pulses and the resulting waveforms in the chamber can be better analyzed and understood since the complex interactions between the pulser induced waves and the propellant combustion are eliminated. In addition, by conducting experiments with an empty chamber, it is possible to obtain data at several axial locations. This results in a more complete description of the propagating wave which, in turn, enables better understanding of wave propagation, wave steepening, and viscous losses. In this series of tests, the chamber was instrumented with six high frequency pressure transducers

212

...unted on the sidewalls at 3, 6, 12, and 24 inches from the pulsed end and on both end ...osures. The pulser units were attached at the fore-end of the chamber.

Performance analyses of the pyro, low brisance, and piston pulsers yielded the temperature and mass flow rate curves that are shown in Figs. 7a through 7c, respectively. The data shown in these curves indicates that the pulser units performed as expected. The time evolution of the pressure oscillations (where time is nondimen- sionalized by multiplying dimensional time by the sound speed divided by the chamber length) initiated in the chamber by the pyro, low brisance, and piston pulsers are shown in Figs. 8, 10a, and 11, respectively. The very short rise and decay periods of the pulse initiated by the low brisance pulser (shown in Fig. 10a) is a result of the low back pressure (in the chamber) acting on the piston surface. Thus, in this case, the pulse and the resulting wave in the chamber are very similar to those generated by the pyro pulser. The wave is already fully shocked after propagating only three inches into the chamber. The pressure oscillations excited by the piston pulser (Fig. 11) feature a very fast rise and decay (similar to the pulse pressure and mass flux variation). The total mass injected by the piston pulser is small compared to the total mass in the chamber (about 0.3%). The relatively large amplitude of the resulting pressure oscillations in the chamber is due to the fact that most of the mass in the piston bore is injected into the chamber in a very short time.

Time evolution of pressure oscillations in the chamber, obtained by utilizing the predicted mass and energy flow rates as boundary conditions for the nonlinear combustion instability program, are shown in Figs. 9, 10b, and 12 for the pyro, low brisance and piston pulsers, respectively. Very good agreement between the measured and predicted waveforms (amplitude and shape) is demonstrated. Table I shows a comparison of the measured and predicted maximum pressure amplitude values at the

213
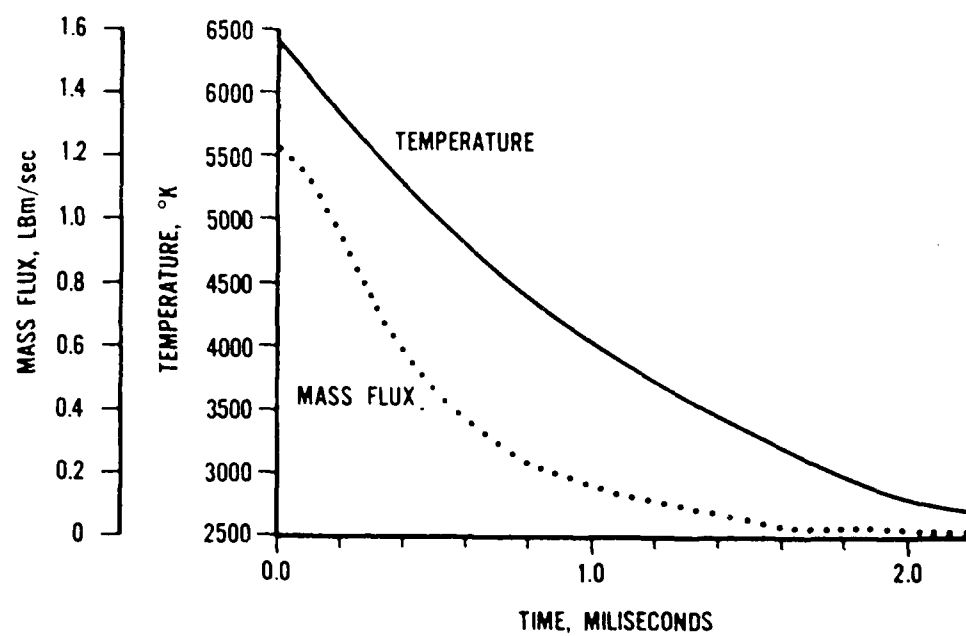
Fig. 7a.   Pyro pulser calculated performance.

214
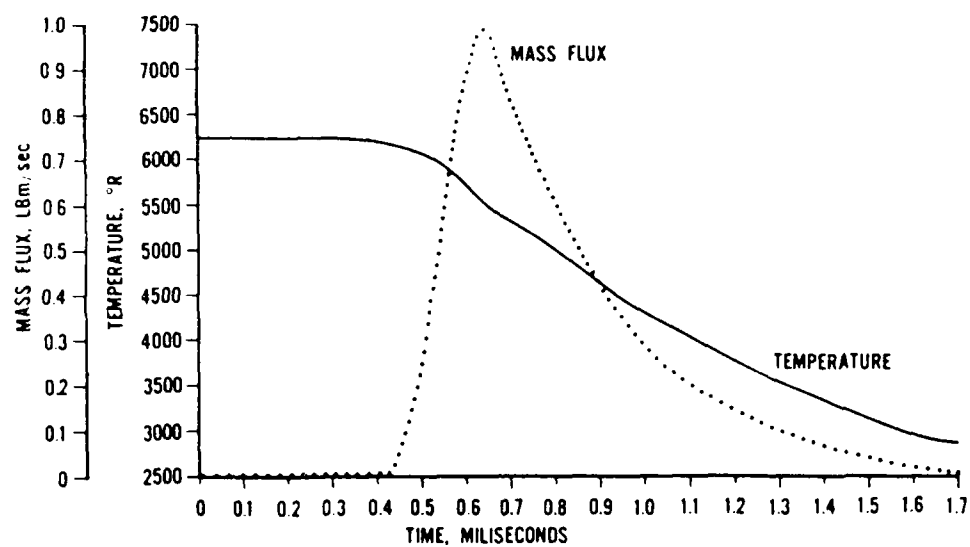
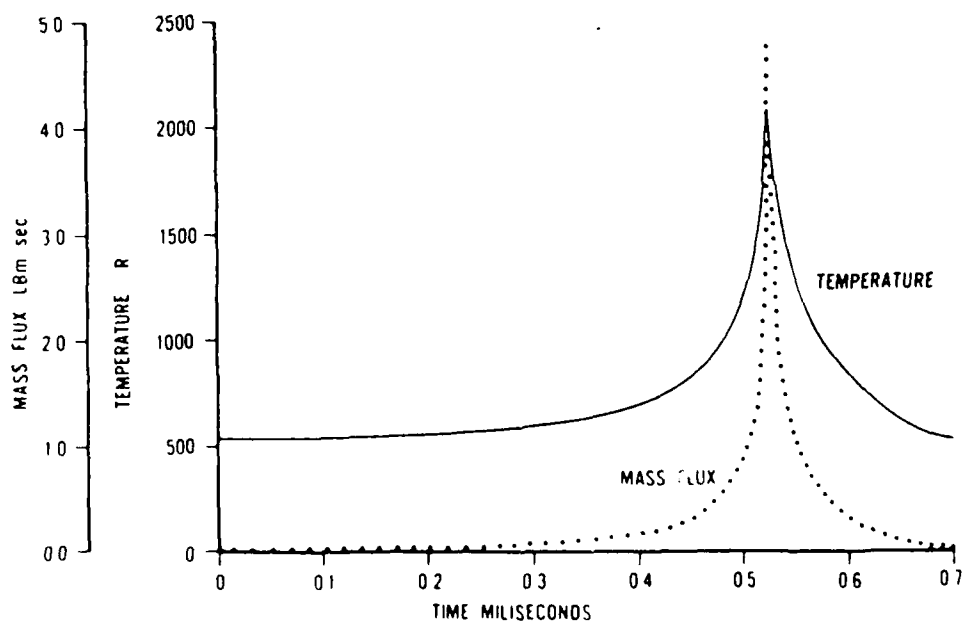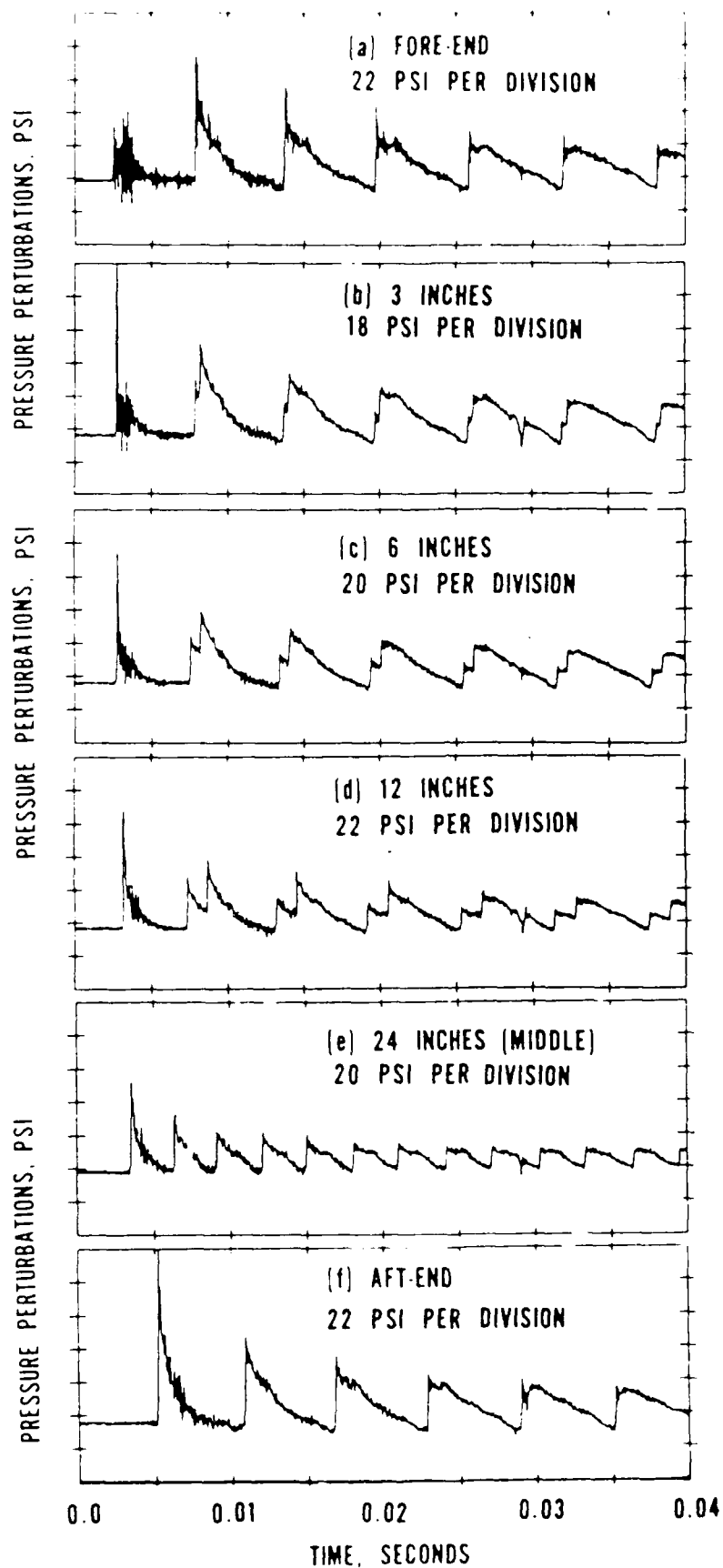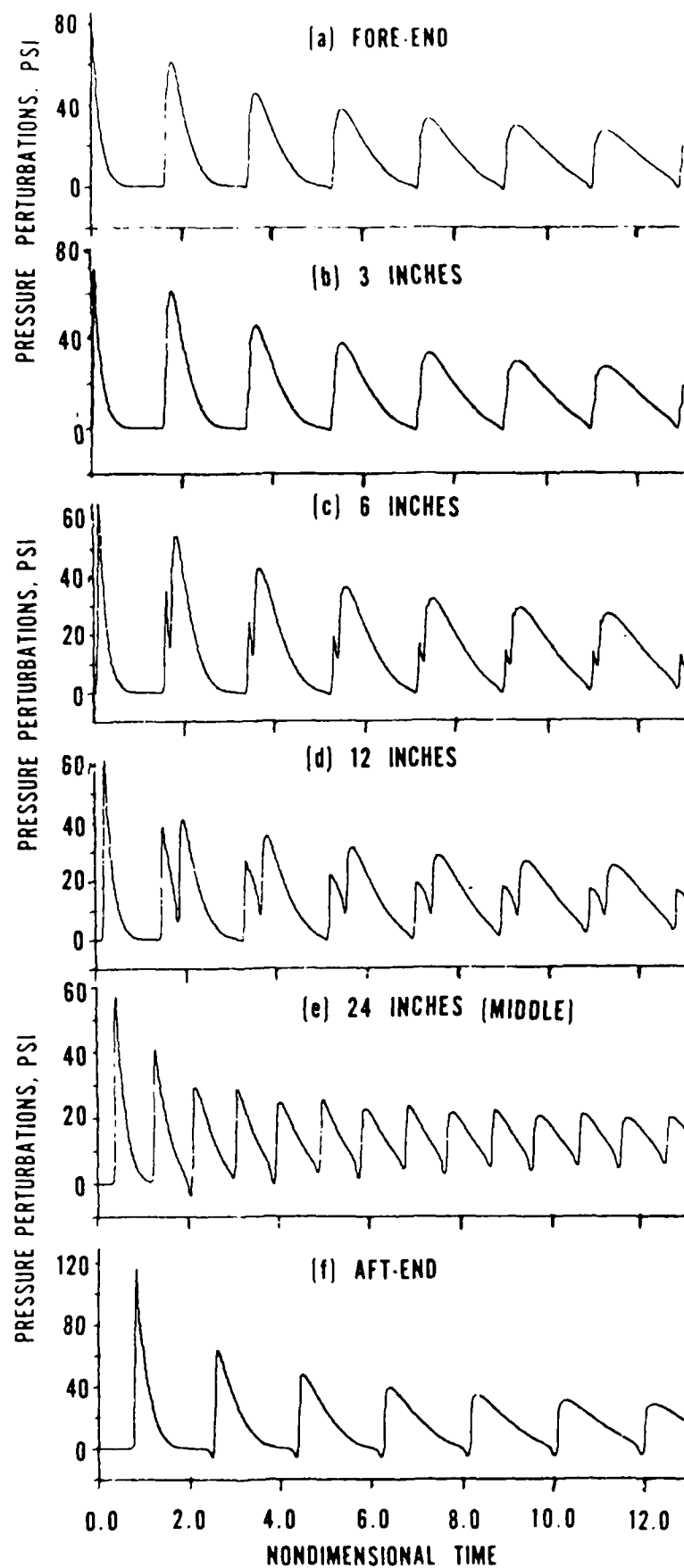Fig. 7b. Low brisance calculated performance.

Fig. 7c. Piston pulser calculated performance.

215

Figs. 8a-f. Time evolution of measured pressure perturbations
at several locations along the chamber generated by the pyro pulser.

Figs. 9a-f. Time evolution of predicted pressure perturbations at several locations along the chamber generated by the pyro pulser.

217

aft-end for the first four wave periods. Excellent agreement is demonstrated. The fact that a simplified one-dimensional model could accurately predict the wave amplitude shape and decay rate for the first 4-5 cycles was somewhat surprising, but also very satisfying. The one-dimensional inviscid model does not account for viscous losses at the walls of the chamber, thus, the predicted decay rates were not expected to match the measured decay rates. The excellent agreement between the predicted and measured decay rates for the first few cycles results from the fact that the initially high decay rates are primarily due to entropy increase resulting from repetitive shock wave processing of the gas in the chamber. During this time interval, viscous wall losses are a relatively insignificant part of the total losses. The capability of the present model to predict entropy increase and waveform decay rates (for several test cases) that are in excellent agreement with closed form analytical results has been demonstrated in Part I of this report. Nevertheless, as expected, results obtained with this inviscid model do not match the experimental decay rates at later times, when viscous wall losses become the major loss mechanism.

A second series of cold flow tests was conducted using helium instead of nitrogen under otherwise identical conditions. Again, excellent agreement was demonstrated between the measured and predicted waveforms.

When hot gases are injected into a cold chamber (cold chambers pulsed by the pyro and low brisance pulsers), a large temperature gradient is formed near the fore-end. This temperature gradient results in partial reflection of the shock returning from the aft-end which, in turn, results in pressure waves that are not as steep-fronted as those predicted at the aft-end. In addition, the development of a slight expansion in front of the shock can also be observed (as shown in Fig. 13). These phenomena are observed in both the measured and predicted data. In the experiment, convection,

Table 1.   Comparison of measured and predicted maximum pressure amplitude values at the aft-end.

| Cycle	Pyro		Low Brisance		Piston	
	measured	predicted	measured	predicted	measured	predicted
1	112.0	118.2	75.2	88.48	20.4	15.16
2	59.9	64.7	48.0	47.68	12.5	12.51
3	46.8	47.62	36.0	36.36	9.6	11.47
4	38.9	39.38	27.5	29.78	7.6	10.8
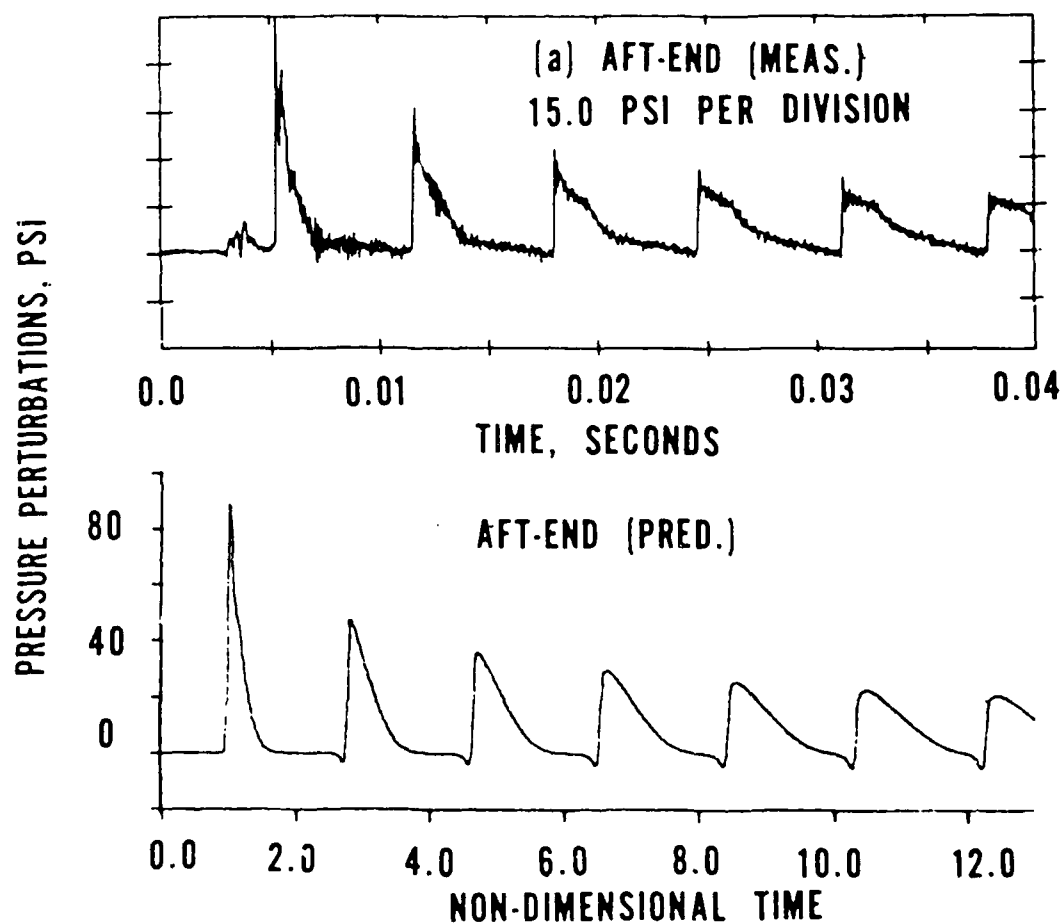
Figs. 10a-b. Low brisance pulser; comparison between measured and predicted pressure perturbations at the aft end.

conduction, and mixing rapidly reduce the temperature gradient. The current analysis does not treat mixing or heat conduction, thus, convection is the only operative heat transfer mechanism. Since convection is a slow process (due to the low velocity of the gases), the calculated temperature gradient remains unrealistically steep for a relatively long period of time. This results in predicted maximum fore-end pressure amplitudes that are lower than the measured data. The predicted results at the center of the tube (Fig. 9c) show the marked difference between waves reflected from the fore-end and waves reflected from the aft-end. This temperature gradient phenomenon should not affect the predicted results when solid rocket motors are hot pulsed, since both the injected pulser gases and the combustion products in the chamber are at approximately the same temperature.

An additional point should be made concerning the performance analysis of the piston pulser. The piston (driven into the bore by the high pressure in the breech volume) is stopped by a Teflon stopper located at the aft-end of the bore volume. The compression of the Teflon stopper has to be accounted for since the pressure and mass injection rates are rapidly increasing as the piston completes its stroke. Because the remaining volume occupied by gases at that time is small, a relatively small error in estimating the final compression distance of the Teflon stopper (referred to herein as stand-off distance) can result in a relatively large error in the predicted maximum amplitude value of the wave initiated in the chamber.

The predictions presented for the piston pulser (Figs. 12a and 12b) were obtained utilizing a stand off distance of 0.0375 inches. The predicted pressure results remain qualitatively the same for different stand-off distances; nevertheless, there are quantitative changes. For instance, the maximum amplitude of the first incident wave

221
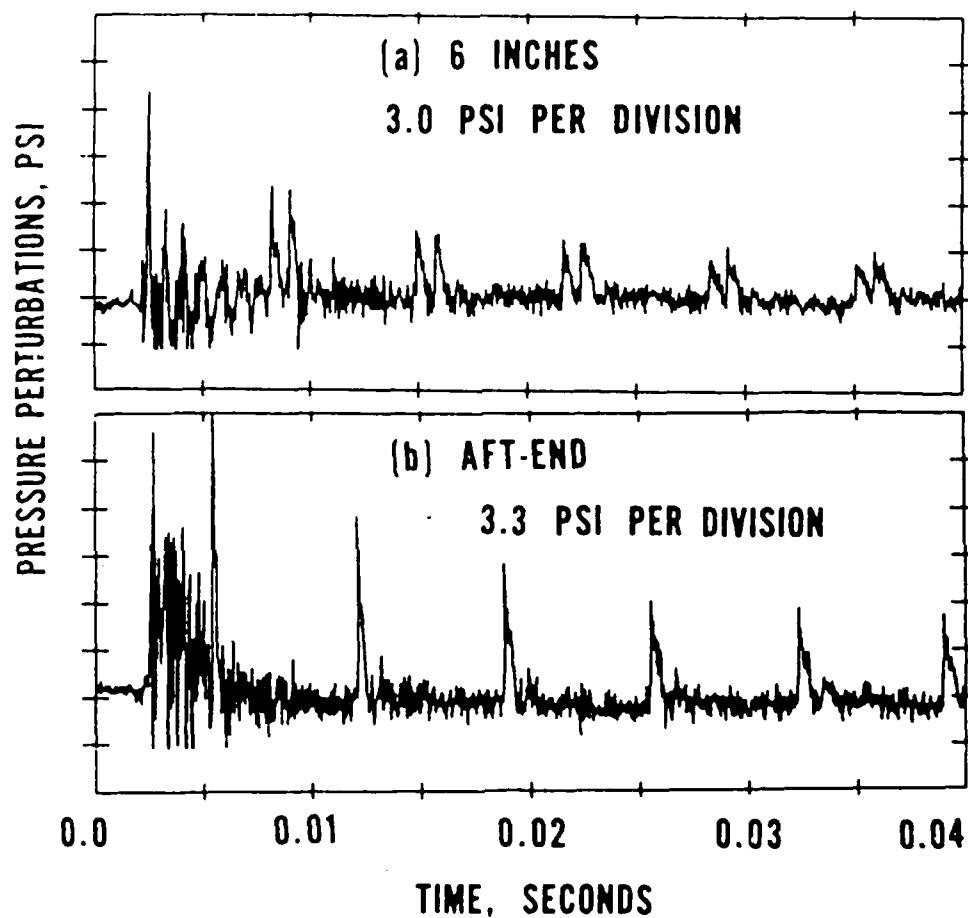
Figs. 11a-b. Piston pulser; time evolution of measured pressure
perturbations at two locations in the chamber.
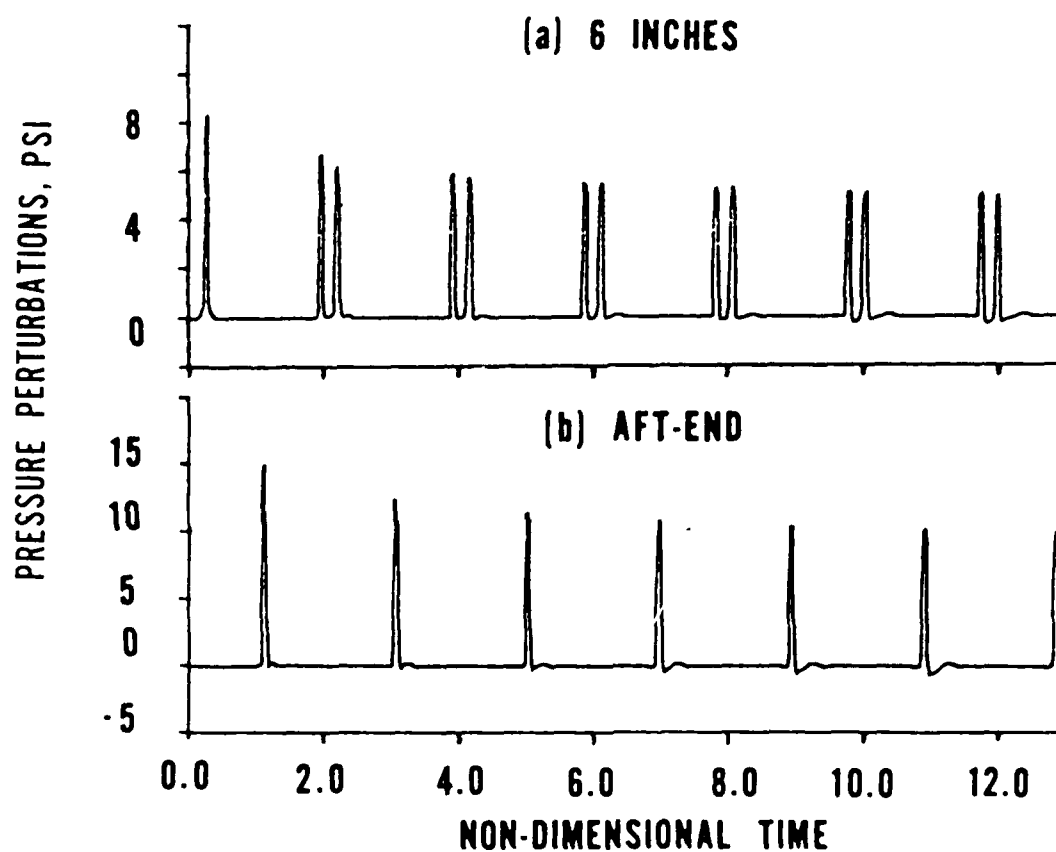
Figs. 12a-b. Piston pulser; time evolution of predicted pressure perturbations at two locations in the chamber.
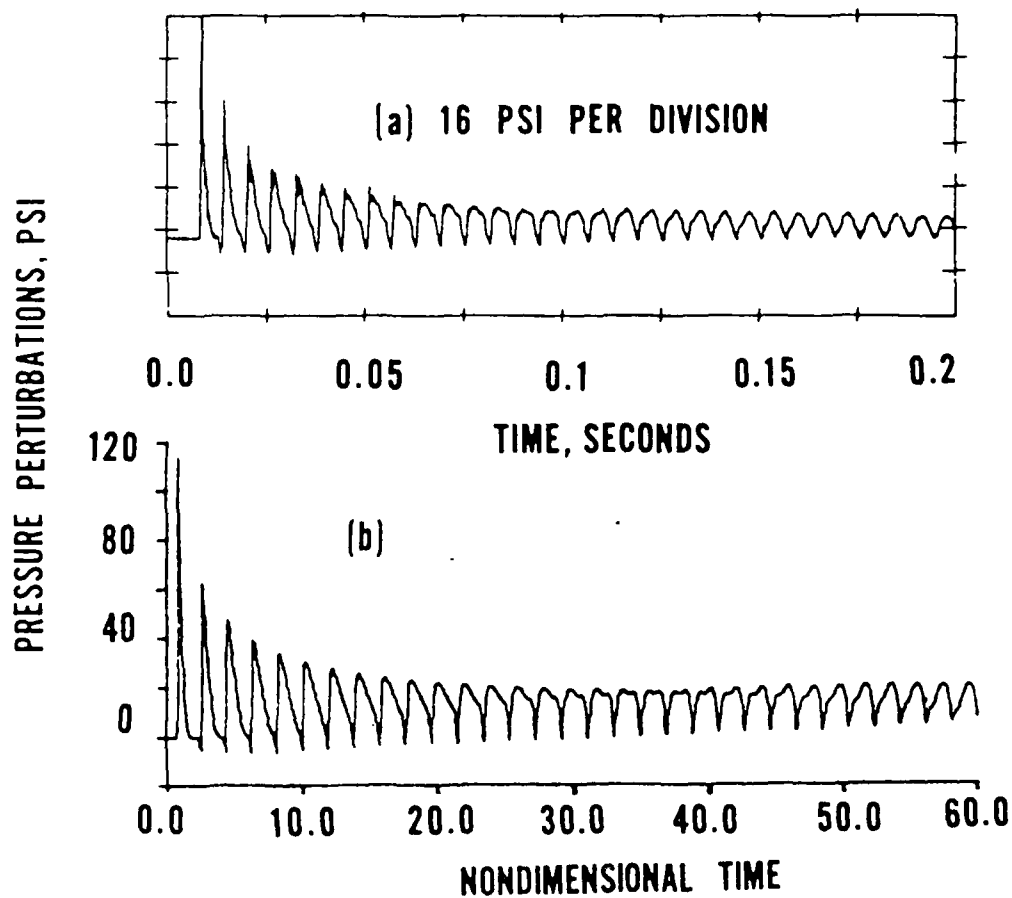
Figs. 13a-b. Pyro pulser; comparison of measured and predicted pressure perturbations at the aft end of the chamber.

at the aft-end is 8 psi with a stand-off distance of 0.10 inches, 10 psi with a stand-off distance of 0.05 inches, and 15 psi with a stand-off distance of 0.0375 inches. Thus, previous knowledge of the stand-off distance is needed for accurate prediction of the pulse amplitude produced by the piston pulser.

Spatial evolution of pressure waves in the first half wave period, as initiated in the chamber by the pyro and piston pulsers is shown in Figs. 14a and 14b, respectively. The differences between these pulses are evident in the figures. The very fast rise and decay times of the pulse generated by the piston pulser result in a very narrow steep-fronted and steep-backed wave. The prediction of such waveforms in a sharp-nonoscillatory manner is a formidable test of a numerical scheme. The ability of the present numerical technique to reproduce these waves with only slight post-expansion oscillations is another indication of the excellence of this shock capturing technique for all types of wave propagation problems. Spectral analysis of the very narrow wave predicted for the piston pulser (results at the fore-end are shown in Fig. 15) indicates a very high percentage of energy in the higher modes. This result is significantly different from spectral analysis results obtained for an N-type waveform (discussed in Part I) for which the energy contained in the higher modes falls as $1/n^2$ with respect to the energy contained in the fundamental mode (where n is the mode number).

A second series of experiments was conducted utilizing a 1.22 meter (48 inch) long, 0.038 meter (1.5 inch) internal diameter chamber filled with hot combustion products. A subsonic vent was utilized to maintain a constant pressure of 6.89 MPa (1000 psi). The chamber was instrumented with six high frequency Kistler pressure transducers. The transducer locations were the same as used in the cold flow experiments. The pyro, low brisance, and piston pulsers were utilized to pulse the chamber at the head end.
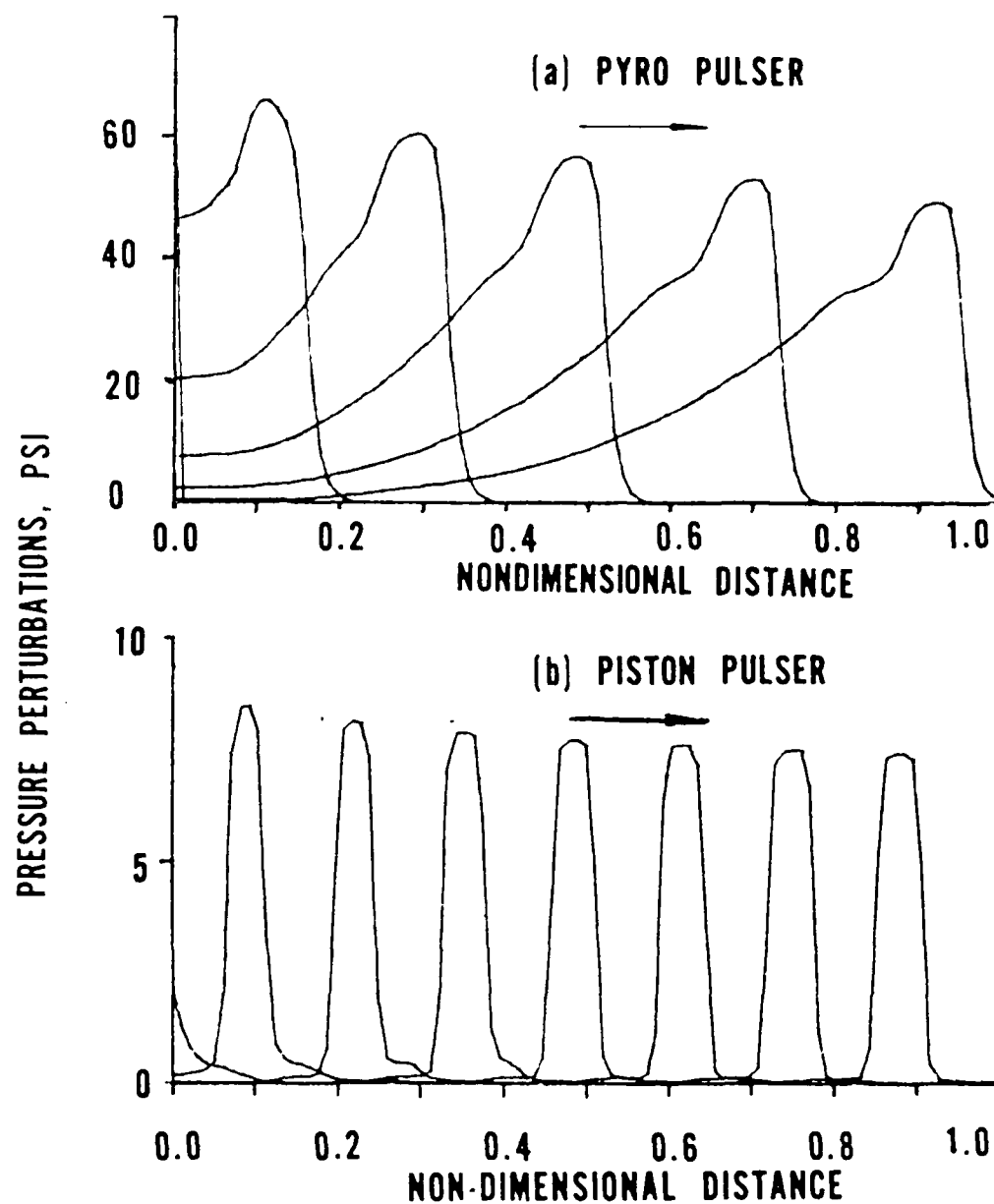
Figs. 14a-b. Spatial evolution of pressure waves in the chamber initiated by the pyro and piston pulsers.

The total mass discharged from each pulser was held constant, with a ratio of mass injected to mass in the chamber of 0.005.

The characteristics of the resulting pressure waves in the chamber obtained with the pyro and piston pulsers are, in general, similar to those obtained in the cold flow series of tests. The low brisance pulser results were, however, significantly different. In the cold flow tests, the back pressure acting on the piston was too low, resulting in a rise time that was too short and a pulse shape very similar to that generated by the pyro pulser. In the hot gas tests, the back pressure is high and a much slower rise time was obtained. The resulting pressure wave in the chamber (shown in Fig. 16a) is significantly different from the wave generated by the pyro pulser (Fig. 16b). The wave generated by the pyro pulser is already fully shocked after propagating 3 inches into the chamber. In contrast, the wave generated by the low brisance pulser is steep but never fully shocked and the transition to a sinusoidal type waveform is faster. Although the total mass injected by the pulsers was identical, the pressure amplitudes of the waves generated are a strong function of the mass injection rate; faster injection yielding higher amplitudes. The maximum amplitude of the first reflected pressure wave at the fore-end generated by the piston pulser was 111 psi, compared to 52 psi for the pyro pulser and 32 psi with the low brisance pulser.
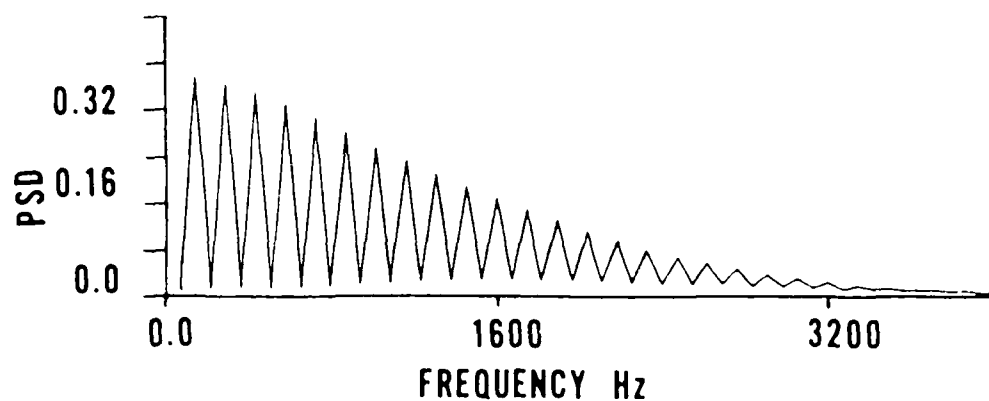
Fig. 15.   Piston pulser; PSD as a function of frequency at the fore-end.
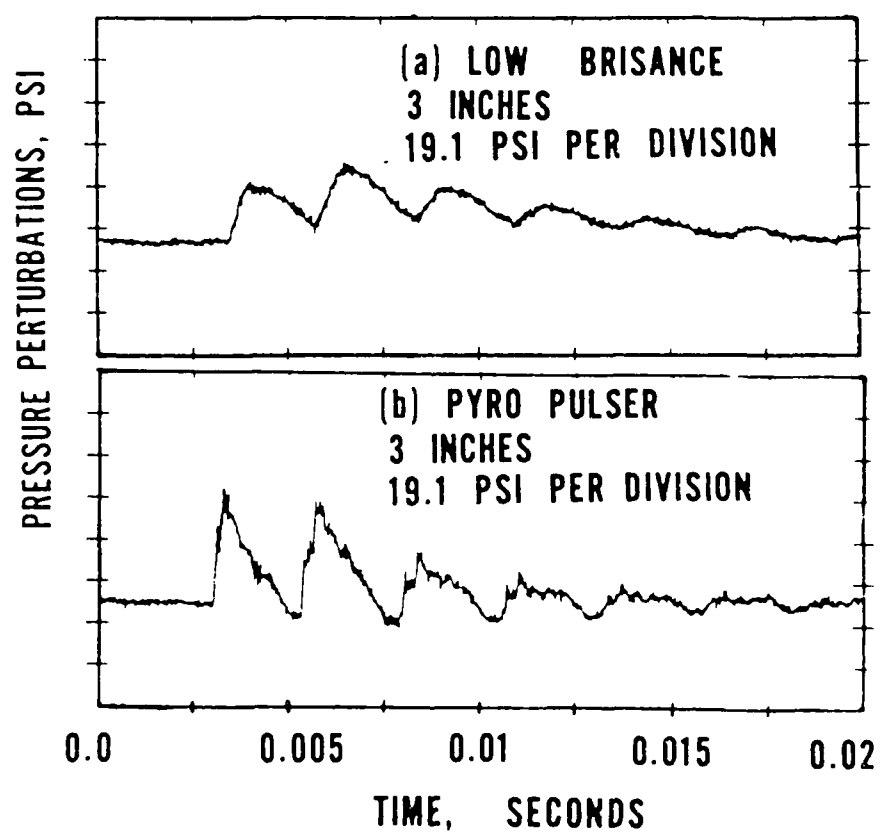
Figs. 16a-b.   Hot flow tests; comparison of measured pressure
perturbations in the chamber initiated by the low brisance and
pyro pulsers.

CHAPTER 3

PREDICTIONS AND EXPERIMENTS FOR LABORATORY AND FULL SCALE MOTORS

LABORATORY SCALE MOTORS

A series of experiments was conducted by Aerojet Tactical Systems Company (under contract F04611-8i-C-0007 with AFRPL) in which several laboratory scale motors with the same propellant and different grain geometries and nozzles were pulsed by different pulsers at different operating pressures.

The test motors were 1.22 meters (48 inches) long and had an internal case diameter of 5.71 centimeters (2.25 inches). Partial length grains were located at the fore-end of the motor. The grains were partially recessed into the case. Thus, at some time towards the end of a firing a flush grain configuration was achieved. Prior to this time, the grain represents an area constriction, and after this time, the grain is recessed relative to the case diameter. Two types of pulsers were used in the tests to be reported herein, i.e., pyrotechnic and piston pulsers[7]. Two pulser units were attached to the fore-end of the motor for each test.

Instrumentation

The pressure oscillations in the motor were recorded at six axial locations using Kistler Model 703 piezoelectric pressure transducers. A single DC (Taber) transducer was used to record mean pressure. The transient pressures in the breech of the pulse units were also measured with piezoelectric transducers. Thermal shielding of the pressure transducers was accomplished using vulcanized rubber (RTV). Based on shock tube calibration tests, it was concluded that an RTV thickness of 0.317 cm (0.125 inch) yields optimal resolution of the high frequency content of the steep-fronted

229

shock waves, within the constraint of adequate insulation. With a 0.125 inch RTV coating, the resonant frequency of the transducer is reduced from approximately 90 kHz to about 64 kHz with an amplitude accuracy within approximately 10 percent. At this level, high frequency measurements can be obtained up to about 20 kHz. Nevertheless, artificial oscillations at very high frequencies (termed transducer ringing) that are observed in the transducer response immediately following the passage of a shock wave, could not be completely eliminated. Therefore, the measured pulse amplitudes reported herein were corrected for this effect, in an approximate manner, whenever present.

Pulse Predictions

The ability of the combined pulser/chamber model to accurately predict the pulse induced waveforms in closed chambers filled with cold inert gases, has been demonstrated in Chapter 2. The validity of the pulser modeling under actual motor firing conditions was examined in this study.

Test PCC3 utilized a grain length of 22.8 centimeters (9 inches) and an initial internal grain diameter of 3.17 centimeters (1.25 inches). Two piston pulsers, each having 0.7 grams of Red Dot powder, but having different stroke lengths, were used. The pulse units were fired at motor burn times of 0.95 and 1.17 seconds, when the mean pressures were 10.37 MPa (1503 psi) and 11.45 MPa (1660 psi), respectively. Figures 17a and 17b compare the measured and predicted pulser breech pressure time histories for the two pulses. Very good agreement was obtained for the primary pulse; however, the analysis cannot predict the small secondary pressure variation that is produced in some cases when the piston bounces off the lead stop instead of sticking to it.
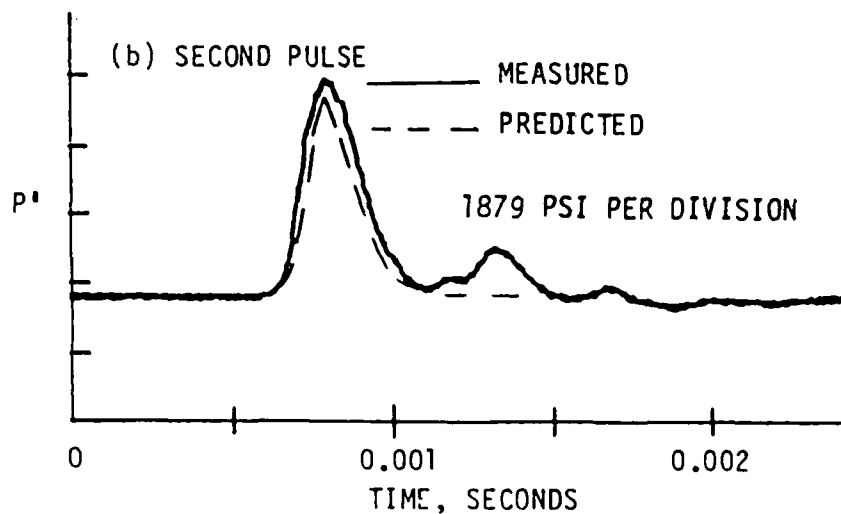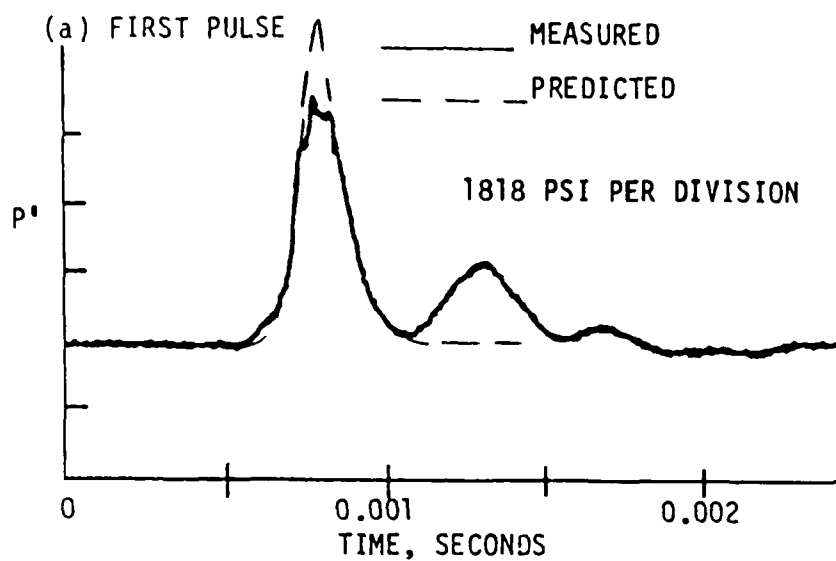
Figs. 17a-b. Comparison of measured and predicted piston pulser breech pressures, test PCC3.

Test PCC4 utilized a grain length of 20.32 cm (8 inches) and an internal grain diameter of 3.17 cm (1.25 inches). In this test, two pyro pulsers having 0.165 grains of Red Dot powder were fired 0.98 and 1.21 seconds into the motor firing, at chamber pressures of 11.12 MPa (1612 psi) and 12.25 MPa (1776 psi), respectively. Figures 18a and 18b show a comparison of the measured and predicted breech pressure time histories. Excellent agreement was obtained, demonstrating the ability of the pulser performance model to predict the breech pressure, and consequently, the mass and energy flux rates into the combustion chamber.

It will be shown in the next subsection that, when the mass and energy flux rates calculated using the piston and pyro pulser performance models were used as boundary conditions for the nonlinear stability analysis, excellent agreement between the predicted and measured pulse amplitudes and waveforms was also obtained. These results, as well as the results of additional comparisons not reported herein, demonstrate the ability of the pulser/chamber model to accurately predict the pressure perturbations produced by laboratory pulse units.

Stability Predictions

It was noted previously that several of the parameters that determine the pressure coupled response versus frequency characteristics of the burning propellant are unknown. To overcome this deficiency, this set of parameters and the magnitude of the velocity coupled response were chosen to yield a best fit for pulse 1 of test PCC3. This test was established as the baseline, and all of the other stability predictions (for the same propellant) were carried out leaving these values unchanged. All of the parameter values utilized here were physically reasonable.
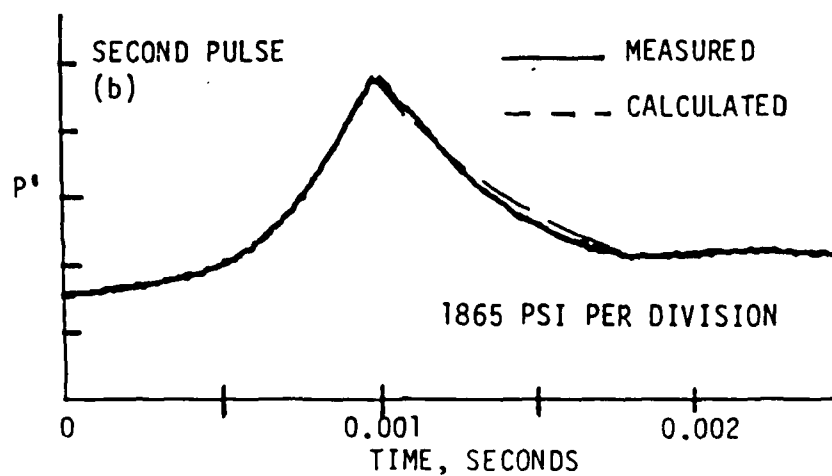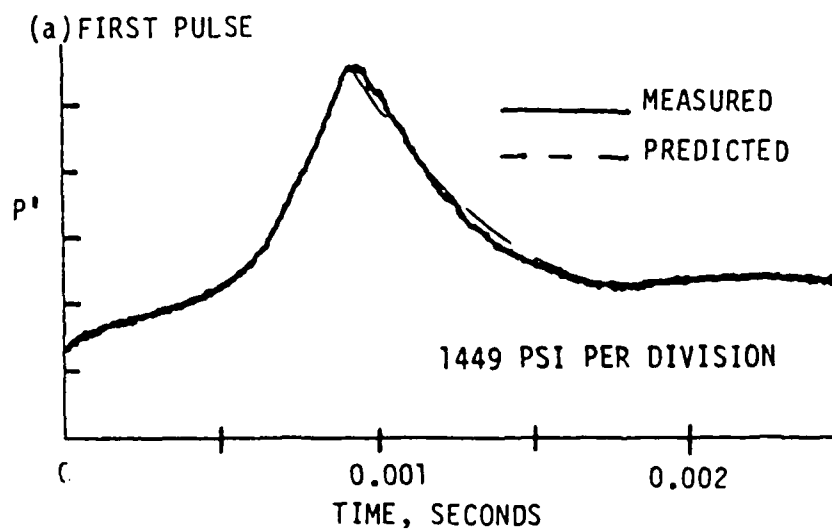
Figs. 18a-b. Comparison of measured and predicted pyro pulser breech measurement, test PCC4.

The time evolution of the mean chamber pressure measured during test PCC3 by a Taber transducer located at the fore-end, is shown in Fig. 19. The motor was stable in response to the first pulse and was driven unstable in response to the second pulse. The measured fore-end pressure oscillations induced in the motor by the first pulse are shown in Fig. 20a. The first piston pulser induced wave has an amplitude of .724 MPa (105 psi, or 7 percent of the mean pressure). It should be noted that all initial pulse amplitudes are quoted at the fore-end of the motor for the first wave reflected from the aft-end. The initial shocked waveform rapidly decays to an almost sinusoidal waveform, indicating that the motor is stable to this pulse. The predicted time evolution of pressure oscillations for this case, obtained by utilizing the predicted mass and energy flow rates as boundary conditions for the nonlinear combustion instability program, is shown in Fig. 20b. The set of parameters listed in Table 2 was utilized in this "baseline" test. Excellent agreement is demonstrated between the measured and predicted initial pulse amplitude and waveform, the decay rate of the pulse, and the temporal evolution of the waveforms decay rate and harmonic content of the waves. The temporal evolution of the waveform, as observed in both the predicted and the measured data, is of special interest. The generation of a second shock wave is attributed to partial reflection from the area discontinuity at the end of the solid propellant grain, a discontinuity that still exists at the time the first pulse is fired. This reflected shock wave is initially amplified in time as the original pulse decays, until it dominates the waveform.

Since the gases injected from the piston pulser are at a significantly lower temperature than the gases in the hot motor, a large temperature gradient is formed near the fore-end, resulting in the formation of expansion waves behind the propagating shock. This phenomenon is observed in both the measured and predicted data. In the experiment, the mixing of the hot propellant products with the cold gases reduces the
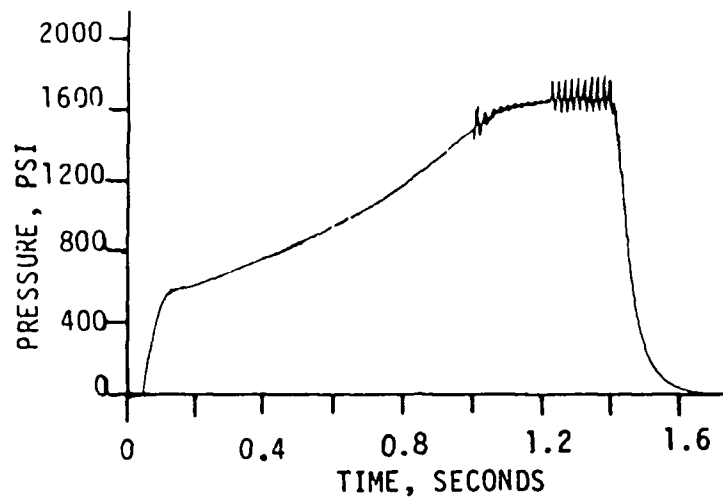
Fig. 19. Chamber pressure as a function of time, test PCC3.

(a)   46 PSI PER DIVISION

(b)
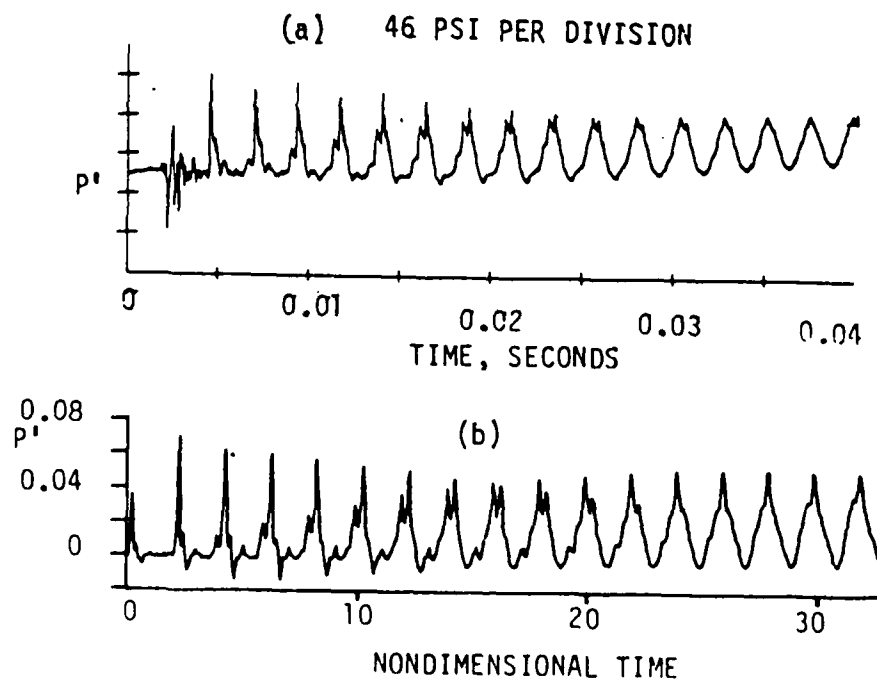
Figs. 20a-b. Comparison of measured and predicted pressure
perturbations at the fore end, test PCC3, first pulse.

235

temperature gradient rapidly. The current analysis does not treat mixing, thus the calculated temperature gradient remains unrealistically steep for a relatively longer period of time (about 7 wave cycles in the predicted data as compared to about 4 in the measured data). In contrast, when hot gases were injected into a cold chamber (Chapter 1), an expansion is developed in front of, rather than behind the shock.

The measured fore-end pressure oscillations for test PCC3 pulse 2 are shown in Fig. 21a. In this case, the piston pulser produced a pulse having an amplitude of about 0.43 MPa (63 psi, or 3.8% of the mean pressure). The predicted pressure history is shown in Fig. 21b. The predicted pulse amplitude (3.8%) and waveform, as well as the temporal evolution of the waves (shape, amplitude and growth rate) are all in excellent agreement with the measured data. For instance, after 15 wave cycles, both the measured and predicted waves have an amplitude of 5.2% of the mean pressure. Without changing any of the parameters (Table 2) from those employed in predicting the first pulse, the analysis was able to correctly predict that the second pulse would trigger a sustained nonlinear instability.

In the second motor firing considered (PCC4), pyro pulsers were employed instead of piston pulsers, the grain was shortened to 20.32 cm (8 inches) and the nozzle diameter was reduced. The mean pressure history for this test is shown in Fig. 22. The pulsers were fired at 0.98 and 1.21 seconds into the motor firing at mean pressures of 11.12 MPa (1612 psi) and 12.25 MPa (1776 psi), respectively. At these conditions, the motor is marginally unstable - in a linear sense - at the second mode frequency, and low level spontaneously initiated oscillations are observed throughout the firing. As in test PCC3, the first pulse of test PCC4 failed to produce sustained nonlinear oscillations, while the second pulse did trigger a nonlinear instability.

(a) 28 PSI PER DIVISION

TIME, SECONDS

(b)

NONDIMENSIONAL TIME
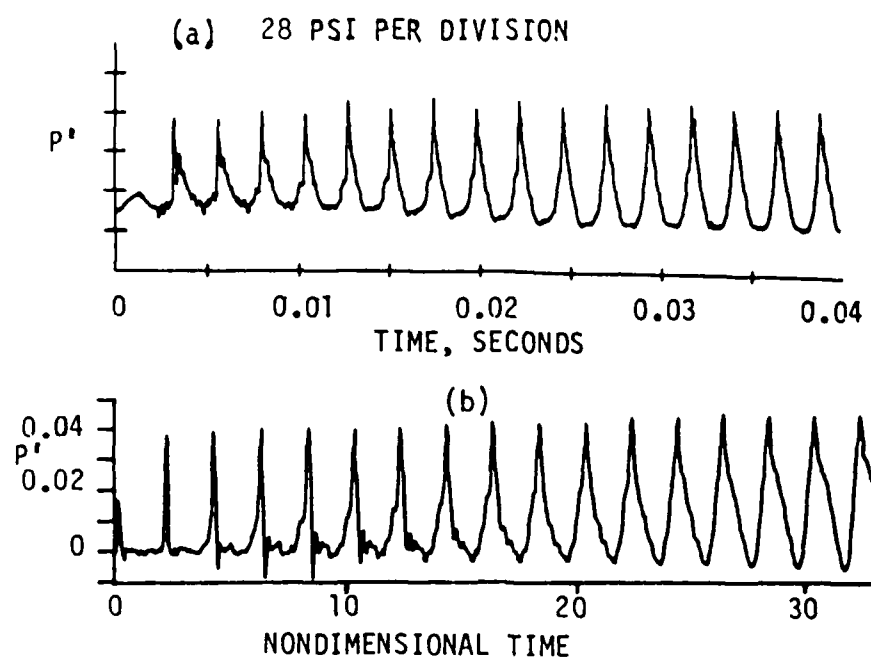
Figs. 21a-b. Comparison of measured and predicted pressure
perturbations at the fore-end, test PCC3, second pulse.
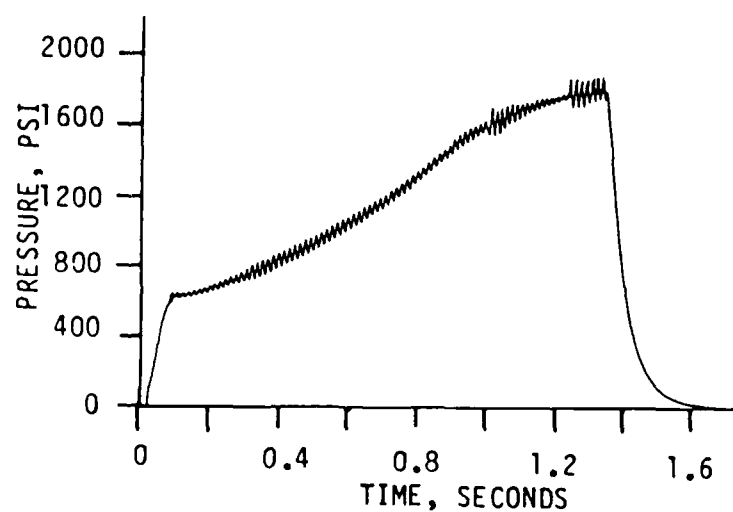
Fig. 22. Chamber pressure as a function of time, test PCC4.

237

Figures 23a and 24a show the measured time evolution of pressure oscillations at the fore-end of the motor induced by the two pulses. The corresponding calculated results are shown in Figs. 23b and 24b. Despite the presence of the residual spontaneous 2nd mode oscillations, which are unaccounted for in the analytical results, the predicted and measured initial pulse amplitudes and waveforms, and the wave growth rate (2nd pulse) and decay rate (1st pulse) are all in very good agreement. The amplitude of the first pulse was measured to be 2.5 percent of the mean pressure, while the predicted value was 2.6 percent. For the second pulse, the measured value was 2.3 percent and the predicted amplitude was 2.4 percent. Here again, the analysis was successful in predicting the motor response to each of the pulses. After the first pulse, both the data and predictions show that the pressure oscillations first increase for about six wave cycles and then decay slowly. The amplitude of the second pulse was near the limit cycle amplitude; hence, the pressure oscillations increase only slightly following the pulse. In both cases, the measured and predicted wave amplitudes at the end of 15 wave cycles are in very good agreement.

The third and last set of data obtained in this series of tests, test PCC2, was also conducted with a 20.32 cm (8 inch) long grain, but at significantly lower chamber pressures. Two piston pulse units were fired during this test at chamber pressures of 8.84 MPa (1282 psi) and 10.21 MPa (1481 psi). The first pulse, with initial amplitude of about 0.33 MPa (48 psi or 3.74 percent of the mean pressure), decayed rapidly into a sinusoidal waveform. The results were qualitatively similar to those obtained in test PCC3, but with a somewhat larger decay rate. The second pulse, with an amplitude of 0.4 MPa (58 psi or 3.9 percent of the mean pressure), increased initially in amplitude (to about 4.6 percent of the mean pressure after 6 wave cycles), but then decayed. Thus, at the lower pressures used in PCC4, both pulses were stable. The theoretical predictions for this motor indicated very good agreement with the measured data. Both

(a)   28 PSI PER DIVISION

TIME, SECONDS

(b)

NONDIMENSIONAL TIME

Figs. 23a-b. Comparison of measured and predicted pressure
perturbations at the fore-end, test PCC4, first pulse.

(a)   23 PSI PER DIVISION

TIME, SECONDS

(b)

NONDIMENSIONAL TIME
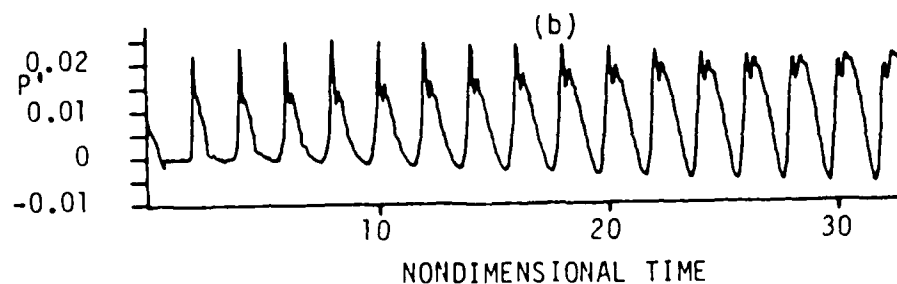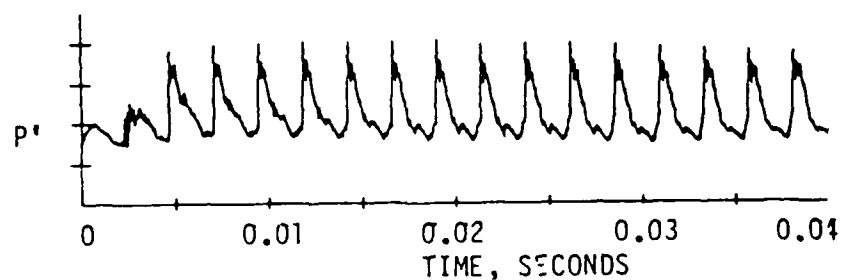
Figs. 24a-b. Comparison of measured and predicted pressure
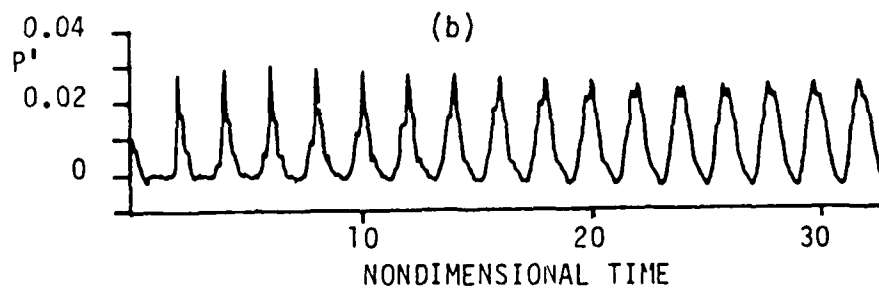perturbations at the fore-end, test PCC4, second pulse.

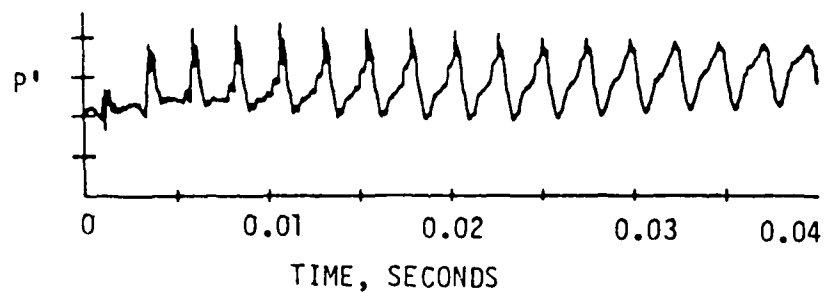be stable and the analysis correctly predicted that the first pulse would decay rapidly and that the second pulse would grow initially and then decay slowly. The initial pulse amplitudes and waveforms were also accurately predicted. The measured data for PCC2 pulse 1 demonstrated reflected wave behavior (from the area discontinuity at the end of the grain) similar to that observed in response to the first pulse of test PCC3. This observed behavior was again correctly predicted by the analysis.

Before applying the nonlinear analysis to the prediction of nonlinear instability in full scale motors, an additional laboratory scale motor comparison was conducted with a more complex and motor-like grain distribution than those employed in the previous tests. The propellant distribution for test firing 4 is depicted in Fig. 25. A pyro pulser (attached to the fore-end) generated a pulse at the time when the propellant burned back to a flush condition, with an amplitude of 5.1% of the 9.897 MPa (1435 psi) mean pressure. The time evolution of the measured and predicted pressure oscillations at the fore-end are shown in Fig. 26. Excellent agreement is demonstrated between the measured and predicted data. The initial pulse amplitude was predicted to be 5.1% of the mean pressure, in agreement with the measured value. After 15 wave cycles, the amplitude of both the measured and predicted waves was 6.2% of the mean pressure. In addition, the measured and predicted waveforms are very similar. It should be mentioned that the composition of the propellant in test 4 was slightly different than that utilized previously. The propellant parameters utilized to predict the pressure-time data for this case are shown in Table 3.

In the laboratory scale tests discussed above, only small ($\pm 1\%$) instability induced mean pressure shifts were observed. The analytical solutions for these cases also predicted only small shifts in mean pressure.
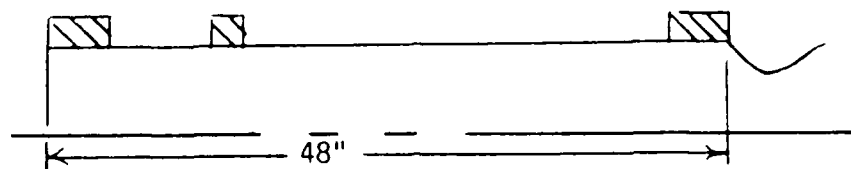
Fig. 25. Propellant grain distribution, test 4.

(a)   18 PSI PER DIVISION

P'

0   0.01   0.02   0.03   0.04

TIME, SECONDS

(b)

0.06

0.04

P' 0.02

0

-0.02

0   10   20   30

NONDIMENSIONAL TIME
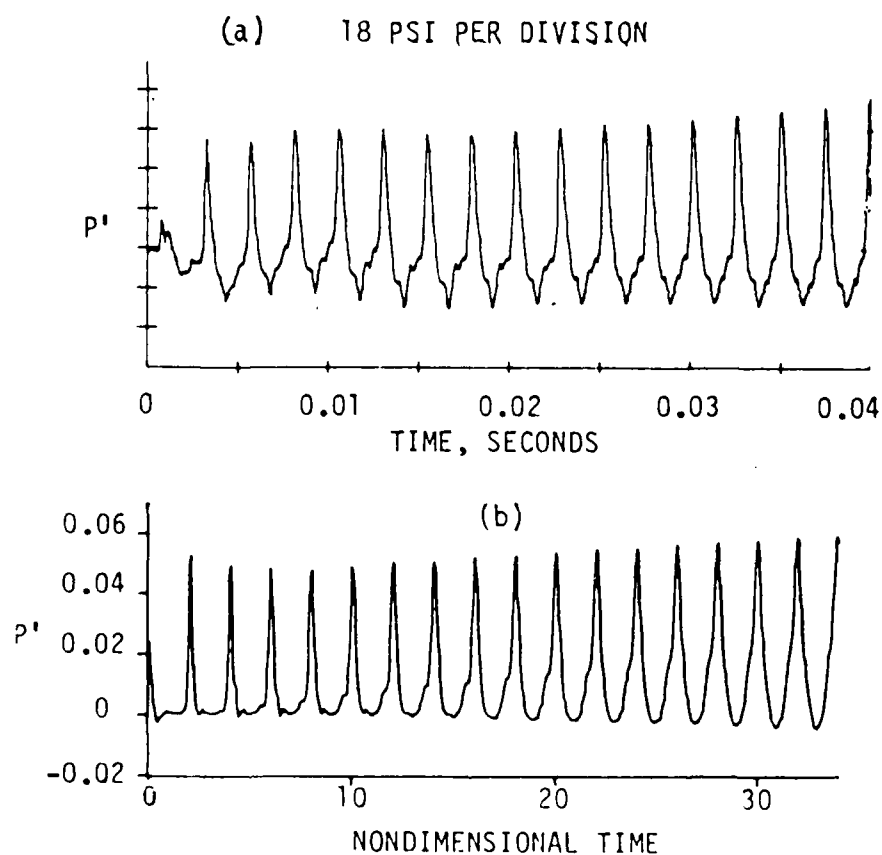
Figs. 26a-b. Comparison of measured and predicted time evolution of pressure perturbations at the fore-end, test 4, second pulse.

FULL SCALE MOTORS

An assessment of the validity of the present nonlinear instability model would not be complete without examining its ability to predict nonlinear instability in full scale motors. Data from two motor firings were selected for use in the present comparison study. Motor A and Motor B, as they will be termed, were development reduced smoke motor designs. Both motors were stable until pulsed; were pulse triggered into sustained nonlinear instability; and exhibited DC shifts in mean pressure after pulsing.

Details of the pulser designs utilized to pulse these motors were not available. Thus, predictions were obtained by varying the input mass flux until the experimentally observed pulse amplitude was reproduced. As in the case of the baseline laboratory scale motor, the parameters which control the characteristics of the pressure and velocity combustion response as a function of frequency were varied to obtain the best agreement possible. It should be recalled that the issue to be addressed in this study was the capability of the present analysis to predict all of the nonlinear characteristics observed in full scale motor instability data and not the capability to a priori predict motor response to pulses.

Motor A

A number of different grain designs and propellants were tested during this motor development program. The motor selected for this comparison study had a five point gear grain configuration, and a grain length of 1.65 meters (65 inches). The propellant utilized was an AP oxidized reduced smoke propellant containing a small amount of stability additive. The motor was pulsed with a piston pulser two seconds into the firing when the chamber pressure was 10.69 MPa (1550 psi). The cross-sectional area and

242

Fig. 27. Motor A; axial variation of flow area and cumulative burn surface area.

Figs. 28a-c. Comparison of measured, corrected and predicted time evolution of pressure oscillations at the fore-end, motor A.

cumulative burn surface area, at the time of pulsing, are plotted in Fig. 27. For the sake of computational efficiency, certain small details of the grain distribution were modified. A single fore-end mounted transducer (Kistler Model 603A) was used to monitor the pressure oscillations. The transducer had a 0.25 cm (0.1 inch) coating of RTV for thermal protection and a stand-off distance of 2.29 cm (0.9 inch). In its mounted configuration, the transducer had a resonant frequency of about 6000 Hz.

The measured time evolution of the pressure oscillations following the pulse are shown in Fig. 28a. Although not evident in this figure (DC pressure changes were filtered out), the motor experienced a 10.9% increase in mean pressure (DC shift) as a result of the pulse induced instability. The waveform of the pressure oscillations is quite nonlinear, and is primarily a single traveling shock wave. The combination of a shocked waveform, with its attendant large high frequency content, and the low resonant frequency of the Kistler transducer in its mounted configuration, resulted in transducer resonance (or ringing) and distortion of the true waveform. This phenomenon is more clearly evident when the analog tape is speed-scaled before digitization and plotting. The presence of this ringing precludes the accurate quantization of the wave amplitude, but hand correction for this effect (see Fig. 28b) produced a wave history that is satisfactory for the present qualitative comparison study.

The parameters shown in Table 4 were utilized as input data for the nonlinear combustion instability model. The predicted time evolution of pressure oscillations is shown in Fig. 28c. Excellent agreement between the measured and predicted data was obtained. Both the predicted and measured oscillations grew from the initial pulse amplitude of 3.4% to amplitudes between 22 and 24% after 11 to 13 wave cycles, and decreased slightly afterwards. The predicted DC pressure shift (11%), and the predicted wave shape, were also both in close agreement with the experimental data.

244

During development work on Motor B, a number of motors were pulse tested to determine their nonlinear stability. The motor selected for this study had a fore-end finocyl grain configuration with three fins. The motor had a grain length of 166.4 cm (65.5 inches) and a fin length of 55.88 cm (22 inches). An AP oxidized reduced smoke propellant containing a burn rate retardant was utilized in this test. The motor was pulsed with a pyro pulser 2.78 seconds into the firing when the chamber pressure was 5.38 MPa (780 psi). The cross-sectional area and cumulative burn surface area, at the time of pulsing, are plotted in Fig. 29. Each motor was instrumented with two Taber transducers for mean pressure measurement, three accelerometers, and a Kistler 606A high frequency transducer located in the fore-end closure. The Kistler was recessed about 1.78 cm (0.7 inch) and was protected by a 0.25 cm (0.1 inch) coating of RTV. The resonant frequency of the transducer was in the range of 5-10 kHz.

It can be seen from the fore-end pressure oscillation history, presented in Fig. 30a, that the instability data for this motor is significantly compromised by transducer ringing. These results demonstrate the importance of keeping the transducer resonance frequency as high as possible in future pulse testing of solid motors.

The time evolution of pressure oscillations for Motor B is more complex than that of Motor A, and is characterized by the presence of multiple, variable amplitude shock waves. Thus, correcting the data for transducer ringing becomes fairly subjective. Nevertheless, it is possible to approximate the true response by mentally removing the thin spike-like top portion of each wave front. As in the laboratory scale motor firings, the complexity and multiple shock wave nature of Motor B's pressure history is
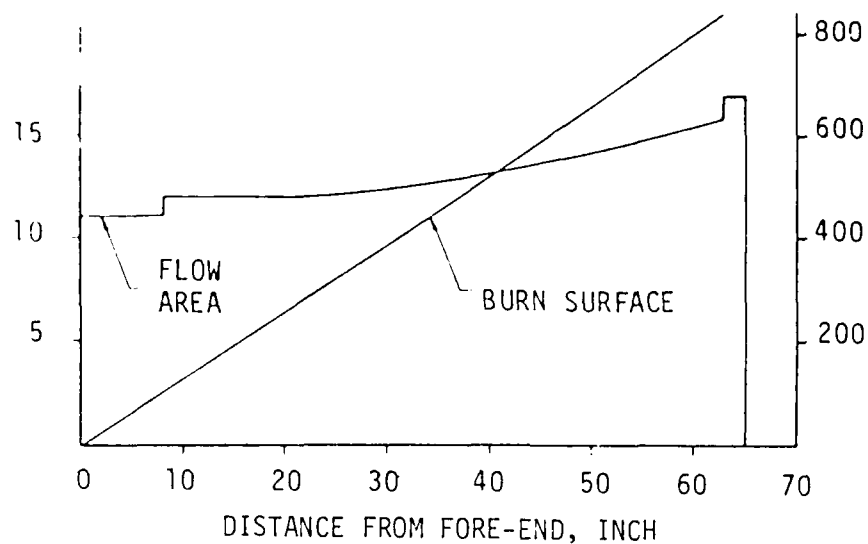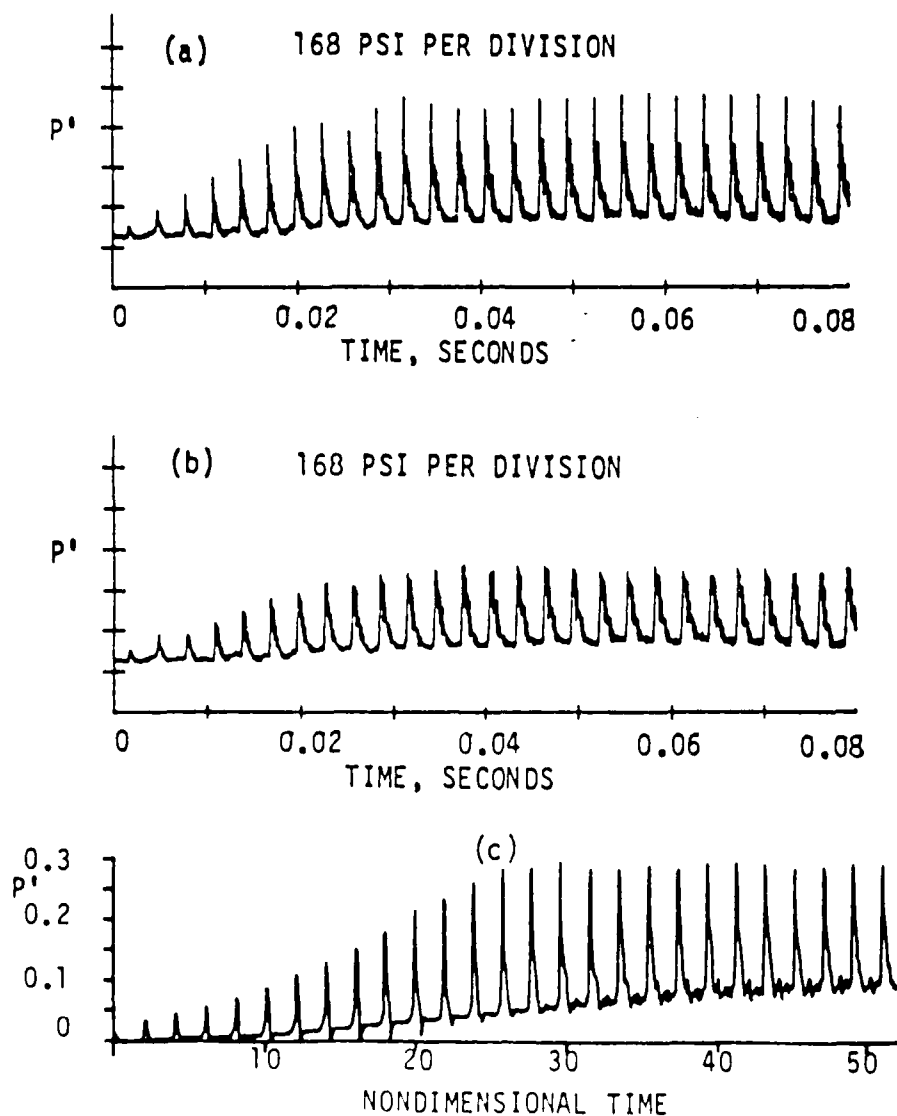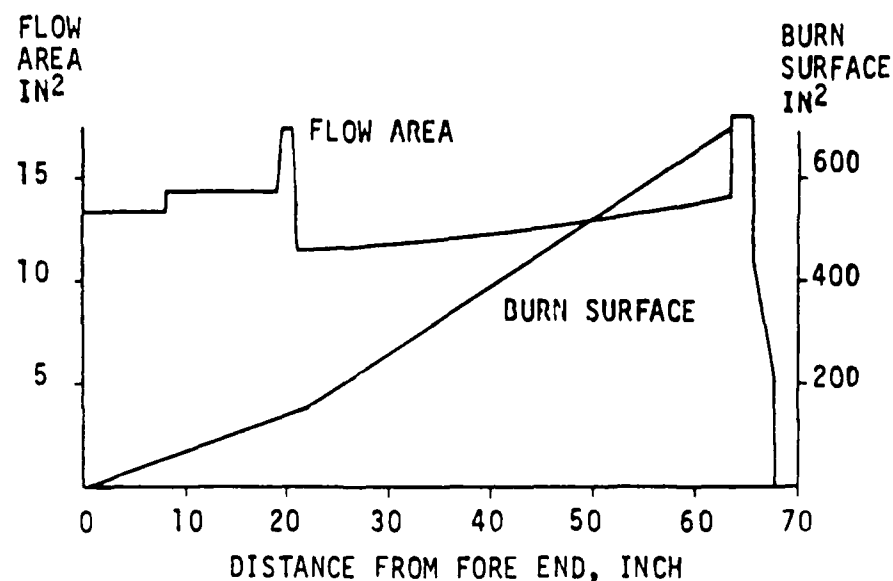
Fig. 29. Motor B; axial variation of flow area and cumulative burn surface area.
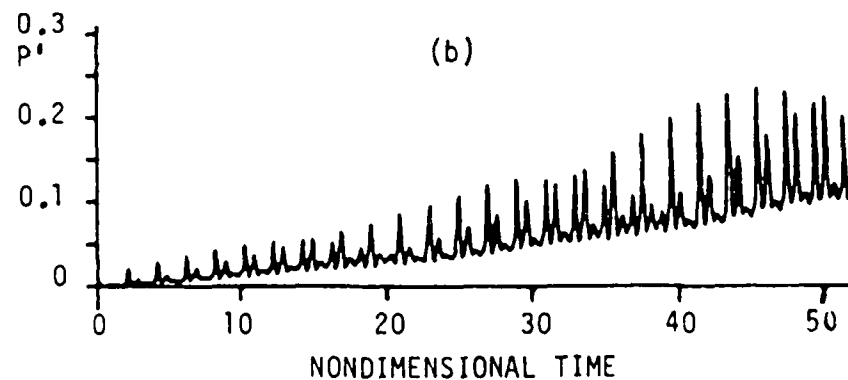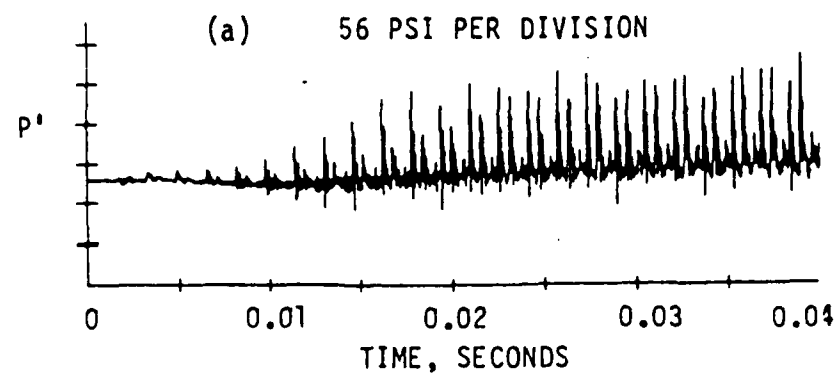
Figs. 30a-b. Comparison of measured and predicted time evolution of pressure perturbations at the fore-end, motor B.

attributed to partial wave reflections from an internal area discontinuity in the chamber. In Motor B (Fig. 29) the only sizeable flow area discontinuity is located approximately one-third of the way between the fore-end and the end of the grain. Correspondingly, the multiple shock waves are spaced at intervals approximately equal to one third of a full wave cycle. It should be mentioned, however, that while not presented herein, existing data and analytical results show that multiple shock waves can also be driven by propellant combustion, e.g., when the propellant transient response is much higher at the second (or higher) longitudinal mode frequency than at the fundamental mode.

The propellant parameters shown in Table 5 were utilized in obtaining the analytically predicted pressure oscillation history for Motor B shown in Fig. 30b. Comparing Figs. 30a and 30b, it is noticed that the theoretical results qualitatively reproduce the complex tertiary shock wave behavior present in the experimental data. Both the experimental and predicted wave histories contain two relatively stronger shock waves and one weak shock wave. In the predicted data, a repetitive pattern is observed in which the weaker of the two dominant waves grows until it becomes the larger shock wave. In the experimental data, the relative amplitudes of the two larger shock waves vary in time, but not in as cyclical a manner. Relatively good agreement between the predicted and measured wave amplitudes and DC pressure shifts was obtained. Both the measured and predicted DC shifts were approximately 10% of the mean chamber pressure (the DC shift in the experimental data was filtered out and is not discernible in Fig. 30a).

	TABLE 2	TABLE 3	TABLE 4	TABLE 5
Burn Rate, in/sec	$0.3899(\frac{\overline{P}}{1000})^{0.43}$	$0.354(\frac{\overline{P}}{1000})^{0.45}$	$0.304(\frac{\overline{P}}{1000})^{0.43}$	$0.31(\frac{\overline{P}}{1000})^{0.40}$
Density of solid propellant g/cc	1.71895	1.71895	1.81895	1.713415
Thermal diffusivity of the propellant, cm2/sec	0.00266461	0.00257327	0.0016129	0.0016129
Adiabatic flame temperature, oR	5378.0	5378.0	5364.0	5274.0
Gas only specific heat, BTU/lboR	0.4568	0.4568	0.4568	0.4565
Gas only isentropic exponent	1.2	1.2	1.2	1.208
Propellant steady state surface temperature, oR	1454.2	1454.2	1454.2	1454.2
Propellant back wall temperature, oR	543	543.0	624.67	543
Propellant only specific heat, BTU/lboR	0.305	0.305	0.305	0.305
A	5.0	11.5	20	6.0
B	0.53	0.86	1.06	0.66
Linear pressure coupled response, R_{pc}	1.092	1.53	1.32	1.344
Velocity coupled response, R_{vc}	3.0	3.0	6.0	5.6

248

CHAPTER 4

EJECTA PULSE STUDIES

EXPERIMENTAL APPARATUS

The ejecta pulse test apparatus consists of a thick walled combustion chamber in which either partial, or full length, cylindrical grains were loaded and fired[10]. Two ejecta pulsers were attached to the fore end of the chamber. A schematic of the ejecta pulse test apparatus is shown in Fig. 31. The combustion chamber had an overall length of 1.22 meters (48 inches) and an internal case diameter of 5.71 centimeters (2.25 inches). Nozzle entrance and exit angles were 45° and 15°, respectively. The partial length cylindrical grains were partially recessed into the case. Thus, at some time toward the end of the firing, a flush grain configuration was achieved. Prior to this time, the grain represented an area constriction. After this time, the grain was recessed relative to the case wall. At predetermined times during the firing, the pulsers ejected a sphere into the chamber which was carried out through the nozzle by the flow of combustion gases. To simulate the range of material densities found in combustion chambers, a series of tests were carried out using spheres made from RTV rubber (utilized in most of the tests), nylon, Teflon, and steel.

The pressure oscillations in the motor were recorded at six axial locations using Kistler 703 piezoelectric pressure transducers. The chamber sidewall was instrumented with four close-coupled pressure transducers, one transducer was located at the fore-end closure and one in the convergent section of the nozzle. The transducer ports were machined so that the transducer diaphragms were offset by 0.125 inch. This cavity was potted with vulcanized rubber (RTV) which is utilized to provide thermal shielding
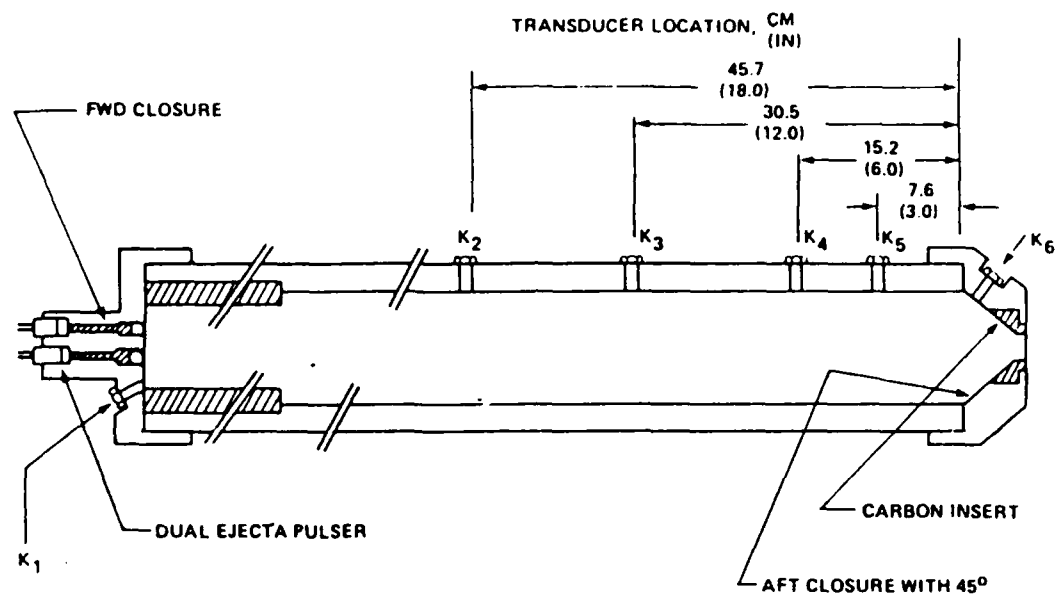
Fig. 31. Schematic of the ejecta pulse test apparatus.

for the pressure transducers. In its mounted configuration, the transducer had a resonant frequency of about 65 kHz, as determined by shock tube tests. With this high value for resonant frequencies, the amplification error should be less than 2 percent for a 12 kHz signal.

Ejecta Trajectory

The prediction of the pressure pulse waveform that results from the transient partial blockage of the nozzle (termed nozzle ejecta) requires calculation of the nozzle constriction as a function of time. Therefore, it is the ejecta velocity as well as its physical size that determines the pressure pulse waveform. The equation of motion for the ejecta is $F = m \frac{du_e}{dt}$, where m is the ejecta mass, u_e is the ejecta velocity, and F is the force acting on the particle. For a particle whose density is large compared to that of the gas medium, and when the fluid acceleration is low, the equation of motion is written as:

$$m \frac{du_e}{dt} = \frac{1}{2} c_d \rho(u-u_e)|u-u_e|A_e \qquad (25)$$

where u is the gas velocity, and c_d is the drag coefficient.

The force acting on the ejecta is a combination of viscous drag and pressure differences across the ejecta surface (termed pressure drag). At high velocities the pressure drag is largely a result of flow separation which causes a non-uniform pressure distribution over the surface of the body. Measured drag coefficients are usually presented as a plot of total drag (viscous plus pressure) as a function of Reynolds number. Schlichting[11] presented sphere drag data for both compressible and incompressible flow. For incompressible flow, the drag coefficient is approximately equal to 0.4 in the range of Reynolds numbers from 10^3 to 3×10^5. At the critical

251

Reynolds number of 3×10^5, the drag coefficient drops sharply. Compressibility effects act to increase both the drag coefficient and the critical Reynolds number. For Mach numbers in the range of 0.8 to 4.5 and Reynolds numbers in the range of 2×10^5 to 9×10^5, the drag coefficient is insensitive to Reynolds number and its value is approximately 0.65 to 0.75. Experimental data obtained during ejecta pulse tests imply average velocities in the throat region of about 600 to 3000 inches per second, depending on the ejecta density, initial injection velocity, and motor mean pressure. With these values, the Reynolds number would be in the range of 2×10^4 to 10^6. This range encompasses the critical Reynolds number for incompressible flow.

The existence of strong, mean flow pressure gradients in the nozzle may have a significant influence on the drag force. Nevertheless, for the sake of simplicity, such potential pressure gradient effects have not been considered in the present work and only the conventional drag force was incorporated in the ejecta trajectory analysis. Pressure measurements at the nozzle entrance were then used to estimate the appropriate value of the drag coefficient. Details of the approximate analysis are described later in this section.

Ejecta Pulse Modeling

The nozzle geometry during spherical ejecta passage is shown in Fig. 32, where; A_c is the nozzle entrance area, A_e, the ejecta area, A_t, the throat area, a, sonic velocity, u, gas velocity, and , is the gas density.

A simple model for calculating the amplitude of the ejecta induced pulse at the nozzle entrance plane was developed. The assumptions involved were: the flow in the nozzle is one-dimensional and isentropic and the ejecta only affects the instantaneous

252
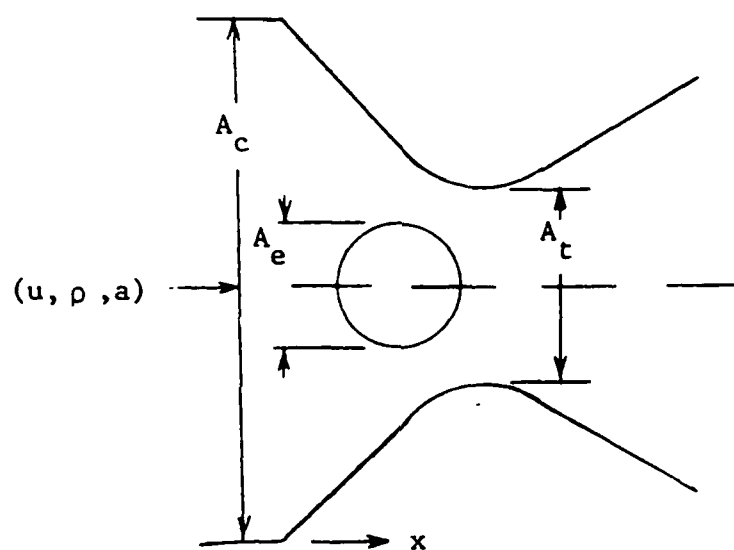
Fig. 32.   Reference areas for ejecta pulsing.

nozzle throat area. As the ejecta enters the throat, a series of weak compression waves propagate upstream towards the nozzle entrance slowing the flow. After the maximum diameter of the ejecta passes through the throat, a series of expansion waves propagate towards the nozzle entrance at a slightly higher velocity than the compression waves. Using linear wave propagation theory, the ratio of the instantaneous pressure at the nozzle entrance, p, to the initial undisturbed entrance pressure, p_1, can eventually be express   as

$$\frac{p}{p_1} = [(1+\frac{\gamma-1}{2} M_1^2)/(1+\frac{\gamma-1}{2} M^2)]^{(2\gamma)/(\gamma-1)} \qquad (26)$$

Thus, the instantaneous pressure is determined once the nozzle entrance Mach number, M, is known. In order to determine M, a quasi-steady nozzle behavior was assumed i.e., the instantaneous Mach number can be calculated using steady-state relations. The initial undisturbed nozzle entrance Mach number is given by

$$M_1 = J[(1+\frac{\gamma-1}{2} M_1^2)(\frac{2}{\gamma+1})]^{(\gamma+1)/2(\gamma-1)} \qquad (27)$$

where $J = A_t/A_c$ is the initial undisturbed value of the nozzle constriction ratio. The Mach number at the nozzle entrance plane during the ejecta passage is then given by Eq. (27) with M_1 replaced by M and J by $J(1-f_b)$ (where f_b is the fraction of the throat area blocked at any instant). The quasi-steady nozzle assumption should be most applicable to larger, slower moving ejecta. As the ejecta velocity increases, the quasi-steady assumption leads to over prediction of the pulse amplitude.

Equation (27) is a transcendental equation for M as a function of J. However, if it is assumed that 0.5 (-1) M_1^2 is small compared with one (M_1 is typically on the order of 0.1 and = 1.23), M_1, and M can then be expressed as

$$M_1 = J\left(\frac{2}{\gamma+1}\right)^{(\gamma+1)/2(\gamma-1)} \tag{28}$$

$$M = J(1-f_b)\left(\frac{2}{\gamma+1}\right)^{(\gamma+1)/2(\gamma-1)}$$

Inserting Eqs. (28) into Eq. (26) and neglecting terms on the order of 0.1J, yields the following expression for pulse amplitude

$$\frac{p_1-p}{p_1} = \frac{\delta p}{p_1} = \left[\gamma\left(\frac{2}{\gamma+1}\right)^{(\gamma+1)/2(\gamma-1)}\right] f_b J \tag{29}$$

with an isentropic exponent, , equal to 1.2, Equation (29) becomes

$$\frac{\delta p}{p_1} = 0.71 \; f_b J \tag{30}$$

Thus, this simple model predicts that the pulse amplitude is proportional to the product of the initial constriction ratio and the fraction of the throat area blocked by the ejecta, and provides a good basis for data correlation. Comparison of predictions obtained utilizing this model with experimental data are shown later in this section.

Numerical Model

A second approach for calculating ejecta pulse amplitudes was developed by modifying the nonlinear combustion instability analysis described in Part I. This computer program, which solves the coupled nonlinear partial differential equations that govern the one-dimensional, two-phase flow in variable cross-sectional area solid rocket motors and the transient combustion of the solid propellant, was modified to accept a time-dependent Mach number boundary condition at the nozzle entrance.

In this approach, the ejecta trajectory is calculated as described previously. The quasi-steady assumption was retained, thus, the nozzle entrance Mach number is given

255

by Eq. (27), with J replaced by the instantaneous nozzle constriction ratio. The program calculates the flow variables at interior mesh points using an advanced shock capturing finite difference integration technique while the method of characteristics is employed at the boundaries. Thus, at the nozzle entrance, the specified Mach number boundary condition that describes effect of ejecta passage through the nozzle (i.e., the generation of compression and expansion waves) is conveyed to the combustion chamber via a left-running (upstream) characteristic.

Since the nonlinear combustion instability analysis treats the whole problem (i.e., the time evolution of oscillations in the motor, coupled with the propellant response), this approach is not limited to the calculation of the ejecta-induced initial pulse amplitude. It is also capable of calculating the waveform of the pulse and the resulting motor behavior, i.e., growth or decay of the disturbance. The ability to model the nonlinear response of solid rocket motors to pulsing had been demonstrated in Chapter 3 for low brisance, piston, and pyrotechnic pulsers attached to the head end of the chamber. A comparison between predictions and experimental data obtained by ejecta pulsing subscale rocket motors is presented in the following sections.

EXPERIMENTAL RESULTS AND COMPARISON WITH THEORY

Experiments

A series of motor firings was carried out using the previously described test apparatus and instrumentation. The results of nine of these tests are considered herein. AP-HTPB propellant grains with lengths varying from 8 to 48 inches, initial inside diameter of 1.25 inches and outside diameter of 2.375 inches were tested. Spherical ejecta of different materials were employed to study the effect of density variations.

256

The materials consisted of nylon, rubber, Teflon, and steel, having densities of 0.039, 0.040, 0.075, and 0.275 lbs/in^3, respectively. Ejecta size was also varied, resulting in throat blockage ranging from 32 to 69 percent. The test conditions are summarized in Table 6.

Pulse Duration - Ejecta Trajectory Model Evaluation

Tests 5, 6, and 7, in which materials of three widely different densities were employed (nylon, Teflon and steel, respectively), provided an excellent means for evaluating the capability of the previously described approximate model to calculate the ejecta trajectory (velocity) as it transits the throat. These tests also provided a basis for assessing the effect of ejecta density variation upon the resulting pulse amplitude and waveform. The initial pulsed waveforms measured at the nozzle entrance and at the chamber fore-end closure in response to the first and second pulses, are shown in Figs 33 and 34, respectively. The test results are summarized in Table 7. The pulse amplitude and duration listed in Table 7 refer to the initial disturbance at the nozzle entrance. Later measurements of the pulse, after it has been reflected from either the fore-end or the nozzle end, show that at that time the pulse has approximately doubled its initial amplitude. This is a consequence of the reflection process for a traveling wave.

Using the previously described methodology, ejecta trajectory calculations were performed for two assumed values of ejecta initial velocity, and three different values of the drag coefficient. The calculated pulse durations (time for ejecta to pass the throat plane) are tabulated in Table 8. From a comparison of Tables 7 and 8, it is concluded that: pulse duration is only weakly dependent upon drag coefficient and initial ejecta entrance velocity; and that a reasonable choice of these parameters

257

TABLE 6.   Comparison of Measured and Predicted Pulse Amplitudes at the Head-End Closure

Test No.	Grain Length(In.)	Ejecta Size(In.)	Fraction Blocked	Ejecta Material	ChamberPressure(Psi)
1	19.7	.4375	.364	RTV	990
2	16	.4375	.45	RTV	832
3	12	.375	.482	RTV	993
4	8	.375	.726	RTV	900
5	16	.4375, .60	.369, .694	NYLON	905,877
6	16	.4375, .60	.369, .694	TEFLON	805,856
7	16	.4375, .60	.369, .694	STEEL	751,811
8	32	.5	.284	TEFLON	1085
9	48	.872	.575	TEFLON	1200
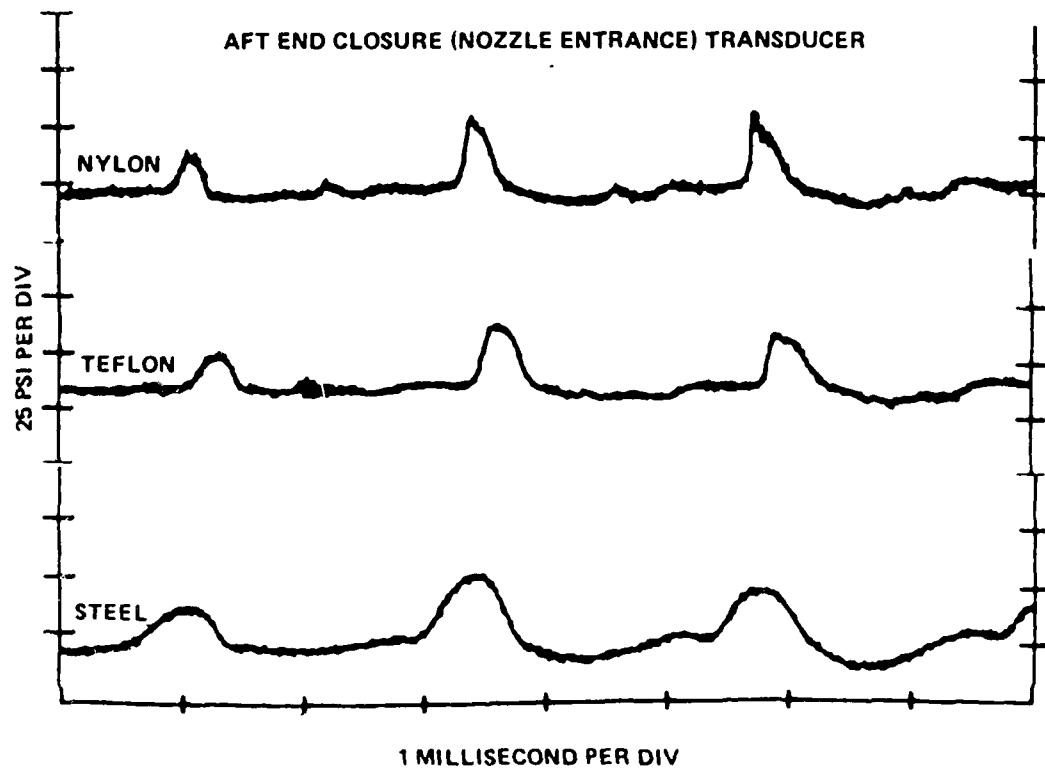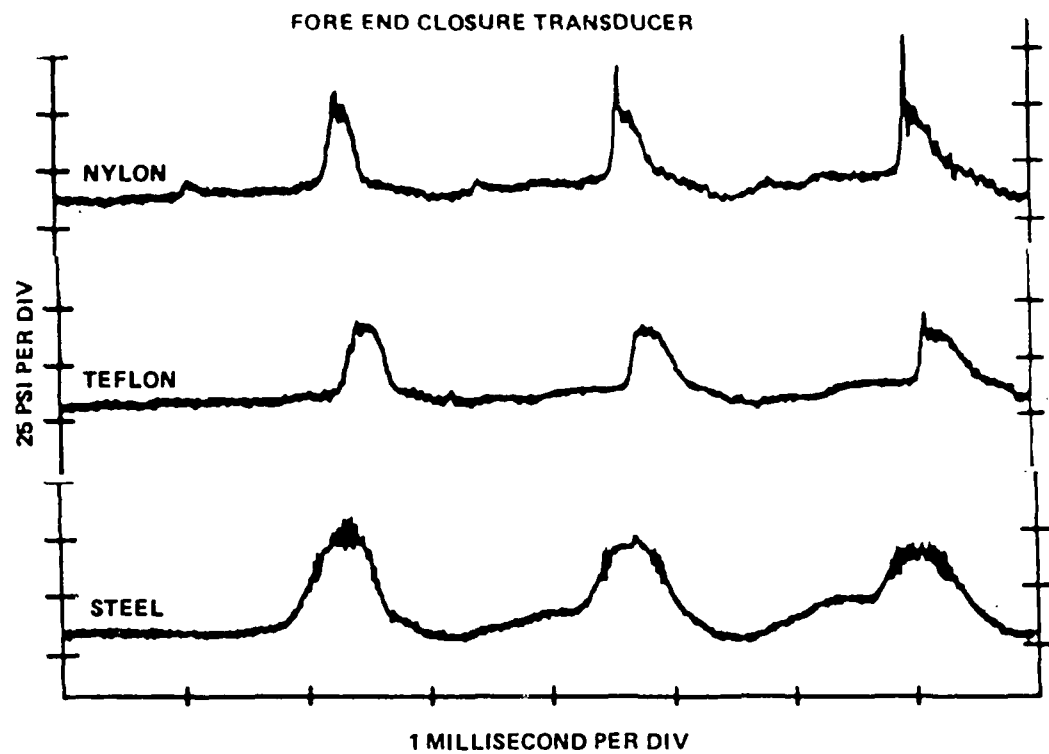
Fig. 33. Measured pressure perturbations at the fore-end and aft-end closures induced by the first pulse, tests 5-7.

FORE END CLOSURE TRANSDUCER

NYLON

TEFLON

STEEL

25 PSI PER DIV

1 MILLISECOND PER DIV

AFT END CLOSURE (NOZZLE ENTRANCE) TRANSDUCER

NYLON

TEFLON

STEEL

25 PSI PER DIV

1 MILLISECOND PER DIV
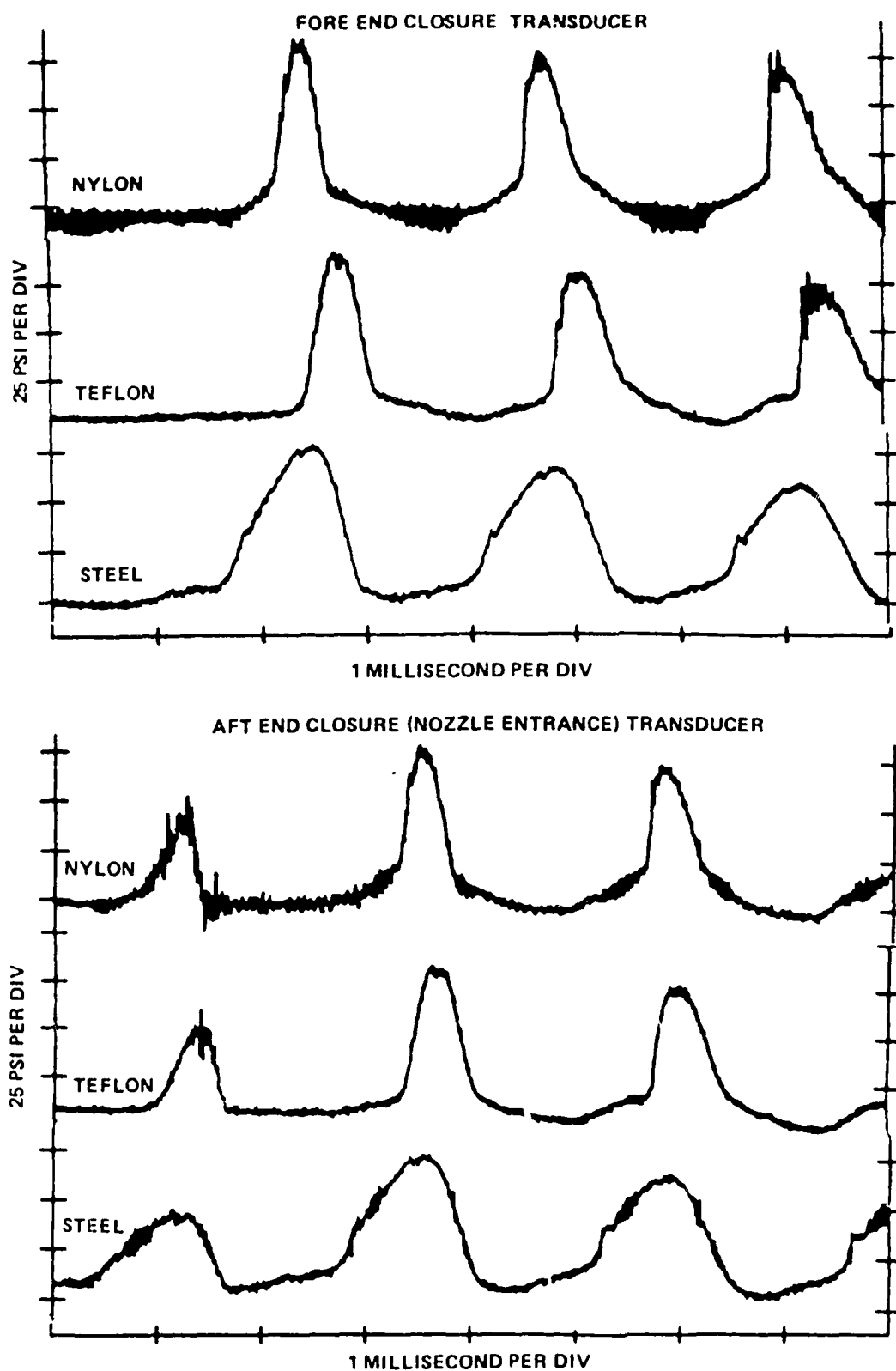
Fig. 34. Measured pressure perturbations at the fore- and aft-end closures induced by the second pulse, tests 5-7.

260

Test No.	Pulse	Ejecta Mat'l	Density (lbs/in³)	Diam. (inches)	f (max) b	Mean Press. (psi)	Pulse Amp. (psi)	Pulse Duration (millisecs.)
5	1	Nylon	0.039	0.4375	0.369	905	15.0	0.34
	2	Nylon	0.039	0.60	0.694	877	39.7	0.59
6	1	Teflon	0.075	0.4375	0.369	805	14.9	0.49
	2	Teflon	0.075	0.60	0.694	856	38.4	0.74
7	1	Steel	0.275	0.4375	0.369	751	17.8	0.88
	2	Steel	0.275	0.60	0.694	811	34.4	1.33

Table 7. Ejecta density variation tests.

Test No.	Ejecta Density (lb/in³)	Ejecta Diam. (inches)	v_e = 100 in/sec		v_e = 300 in/sec	
			C_D	Duration (millisecs)	C_D	Duration (millisecs)
5	0.039	0.4375	0.5	0.36	0.4	0.40
			0.6	0.34	0.5	0.36
			0.7	0.32	0.6	0.32
		0.60	0.5	0.54	0.4	0.58
			0.6	0.50	0.5	0.52
			0.7	0.46	0.6	0.50
6	0.075	0.4375	0.5	0.52	0.4	0.56
			0.6	0.48	0.5	0.50
			0.7	0.44	0.6	0.46
		0.60	0.5	0.74	0.4	0.78
			0.6	0.66	0.5	0.70
			0.7	0.64	0.6	0.66
7	0.275	0.4375	0.5	0.99	0.4	0.94
			0.6	0.90	0.5	0.86
			0.7	0.82	0.6	0.82
		0.60	0.5	1.38	0.4	1.32
			0.6	1.28	0.5	1.22
			0.7	1.16	0.6	1.16

Table 8. Computed pulse durations.

$C_D=0.6$, $v_e=100$ in/sec
f_b (max)=0.369

.75

.50 Nylon   Teflon

.25   Steel

Fraction Blocked

.4   .8
Time. Millisecs
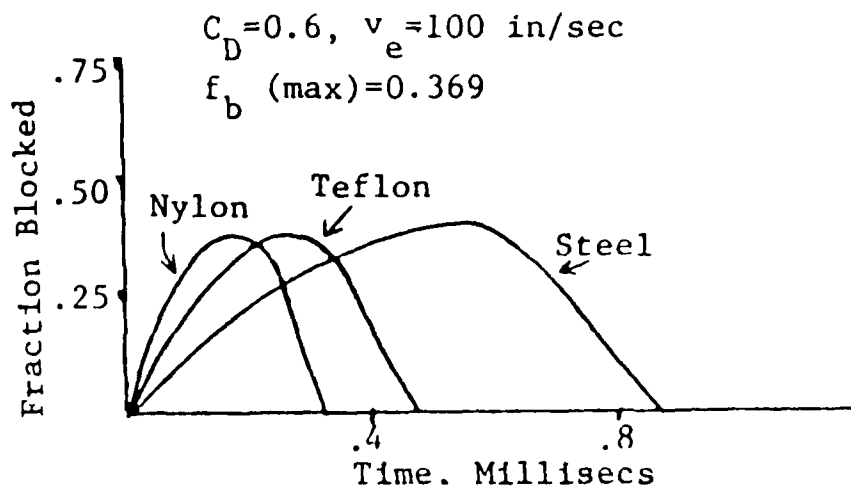
Fig. 35. Computed fraction blocked vs. time, first pulse, tests 5-7.

$C_D=0.6$, $v_e=100$ in/sec
f_b (max)=0.694

.75 Nylon   Teflon   Steel

.50

.25

Fraction Blocked

.4   .8   1.2
Time. Millisecs

Fig. 36. Computed fraction blocked vs. time, second pulse, tests 5-7.
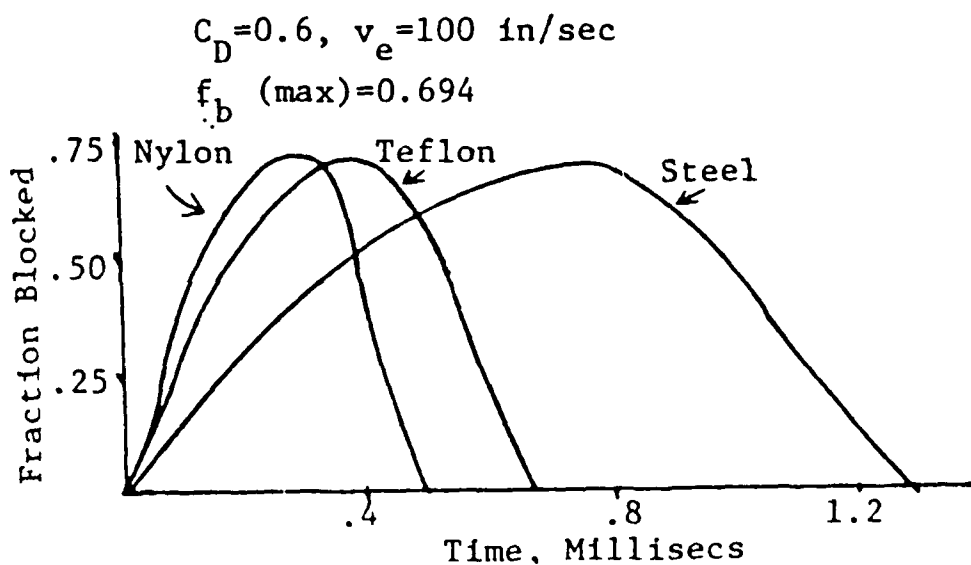
results in calculated pulse durations that are approximately correct. The resulting pulse amplitude is also relatively insensitive to ejecta velocity (except, as will be pointed out later, for very fast ejecta velocities). Thus, efforts to improve upon the present simple ejecta trajectory prediction methodology do not appear to be warranted.

For present purposes, the remainder of the ejecta trajectory calculations were carried out using an entrance velocity of 100 inches/second and a drag coefficient equal to 0.6. Using these values, the fraction of throat area blocked was calculated. Figures 35 and 36 show the variation of fraction of throat area blocked as a function of time for the first and second pulses of tests 5-7, respectively. The ejecta velocity increases monotonically with time as it passes through the nozzle (barring collision with the nozzle walls). Thus, the time interval from initial blockage to maximum throat blockage is longer than the time required to return from maximum blockage to the original cleared throat area. Hence, the initial waveform of the ejecta pulse, measured at the nozzle entrance, should have a shallower front (rise) and a steeper back (decay). The initial measured waveforms all have this characteristic (which is especially evident with the slower steel balls); however, nonlinear wave propagation effects (i.e., steepening, viscosity, viscous wall losses, etc.) rapidly cause the wave shape to change to a steeper wave front and a shallower back.

EVALUATION OF PULSE AMPLITUDE PREDICTION MODELS
Semi-Empirical Model

The experimental ejecta pulse test results that are shown in Table 7 were also used to examine the validity of the previously described pulse amplitude prediction models. Since Eq. (30) predicts that the pulse amplitude is proportional to the product $f_b J$, the measured pulse amplitudes were plotted as a function of $f_b J$ (Fig. 37). The

data fall below the theoretically predicted line ($\delta p/p_1 = 0.71$ f_bJ), and is reasonably correlated by $\delta p/p_1 = 0.6$ f_bJ. The over prediction of pulse amplitude is most likely a result of imposing a quasi-steady approximation in the model development. As expected, the greatest deviations from the predicted values are for the smallest, fastest moving, ejecta. The two lowest pulse amplitudes shown in Fig. 37 (having the largest deviations) were obtained using smaller rubber ejecta injected into the motor at higher velocities than the other ejecta (larger quantities of black powder were utilized in the ejecta pulser unit). The measured pulse durations of these ejecta at the nozzle entrance were only 0.3 milliseconds. Conversely, the two nylon ejecta data points at f_bJ values of 0.035 and 0.0435 were obtained for larger (slower) ejecta in a 3.0 inch diameter test motor. Until a more accurate, fully transient, two dimensional model describing ejecta motion through a nozzle is developed, the relation $\delta p/p_1 = 0.4$ f_bJ should probably be used instead of the aforementioned relation when ejecta pulse durations are expected to be in the range of 0.2 to 0.4 milliseconds.

In full scale motors, the larger ejecta necessary to produce reasonable pulse amplitudes should have dwell times on the order of a millisecond, and the relation $\delta p/p_1 = 0.6$ f_bJ should yield reasonably accurate predictions of initial pulse amplitude.

Numerical Model

The task of defining pulse amplitude is not as straightforward as it seems since the amplitude of the pulse varies with axial location in the motor. Thus, simple correlations of predicted and measured "pulse amplitude" values cannot tell the whole story. It has already been mentioned that when a traveling pulse reflects from the head-end closure, its amplitude at the head end is approximately double its amplitude at the middle of the chamber. Several other physical processes involved in wave
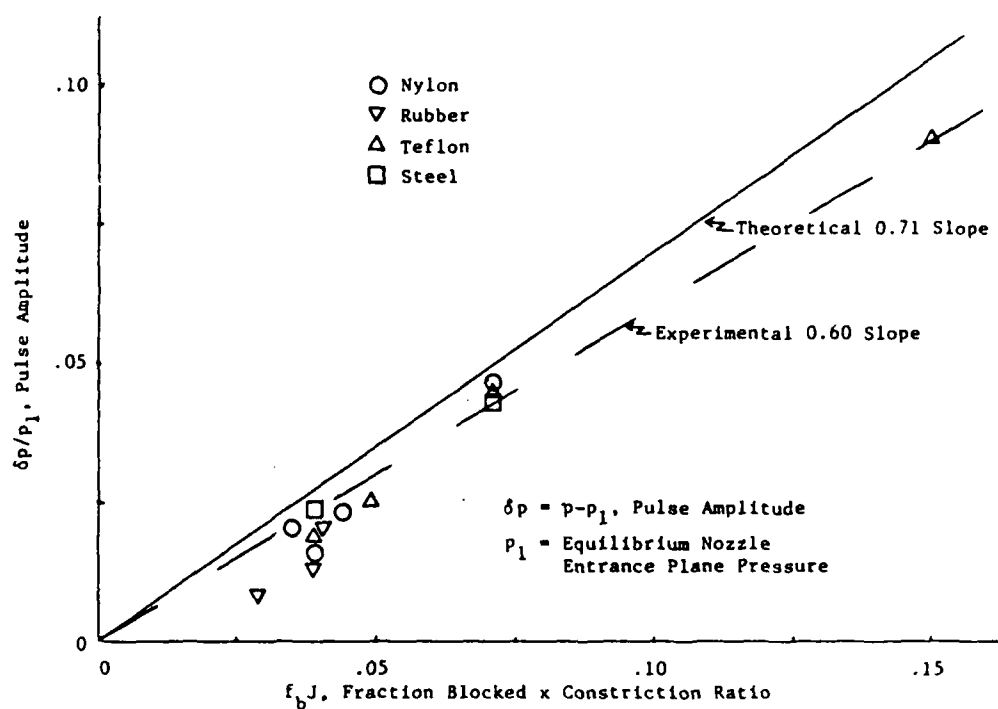
Fig. 37. Ejecta pulse amplitude vs. fraction blocked times constriction ratio.

265

propagation can affect the measured pulse amplitude. One such effect is the formation of a system of multiple shock waves that results from the partial reflection of the pulse from area or grain discontinuities or the continuous partial reflection/transmission of a pulse traveling in a variable cross section area chamber.

Since the numerical model properly treats the operative nonlinear wave propagation mechanisms, it can treat the pulse amplitude prediction problem without the necessity of defining a single value for "pulse amplitude." In addition, being a complete nonlinear combustion analysis, the numerical approach can also be used to predict the motor response to ejecta pulsing (see next subsection).

Although the present numerical model has the above advantages, it still employs a quasi-steady assumption in specifying the time dependent Mach number boundary condition at the nozzle entrance. Thus, it was expected that some empirical correction of the boundary condition would be necessary to achieve accurate pulse amplitude predictions. The calculated results bore out that expectation. When the fraction of throat area blocked as a function of time was empirically modified, using the results shown in Fig. 37 as a guide, the predicted and measured pulse amplitudes were in excellent agreement, as shown in Table 9. The results also verified the ability of the analysis to predict the observed waveforms, and its ability to correctly predict the change in pulse amplitude and waveform as it traverses the combustion chamber (over several wave cycles).

Motor Response to Ejecta Pulsing

Triggered nonlinear instabilities were observed in all of the tests shown in Table 9. In tests 1, 2, 3, 8, and 9, the first ejecta triggered the instability, while in

TABLE 9

Comparison of Measured and Predicted Pulse Amplitudes
(in Percentage of Mean Pressure)
at the Head End Closure

Test Number	Head End	
	Measured	Predicted
1 first pulse	3.4	3.5
2 first pulse	3.6	3.7
3 first pulse	1.7	1.8
4 first pulse	1.6	1.6
5 first pulse	3.9	3.8
5 second pulse	9.6	10.8
6 first pulse	4.4	4.7
6 second pulse	9.7	10.2
7 first pulse	5.9	6.1
7 second pulse	9.2	10.3
8 first pulse	6.6	7.8
9 first pulse	19.9	22.7

tests 4, 5, 6, and 7 the motor was stable in response to the first pulse but unstable in response to the second pulse. It has been observed that the amplitude of the oscillations increased as the grain was lengthened. Small increases in mean chamber pressures (DC shifts) were observed whenever the motor sustained nonlinear instability. The DC shift also increased in magnitude as the length of the propellant grains was increased. In addition, significant changes in the oscillations waveform were observed. As the grain was lengthened, the waveform became narrower and steeper (both front and back). Thus, it was concluded that longer grains are capable of sustaining waves with considerably more high frequency content than shorter grains.

The nonlinear combustion instability analysis was utilized in Chapter 3 to predict the response of solid rocket motors to piston, low brisance, and pyrotechnic pulsers. Excellent agreement between the measured and predicted motor response was demonstrated. As explained therein, present deficiencies in combustion response modeling require that some of the parameters in the transient combustion models be empirically adjusted to best fit the experimental data. In the piston and pyro pulsing investigation, the constants were determined from one test and were used successfully in predicting the results of five other pulses. The motors and propellant used in this previous study were the same as used herein, except that the grain lengths were not significantly varied (8 to 9 inches), and the motors were pulsed at considerably higher chamber pressures (1500-1900 psi). Results obtained using the nonlinear model to predict motor response to ejecta pulsing are discussed below.

Figures 38 to 41 show comparisons between the predicted and measured head-end pressure oscillations for tests 1, 6, 7, and 9. Since the ejecta tests used the same propellant as the earlier piston and pyro pulser tests, the initial ejecta calculations were made using the same combustion response parameters. The final solutions shown

in these figures employed the same values for the parameters that determine the pressure coupled response. Nevertheless, as expected, the velocity coupled response function values had to be varied, as the grain length varied, in order to achieve best agreement with the data. The ad hoc velocity coupling formulation used in the present analysis does not model the governing fundamental physical mechanisms (which remain to be identified). Thus, the fact that it cannot predict the proper variation of velocity coupling with grain length should not be surprising.

The velocity coupled response functions used in the predictions ranged from 2.9 to 4.6. In general, the longer the grain, the lower the value of R_{vc} used. In Chapter 3, a value of R_{vc} equal to 3.5 was used with 8-inch long grains; however, the chamber pressure in the earlier tests was about double that of the present tests.

In test 1, the motor was driven unstable by the first pulse. At this time in the firing, the partial grain is not flush with the chamber wall. As discussed in Chapter 3, the area discontinuity causes multiple reflections of the primary shock wave as it traverses the chamber. Figure 38 shows that the analysis predicts the observed occurrence of multiple waves (one reflection before and one reflection following the primary shock wave), and also shows the ability to predict the observed growth rate of the oscillations.

Figures 39 and 40 for tests 6 and 7, respectively, demonstrate the effect of ejecta density on motor response. Both motors were stable in response to the first pulse and unstable in response to the second pulse. As previously discussed, both the Teflon (test 6) and steel (test 7) ejecta produced approximately the same initial pulse amplitudes (at the nozzle entrance), however, the lighter Teflon ejecta produced a much narrower pulse than the steel ball. The Teflon induced pulse is already shocked by the time the
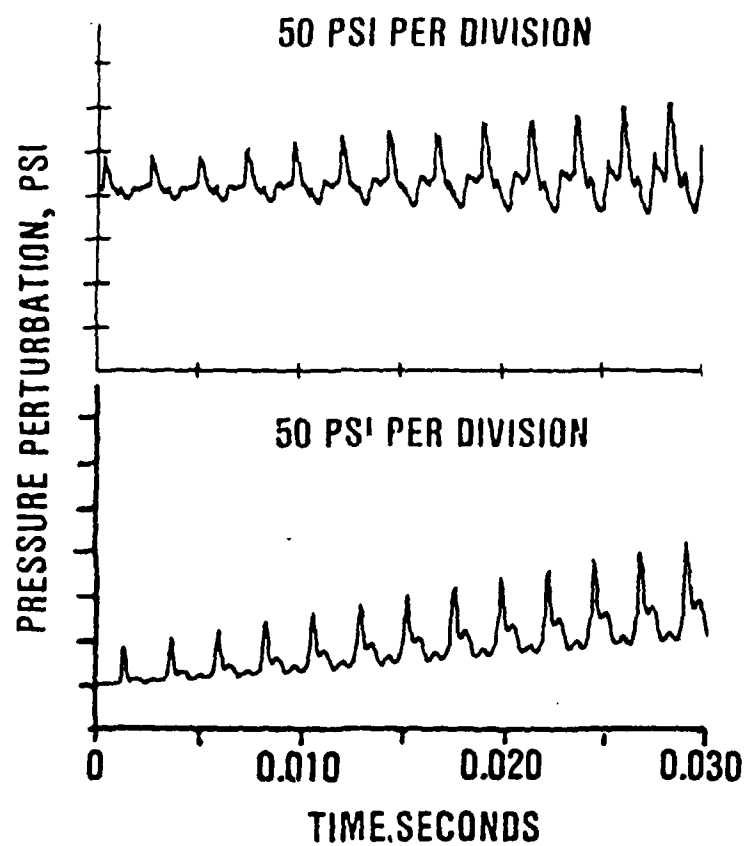
269

Fig. 38.   Comparison of measured and predicted pressure
perturbations at the head-end, test 1.

270

pulse reaches the head-end of the motor. As time progresses, this pulse slowly widens and decays in amplitude until limit cycle conditions (amplitude and waveform) were achieved. The response to the steel ejecta is considerably more complex. The steel induced initial waveform is almost a pure fundamental mode disturbance with very little higher harmonic content. The transformation to a steep fronted wave takes about nine wave cycles (during which time the amplitude continuously decays). Only when the wave becomes a traveling shock does it begin to grow. As the wave grows it changes shape, and eventually reaches approximately the same limiting amplitude and waveform as the teflon pulsed motor.

The predicted behavior for tests 6 and 7 (shown in Figs. 39 and 40) closely parallels the observed motor response. The initial pulse amplitude and waveform, the time evolution of the pressure wave and limiting amplitude are all correctly reproduced. The ability of the analysis to correctly reproduce the complex behavior of test 7 was particularly gratifying.

Figure 41 shows the pressure data measured at the head end for test 9 (full length grain). The first ejecta produced a narrow pulse, with a measured amplitude at the head end closure of 250 psi. This pulse initiated a sustained instability in the motor. The waveform development in this case was distinctly different from that in motors with short partial length grains. The narrow initial pulse became even a narrower, spike-like wave, followed by a small second compression wave. The full length grain also produced a substantially larger mean pressure increase (DC shift) than the partial length grains. The DC shift of about 10 percent is not apparent in the experimental data because the DC pressure component of the transducer signal has been filtered out. The DC shift is apparent in the calculated results, which in addition to predicting the observed mean pressure shift, also correctly predicts the initial and the time evolution of the amplitude, waveform growth, and harmonic content.
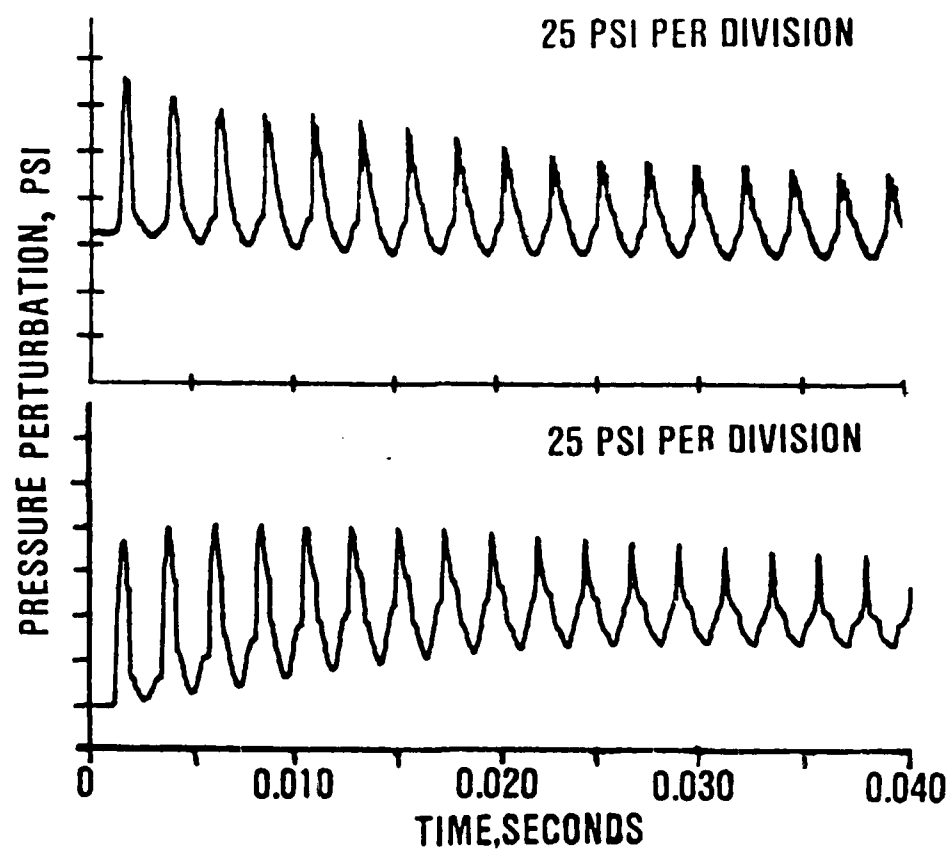
271

Fig. 39. Comparison of measured and predicted pressure perturbations at the head-end, test 6, second pulse.
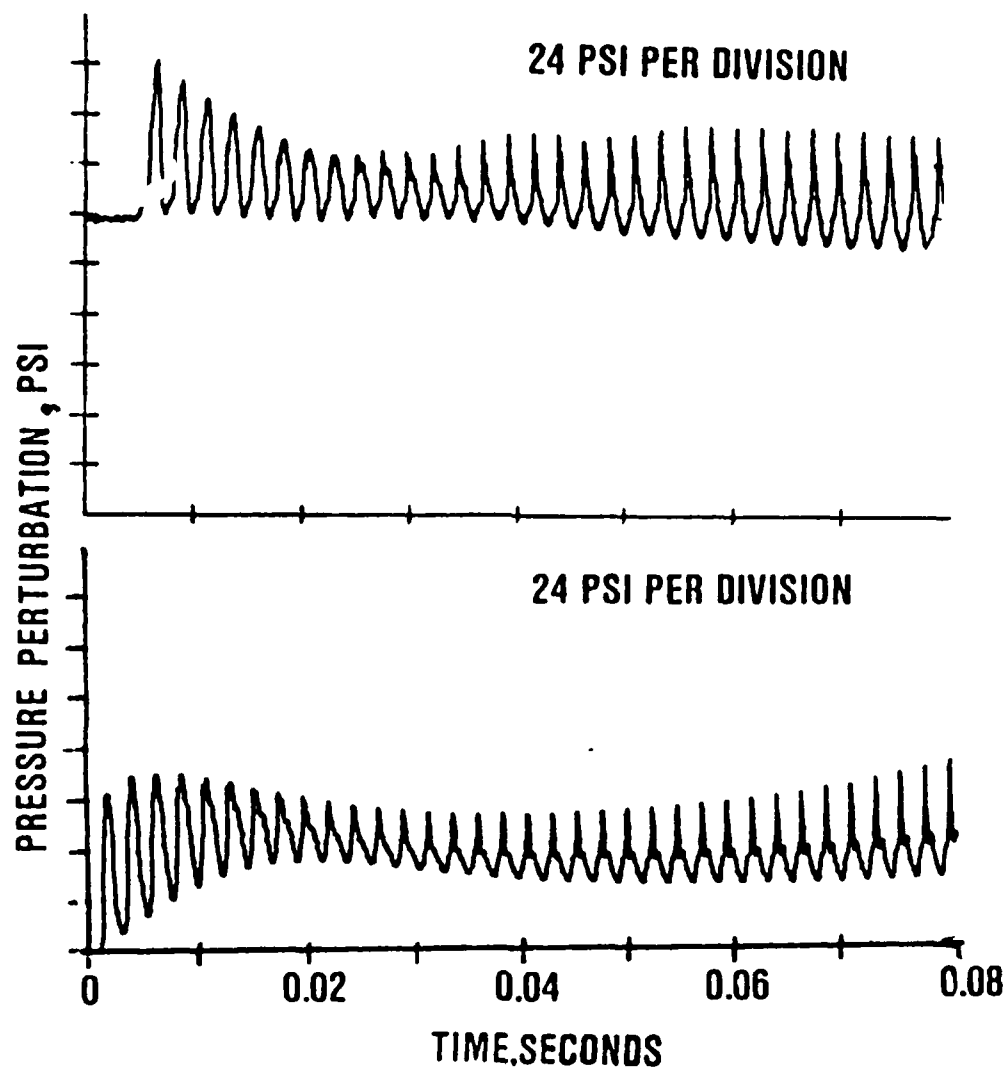
Fig. 40. Comparison of measured and predicted pressure perturbations at the head-end, test 7, second pulse.
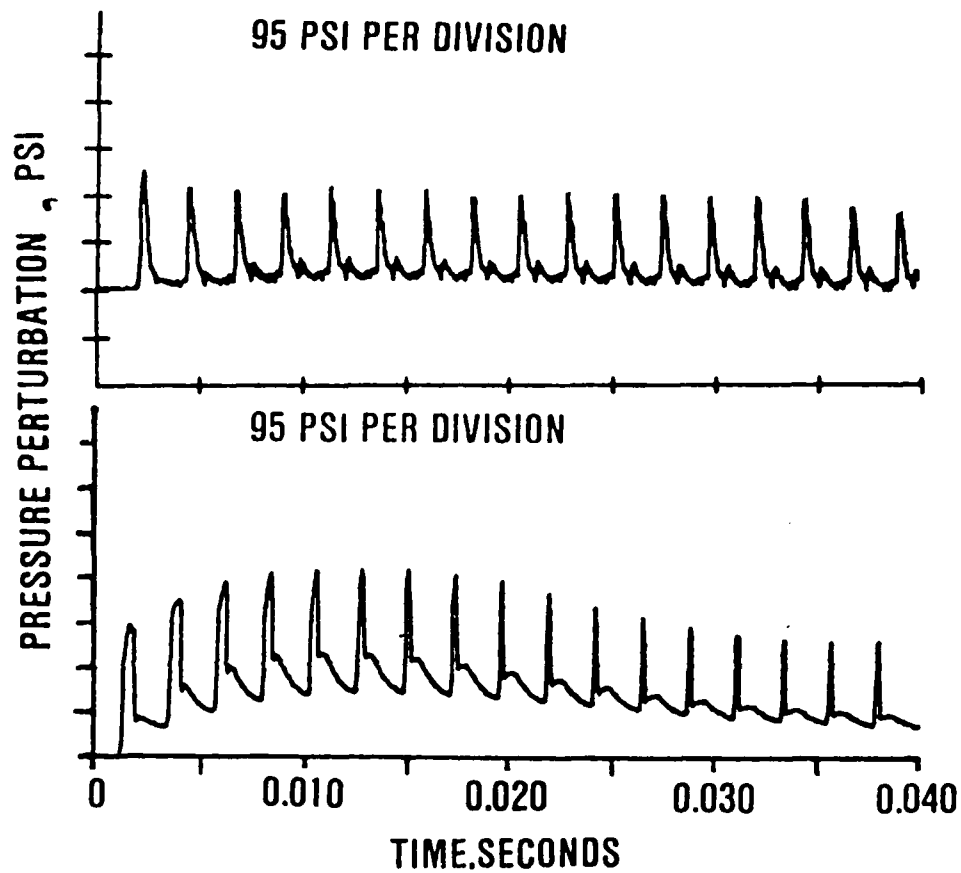
Fig. 41. Comparison of measured and predicted pressure
perturbations at the head-end, test 9, second pulse.

Although not shown herein, good agreement was also obtained between the predicted and measured results for tests 2, 3, 4, 5, and 8. In all cases where the first pulse was stable and the second unstable (tests 4, 5, 6, and 7), the analyses correctly predicted that behavior without any need to adjust the combustion response parameters. It should also be mentioned that tests 6 and 7 are two of the best examples, to date, of experimental evidence supporting previous analytical predictions that the limit cycle is independent of the characteristics of the initiating disturbance.

CHAPTER 5

CONCLUSIONS

Based on the results obtained in this investigation, it was concluded that the original objective of developing a model capable of the accurate, a priori, prediction of mass and energy flow rates produced by four different types of laboratory pulsers and the waveforms produced by these pulsers inside a chamber (i.e., motor response to pulses produced by these pulsers), was achieved.

Ballistic models of the pyro, low brisance, and piston pulsers were developed utilizing a simple lumped volume treatment. The mass and energy flow rates calculated using these pulser performance models are utilized as boundary conditions for the chamber flow problem, which is solved using a modified nonlinear combustion instability model. The ability of the combined pulser/chamber flow models to predict the pulsed waveforms (amplitude and harmonic content) in a closed chamber filled with cold gases (nitrogen and helium) was demonstrated in this report. Excellent agreement between the measured and predicted pressure waves in the chamber was demonstrated even though a simple one-dimensional inviscid analysis was utilized to model a complex two-dimensional viscous process.

Both the experimental and analytical results demonstrate that the pulse characteristics are primarily governed by the mass flux rate from the pulser into the chamber. The pulse waveform was very similar to the shape of the respective pulser mass flux curves for each of the three types of pulsers tested.

On the basis of the comparisons with motor firing data carried out to date with the pyro, low brisance, and piston pulsers, the following conclusions have been drawn:

276

The ability of the developed pulser/chamber model to accurately, a priori, predict both initial pulse amplitude and waveform, under actual solid rocket motor firing conditions, has been demonstrated.

When the parameters which control the pressure and velocity coupled propellant response were empirically fixed on the basis of a single "baseline" pulse test, the nonlinear model was shown to be able to quantitatively predict the measured nonlinear stability of five other pulse tests with the same propellant, but with varying grain geometry, operating conditions, pulser types, and pulse amplitudes. Thus, the present analysis should provide a useful preliminary design tool for predicting the relative nonlinear stability of candidate motor design variations. With further advances in combustion response modeling, the nonlinear model should eventually provide an a priori means for quantitatively predicting the nonlinear longitudinal stability of solid rocket motors.

In view of the known deficiencies in the combustion response models utilized, the ability of the analysis to simultaneously match measured wave amplitudes, waveforms, DC shifts, and in many cases, growth (or decay) rates, was satisfying, although somewhat surprising. It seems likely, therefore, that the present combustion models at least contain all of the essential factors which produce the nonlinear behavior that can be attributed to the propellant response.

A series of ejecta pulsed motor firings was conducted in simple laboratory scale motors with full and partial length cylindrical grains. Ejecta size and density were varied to provide information on the effect of these parameters on pulse amplitude, pulse waveform, and the ability to trigger nonlinear instability. Each of the motors was pulsed twice, and all were triggered into sustained nonlinear instability.

A simple trajectory analysis was developed to calculate the velocity of the ejecta as it transits the nozzle. The model considers only the drag force on the ejecta and neglects effects due to gas flow pressure gradients and ejecta-flowfield interactions. Relatively good agreement between predicted and measured pulse durations was obtained. Parametric calculations demonstrated that the pulse duration is only weakly dependent on initial ejecta velocity and the value used for the drag coefficient; thus, an effort to develop a more complete model of the ejecta dynamics does not appear to be warranted.

Two models for predicting ejecta pulse amplitudes were developed. A simple model based on linear wave propagation theory and the assumption of quasi-steady nozzle behavior, and a numerical model which utilizes the quasi-steady nozzle assumption to provide a nozzle entrance boundary condition for a comprehensive nonlinear instability analysis. The simple model is limited to the prediction of the ejecta induced pulse amplitude at the nozzle entrance plane. The numerical model is more complete and can predict the initial pulse amplitude and waveform at all locations in the motor (not just the nozzle entrance plane) as well as the temporal and spatial evolution of the pulse, i.e., the motor response to ejecta pulsing. The simple method predicts the pulse amplitude to be proportional to the product of the fraction of the nozzle area blocked and the initial constriction ratio of the nozzle $\delta p/p = 0.71 \, f_b J$. A semi-empirical expression of the form $\delta p/p = 0.6 \, f_b J$ yields a good correlation of the data, supporting the validity of the analysis and demonstrating that the quasi-steady assumption leads to over prediction of pulse amplitude. As ejecta size decreases, velocity increases and pulse duration decreases. When pulse duration is decreased to the range of about 0.2 - 0.4 milliseconds, the data is better correlated by $\delta p/p_1 = 0.4 \, f_b J$. Comparisons with data verified the ability of the analysis to predict the observed waveforms, and its ability to correctly predict the change in pulse amplitude as it traverses the combustion chamber.

278

The test results demonstrated that both pulse amplitude and pulse duration influence the ability of a pulse to trigger instability (higher amplitudes and shorter pulse durations enhance triggering potential). The observed greater susceptibility of motors to triggering at later burn times agrees with many other previous observations. Oscillation amplitudes, DC shifts, and amount of high frequency content were all observed to increase with increase of grain length (in a motor of fixed length). The existence of area discontinuities, when the partial length grains are not flush with the case, results in multiple wave reflections, which, in general, make it more difficult to trigger such configurations into instability.

Many of the complexities observed in unstable motor oscillations are caused, or strongly influenced, by discontinuities in the grain geometry. This is especially true for multiple shock wave behavior induced by partial shock wave reflection at area discontinuities.

The wide range of waveforms and nonlinear behavior observed in the experiments result from interactions between a number of complex nonlinear physical phenomena. Comparisons between predictions obtained with the present comprehensive nonlinear instability analysis and the experimental data indicate that the model is capable of predicting all of the observed characteristics, i.e., pulse amplitude and waveform, waveform evolution, growth rate, DC shifts, waves that decay and then grow (and vice versa), etc.

Although the present analysis appears to contain all of the essential factors necessary to produce the observed nonlinear behavior of solid rocket motor instabilities, the results of the present comparison study, in which grain lengths were systematically varied, point out deficiencies in the existing modeling of the effect of acoustic velocity

oscillations on the combustion response of the propellant (velocity coupling). The present predictions require empirical adjustment of the velocity coupled response to obtain the best possible agreement. Further progress in the understanding and modeling of the physical mechanisms which govern the combustion response of solid propellants must be accomplished before quantitative, a priori, stability predictions can be obtained.

It is strongly recommended that great care be taken in future motor pulse testing to ensure that the piezoelectric pressure transducers are mounted and protected in a manner that will keep the resonant frequency of the transducer as high as possible. Resonant frequencies above 60 kHz should be sought in order to keep transducer "ringing" effects from significantly compromising the integrity of the data.

Additional comparisons with motor data should be carried out to further evaluate the ability of the present analysis to predict the effect of grain design, pulse type and pulse amplitude, for a wider range of propellants, motor operating conditions, and pulse characteristics than contained herein.

REFERENCES

1. Combs, L. P., et al: "Improvement of Bombs and Pulse Guns as Combustion Stability Ratings Devices," AFRPL-TR-68-18, Mar 1968.

2. Dickinson, L. A., "Command Initiation of Finite Wave Axial Combustion Instability in Solid Propellant Rocket Motors," ARS J., Vol. 32, 1962, p. 643.

3. Roberts, A. K., "Development of the 9K 11000 Black Brant III Rocket Engine," CAS J., 1962, pp. 137-143.

4. Morris, E. P., "A Pulse Technique for the Evaluation of Combustion Instability in Solid Propellant Rocket Motors," CAS J., 1965, pp. 329-333.

5. Brownlee, W. G., "Nonlinear Axial Combustion Instability in Solid Propellant Motors," AIAA J., Vol. 2, No. 2, 1964, pp. 275-284.

6. Murray, J. A., et. al., "Pulsing Criteria for Solid rocket Motors," Volume I, Final Report, and Volume II, "Motor Pulsing Design Manual," AFRPL-TR-79-45, 1980.

7. Lovine, R. L., "Nonlinear Stability for Tactical Motors-Pulsing Consideration," presented in the 18th JANNAF Combustion Meeting, October 19-23, 1981, Pasadena, California. Vol. III, CPIA Publication 347, Oct 1981, pp. 73-79.

8. Levine, J. N. and Culick, F. E. C., "Nonlinear Analysis of Solid Rocket Combustion Instability," AFRPL-TR-74-45, Oct 1974.

9. Beckstead, M. W., "Report of the Workshop on Velocity Coupling," presented at the 17th JANNAF Combustion Meeting, Vol. I, CPIA Publication 324, Nov 1980, pp. 197-200.

10. Lovine, R. L. and Mockenhaupt, J. D., "Nozzle Ejecta Pulse Tests of Solid Rocket Motors," presented at the 19th JANNAF Combustion Meeting, October 4-7, 1982, NASA Goddard Space Flight Center, Greenbelt, Maryland. Vol. II, CPIA Publication 366, Oct 1982, pp. 135-146.

11. Schlichting, H., Boundary Layer Theory, McGraw-Hill Book Company, New York, Seventh Edition, 1979.

NOMENCLATURE

a	gas only, speed of sound
A	vent area
A_p	piston area
A_1	chamber area
C	charge weight
C_d	orifice coefficient
c_p	isobaric heat capacity
C_s	subcritical flow correction
c_v	isochoric heat capacity
C_w	sonic flow coefficient
d_v	vent diameter
E_i	energy venting rate into the chamber
f	fraction of burning pellets remaining in pyro pulser
F	pyro pulser coefficient, RT_o
f_v	fraction vent area opened by piston travel in brisance pulser
g	gravitational constant
K	a parameter defined in Eq. 5
m	mass of gas in combustion chamber
$\dot{m}_b$	mass burning rate of pyro charge
$\dot{m}_i$	mass venting rate into chamber
$\dot{m}_o$	mass flow rate out of pulser

n	charge burning rate exponent
N	number of charge pellets in chamber
p	pressure
p_b	bore pressure
p_c	motor chamber pressure
R	specific gas constant
r_v	vent radius
s	web fraction burned
$\dot{s}$	rate of change of web fraction burned
t	time
T	gas temperature
T_i	temperature of the combustion products entering the breech
T_o	isochoric flame temperature
u	piston velocity
u_1	gas velocity at chamber fore-end
v, v_o	volume, and initial volume, respectively
x, x_s	piston travel, and total stroke, respectively
γ	isentropic constant
ρ	density

Subscripts

1 - mesh point No. 1 located at the fore-end

1' - origin of left running characteristics reaching point No. 1.